Northumbria Research Link

Citation: Nwankwo, Stephen Ndubuisi (2019) Process and Post-annealing Optimisation of SnS Thin Films with Alternative Buffer layers. Doctoral thesis, Northumbria University.

This version was downloaded from Northumbria Research Link: http://nrl.northumbria.ac.uk/41989/

Northumbria University has developed Northumbria Research Link (NRL) to enable users to access the University's research output. Copyright © and moral rights for items on NRL are retained by the individual author(s) and/or other copyright owners. Single copies of full items can be reproduced, displayed or performed, and given to third parties in any format or medium for personal research or study, educational, or not-for-profit purposes without prior permission or charge, provided the authors, title and full bibliographic details are given, as well as a hyperlink and/or URL to the original metadata page. The content must not be changed in any way. Full items must not be sold commercially in any format or medium without formal permission of the copyright holder. The full policy is available online: http://nrl.northumbria.ac.uk/policies.html

Northumbria University NEWCASTLE

UniversityLibrary

Process and Post-annealing Optimisation of SnS Thin Films with Alternative Buffer layers

Stephen Ndubuisi Nwankwo

A thesis submitted in partial fulfilment of the requirements of the University of Northumbria at Newcastle for the degree of Doctor of Philosophy

Research undertaken in the Faculty of Engineering and Environment

September 2019

Abstract

Tin sulphide (SnS) is an environmentally friendly, Earth abundant and easy to fabricate thin film solar absorber for photovoltaic solar cell application. This work examines the properties of thermally evaporated SnS thin films, as a function of deposition parameters. Films were also subjected to a range of post-deposition treatments in vacuum, atmospheric pressure, chlorine and selenium ambient.

SnS solar absorber layers were successfully deposited at low temperature (100 ^{o}C) to a thickness range from 100 to 3500 nm using thermal evaporation. Grain growth was partly dependent on the layer thickness where a progressive increase in grain size was noticed with increasing film thickness from 100 to 1500 nm; above 1500 nm thickness no further visible increase in the grains could be seen. Films grown to a thickness of 800 nm are found to be near stoichiometry with optimum energy bandgap compared to the thinner or thicker films. However, the SnS thin films showed strong dependence on substrate temperature. The temperature dependent study reveals that higher substrate temperatures lead to an increase in adatoms mobility, thereby promoting coalescences of smaller grains to form bigger grains. The increase in grain size with substrate temperature however stagnates after 350 ^{o}C such that further increasing the temperature does not induce further grain growth. Samples deposited at 350 ^{o}C substrate temperature were stoichiometric (Sn/S = 1.00) and with energy bandgap of 1.37 eV. Texture coefficient calculations showed that (111) orientation is more likely associated with the substrate temperatures $\leq$ 300 ^{o}C while, the (040) diffraction plane is related to higher temperatures ($\geq$350 ^{o}C). Photoluminescence measurements demonstrated that controlling the film composition and optical bandgap is critical to produce a film that will luminesce, a requisite for any implementation in solar devices. On the other hand, the type of susbtrate material was found to significantly influence the properties of the SnS absorber films.The substrates studied include soda lime glass (SLG), quartz (Q), indium tin oxide (ITO) and fluorine-doped tin oxide (FTO) coated glass, molybdenum (Mo) coated SLG and quartz.

Films composition remains stoichiometric (Sn/S = 1.00 ± 0.01) across the range of substrates. For the Na-free samples, reduction in micro-strain followed an increase in grain size. Unlike kesterite or chalcopyrite materials, the absence of Na in the substrate induces a significant grain growth with the average grain size increasing from 0.14 μm on SLG to 0.32 μm on quartz, ITO and FTO. SnS absorber layers deposited at 350 °C (thickness of 800 nm) were subjected to heat treatment in diverse environments such as vacuum (P = $\leq 10^{-6}$ mbar, 60 min), nitrogen (P=1000 mbar, 60 min) and selenium (20 min under 10 mbar argon pressure) for temperatures greater than the growth temperature (400-500 °C). Vacuum annealing was ineffective in both inducing grain growth and achieving recrystallisation. Nitrogen ambient revealed a recrystallised structure with slight increase in grain sizes and ~6% decrease in the bandgap compared to the reference 1.37 eV for the as-grown layer due to loss of sulphur (Sn/S ratio increased from 1.00 to 1.27 following anneal). The incorporation of Se led to substantial increase in grains with an average grain size of ~2.0 μm compared to 0.14 μm for as-grown films, with a nearly complete sulphur substitution by selenium. In addition, Se incorporation minimised voids while reducing the bandgap to 1.28 eV, improving photoluminescence yield and the open circuit voltage. Finally, this thesis explores a range of n-type buffer layers in order to fabricate devices. Numerical simulations show that ZnS buffer layer has potential to replace conventional CdS in fabricating SnS-based solar cells as it offers the most appropriate band alignment. Working devices could only be fabricated when combining the selenium heat treatment and the ZnS buffer layer.

List of contents

Abstract i

List of contents iii

Acknowledgements vii

Declaration viii

List of publications and conference presentations ix

Chapter 1 1

Introduction to Thin Film Photovoltaic Technology 1

1.1 Motivations 1

1.2 Thin film photovoltaic technology 4

1.3 Fundamentals of semiconductors 5

1.3.1 Semiconductor band structure and light absorption 6

1.3.2 Carrier generation, transport and recombination 8

1.3.3 Intrinsic and extrinsic semiconductors 12

1.3.4 The *p*-*n* junction physics 16

1.3.5 Heterojunctions 20

1.3.6 Theory of solar cells and current density-voltage characteristics 21

1.4 Aims of the thesis 25

1.5 Objectives of the thesis 25

1.6 Contribution to knowledge of the thesis 26

1.7 Thesis structure 26

Chapter 2 28

Literature Review 28

2.1 Introduction 28

2.2 Overview of SnS solar absorber 29

2.2.1 SnS phase purity and control 30
2.2.2 Intrinsic defects of SnS 33
2.2.3 Crystal structure 34
2.2.4 Optoelectronic properties 36
2.3 SnS-based thin film solar cell structure 37
2.4 Layer properties of SnS-based devices 41
2.4.1 The substrate 41
2.4.2 The back contact 42
2.4.3 The absorber layer and deposition methods 43
2.4.4 The buffer layer 51
2.4.5 The transparent conducting oxide layer 52
2.4.6 Top contact grid 52
2.5 Conclusions 53
Chapter 3 54
Experimental and Characterisation Methods 54
3.1 Introduction 54
3.2. Substrate preparation 54
3.3 Sample deposition methods 55
3.3.1 Thermal evaporation 55
3.3.2 Magnetron sputtering 58
3.3.3 Electron beam evaporation 61
3.3.4 Chemical bath deposition 62
3.4 Post deposition heat treatment of the samples 64
3.5 Device fabrication processes 66
3.6 Characterisation techniques 67
3.6.1 Thickness measurement 67

3.6.2 Scanning electron microscopy and energy dispersive X-ray spectroscopy 67
3.6.3 X-Ray diffraction 68
3.6.4 Secondary ion mass spectrometry 70
3.6.5 Raman spectrometry 71
3.6.6 Spectrophotometry 72
3.6.7 Hot point probe 73
3.6.8 Photoluminescence spectroscopy 74
3.6.9 Simulated device characteristics 75
3.6.10 Experimental device characteristics 76
Chapter 4 78
Growth and Characterisation of SnS Solar Absorbers 78
4.1 Introduction 78
4.2 SnS sample properties 79
4.3 Results and discussions 79
4.3.1 Optimisation of SnS solar absorber thickness 80
4.3.2 Substrate temperature dependent properties 90
4.3.3 Substrate type dependent properties 111
4.4 Conclusion 118
Chapter 5 120
Post Annealing Treatments and Se-S Substitution 120
5.1 Introduction 120
5.2 Post-deposition heat treatment of SnS thin films 121
5.3 Influence of Se/S substitution on the Sn(S,Se) solar absorber 132
5.4 Conclusions 143
Chapter 6 144
Role of Buffer Layer in SnS Heterojunction device 144

6.1 Introduction ... 144

6.2 Properties of CdS, In_2S_3 and ZnS buffer layers ... 145

6.3 SnS band alignment studies ... 150

6.4 SnS device properties ... 154

6.5 Conclusions ... 158

Chapter 7 ... 160

Conclusions ... 160

7.1 Thesis summary ... 160

7.2 Suggestions for future works ... 163

List of references ... 164

Acknowledgements

I am grateful to the following people and institutes for all their help during my PhD study. Specifically my principal supervisor, Dr Guillaume Zoppi for his great mentorship, guidance and encouragement in my research and life in Northumbria University, Newcastle. I sincerely thank him for giving me the opportunity to undertake the research under his supervision, working with him has been an immeasurable privilege. I would also like to acknowledge Dr Neil Beattie, Dr Vincent Barrioz and Professor Robert Miles for their support and guidance.

I extend my gratitude to Professor Rosie Parnell former faculty director, as well as Faculty of Engineering and Environment Northumbria University for providing me the financial assistance and facilities to carry out my research. This research was also partly funded by the Ebonyi State Government of Nigeria, as well as the UK India Education and Research Initiative (UKIERI). I also appreciate the financial support from Northumbria Graduate School, Institute of Physics and EPSRC SuperSolar Network for allowing me to attend conferences. I equally thank Apostle Dr and Mrs John Ameobi for providing AHFIS grant.

I would also like to thank Professor K.T. Ramakrishna Reddy from Sri Venkateswara University who made my research meetings under UKIERI at Tirupati in India a memorable and fulfilling experience. I am also grateful to NEXUS at Newcastle University for performing XPS measurements. Members of Northumbria photovoltaic research group have been helpful, thank you all for providing good research environment and your individual support. I also acknowledge with thanks the various authors, publishers and owners of copyright materials whose work were made reference to in this thesis.

I sincerely thank my family, especially my wife for their overwhelming support and love to me over the years.

Finally, I owe everything to Almighty God for His Grace and Kindness.

Declaration

I declare that the work contained in this thesis has not been submitted for any other degree and the candidate carried out all the work presented in this thesis except those procedures listed below.

The XPS measurements were taken at National EPSRC XPS User's Service (NEXUS) at Newcastle University. Professor K.T. Ramakrishna Reddy at Sri Venkateswara University in India performed part of Raman measurements included.

Any ethical clearance for the research presented in this thesis has been approved. Approval has been sought and granted by the University Ethics Committee on 14th of December 2015.

I declare that the word count of this thesis is 36,932 words

Name: Stephen Ndubuisi Nwankwo

Signature:

Date: 19/08/2019

List of publications and conference presentations

The study has led to a number of publications and conference papers, which are listed below.

(1) S N. Nwankwo, S. Campbell, K T R. Reddy, N S. Beattie, V. Barrioz, and G. Zoppi, "Temperature controlled properties of sub-micron thin SnS films," *Semiconductor Science and Technology,* vol. 33, no. 6, p. 065002, 2018.

(2) S N. Nwankwo, G.P. Reddy, K T R. Reddy, N S. Beattie, V. Barrioz, R W. Miles and G. Zoppi, "Optimised growth of thermally evaporated tin sulphide (SnS) thin films" Proceedings of the 12th Photovoltaic Science, Applications and Technology Conference, Liverpool, UK, 6 - 8 April, 2016, 11-14.

(3) S N. Nwankwo, N S. Beattie, R.W. Miles and G. Zoppi, "Growth of tin sulphide (SnS) thin films for photovoltaic applications" National conference on Advanced Functional Materials, Tirupati, India, 23 - 24 March, 2016. (Oral presentation).

(4) S N. Nwankwo, N S. Beattie, V. Barrioz and G. Zoppi, "Development of SnS-based thin films and solar cells" Northumbria research conference, Northumbria University, UK, June 15, 2017. (Poster presentation).

(5) S N. Nwankwo, N S. Beattie, V. Barrioz and G. Zoppi, "Effect of substrate type on thermally evaporated SnS thin films" North East Energy Materials Symposium, Durham, April 21, 2017. (Poster presentation).

(6) S N. Nwankwo, N S. Beattie, V. Barrioz and G. Zoppi, "New ways to generate grain growth in SnS absorber layers by post-deposition heat treatment" Northumbria research conference, Northumbria University, UK, June 21, 2018. (Oral presentation).

(7) S N. Nwankwo, K T R. Reddy, N S. Beattie, V. Barrioz, R W. Miles and G. Zoppi "Substrate type dependent properties of sub-micron SnS thin films" Proceedings of the 15th Photovoltaic Science, Applications and Technology Conference, Warwick, 10 - 12 April, 2019.

(8) S N. Nwankwo, K T R. Reddy, N S. Beattie, V. Barrioz, R W. Miles and G. Zoppi, "Optimisation of deposition parameters and chalcogen substitution for SnS thin films,

Supersolar Summer Technical Meeting, Swansea, Wales, 9 - 10 July, 2019. (Oral Presentation).

(9) S N. Nwankwo, K T R. Reddy, N S. Beattie, V. Barrioz, R W. Miles and G. Zoppi "Influence of heat treatments and Se - S substitution on SnS solar absorbers" International Conference on Energy Materials and Interfaces, Newcastle University, 29 July - 01 August, 2019. (Oral presentation).

Chapter 1

Introduction to Thin Film Photovoltaic Technology

1.1 Motivations

Development of environmentally friendly and alternative source of energy have become a global concern to supplement the fast dwindling fossil fuels. Several categories of these alternative or renewable energy technologies exist such as solar, biomass, hydropower, geothermal, tidal and wind. Fossil fuels need to be phased out and possibly replaced by low-carbon source of energy in order to meet the 2 ^{o}C and near zero carbon emission goal of the Paris Agreement [1]. This requires significant (over 80%) use of low carbon energy sources (nuclear and renewables) and a rapid shift towards green electricity before 2050. Solar energy from the sun, which is effectively inexhaustible is the most useful among all forms of renewable energy sources (all other forms of renewable energy sources directly or indirectly depends on the sun) and is reported to possess the potential to contribute significantly to electrical energy generation [2]. The total power of the incident solar radiation on Earth's surface can be estimated from the solar contact (1367 Wm^{-2}) and the cross-sectional area of the Earth covered by land (1.48 $\times 10^{8}$ km^{2}). This will give 2.0×10^{5} TW, which is about 10,000 times the estimated world power requirement for 2050 [3, 4]. However, the distribution of this solar energy on the earth's surface is not uniform due to diverse topography and latitude. Covering only 0.4% of the land area or 1.2% of Sahara desert with 10% efficiency solar panels can provide the current global energy demand [4, 5]. The Sun is the centre of our solar system with an average distance of 1.5×10^{11} m from the Earth. In addition, by far the most crucial source of energy for life on Earth including electricity generation. The Sun is a sphere of a hot gaseous matter with a diameter of about 1.39×10^{9} m and a blackbody surface temperature of 5,778 K under a hydrogen-helium fusion reaction. It radiates solar energy by electromagnetic waves over a wavelength range of 290 - 4000 nm referred to as the solar spectrum. This energy is in the form of photons and depends on variables such as latitude,

time of the day and atmospheric conditions. The intensity of the solar radiation outside the Earth's atmosphere, at the mean Earth-Sun distance is expressed as the solar constant that has value of 1367 Wm^{-2} [6]. The efficiency of a PV cell is sensitive to variations in the spectrum of the incident solar radiation. Following this, ASTM International has developed the standard for the solar spectra for diverse radiation received outside the Earth's atmosphere and at the Earth's surface [7]. These diverse radiations are mostly due to attenuation effects due to atmospheric scattering and absorption, which are defined by air mass (AM). The air mass is the amount of atmosphere that solar radiation have to travel through to reach the surface of the earth and it depends mainly on the position of the sun, while the air mass number indicates the distance travelled by solar radiation in the earth's atmosphere. As shown in figure 1.1, ASTM E490 corresponding to AM0 is the photon incident outside the earth's atmosphere and is useful in space applications. However, the standard spectrum at the earth's surface is the AM1.5G (the G stands for global, which includes both direct and diffuse radiation) or AM1.5D (which includes the direct radiation only) based on standard ASTM G173 (see figure 1.1).

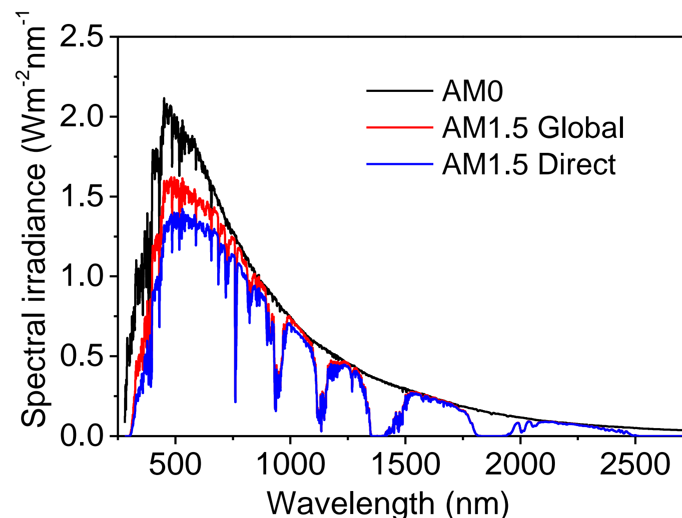

Figure 1.1 Standard solar spectra [8].

The sum of radiation received on the Earth's surface is an integral of the AM1.5G spectrum otherwise called the spectral power density and equals 960 Wm^{-2}, normally rounded up to 1000 Wm^{-2} for ease of use and comparison. This value is used as the standard irradiance on

PV devices, for fair and convenient comparison of solar cells. Thin film solar cells are semiconductor devices, which directly convert solar radiation into electricity. The crucial integral part of any solar cell device is the solar absorbing material, which absorbs sunlight and transports the resulting charge carriers to the electrical contacts via other supporting components. The most used solar absorber to date is the multi-crystalline silicon (Si) but requires thick layer of material about 100 μm to absorb incident light, whereas the use of thin films that require not more than 2.0 μm to absorb most of the incident photon is currently paving the way for cost and material reduction in the photovoltaic industry. Thin films are quasi two-dimensional layers ranging from fractions of a nanometre to several micrometre in thickness. The thickness of the layer is mostly controlled during film deposition. Thin films are crucial in the development and study of materials with new properties such as solar absorbers and photovoltaic devices.

Recent market trends reveals rapid take-up of solar energy in both established and emerging markets as revealed in the PV annual installation in figure 1.2. This trend if sustained with further improvement could guarantee a stable power system with up to 30% solar energy before 2030 [1].

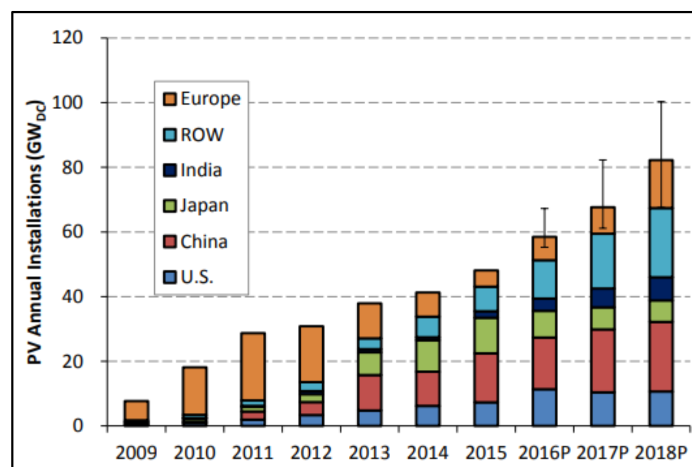

Figure 1.2. Recent trend in market uptake by region of PV installation (P, projected; ROW, rest of the world). Taken from supplementary information [9].

Therefore, the development of low cost and efficient PV technologies is crucial for providing electricity to the growing world population and arresting man-made climate change [10].

1.2 Thin film photovoltaic technology

Thin film photovoltaic (PV) technology involves the direct conversion of sunlight into electricity using an electrochemical or *p-n* junctions made from semiconductor materials via a process called photovoltaic effect. The photovoltaic (PV) effect was discovered by Edmond Becquerel in 1839 [11], when he noticed that a platinum electrodes in a dilute sulphuric acid solution exposed to light produced a voltage. The PV effect occurs in solar cells (the type of cell that composes solar panels) and it can continue to provide voltage and current (product of which gave electrical power in watts, W) as long as light continues to shine on the *p-n* junction materials. Solar cells were first used to provide power in remote locations for communication system, weather monitoring and to power satellites and space vehicles [12, 13]. The energy crisis of 1970 triggered much interest in the use of solar cells for terrestrial applications and to date this technology is being used in diverse areas including consumer products (clocks, toys, calculators), businesses, remote areas in developed and developing world [13]. Production and sales in the PV market has been dominated by crystalline silicon (c-Si), where wafer costs is over 50% of the total module cost. For significant contribution of PV technology to world's energy demand, the major cost component can be eliminated by replacing wafers with thin films of semiconductors deposited on supporting substrates. Thin film technology offers two major advantages over c-Si, which include the possibility of significant reduction (up to 98%) in the active material requirements and ease of adaptation for large area deposition. Light absorber materials of cadmium telluride (CdTe) and copper indium gallium selenide (CIGS) are mostly used for producing thin film solar cells and devices based on both technologies have shown efficiencies > 22% [14]. However, toxicity issues related to use of cadmium in addition to the lack of abundance of tellurium and indium (see figure 3) make these materials sensitive to market fluctuation [3, 15]. As shown in figure 1.3, the availability of tellurium, indium and cadmium in the Earth's crust were estimated to be 0.001, 0.333 and 0.023 parts

per million (ppm), respectively. Unlike CdTe and CIGS, SnS light absorber materials are relatively cheap, non-toxic and earth abundant (availability of 4.8 and 66.5 ppm for tin and sulphur, respectively).

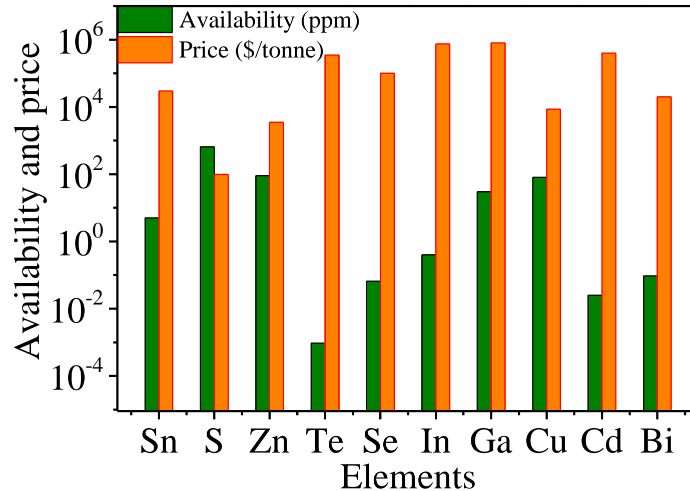

Figure 1.3 Natural occurrence in the Earth's crust and current world trading price of the elements relevant to thin film photovoltaics such as SnS, copper zinc tin sulphide (CZTS), CdTe and CIGS, adapted from [3].

1.3 Fundamentals of semiconductors

Semiconductor materials, which are neither good conductors nor good insulators, have their electrical properties in the middle between those of conductors and insulators. These materials have range of useful properties that include passing current in one direction easily rather than the other, displaying variable resistance and sensitivity to incident photon. In photovoltaic application, the interaction of incident photons with the semiconductor can lead to generation of carriers that can be collected to create electric current. For this to happen, the incident photon energy (eV) must reach the semiconductor surface and be equal to or greater than the energy bandgap of the semiconductor to trigger flow of electrons from the valence band (VB) to conduction band (CB). The best-developed semiconductor materials are silicon (Si) and germanium (Ge) which are in the group IV of the periodic table. Others include the combination of elements from different groups, such as IV-VI to yield SnS, PbS, PbTe semiconductor

compounds. The most vital parameters of semiconductor materials for solar cell application include the energy bandgap, the number of free carriers (holes and electrons) available for conduction and the generation and recombination of free carriers.

1.3.1 Semiconductor band structure and light absorption

The modern interpretation of the properties of semiconductors relies on quantum states for electrons (by Pauli exclusion principle) to explain the movement of charge carriers in a crystal lattice. The electrons of an isolated atom orbiting the nucleus occupy discrete energy levels with each defining an electronic layer. In a crystallised state where set of atoms is evenly distributed, the energy states of the electrons become bands separated by empty spaces called the energy bandgap due to the interaction between the atoms of the crystal. As shown in figure 1.4, the upper band is the conduction band while the lower band is the valance band and since the electrons in the valence bands are bound to the nucleus, the electric transport will occur in the upper band. The bandgap is normally small usually in the range of $0 < Eg < 3.0$ eV (for example polycrystalline SnS has 1.35 eV [15]) to allow an electric field to move an electron from the valence band to the conduction band.

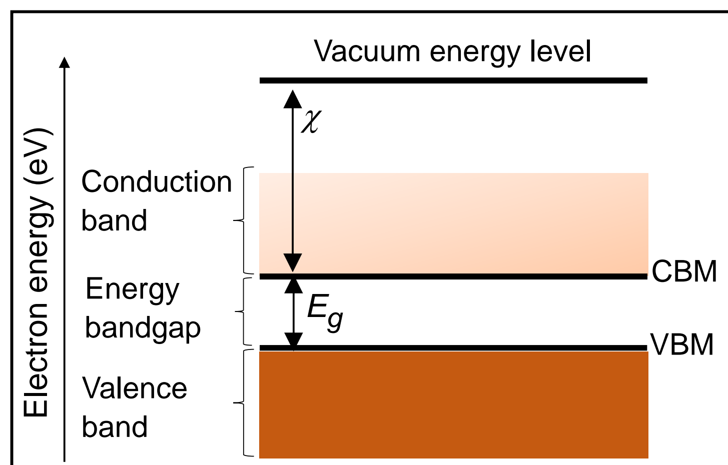

Figure 1.4 Schematic energy band structure of a semiconductor (0 K).

The band structure also reveals the almost-empty conduction band by a set of horizontal lines, where the bottom line indicate the bottom edge of the conduction band given by conduction band minimum (CBM). Similarly, the top of the almost filled valence band is indicated by

valence band maximum (VBM), while the distance between the CBM and the energy of a free electron outside the crystal (vacuum energy level) is quantified by the electron affinity (χ). The energy bandgap (E_g) otherwise referred to as the width of the forbidden band is the difference in energy levels between the CBM and the VBM. Energy bandgap is equally the minimum energy needed from the solar radiation to create an electron hole (e-h) pair. Once this bandgap energy is met, the electron is excited into a free state (from VB to CB) and can then participate in conduction. The energy of each packet of light (the photon) entering the surface of the semiconductor can be related to the wavelength of the light as:

$$E\ (eV) = \frac{1.24}{\lambda\ (\mu m)} \tag{1.1}$$

The creation of electron-hole pairs via the absorption of sunlight is crucial to the operation of thin film solar cell therefore the total energy and momentum of particles participating in the absorption process need to be conserved. The absorption of photon (α) by semiconductor is influenced by the position of VBM and CBM in the energy momentum (E-K) characteristics (see figure 1.5). Based on this, semiconductors are grouped into direct and indirect bandgap materials.

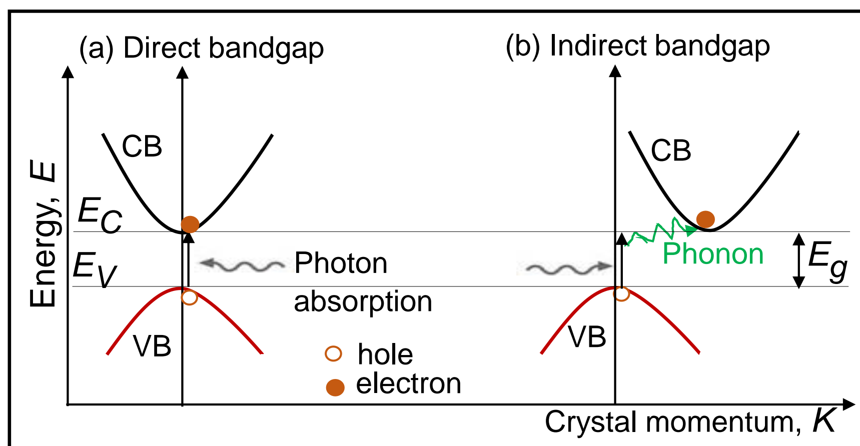

Figure 1.5 Diagram of photon absorption (a) direct and (b) indirect bandgap semiconductor.

In the direct bandgap semiconductors, electron can be excited from VB to CB giving off smallest possible energy difference ($E_g = E_c - E_v$) as a photon of light without a change in the crystal momentum value (see figure 1.5a). In this case, the valence band maximum (VBM)

and conduction band minimum (CBM) occur at the same value of crystal momentum, *K,* this characterises the direct bandgap semiconductors such as GaAs, CIGS, CdTe and SnS. In addition, direct bandgap semiconductors show a sharp change in photon absorption (α) from zero for $h\nu < E_g$ to values > 10^4 cm^{-1} for $h\nu > E_g$ [16], the relationships between α, $h\nu$ and E_g are explained in chapter three (section 3.7.6).

For indirect bandgap semiconductors (such as Si and Ge), the VBM and CBM do not occur at the same value of *K,* therefore crystal momentum is not conserved in band to band carrier transitions (see figure 1.5b). Since a change in crystal momentum is required for photon absorption or emission, a two-step process is needed involving phonon scattering (phonon absorption or emission) to conserve *K.* Phonons are the particle form of lattice vibrations in the semiconductor and they are characterised by low-energy particles with relatively high momentum. The absorption coefficient for indirect transitions are relatively small compared with direct transitions due to their dependence on both photon and phonon transitions. As a result, light penetrates more deeply into indirect bandgap than direct bandgap semiconductors [17], hence the reason why a substantial thickness is needed when such materials are used as an absorber layer for PV device fabrication.

1.3.2 Carrier generation, transport and recombination

Carrier generation occurs when an electron makes transition from VB to CB in a semiconductor as a result of interaction with other electrons, holes, photons or phonons. Generation alongside recombination processes are crucial in shaping the characteristics of a semiconductor device. Figure 1.6 (a-c) depicts the optical absorption process that can result to carrier generation. In (a) when $h\nu < E_g$, e-h pairs are not generated under intrinsic conditions. Under extrinsic condition, photon absorption occurs due to the available energy states in the forbidden gap because of chemical impurities. For $h\nu = E_g$, e-h pairs are generated (see figure 1.6b) and similarly, for $h\nu > E_g$, e-h pairs are generated and the excess energy ($h\nu$ - E_g) is given off as heat. The excitation of the electrons across the E_g leaves positively charged holes (vacancies) in the VB. However, figure 1.6 (d) depicts generation process called impact

ionisation which occur when a highly energetic carrier (electron or hole) donates its excess energy to excite an electron from *VB* to *CB* generating another e-h pair. The newly generated electron with the presence of high electric field can get high energy and generate further carriers, which can cause avalanche multiplication of carrier generation. While the generation due to light absorption depends on carrier concentration, for the impact ionisation (caused by an electron with an energy, which is much higher than the E_C) it is purely the current density.

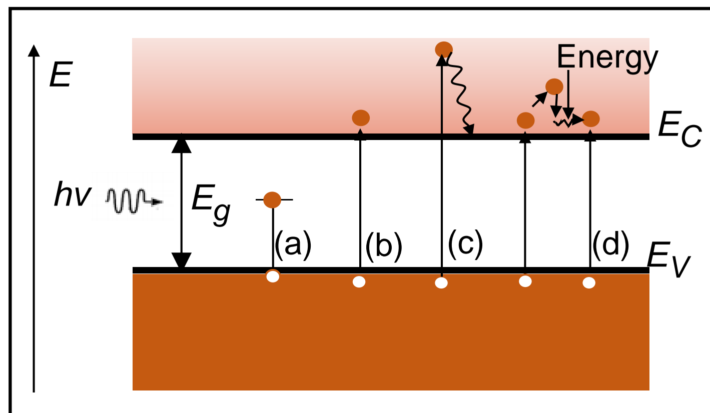

Figure 1.6 Schematic illustration of photon transition in semiconductor due to (a-c) light absorption $hv < E_g$, $hv = E_g$, $hv > E_g$ and (d) impact ionisation [17, 18].

Since there are many empty states in the CB, a small applied potential can move these electrons, resulting in a moderate electric current. Therefore, *e* and *h* can flow under the influence of the classical processes of a drift (electric field) and a diffusion (concentration gradient). Drift stands for the charged particle's response to the electric field ($\vec{E}$). When $\vec{E}$ is applied across a uniformly doped semiconductor, the bands tend to bend towards the upward direction of the applied electric field with holes moving in the same direction of the applied field while electrons move in the opposite direction. The drift current densities for electrons and holes ($\vec{J}_n^{drift}$and$\vec{J}_p^{drift}$), respectively can be written as:

$$\vec{J}_n^{drift} = qn\mu_n\vec{E} \tag{1.2}$$

$$\vec{J}_p^{drift} = qp\mu_p\vec{E} \tag{1.3}$$

where q is the electric charge, n and p is the number of electrons and holes, μ_n, μ_p are the respective mobility and $\vec{E}$ is the electric field in the x-direction. Electrons and holes in semiconductors also tend to diffuse (move) from regions of high concentration to regions of lower concentration because of their random thermal motion. Similar to the way the air in a balloon is distributed evenly within the volume of the balloon, in the absence of any external forces, carriers will equally tend to distribute themselves evenly within the semiconductor material [22]. This process stands for diffusion. The diffusion current densities for electrons ($\vec{J}_n^{diff}$) and holes ($\vec{J}_p^{diff}$) can be respectively written as:

$$\vec{J}_n^{diff} = qD_n \frac{dn}{dx} \tag{1.4}$$

$$\vec{J}_p^{diff} = -qD_p \frac{dp}{dx} \tag{1.5}$$

where D_n, Dp are diffusion coefficients for electron and hole. At the core of drift and diffusion is the same physics of collisions among particles and medium atoms, hence the existence of the relationship between D and μ given by the Einstein relation [17, 19]:

$$\mu_{n,p} = \frac{qD_{n,p}}{kT} \tag{1.6}$$

where q/kT is equivalent to thermal voltage and at room temperature equal to 25 mV. The total electron and hole currents can be given by the sum of their drift and diffusion components [19].

$$J_n = qn\mu_n\vec{E} + qD_n \frac{dn}{dx} \tag{1.7}$$

$$J_p = qn\mu_p\vec{E} - qD_p \frac{dn}{dx} \tag{1.8}$$

Recombination is the process through which both electron and hole carriers annihilate each other. It is the reverse of generation and acts to restore the equilibrium condition of the carriers, such that in equilibrium the generation rate (G) and recombination rate (R) are in dynamic

balance, *R* = *G*. In this case the equilibrium carrier concentrations *p* and *n* are related to the intrinsic carrier concentration (n_i) by the mass-action law: $pn = n_i^2$. In non-equilibrium conditions, where $R \neq G$ and $pn \neq n_i^2$, by either illumination and/or current injection, the concentrations of *e* and *h* tend to relax back toward their equilibrium values by recombination in which an electron falls from CB to VB and eliminates a VB hole. Crucial recombination mechanism for solar cell operations include non-radiative recombination, radiative recombination and Auger recombination. Non-radiative recombination occurs through traps (defects) in the forbidden gap (bandgap) as depicted in figure 1.7 (a). Here the rate of *e-h* recombination (R_{SLT}) for a single trap state (*SLT*) in the bandgap is given by the Shockley-Read-Hall recombination formula [20]:

$$R_{SLT} = \frac{pn - n_i^2}{\tau_n(p + p_t) + \tau_p(n + n_t)} \tag{1.9}$$

where τ_n and τ_p are the average lifetime the excess minority carriers of electrons and holes, respectively will live in a sea of majority carriers, n_t and p_t are the densities of the available trap states at equilibrium. Equation 1.9 applies to the steady state situation, in addition provides the net recombination rate for the electrons and holes.

Radiative (band-to-band) recombination occurs when an electron recombines with a hole to emit a photon as shown in figure 1.7 (b). Some of the emitted energy can be shared with a phonon in an indirect bandgap semiconductor. This is also the opposite of the optical generation process and is much more efficient in direct bandgap than in indirect bandgap semiconductors and the net recombination rate due to radiative processes with *B* as a constant is given by [17]:

$$R_\lambda = B(pn - n_i^2) \tag{1.10}$$

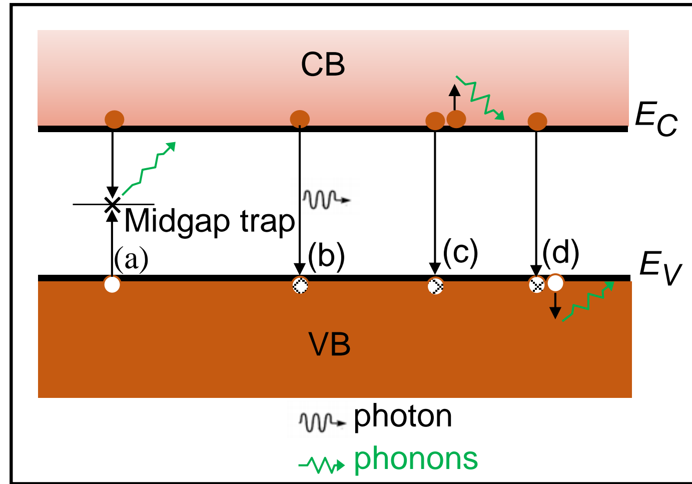

Figure 1.7 Recombination process in semiconductors (a) non-radioactive, (b) radioactive, and Auger recombination at (c) CB, (d) VB [17].

Auger recombination (R_{Auger}) is similar to radiative recombination except that the energy of transition is given to a second carrier in either the CB (see figure 1.7c) or the VB (see figure 1.7d). This electron or hole then relaxes thermally releasing its excess energy and momentum to a phonon. Auger recombination is the inverse process of impact ionisation, the creation of e-h pair when an energetic electron collides with a crystal atom and breaks the bond. The net recombination rate due to Auger processes is given by [17]:

$$R_{Auger} = (C_n n + C_p p)(pn - n_i^2) \tag{1.11}$$

where C_n and C_p are comparable constants.

Generally, non-radiative recombination is common in indirect bandgap semiconductors, radiative recombination in direct bandgap semiconductors while Auger recombination is common in heavily doped semiconductors.

1.3.3 Intrinsic and extrinsic semiconductors

Light absorption in semiconductors is said to be intrinsic, when the energy of each absorbed photon is consumed by raising an electron from the VB to CB thereby creating e-h pair by the

atoms of the semiconductor. Here the probability of occupancy of an energy level by an electron with energy (E) obeys Fermi-Dirac distribution given by [17]:

$$F(E) = \frac{1}{1 + e^{(E-E_F)/kT}} \qquad (1.12)$$

where E_F is the Fermi energy that is the average statistical level occupied by all of the charge carriers and at whatever temperature, probability of occupancy for this state energy is always one-half, k is Boltzmann's constant, and T is the Kelvin temperature. As shown in figure 1.8, the Fermi distribution function is a strong function of temperature. At absolute zero, $F(E)$ is a step function and all the states below E_F are filled with electrons while those above E_F are completely empty. With increasing temperature, thermal excitation will leave some states below E_F empty, while the corresponding number of states above E_F are filled with the excited electron [17].

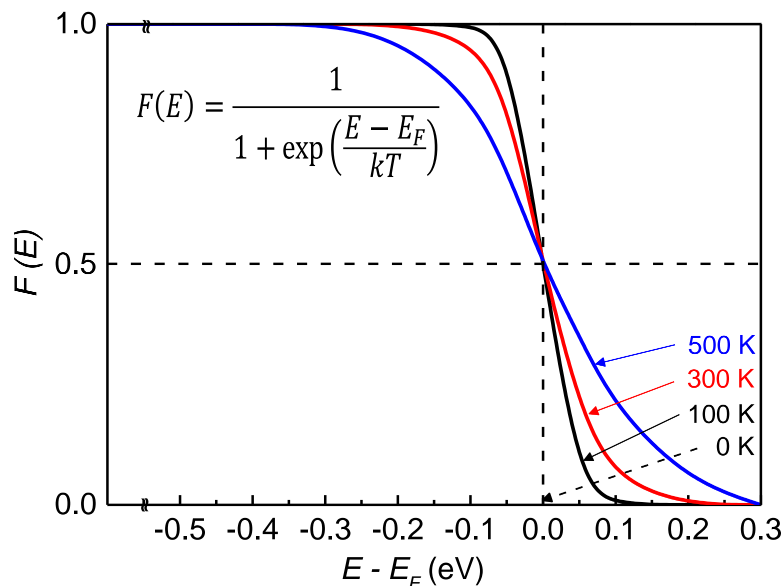

Figure 1.8 The Fermi distribution function $F(E)$ versus (E-E_F) at various temperatures [19, 20].

When E_F is sufficiently far (> 3kT) from either band edge in intrinsic semiconductor, the carrier concentration can be well approximated as [17, 20].

$$n = N_C e^{(E_F - E_C)}/_{kT} \quad (1.13)$$

$$p = N_V e^{(E_V - E_F)}/_{kT} \quad (1.14)$$

where N_C and N_V are the CB and VB effective density of states (cm^{-3}) which are respectively given by:

$$N_C = 2\left(\frac{2\pi m_n^* kT}{h^2}\right)^{3/2} \quad (1.15)$$

$$N_V = 2\left(\frac{2\pi m_p^* kT}{h^2}\right)^{3/2} \quad (1.16)$$

where m_n^* and m_p^* are the effective mass of electrons and holes, respectively. For the intrinsic semiconductor, $n_p = n_i$ (n_i is the intrinsic carrier concentration) and, $\left(E_g = E_C - E_V\right)$ such that:

$$n_i^2 = np = N_C N_V e^{(E_g/kT)} \quad (1.17)$$

In the complete ionisation conditions, the free electron density *n*-type semiconductor (where *n* >> *p*), $n = N_D$ and the hole concentration in equilibrium is given by $p = n_i^2/N_D$. Similarly, the free hole density in *p*-type semiconductor with a density of N_A of acceptor ions, $p = N_A$ and $n = n_i^2/N_{A,}$ can both be expressed as:

$$n = N_D = N_C e^{(E_F - E_C)/kT} = N_C e^{(E_F - E_C)/kT} e^{(E_F - E_I)/kT} = n_i e^{(E_F - E_i)/kT} \quad (1.18)$$

Similarly,

$$p = n_i e^{(E_i - E_F)/kT} \quad (1.19)$$

Equation 1.17, which depicts the product of equations 1.18 and 1.19, remains constant at n_i^2 at a given temperature and the relationship $np = n_i^2$ represents the law of mass action.

The Fermi level in an intrinsic semiconductor, $E_i = E_F$ and is given by:

$$E_i = \frac{E_C E_V}{2} + \frac{kT}{2} ln\left(\frac{N_V}{N_C}\right) \quad (1.20)$$

which is typically very close to the middle of the bandgap (E_g). Number of free electrons influences the conductivity of semiconductor, when this number increases the conductivity increases therefore, the conductivity of an intrinsic semiconductor increases with temperature.

However, the number of electrons and holes in their respective bands and hence the conductivity of the semiconductor can as well be controlled via the introduction of controlled impurities of dopants, called donors and acceptors. The doped intrinsic semiconductor is called extrinsic semiconductor where optical absorption is via deep localised states. Donors are dopants, which can donate an electron to the conduction band while acceptors are dopants that can accept an electron from the valence band and thus create a hole [21]. The controlled introduction of donor and acceptor impurities into a semiconductor allows creation of *n*-type and *p*-type semiconductor. The impurities also introduce additional localised electronic state into the energy band structure within the forbidden band. If the energy of the state E_D introduced by donor is sufficiently close to the E_c (within a few kT), there will be sufficient thermal energy to allow the extra electron to occupy a state in the CB and the donor state will be positively charged (ionised). Similarly, an acceptor atom will introduce a negatively charged (ionised) state at the energy E_A. The number of ionised donors and acceptors are given by [17]:

$$N_D^+ = \frac{N_D}{1 + e^{(E_F - E_D)/kT}} \qquad (1.21)$$

$$N_A^- = \frac{N_A}{1 + e^{(E_A - E_F)/kT}} \qquad (1.22)$$

When donors and acceptors are ionised such that $n_o \approx N_D$ in n-type and $p_o \approx N_A$ in p-type semiconductors, the Fermi energy can then respectively, be written as:

$$E_F = E_i + kT \ln \frac{N_D}{n_i} \qquad (1.23)$$

$$E_F = E_i - kT \ln \frac{N_A}{n_i} \qquad (1.24)$$

Generally, electrical conduction is due to the mobile charge carriers in semiconductors, electrons or holes, which are provided by impurities or dopants in the crystal. In an extrinsic semiconductor, the concentration of doping atoms in the crystal largely influence the density of charge carriers, which determines its electrical conductivity.

1.3.4 The *p-n* junction physics

The *p-n* junction is simply an interface between two types of semiconductor materials, *p*-type (positive side with excess of holes) and *n*-type (negative side with an excess of electrons) in intimate contact. In optical absorption process of semiconductors, the excited minority carriers normally recombine with the majority carriers and thus do not contribute to a photocurrent. Figure 1.9 depicts the uniformly doped and physically separated *p* and *n* type semiconductor before bring them into intimate contact. The electron affinity (χ_p or χ_n), which represents the energy difference between the conduction band and the vacuum level, is indicated along with the work function (φ_p or φ_n). The work function stands for the energy required to remove an electron from the semiconductor to the 'free' vacuum level and is the difference between the vacuum level and the Fermi level [21]. Notice that the Fermi level, E_F, is near the E_V for the *p*-type and E_C for the *n*-type semiconductors.

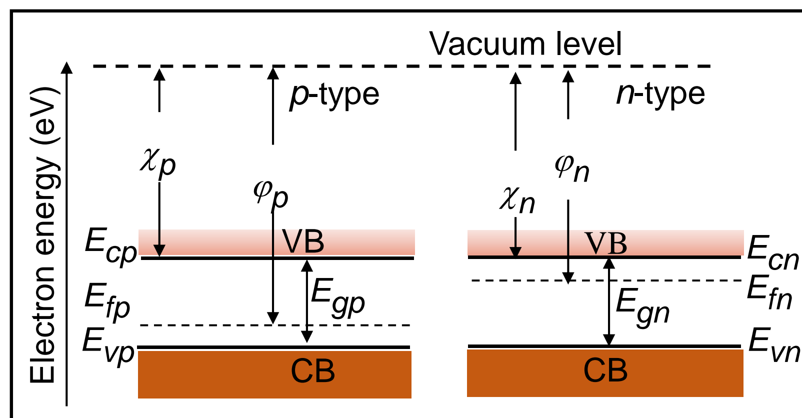

Figure 1.9 Schematic illustration of uniformly doped (a) *p*-type and (b) *n*-type semiconductors before the p-n junction formation.

A built-in electric field is therefore needed to separate and collect the photo-generated carriers before recombination. In inorganic cells, such fields are introduced by a *p-n* junction formation when a *p*-type and *n*-type semiconductors are brought into intimate contact as illustrated in figure 1.10 (a). Due to the differences in the electron and hole concentrations in the opposite sides, the excess holes in *p*-side and excess electrons in *n*-side will tend to diffuse to opposite side. This causes a build-up of positive and negative charges on the *n*-type and *p*-type regions, respectively. The negatively charged fixed acceptor ions in *p*-type side and positively charged fixed donor ions in *n*-type side near the junction in the semiconductor lattice creates electron field at the junction. The excess carriers near the junction are then removed by the field resulting in the creation of a depletion region and the direction of the electric field in this region is from *n*-type side to *p*-type side, which opposes the majority carrier diffusion process (see figure 1.10 b). Similarly, the minority carriers on reaching the junction can drift across the depletion region and become majority carriers in the other side. Such that equilibrium will exist when the diffusion current equals the drift current, and this will cause the net current across the junction to be zero. Figure 1.10 (c) shows the space charge region (*W*) which is the transition region between the *n* and *p* type semiconductor materials.

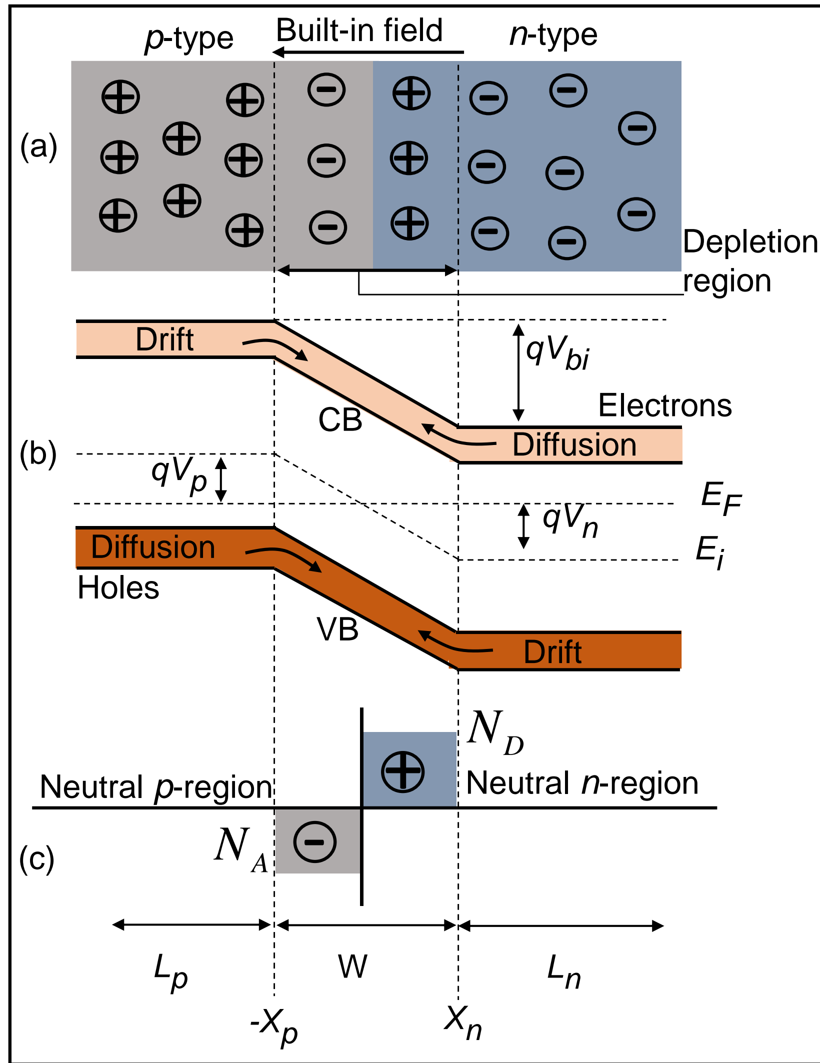

Figure 1.10 Schematic illustration of a uniformly doped *p*-*n* junction (a) under equilibrium, (b) energy band diagram and (c) space charge distribution.

From figure 1.10 (b), the energy difference between E_F and E_i away from the junction on the *p*-type side is given by [17, 18]:

$$qV_n = E_F - E_i \tag{1.25}$$

$$qV_p = E_i - E_F \tag{1.26}$$

Using equations 1.18 and 1.19 in equation 1.25 and 1.26, respectively and considering complete ionisation will give:

$$qV_n = kT\ ln\left(\frac{N_D}{n_i}\right) \tag{1.27}$$

$$qV_p = kT\,ln\left(\frac{N_A}{n_i}\right) \quad (1.28)$$

The sum of equations 1.27 and 1.28 give the built-in voltage (V_{bi}), which represents the electrostatic potential difference due to the junction formation and can be expressed as [17]:

$$qV_{bi} = kT\,ln\left(\frac{N_A N_D}{n_i^2}\right) \quad (1.29)$$

Due to the space charge neutrality condition of the semiconductor, the total negative charge per unit area on the *p*-region is equal to the total charge per unit area in the *n*-region, which is given by:

$$x_p N_A = x_n N_D \quad (1.30)$$

where x_p and x_n are the extent of the depletion region penetrating into the *p* and *n* type semiconductors, respectively (see figure 2.8 c). The total depletion region width, *W*, as a function of V_{bi} is given by:

$$W = x_p + x_n = \sqrt{\frac{2\varepsilon_s}{q}\left(\frac{N_A + N_D}{N_A N_D}\right)V_{bi}} \quad (1.31)$$

where $2\varepsilon_s$ is the semiconductor permittivity. It can be seen from equation 1.31 that *W* strongly depends on the doping concentrations of the *p* and *n* regions. Therefore, a one sided abrupt junction can be formed if one side is more heavily doped than the other is, and in some cases for solar cells, $N_D >> N_A$ such that equation (1.31) simplifies to:

$$W \cong x_n = \sqrt{\frac{2\varepsilon_s V_{bi}}{qN_D}} \quad (1.32)$$

In addition, if a positive voltage V_F is applied to the *p* region with respect to the *n*-region, the *pn* junction becomes forward-biased and the total electrostatic potential across the junction reduces by $V_{bi} - V_F$. However, if a positive voltage is applied to the *n*-region with respect to the *p*-region, the *pn* junction becomes reverse-biased and the total electrostatic potential

across the junction increases to $V_{bi} + V_R$. In a one-sided heavily doped junction, the depletion region width (*W*) can be rewritten as:

$$W = \sqrt{\frac{2\varepsilon_s(V_{bi} - V)}{qN_B}} \qquad (1.33)$$

where N_B is the doping concentration of the lightly doped semiconductor material, *V* is positive for forward bias and negative for reverse bias. Notice that forward bias reduces depletion region width while the reverse bias increases the depletion region width. In figure 2.9 (c), L_n and L_p are minority carrier diffusion lengths of electrons in the *p*-region and holes in the *n*-region, respectively. The minority carrier diffusion length is the average distance a minority carrier can travel from the point of generation to the depletion region before recombination with majority carrier. L_n and L_p are equal to $\sqrt{D_n\tau_n}$ and $\sqrt{D_p\tau_p}$, respectively, D_p and τ_p have been defined in equations (1.7) - (1.9).

1.3.5 Heterojunctions

A heterojunction represents the interface between two regions of dissimilar solid-state materials with unequal bandgaps in contrast to homojunctions. The two dissimilar materials must also have unequal electron affinity, work function and it could be in the form of a semiconductor (*p-n* or *p-i-n*) or metal-semiconductor configuration (Schottky junction). The coupling of multiple heterojunctions in a solar cell leads to the formation of a hetero-structure. As detailed in chapter six (section 6.3), when the two dissimilar semiconductors with unequal bandgap and electron affinity are brought into intimate contact, charge is transferred until the Fermi levels in the two materials are equal. The behaviour of the resulting heterojunction depends crucially on the alignment of the energy bands at the interface, which can be categorised into three to include straddled alignment (type I), staggered alignment (type II) and broken-gap (type III) alignments as illustrated in figure 1.11.

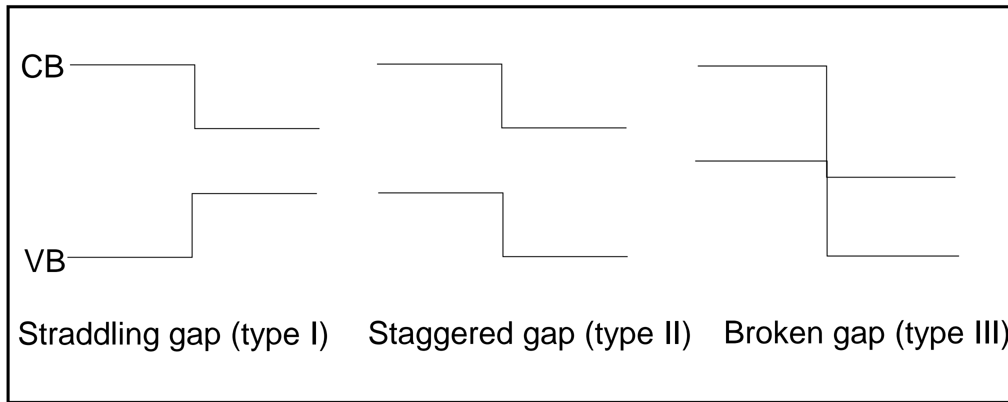

Figure 1.11. Schematic representation of semiconductor heterojunction band alignments.

Away from the interface, the energy band profile in the absence of interface states depends mainly on the electron affinities, energy bandgap and work function of the two semiconductors forming the junction. The arrangements of the energy band alignments near the junction for the various heterojunctions have been proposed by Anderson [22] which neglected the interface states and Oldham and Milnes [23] that included the effect of interface states. Energy band profiles based on Anderson is considered the good approximation for many heterojunctions and shape of the band bending has been predicted by Sharma and Purohit [24].

1.3.6 Theory of solar cells and current density-voltage characteristics

Solar cells are materials that converts light directly into electricity via photovoltaic effect. The photovoltaic effect involves the creation of a voltage and electric current in a device upon exposure to light. The photovoltaic effect is closely related to the photoelectric effect, but unlike in the later where electron is ejected out of the material, in the PV effect the excited charge carrier is still contained within the material. Due to the depletion region and built-in voltage, a *p-n* junction only allows current to flow in one direction when a bias is applied. A solar cell has the same current-voltage (*I-V*) characteristics as a diode when operating in the dark. The ideal diode law describes the response of a diode to an applied voltage, which does not account for a photocurrent. The total dark current density otherwise called the ideal diode law or Shockley equation is given by [19, 21]:

$$J = J_o\left(e^{\frac{qV}{kT}-1}\right) \tag{1.34}$$

where q is the elementary charge, V is the applied voltage, k is the Boltzmann constant, T is the temperature and J_o is the pre-factor of the diode equation called the saturation current density and is a measure of the recombination rate in a device. It can be expressed as:

$$J_o = \frac{qD_p p_{no}}{L_p} + \frac{qD_n n_{po}}{L_n} \tag{1.35}$$

However, when a solar cell is illuminated, electron-hole pairs are generated within the minority carrier diffusion length from the boundary of the depletion region. The light generated minority carriers can be separated and collected by the depletion region to create a photocurrent (see figure 1.12 (a) and the equivalent circuit of an ideal solar cell is shown in figure 1.12 (b). Under the illumination, the current flow in the solar cell and the applied voltage can be controlled by diode such that the shape of the current density-voltage curve (*J*-*V*) curve is determined only by the diode [25]. The light generated current will oppose the diode dark current, therefore the total current density (*J*) becomes:

$$J = J_o\left(e^{\frac{qV}{AkT}-1}\right) - J_L \tag{1.36}$$

where J_L is the light generated current density and *A* is the diode ideality or quality factor, which is equals to 1 or 2 when recombination in the quasi-neutral regions and depletion region dominate the devices, respectively. In practical cases, parasitic resistances, which are always present in the real solar cell brings about power losses in the device. To account for these power losses, the series and shunt resistances are incorporated into the equivalent ideal circuit as shown in figure 1.12 (c). Series resistance, R_s arise from both the bulk resistance of the semiconductor and the electrical contacts, as well as the contact resistance between them. Shunt resistance, R_{sh} develops from the defects of the device such as light generated current leakage from the edge of the solar cell or due to pinholes in the device [25]. Introducing R_s and R_{sh} in equation (1.36) will yield:

$$J = J_o \left[e^{\left(\frac{q(V - JR_s)}{AkT} \right)} - 1 \right] + \frac{V - JR_s}{R_{sh}} - J_L \quad (1.37)$$

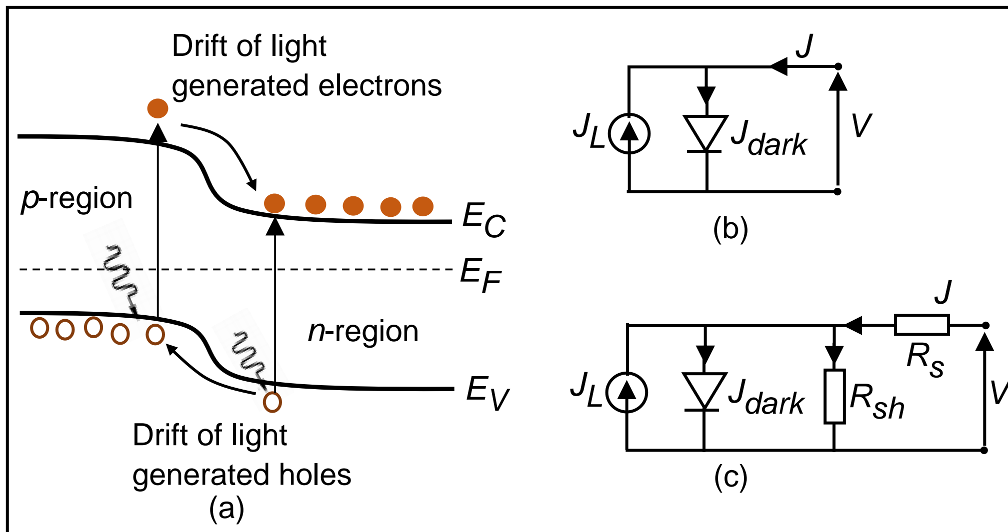

Figure 1.12 (a) Energy band diagram of a device under illumination and equivalent circuit of (b) ideal solar cell and (c) real solar cell with its parasitic losses (series, R_s and shunt, R_{sh} resistances). J_L is the illuminated current density, J_{dark} is the current density of the diode, J is the current flow in the load and V is the applied voltage, adapted from [25].

The *J-V* characteristics of a solar cell in the dark and under illumination are shown in figure 1.13, where V_{mp} and J_{mp} are the voltage and current density at the maximum output power (P_{max}) of the solar cell.

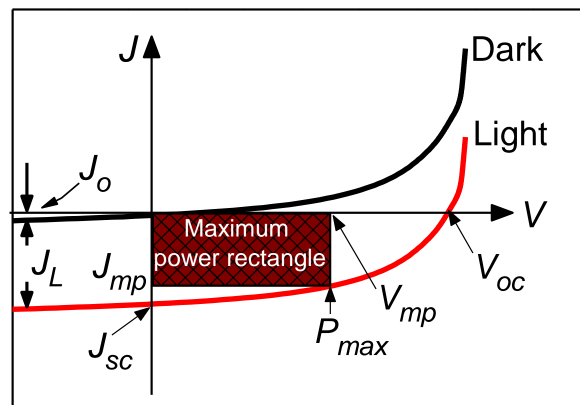

Figure 1.13 *J-V* characteristics of a solar cell in the dark and under illumination, adapted from [25].

The crucial performance parameters of a solar cell that can be estimated from figure 1.13 include the short circuit current density (J_{SC}), open circuit voltage (V_{OC}), fil factor (*FF*) and power conversion efficiency (η).

J_{SC} (mA/cm^2) represents the maximum current density when no bias is applied and in an ideal solar cell is equal to J_L. The V_{oc} is the maximum voltage from the solar cell that occurs when light generated current is equal and opposite to forward bias diffusion current. The open circuit voltage is limited by interface defects and recombination losses [26]. The V_{oc} in ideal solar cell is estimated when the total current is zero using:

$$V_{oc} = \frac{AkT}{q} ln\left(\frac{J_L}{J_o} + 1\right) \quad (1.38)$$

The fill factor (*FF*) represents the measure of the "squareness" of the *J-V* curve or the quality of the solar cell. *FF* is estimated by the ratio of obtainable maximum power ($P_{max} = V_{mp}J_{mp}$) shown in figure 1.13 to the product of V_{oc} and J_{sc} as follows:

$$FF = \frac{V_{mp}J_{mp}}{V_{oc}J_{sc}} \quad (1.39)$$

The efficiency (η) is commonly used parameter to compare the performance of one solar cell to another. It is the ratio of useful electrical power (P_{max}) produced by the solar cell to the incident illumination power (P_{in}) under standardised testing conditions and given by:

$$\eta = \frac{P_{max}}{P_{in}} = \frac{V_{oc}J_{sc}FF}{(solar\ cell\ area)(incident\ light\ power\ density)} \quad (1.40)$$

Researchers are finding new ways over the past 30 years to make solar cells convert more of the incident illumination power into electricity, but several aspect of photovoltaic process and losses (summarised in figure 1.14) are limiting the power conversion efficiency of solar cells.

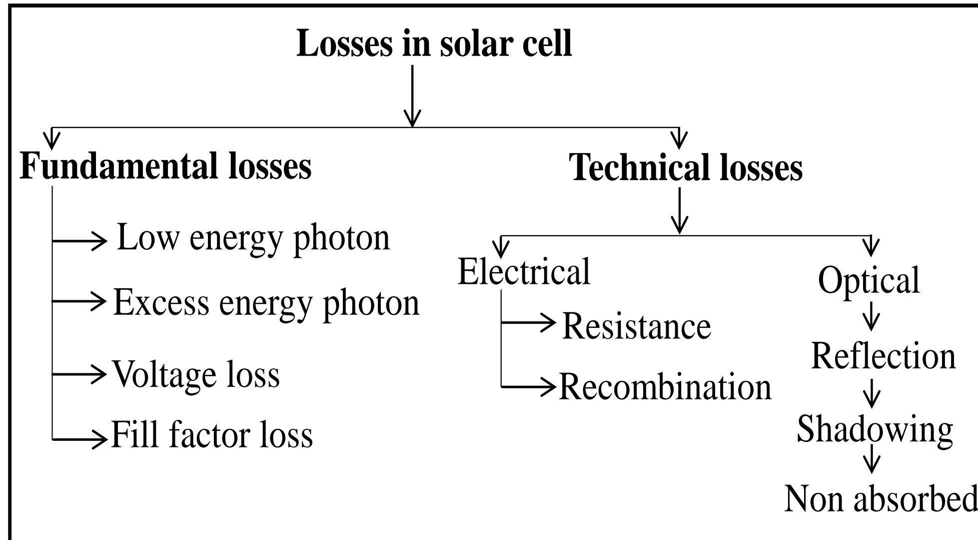

Figure 1.14 Losses in solar cell.

Most of these losses given in figure 1.14 can be minimised via selection of materials with optimum bandgap, increasing film thickness, reducing interface defects, use of anti-reflective coating and surface texturing.

1.4 Aims of the thesis

This thesis will systematically address the critical issues of secondary phases, non-stoichiometric nature of constituent elements (tin and sulphur) and small grain sizes that limit SnS photovoltaic applications and introduce new eco-friendly pathways to generate grain growth. This will be achieved via deposition process (thickness, temperature and substrate material) and post-heat treatment optimisations of thermally evaporated SnS solar absorbing thin films. Alternative buffer layers will also be explored to replace the conventional cadmium sulphide (CdS) material due to toxicity of cadmium.

1.5 Objectives of the thesis

This thesis describes the process and optimisation of thermally evaporated SnS solar absorbing thin films. The objectives of the project include the following,

- Optimise the film thickness, temperature and substrate materials dependent properties of thermally evaporated SnS thin films.

- Investigate the effect of post annealing treatments and Se - S substitution on the SnS thin films.
- Assess the influence of chlorine ($SnCl_2$ or $MgCl_2$) treatment on the physical (grain growth) of SnS thin films
- Study the role of different buffer layers (CdS, ZnS, ZnO and In_2S_3) and their band alignment on the junction formation and performance of SnS devices.

1.6 Contribution to knowledge of the thesis

The state of research on SnS is under developed (Web of knowledge in 2014: 72 research papers for SnS compare to 230 and 470 for CZTS and Perovskites new solar cells, respectively) despite SnS being a promising absorber material. The thesis aims to exploit this loophole and fill many gaps in the knowledge database. This study has investigated the incorporation of selenium (Se) in annealing optimisation process of SnS by adopting the established selenisation process for CZTSSe [27] to overcome the use of H_2S that is more complicated and dangerous to use [28]. The S-Se anion exchange is found to bring significant grain growth and recrystallisation whilst maintaining good thin film quality.

1.7 Thesis structure

The thesis is divided into seven (7) chapters. Following this introduction to thin film photovoltaic technology (chapter 1), the review of the history of SnS thin film development, material properties and technologies are presented in chapter 2. Specifically the thermal evaporation method, which can provide easy and inexpensive scalable route to deposit SnS solar absorbers is described in detail. This is followed by the experimental and characterisation methods used throughout this work (chapter 3). The experimental results are analysed and discussed in the following three chapters. Chapter 4 detailed the influence of layer thickness, substrate temperature and substrate type (SLG, quartz, ITO, FTO, Mo coated SLG and quartz) on the microscopic, optical and crystallographic properties of SnS solar absorbing thin films. However, the link between heat treatments in diverse environment (including Se - S

substitution and the recrystallisation of the SnS absorber layers are presented in chapter 5, while chapter 6 depicts the role of buffer layers on the SnS thin films solar cell. Finally, the conclusions from the research work and suggestions for future work is presented in chapter 7.

Chapter 2

Literature Review

This chapter focuses on the literature review of SnS solar absorbers and devices used in photovoltaic applications. After brief introduction in section 2.1, the general overview of SnS solar absorber is presented in section 2.2. The SnS-based solar cell structure in substrate and superstrate configurations are discussed in section 2.3 followed by the device layer components in section 2.4 and finally the conclusions presented in 2.5.

2.1 Introduction

Solar absorber otherwise called thin film in this study is a layer of material ranging from few to thousands of nanometres in thickness. Solar absorbers are the building block of solar cells, which are being developed as a way of significantly reducing the cost of solar cells. The key point is to absorb photons from a certain range of wavelength (visible light and near infrared) as efficiently as possible with minimised reflection. Photovoltaic solar cells have been making a steady substantial progress and currently on track toward meeting more than 1% of the world energy demand. Going forward requires more research in photovoltaic solar cell absorbers and technologies that face no scalability constraints in generating up to 10% of the global electricity consumption. The motivation for the thin film solar cell research are due to reduced active material requirement and low energy costs [13]. Solar absorbers can be grown using different methods of physical or chemical deposition in either vacuum or atmospheric pressure conditions. The resulting material properties such as phase purity, crystallographic, optical and microscopic structures can vary based on the growth method and conditions. Non-toxicity and earth abundancy are crucial for solar absorber that has a potential for low cost photovoltaic devices and contribute to providing substantial fraction of the world's energy demand. Simple binary SnS solar absorbers, which are earth abundant, inexpensive and

environment friendly, have recently experienced a renewed interest in the thin film solar cell community.

2.2 Overview of SnS solar absorber

Research on Tin Sulphide (SnS) absorber materials have been evolving for the past 20 years. SnS is one of the most promising yet under-explored photovoltaic solar absorber material for cost effective and good efficiency solar cell devices. SnS is a dark brown solid material, insoluble in water and belongs to group IV-VI compound usually comprised of multiple phases [29, 30]. Its origin is usually associated to a Latvian-German Chemist, Robert Herzenberg who discovered it in 1934 [31], the reason the mineral is called Herzenbergite. However, prior to this tin and sulphur have been used in the eighteenth century in making 'aurum mosaicum'(SnS_2 obtained as a yellow scaly crystalline powder used as pigment in bronzing and gilding wood and metal work) [32]. Herzenberg also first reported the growth of single crystal SnS by reacting stoichiometric tin and sulphur. Some of the earlier works on the development of SnS-based solar absorbers during the last century [33-37] sparked research interest of PV community and have provided a gateway to the recent investigations mainly dominated by polycrystalline layers [38-42]. The major challenges that are yet to be adequately addressed are the existence of secondary phases such as SnS_2 and Sn_2S_3, small grain sizes and poor band alignments with n-buffer layers. These have limited the application of SnS thin films in solar cell devices. Reviewing SnS phase, intrinsic defects, crystal and optoelectronic properties are vital to understand the property sensitivity of SnS films to advance the improvement in device performance. SnS is an environmental friendly and earth abundant p-type semiconductor with good physical, optical and electrical properties such that only a few microns (< 2.0 μm) of the layer are needed to absorb most of the incident photon. Some of these main properties of SnS solar absorber are presented in table 2.1.

Table 2.1. Basic properties of SnS solar absorber.

Parameters	Values	References
Energy bandgap *Eg* (eV)	Eg_{direct} 1.35	[15, 36, 39,
	Reported range (1.00-1.70)	43-50]
	$Eg_{indirect}$ 1.1	
	Reported range (1.00-1.45)	
Absorption coefficient (cm^{-1})	$>10^4$	[15, 48, 51]
Refractive index	1.60-3.52	[15, 48]
Conductivity type	*p* Intrinsically	[51, 52]
	n $SnCl_4/CH_3OH$ heat treatment	[53]
	Isolation ion substitution (Pb^{2+} for Sn^{2+})	[54-56]
Intrinsic resistivity (Ω-cm)	13-20	[15]
Rel. dielectric permittivity ε_r	13	[57]
CB effective density (cm^{-3})	1.18×10^{18}	[57]
VB effective density (cm^{-3})	4.76×10^{18}	[57]
e^- mobility μ_n (cm^2Vs^{-1})	15-25	[57, 58]
Hole mobility μ_p (cm^2Vs^{-1})	90-100	[57, 58]
Acceptor density N_A (cm^{-3})	10^{17}	[57, 58]
Electron affinity χ (eV)	4.20	[59]
Work function φ_s (eV)	4.78	[60]
Binding energies (eV)	Sn $^3d_{5/2}$ = 485.3, S $^2p_{3/2}$ = 161.4	[15]
Crystal structure	Orthorhombic	[61]
Space group	Pnma, Cmcm	[61, 62]
United cell volume ($Å^3$)	192.67	[63]
Density (gcm^{-3})	5.08	[64]
Lattice constant (Å)	a = 4.33, b = 11.18, c = 3.98	[15, 50, 63]
Bulk modulus (GPa)	~36.6	[63]
Melting point (K)	1143-1163	[33, 35]

2.2.1 SnS phase purity and control

The challenge in identifying possible phase impurities in SnS may be a key factor in SnS solar cells having to date yet to exceed the 4.4% efficiency limit [28]. SnS is composed of tin and sulphur with Sn having dual valency (Sn^{2+} and Sn^{4+}) which leads to formation of various phases dependent on the atomic composition [29, 65]. This Sn dual valence exists as Sn(II)

((Kr)$4d^{10}5s^{2}5p^{0}$) and Sn(IV) ((Kr)$4d^{10}5s^{o}5p^{o}$) oxidation states, while SnS and SnS_2 adopts single oxidation states of Sn and Sn_2S_3 has two oxidation state of Sn [29]. In order to synthesize pure SnS crystals, it is important to know the phase diagram (see figure 2.1) and this shows that adequate control of Sn and S composition can lead to pure SnS phase. These multiple phases include SnS (orthorhombic), SnS_2 (trigonal), Sn_2S_3 (rhombic), Sn_3S_4 (tetragonal) and Sn_4S_5 with SnS, SnS_2 and Sn_2S_3 the distinct and stable phases. The presence of secondary phases in SnS thin films has been shown to have a negative impact on the power conversion efficiency of SnS-based photovoltaic devices [61], with SnS_2 specifically being suggested to act as a recombination centre for holes and electrons while Sn_2S_3 can act as a hole trap [66]. A good understanding of the SnS phase formation would be useful to provide guidance on the deposition processes that can lead to obtaining pure SnS layer with suitable properties for photovoltaic application. Only SnS phase which is associated with a p-type conduction, has significant potential for application as photovoltaic light absorber due to its attractive properties [15, 42, 67], though both SnS_2 and Sn_2S_3 can also be useful in other PV applications. For instance SnS_2 that shows n-type conductivity and energy bandgap range of 2.18-2.27eV [68, 69] can be a possible candidate for use as buffer layer material in thin film solar cells, as a high surface area photo-catalyst [70] and as a photodetector [71]. Sn_2S_3 exhibits both p- and n-type conductivity with bandgap range of 1.05-2.12 eV [72-75] depending on its deposition condition and crystalline structure. This has been suggested to be useful for near lattice-match heterojunctions with CdTe, GaSb and AlSb, which can be applied in the detection and generation of infrared radiation [74]. In solar cell applications, obtaining a stoichiometric p-type SnS phase is critical to enhance performance as studies have shown that a deviation from ideal stoichiometry of only 15% is enough to change SnS conduction from p- to n-type [66] and this has been the major reason for poor device performance.

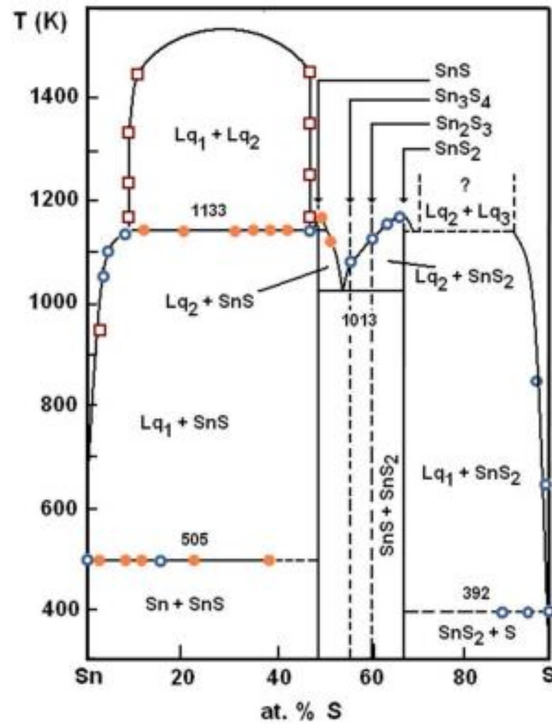

Figure 2.1 The phase diagram of the SnS thin films [76].

In addition to these SnS, phases arising due to different compositions and preparation methods, several other known or proposed polymorphs exist. These include the *α*-SnS with orthorhombic structure (space group *Pnma*) stable at room temperature, *β*-SnS also with orthorhombic structure (space group *Cmcm*) but forms and are stable at high temperatures. Others are the rock salt phase (space group *Fm-3m*), as well as the zinc blende phase, which exist in inform of bulk cubic SnS and finally, the newest π-cubic phase [61, 62, 77-80]. Ettema *et al.* [81] reported two different forms of SnS namely, *α*-SnS and *β*-SnS that show similar charge distribution with *α*-phase having higher direct energy bandgap (1.6 eV) than the *β*-phase (range of 1.0 – 1.5 eV [15]). They observed that the *α*-SnS is a low temperature phase compound with lower symmetry than the higher temperature *β*-SnS phase.

Several techniques have proven useful in confirming and identifying the phase and purity of SnS thin films. X-ray diffraction (XRD) measurements have shown that with accurate reference powder diffraction files, this technique can reliably distinguish between SnS, SnS_2 and Sn_2S_3 [66, 82, 83]. X-ray photoemission spectroscopy (XPS) can also show the presence of

secondary phases when analysed at suitable energy resolution and careful analysis [81, 84, 85]. To complement XRD, Raman spectroscopy is therefore, used to clearly characterise and identify the binary phases of the polycrystalline SnS layers.

2.2.2 Intrinsic defects of SnS

Intrinsic defects are crucial to the SnS solar absorber application in photovoltaic devices as they can influence the concentration, mobility and lifetime of the photo-generated charge carriers. Recent progress in the improvement of the power conversion efficiency of SnS-based devices is due to the reduction of interface recombination defects. This was achieved through the growth of enlarged grain sizes and adjustments of buffer layer materials in order to optimise the band offsets [28]. Here, some basic defects are reviewed in order to assist with the experimental efforts to optimise the deposition conditions and SnS absorber quality. Since the sulphur vapour pressure is higher than tin [86], producing stoichiometric SnS solar absorber and maintaining it following annealing is challenging, thus the existence of intrinsic defect is likely to happen. There are six fundamental intrinsic defects in binary chalcogenide SnS thin film; these include tin and sulphur vacancies (V_{Sn}, V_S), tin-on-sulphur and sulphur-on-tin antisites (Sn_S, S_{Sn}) and tin and sulphur interstitial (Sn_i, S_i) defects [52, 87, 88]. As shown in figure 2.2, V_{Sn} and V_S are lattice site that would have been occupied by tin and sulphur atom, respectively, are vacant giving rise to vacancy defects. Sn_S and S_{Sn} are anti-site defects, which occur, in ordered alloy when Sn and S atoms occupy the position that should have been occupied by S and Sn atoms, respectively. Sn_i and S_i are interstitial defects, which occurs due to Sn and S atoms occupying a site in the crystal lattice at which there is usually not an atom. These intrinsic point defects in SnS can also be categorised into positively and negatively charged defects, which acts as donors and acceptors, respectively. Few experimental studies on the defects in SnS solar absorbing thin films using photoluminescence (PL) technique are available [89, 90]. In addition, theoretical analysis have also been reported, which are obtained from both density functional theory (DFT) [52, 87] and projected augmented-wave method (PAW) [88]. Figure 2.2 shows the calculated formation energies of the intrinsic defects in (a)

Sn poor, S rich and (b) Sn rich, S poor SnS thin films [52]. From these defects, V_{Sn}, Sn_S and V_S defects have sufficiently low formation energies to modify the intrinsic properties of SnS.

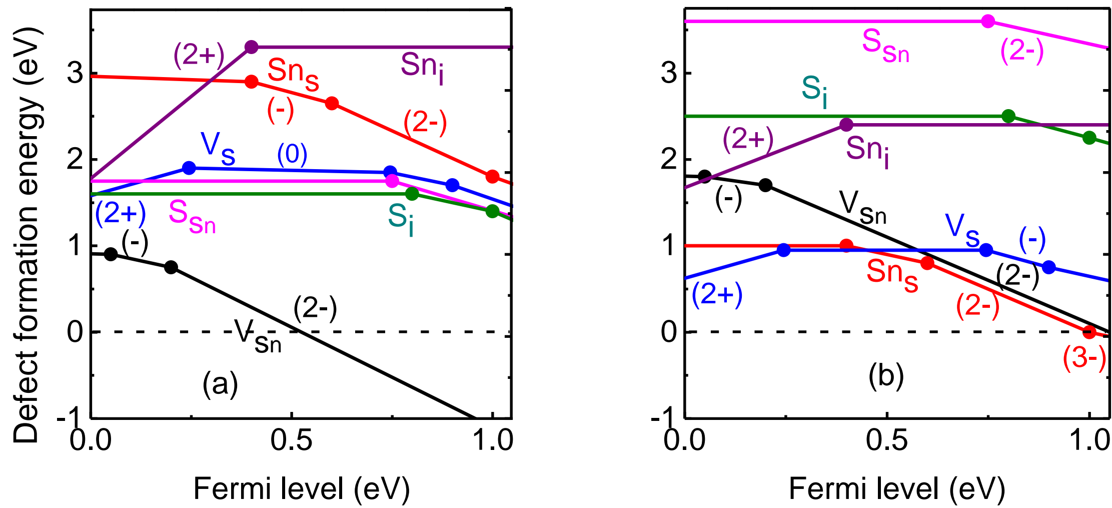

Figure 2.2 Defect formation energies of intirnsic defects in SnS as a function of the Fermi level in the (a) Sn poor, S rich and (b) Sn rich, S poor, adapted from [52].

The defect calculations suggest that the tin vacancy (V_{Sn}) acts as a shallow acceptor, which is mainly responsible for the intrinsic *p*-type conductivity of SnS in support of experimental observations. Sulphur vacancy (V_S) acts as a donor-type defect but its formation energy is larger than that of tin, therefore V_S defects will ineffectively compensate the positive carrier excess due to V_{Sn}. In addition, V_S has negatively charged states inside the band gap that can act as electron traps and Sn_S can yield deep gap states, which are detrimental for photo-generated carrier transport [52, 87]. These intrinsic defects can however be significantly minimised by adjusting the growth of SnS towards the S-rich conditions defined by the phase diagram in figure 2.1 but not too much so as to maintain suppression of secondary phases. Therefore, there is still considerable potential to optimise SnS solar absorber and improved SnS-based photovoltaic devices.

2.2.3 Crystal structure

SnS is comprised of diverse crystal lattice structures driven mainly by the ability of Sn to adopt two different oxidation states, Sn(II) and Sn(IV). The rich crystal lattice diversity of the SnS

system presents a challenge to its growth and characterisation. Naturally, SnS takes the form of a herzenbergite, which in its ground state and low temperatures crystallizes into the layered orthorhombic crystal structure with space group *Pnma* that are composed of layered 2D sheets as shown in figure 2.3 (a). Here Sn^{2+} ion coordinates to three S^{2-} ions with the Sn $5s^2$ lone pair of electrons occupying the last position of the tetrahedral site [62]. Other SnS crystal structures are the rocksalt with space group *Fm3m* shown in figure 2.3 (b), as well as the high temperature orthorhombic *Cmcm* and the Zincblende *F-43m* shown in figures 2.3 (c) and (d), respectively.

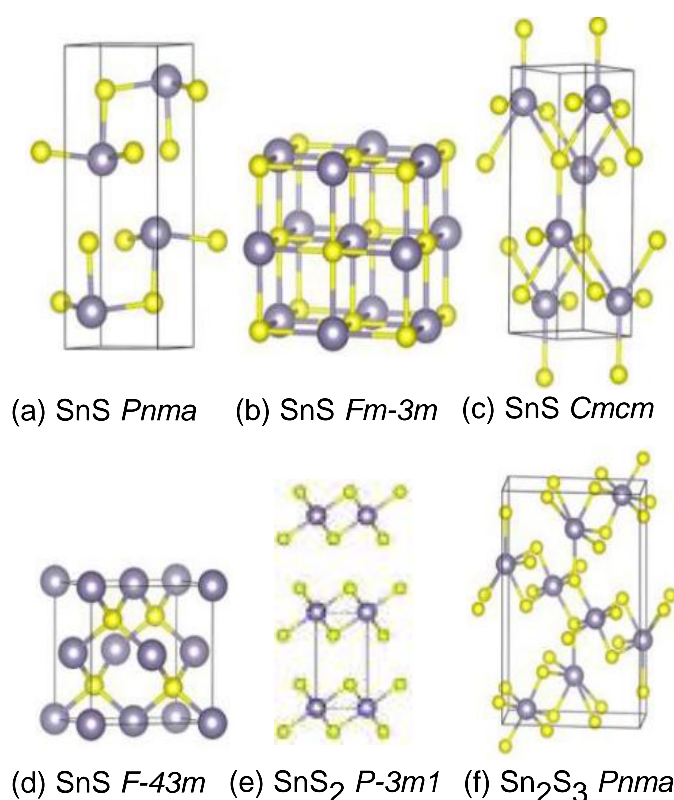

Figure 2.3. (a-d) crystal structure of various SnS polymorphs, (e) SnS_2 and (f) Sn_2S_3 (Sn and S in grey and yellow colour, respectively) [62]

Figure 2.3 (e) shows the *P*-3m1 crystal structure of tin disulphide (SnS_2). SnS_2 is probably the first known SnS compound which its laboratory synthesis dates back to over 200 years ago [32]. SnS_2 has Sn(IV) where 2D planes of edge-sharing SnS_6 tends to favour octahedral coordination environments. SnS_2 in its ground state crystallise to a hexagonal layered structure composed of SnS_2 trilayers, where the Sn(IV) ion coordinates to six sulphur ions

similar to that found in rutile-structured SnO_2. Each sheet of Sn atom is sandwiched between two sheets of S atoms, where each S-Sn-S layer is held by weak Van der Waals interactions [61]. Figure 2.3 (f) shows the Pnma crystal structure of tin sesquisulphie (Sn_2S_3), which usually exhibits equal proportion of Sn(II) and Sn(IV) oxidation states. Similar to SnS at ground state, it crystallises into an orthorhombic *Pnma* structure, but consists of 1D chains where Sn(IV) ions adopts chain centre positons with octahedral coordination to sulphur, and the Sn(II) ions adopting the chain end locations in the preferred trigonal-pyramidal arrangements. Sn_2S_3 due to its mixed valence state has reduced dimensionality compared to the single valence structures [61, 62]. In this work, both the SnS orthorhombic structure in ground state (*Pnma*) and high temperature (*Cmcm*) as well as the SnS_2 and Sn_2Sn_3 were identified with the help of X-ray diffraction (XRD) and Raman spectroscopy.

2.2.4 Optoelectronic properties

Figure 2.4 shows the theoretical calculations of Shockley-Queisser limit indicating realistic conversion efficiency of ~33% under AM1.5 (explained in chapter 1) for single-junction solar devices [91-93].

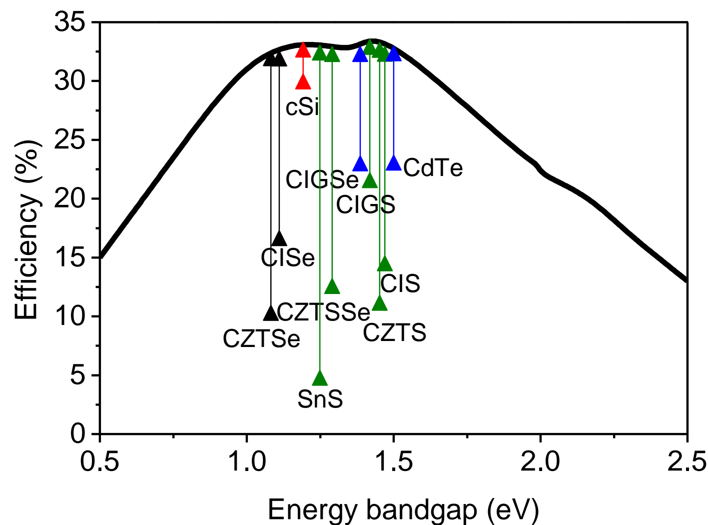

Figure 2.4 Illustration of the Schockley-Queisser theoretical efficiency limits for single junction solar cells under AM1.5 illumination as a function of energy bandgap, adapted from [91, 92], recent efficiencies taken from [14]. Various absorber materials (cSi, SnS, CZTS, CdTe etc.) are shown for comparison.

Notice from figure 2.4 that the bandgap of sulphides (CZTS, CIS and CIGS) can be tuned by controlling Se/S ratio to enhance the power conversion efficiency of the solar cell, therefore this can be extended to SnS (no record or report exist for the S-Se substitution for SnS thin films). This limit is defined by balancing the photocurrent produced when an incident photon has sufficient energy to excite an electron from the VBM to the CBM with the loss mechanism. The loss mechanisms, which may arise from the nature of material or design issues makes the predicted efficiencies difficult to achieve experimentally. These losses include blackbody radiation, radiative recombination (significant in direct energy bandgap materials) and spectrum losses [94]. Spectrum losses however has greater impact in choosing solar absorbers for PV applications. Spectrum losses results in thermalisation of carriers when photons with $h\nu > E_g$ pass through the absorber in which the excess of the energy bandgap is wasted as heat. In addition, transmission losses also results where photons with $h\nu < Eg$ pass through the absorber without generation of e-h pair therefore do not contribute to the photocurrent. Therefore choosing solar absorber materials with appropriate bandgap is crucial in fabricating high efficiency PV devices. It can be deduced from figure 2.4 that absorber materials with bandgaps range of 1-1.5 eV can yield over 30% power conversion efficiency. The ideal direct energy bandgap of SnS solar absorber range of 1.30-1.50 eV [15, 42, 86] and high optical absorption coefficient in the excess of 10^4 cm^{-1} [95] makes SnS suitable choice for PV devices.

2.3 SnS-based thin film solar cell structure

The use of SnS absorber material in solar cells started 30 years ago, when Sharon and Basavaswaran in 1988 [96], observed the PV potential of SnS in photo-electrochemical (PEC) cell exhibiting a photo conversion efficiency of 0.63% with the structure SnS/Ce^{4+}, Ce^{3+}/Pt. SnS solar absorbers were grown by passing H_2S through an acidic solution of stannous chloride ($SnCl_2$). Other SnS absorbers synthesised by different chemical routes used in PEC cells show similar PV characteristics of > 0.50% conversion efficiency with fill factor >0.6 [97]. Research towards using vacuum evaporated SnS absorbers in solar cells started in 1994,

Noguchi *et al.* [36] successfully synthesised SnS absorber using thermal evaporation technique and produced ITO/*n*-CdS/*p*-SnS/Ag cell structure. It showed an open circuit voltage (*Voc*) of 120 mV, a short circuit current density (J_{sc}) of 7 mAcm^{-2}, a fill factor (*FF*) of 35% and conversion efficiency (η) of 0.29%. This work appeared to have spurred the research interest of PV community into SnS material with Reddy *et al* 1997 [37] fabricating Al/n-CdS/p-SnS/Ag device structure with a J_{sc} and η of 8.4 mAcm^{-2} and 0.5%, respectively. SnS-based solar cells can be fabricated in the substrate or superstrate configurations. Figure 2.5 shows the schematic illustration of a typical SnS solar cell in substrate and superstrate configuration.

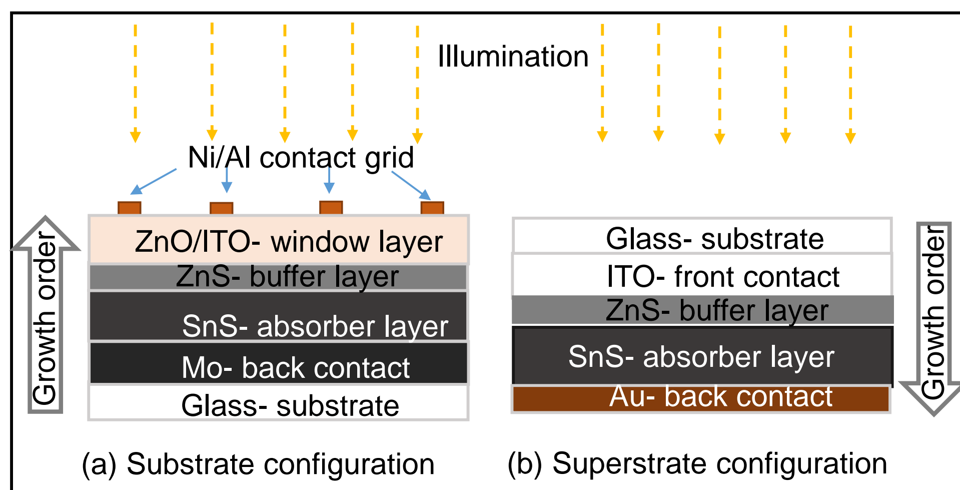

Figure 2.5. Schematic illustration of substrate and superstrate configurations for a typical SnS solar cell.

Generally for the substrate configuration, there is the glass substrate, the metallic back contact (normally Mo or Cu), the absorber layer (*p*-type), the buffer layer (*n*-type), the transparent conducting oxide (e.g *i*-ZnO/ITO) and metal front contact (e.g Ni/Al). The stacking sequence is glass/Mo/p-SnS/*n*-ZnS/*i*-ZnO/ITO/Ni-Al and the illumination takes place through the front contact. The first-ever produced SnS-based working device was in substrate configuration with power conversion efficiency of 0.63% [96], this was followed by Reddy *et al.* in 2006 [47] synthesised SnS onto glass/SnO_2 substrate via chemical spray pyrolysis. Reddy *et al.* coated the SnS absorber with evaporated indium doped (CdS:In) buffer layer (*p*-SnS/*n*-CdS junction) before finally depositing a 400 nm thick indium to form the top contact. The best cell exhibited

an open circuit voltage of 260 mV, a short circuit current of 9.6 $mAcm^{-2}$, a fill factor of 53% and efficiency of 1.3%. The best efficiency reported so far on *p*-SnS/*n*-CdS in substrate configuration is 2.53% via thermal evaporation of SnS absorber [98]. The substrate configuration further progressed with the use of alternative wider bandgap buffer layers to replace CdS. Recently Reddy *et al* in 2015 achieved an improved efficiency of 2.02% by replacing CdS with ZnMgO using the configuration of Mo/SnS/$Zn_{0.76}Mg_{0.24}O$/ZnO:Al/Ag [99]. Other *J*-*V* characteristics reported are Voc = 575 mV, J_{sc} = 9.96 $mAcm^{-2}$ and FF = 36.4%, they attributed high V_{oc} to the reduction in the recombination due to low J_{sc}. They synthesised the SnS absorber by sulphurisation of sputtered Sn precursor layers in a closed chamber, while the $Zn_{0.76}Mg_{0.24}O$ buffer layer was grown by chemical spray pyrolysis. Power conversion efficiencies of over 2% was reported via modifications in device design (Mo/SnS/Zn(O,S)/ZnO/ITO), post deposition heat treatments and optimisation of *p*-absorber/*n*-buffer band alignments via tuning of the conduction band offset (CBO) [100, 101]. This efficiency was nearly doubled by adding thin layer of SnO_2 (1nm) at SnS/Zn(O,S) interface, reaching efficiency of 3.88% as reported for SnS deposited via congruent thermal evaporation [102] and world record efficiency of 4.4% [28] for SnS synthesised via atomic layer deposition (ALD). This record efficiency device exhibited V_{oc}, J_{sc} and FF of 372 mV, 20.2 $mAcm^{-2}$ and 58.0%, respectively in a cell area of 0.232 cm^2. This high efficiency device was achieved following the annealing of SnS layer in H_2S to enlarge grains and reduce recombination loss at grain boundaries and oxidizing SnS surface before junction formation to suppress recombination centre losses to the junction.

On the other hand, superstrate configuration is fabricated in a reverse order compared to substrate configuration (see figure 2.5b) in the following stacking sequence: glass substrate/front contact/*n*-ZnS/*p*-SnS/metal back contact. Note that front contact can be indium tin oxide (ITO), fluorine-doped tin oxide (FTO) or aluminium zinc oxide (AZO). The n-buffer layer can be zinc sulphide (ZnS), cadmium sulphide (CdS), indium sulphide (In_2S_3) or zinc oxide (ZnO), while the back contact can be silver (Ag), gold (Au), aluminium (Al) or

molybdenum (Mo). Research into fabrication of SnS-based solar cell in superstrate configuration started in 1994 when Noguchi *et al.* [36] produced an ITO/CdS/SnS/Ag structure. The SnS absorber was deposited via vacuum evaporation method, best cell exhibited an open circuit voltage of 120 mV, a short circuit current density of 7 $mAcm^{-2}$, a fill factor of 35% and a conversion efficiency of 0.29%. Reddy *et al* in 1995 reproduced same structure but replaced ITO with aluminium using spray pyrolysis method to synthesis SnS absorber and vacuum evaporated CdS. They produced an improved current-voltage properties as follows: V_{oc} = 140 mV, J_{sc} = 8.4 $mAcm^{-2}$, FF = 38% and η = 0.5% [37]. An attempt in 2009 by Ghost *et al.* to fabricate SnS in superstrate configuration by thermally evaporating SnS onto ZnO buffer layer resulted in inefficient device [103]. The glass/ITO/ZnO/SnS/In structure used exhibited *Voc*, J_{sc}, *FF* and η of 120 mV, 0.04 mA, 33% and 0.003%, respectively in a cell area of 0.4 cm^2. Following this, efficiency of SnS solar cells in superstrate configuration stagnated until recently in 2013 Schneikart *et al.* fabricated a CdS/SnS heterojunction device via thermal evaporation of the SnS absorber [104]. The best device exhibited an open circuit voltage of 217 mV, a short circuit current of 19.0 $mAcm^{-2}$, a fill factor of 39.2% and a power conversion efficiency of 1.6%. They attributed the low open circuit voltage to possible existence of pinholes in the SnS layer and the cliff at the CdS/SnS interface. Similar to the substrate configuration, replacing the CdS layer with wider bandgap material may be the way forward. Ikuno *et al* in 2013 [105] further improved the power conversion efficiency of SnS device in superstrate configuration to 2.1% by replacing CdS with wider bandgap buffer layer material of $Zn_{1-x}Mg_xO$ to optimise the CBO and post fabrication annealing. The device also exhibited V_{oc} , J_{sc} and *FF* of 270 mV, 12.1 $mAcm^{-2}$ and 64%, respectively. They attributed the improvement to mainly conduction band offset optimisation.

From the literature, it is evident that each of the different layer components that make up a working device can affect the performance of the solar cells. As their properties differ in microcrystalline structure, carrier mobility and optical bandgap, there are bound to be, recombination centres, inter diffusion, chemical changes, defects and interface states that can

result in electrical and optoelectronic changes [106]. Therefore, the properties of materials used for these layers should be investigated before their application in solar cells.

2.4 Layer properties of SnS-based devices

This sub-section focuses on the properties and deposition process of the different layers in SnS-based solar cell structure. As stated in section 2.3, substrate and superstrate configuration are the inverse of each other, so the layer properties are reviewed following the substrate configuration order.

2.4.1 The substrate

Substrate here refers to the integral part of a device that serves as a base material for the deposition of the other component parts that complete the solar cell. Different substrates have diverse influence on the microcrystalline structure, grain growth, optoelectronic properties and device performance of SnS-based solar absorber and solar cells. These effects can result from the chemical nature, surface quality and thermal stability of the substrate material [40, 107, 108]. Therefore, selection of suitable substrate is crucial to obtaining good quality SnS absorber that can enhance device performance. Substrate should be stable at the production temperature of the solar cell. There must be chemical compatibility of substrate and SnS absorber material ideally, no chemical reaction should exist between the substrate and the film layer as interdiffusion can cause inclusion of undesired atoms in both SnS absorber and substrate.

Generally glass usually with thickness of 2-4 mm is used for deposition of SnS solar absorber as well as fabrication of both substrate and superstrate solar cell structures. A common type of glass used is soda lime glass (SLG) composed of soda (Na_2O) 16%, lime (CaO) 10 % and silica (SiO_2) 74%. SLG preference is due to its robustness to processing, cost effectiveness and ability to withstand relatively high temperature up to 500 ^{o}C [109]. Some impurities in SLG such as sodium (Na) can diffuse during thermal processes into the absorber layers and this

can be detrimental for SnS photovoltaic applications [110, 111] but beneficial to other solar absorbing thin films such as CIGS [112].

Very few investigations have been done to date to compare the influence of the various substrate for SnS solar absorber application. Revathi *et al.* initiated the study of substrate influence on SnS solar absorber in 2013 using glass, ITO and Mo-coated glass [108]. They reported that the layers deposited onto ITO and Mo-coated glass substrates exhibited single SnS phase only, while the film grown on glass had traces of SnS_2 in addition to the dominant SnS phase. This was followed by Reddy *et al.* in 2016 who investigated the influence of aluminium, silicon, molybdenum, nickel, indium tin oxide and SLG substrates on the properties of sulphurised SnS solar absorber [40]. However, they observed pure phase and high quality SnS layer across the substrates but films on aluminium substrate exhibited bigger grain sizes and low electrical resistivity. Recently Basak *et al.* 2018 investigated the behaviour of SnS solar absorber on the substrate configurations of glass/ZnO:Al, glass/ITO and glass/CdS via thermal evaporation. They observed better crystallinity for samples deposited on glass/ZnO:Al in addition to lesser dislocation density, higher optical density better mobility and less resistivity. Also the *J-V* characteristics of the glass/ITO forms ohmic junction with SnS while, that of glass/ZnO:Al shows a rectifying contact. They attributed diverse behaviour to the difference in work function of the substrates [113].

2.4.2 The back contact

The absorber/metal back contact junction is one of the interface of the SnS device structure. One of the the crucial issue with the fabrication of SnS solar devices in a substrate configuration is the formation of a quasi-ohmic electrical back contact that withstand the post deposition heat treatments and the formation of the *p-n* interface with reduced recombination losses. The criteria of matching work function and thermal expansion coefficients, limit the choice of available materials. Studies have looked at some metals to assess their compatibility with SnS. Devika *et al.* [114] investigated some of possible metals for SnS back contacts such as Ag (ϕ_{Ag} = 4.3 eV), Al (ϕ_{Al} = 4.25 eV), In (ϕ_{In} = 3.83 eV) and Sn (ϕ_{Sn} = 4.42 eV) circular metal

contacts on p-type SnS. The authors reported a work function of 4.2 eV for SnS, which differs from other sources [115]. From transmission line method, they found that Al, In and Sn exhibited ohmic contacts while Ag did not and reported that the highest current flow is with In contacts probably due to In diffusion into the film. Reddy *et al* [116] studied Zn/p-SnS contacts and found significant reduction in resistivity compared to Ag. They observed that Zn metals pins the Fermi level in SnS at about 0.57 eV, and it slightly diffused into SnS layer. However, these investigations suggest good options for ohmic contacts with SnS, leading SnS-based solar cells use Mo as the metal back contact [28, 102]. Patel and Ray [117] tested several back contacts such as graphite, Cu, Mo and Ni in superstrate device with a configuration Glass/F:SnO_2/In_2S_3/SnS/M (M= Graphite, Cu, Mo and Ni). They noted that Mo and Ni are poor choices due to increased series resistance and decreased shunt resistance resulting from tunnelling assisted recombination. The authors found graphite and Cu to be suitable alternatives to these materials, with Cu being the best option. However, Mo has been the choice for CIGS and CZTS-based devices, the literature showing that exchanging Mo for Cu or graphite could significantly enhance the fill factor of SnS-based solar cells, which is presently very low compared to other materials [118]. In addition to high quality material, SnS devices should have optimised back contact interfaces to minimise recombination and resistive losses.

2.4.3 The absorber layer and deposition methods

The absorber layer is responsible for light absorption and conversion of the incident photon into electricity. The promising properties that make SnS a good choice for solar cell applications and some challenges that may limit its performance had been highlighted in section 2.2. This sub-section will focus on how the various deposition routes can influence the properties of SnS absorber. As shown in figure 2.6 for the best performing SnS-based device, the route chosen to grow the absorber layer must guarantee the formation of polycrystalline layer with large columnar grains (see figure 2.6 b and c) to minimise grain boundaries. Grain

boundaries are regions of increased recombination in the absorber and they can impede carrier transport via charge trapping to form potential barriers.

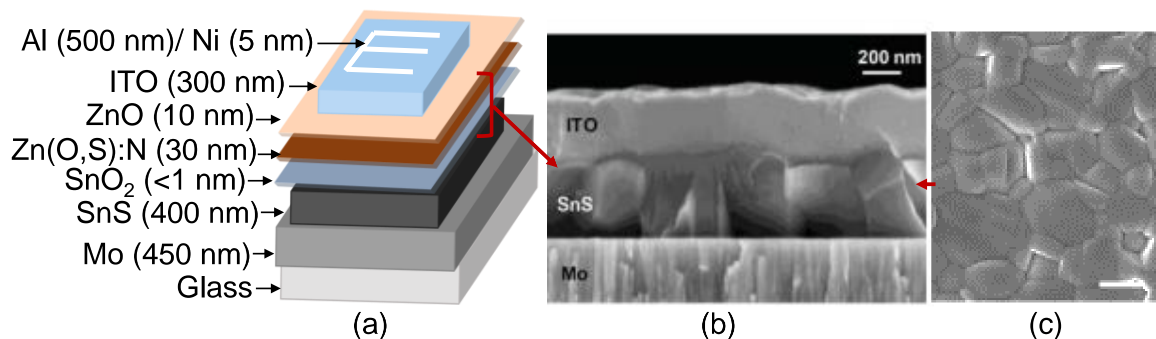

Figure 2.6 (a) device structure, (b) cross-section and (c) top view scanning electron microscope (SEM) image showing the absorber of the record efficiency SnS-based solar cell [28]. Scale bar in (c) denote 500 nm.

The routes to deposition of SnS solar absorber have been evolving with crucial modifications over the last two decades. Most of the physical properties of SnS layers depends on the synthesis routes, which can be divided into three categories. The first route that initiated the work on SnS involves solution-based methods such as chemical bath deposition (CBD) [119-125], successive ionic layer adsorption and reaction (SILAR) [126, 127], brush plating [128] and electrochemical deposition (ECD) [46, 96, 129, 130]. The second route involves the physical vapour deposition from the SnS source material or target such as thermal evaporation [15, 36, 39, 102, 104, 113], sulphurisation (2-step process) [40, 131-134], RF sputtering [105, 135-137], molecular beam epitaxy (MBE) [138-140], electron beam evaporation [141-143] and closed space vapour transport [144, 145]. The last route uses transport by chemical vapours to form the film layer, this include chemical spray pyrolysis (CSP) [47, 50, 146, 147], chemical vapour deposition (CVD) [100, 148, 149], metal organic chemical vapour deposition (MOCVD)[150-152], plasma enhanced chemical vapour deposition (PECVD) [153, 154] and atomic layer deposition (ALD) [28, 67, 155]. Figure 2.7 (a-i) shows the schematic diagram of some of the deposition methods for the SnS-based solar absorber, the different deposition methods has diverse influence on the properties of the films.

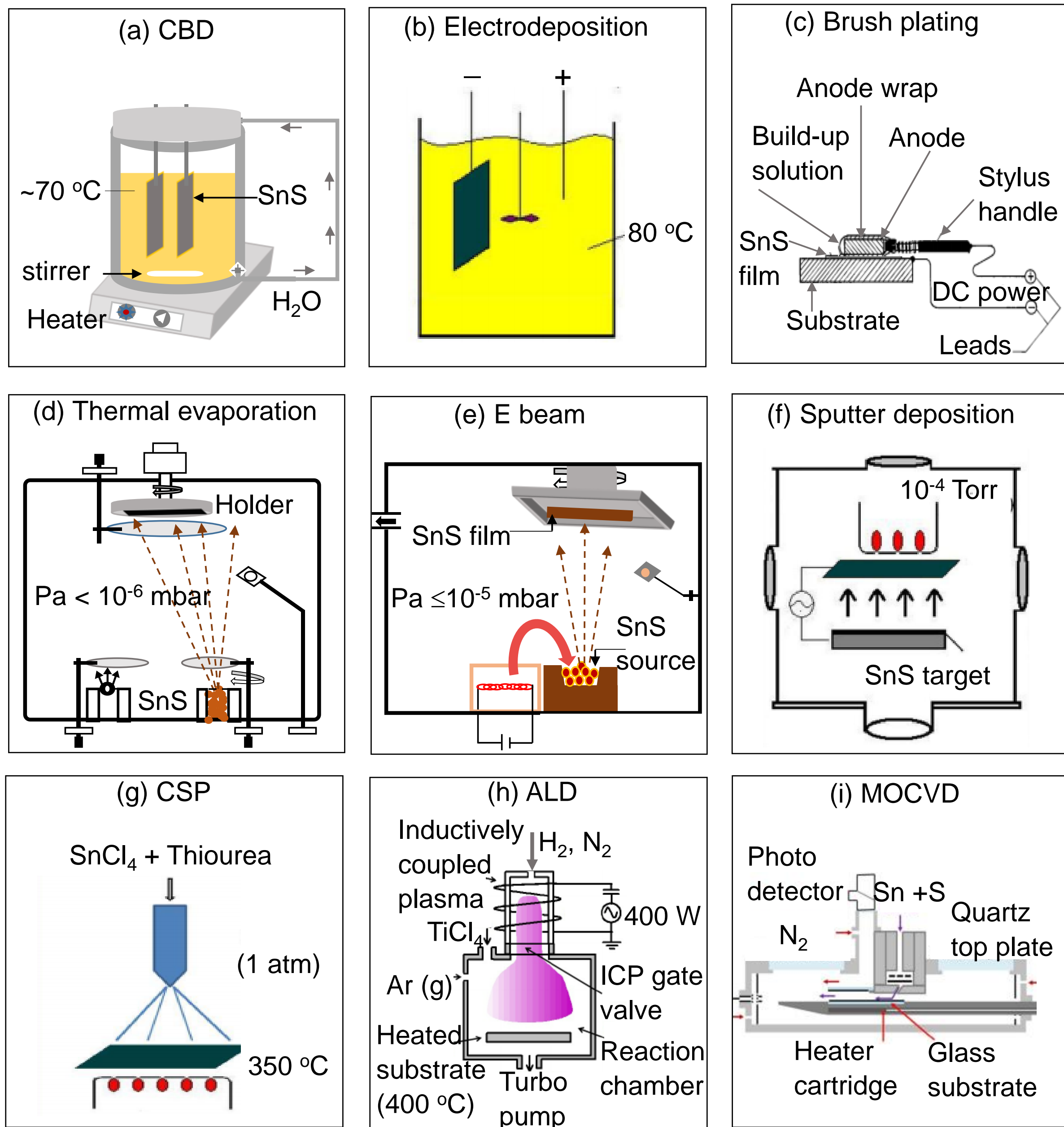

Figure 2.7 (a-i). Schematic diagram of SnS absorber deposition methods [143, 152, 156].

Thermal evaporation and atomic layer deposition have shown the best reported efficiencies of 3.88% [102] and 4.4% [28], respectively to date. However, atomic layer deposition (ALD) is self-limiting and has been reported to be highly expensive and unsuitable to industrial scale-up [102]. Hence alternative deposition method more suitable to manufacturing process and easy to use needs to be further investigating including thermal evaporation, which is a highly

scalable technique. The use of thermal evaporation to produce SnS solar absorber is therefore reviewed in sub-section 2.4.3.1.

2.4.3.1 SnS deposition by thermal evaporation

Thermal evaporation method is the simplest method conceptually, corresponding to raising the temperature of the source material in an open boat, crucible or suspended on wire (inside vacuum or non-vacuum chamber) so that the material evaporates or sublimes onto the substrate. The boat or wire materials are selected as a high temperature material (for example Mo, quartz or graphite crucible) and must not react adversely with the evaporant. SnS source material is heated in order to attain the requisite vapour pressure for the evaporation to take place, the evaporation rate is then governed by the Langmuir-Dushman equation [157].

$$N_e = 3.513 \times 10^{22} P_e \sqrt{\frac{1}{MT}} \tag{2.1}$$

where P_e is the equilibrium vapour pressure of the evaporated SnS material under saturated vapour conditions at a temperature T and M is the molecular weight of the material. The production of uniform SnS layers with high throughput is a requirement for good efficiency devices, and this usually means that the substrate has to be rotated. When source materials are heated in high vacuum, the evaporating atoms travel in a straight line to hit the substrate, part of the substrate directly facing the source material receives more coating than the edges, substrate rotation is used to ensure uniform coating [158]. In thin film coating process, steps are always taken to assure good film adhesion and to control various properties of the layers as desired. Fortunately, thermal evaporation system design and methods can allow adjustability of a number of parameters such as film thickness, substrate temperature, rate of deposition, substrate rotation and source-substrate distance. This gives opportunity to achieve desired results in the uniformity, adhesion strength, grain structure, optoelectronic and crystallographic properties of the films.

The use of thermal evaporation to deposit SnS solar absorber dates back to 1994 when Noguchi *et al.* [36] explored the advantage of variable substrate temperature range of 150-350 ^{o}C to deposit SnS films and fabricated n-CdS/p-SnS heterojunction solar cell. They reported a change in the prominent diffraction peak from (111) to (040) as the substrate temperature increases. They recorded a direct energy bandgap of 1.48 eV, which they attributed to the presence of SnS_2. The SnS films had *p*-type conductivity with a resistivity, carrier density and Hall mobility range of 13 - 20 Ωcm, 6.3×10^{14} - 1.2×10^{15} cm^{-3} and 400 - 500 $cm^2V^{-1}s^{-1}$, respectively. Their completed working device exhibited a power conversion efficiency of 0.29% under 100 $mWcm^{-2}$ illumination. This was followed by Deraman *et al.* [159] in the same year investigating electrical conductivity of SnS using a substrate temperature range of 50-300 ^{o}C. They observed that the conductivity of the layers increase from 0.5-2.0 Sm^{-1} with an increase in the substrate temperature from 50-250 ^{o}C and attributed this effect to the changing film composition. Since then to date, thermal evaporation of SnS thin films has been evolving with diverse optimisation of the deposition parameters. Difference in the vapour pressure of tin and sulphur has also been reported to influence the composition of the deposited films by Nwofe *et al.* [160] and Devika *et al.* [15]. Nwofe *et al.* investigated the properties of the films at substrate temperature range of 280-360 ^{o}C and found non-stoichiometric films to form at $300 \leq T \leq 340$ ^{o}C, as well as a higher crystallinity for the higher substrate temperatures. The layers contained densely packed large grains and the film thickness was 2.0-3.6 μm, while the deposition rate was not reported. However, Devika *et al.* adjusted substrate temperature from room to 325 ^{o}C using a deposition rate and film thickness of 10 $Ås^{-1}$ and 0.5 μm, respectively. They found smaller grain size for lower temperature and the Sn/S ratio ranged from 0.85-1.10 corresponding to a substrate temperature range of 50-350 ^{o}C. Secondary phase (SnS_2) was present in the layer deposited at 50 ^{o}C substrate temperature. From the Devika *et al.* observations, optimal substrate temperature exist at 275 ^{o}C for achieving stoichiometric films, which differs from the findings of Nwofe *et al* by 25-65 ^{o}C. This difference exist because the film thickness are not the same. Similarly, Reddy *et al.*

[161-163] observed that the Sn and S composition gradually changed from sulphur-rich to tin-rich with the increase of growth temperature, also reported is a change of orientation from (111) to (040) direction as temperature increased from 275-350 °C. The authors noted that the films were single phase following Raman analysis. The films exhibited a direct energy bandgap that decreased with an increase in the growth temperature while, the electrical resisitivity decreased from 335-97 Ωcm with the growth temperature from 275-350 °C.

Other researchers have also explored the adjustability of substrate temperature to optimise the microscopic, crystallographic and optoelectronic characteristics of SnS films. Hegde *et al.* [164] studied these SnS properties at substrate temperature range of 50-300 °C and observed that only the films deposited at 300 °C showed single stoichiometric SnS phase with (111) preferred orientation. They employed a source-substrate distance, deposition rate and film thickness of 15cm, 8 $Ås^{-1}$ and 500 nm, respectively. The authors found the average grain size and crystallites of the films to increase with the substrate temperatures. Miles *et al* [39] coupled the effect of film thickness, source and substrate temperature on thermally evaporated SnS films. They observed a bandgap value of 1.55-1.70 eV for a film thickness of 0.8 μm, while further increase in thickness resulted in the reduction of the bandgap. The authors also noted that with thermal evaporation, densely packed columnar grains, stoichiometric, conformal and pinhole free SnS films can be produced. The substrate temperature has also been used to tune the crystallographic and electrical properties of SnS to fabricated good efficiency SnS-based solar cells by Kawano *et al.* [98]. They reported best device efficiency of 2.53% for the SnS absorber deposited at substrate temperature of 200 °C compared to 1.36 and 1.01% efficiency of the films deposited at 175 and 225 °C, respectively. In this report, the SnS absorber was deposited for 120 min without control of the substrate temperature and film thickness.

Layer thickness also plays a vital role in SnS-based thin films as it can be used to tune the intrinsic property of the films to get desired quality for solar cell application. To date few reports exist on the SnS layer thickness optimisation. Devika *et al* [165] found that optical band gap,

resistivity and preferred orientation of SnS films are strongly related to the film thickness. They varied the thickness between 0.10 to 1.25 µm using a constant temperature of 300 °C and deposition rate of 10 Ås^{-1}. The report suggested that good crystalline SnS quality could be obtained at thickness ≥ 0.75 µm with optimum bandgap of 1.5 eV. Nwofe *et al.* [95], Jain and Arun [166] respectively noted that increase in the films thickness leads to decrease in energy bandgap and the XRD peaks become stronger.

2.4.3.2 Post deposition heat treatments

In addition to the issue of non-stoichiometry of tin and sulphur in SnS due to high volatility of S, as-deposited SnS films show poor crystalline quality and small grains. This limits the power conversion efficiencies of the device due to high carrier recombination at the grain boundaries. Thermal annealing is generally used in thin film semiconductors to favour crystalline quality, grain growth and optoelectronic properties. The post deposition heat treatment process usually leads to the formation of larger grains, decreasing of the surface roughness and improvement in device performance [28, 157]. In SnS solar cells, a high quality layer comprised of large grain is necessary to facilitate the transport of photo-generated carriers, reduce grain boundary recombination and thus potentially enhance the power conversion efficiency of the device. Several investigations have been made on the influence of heat treatments on SnS solar absorbing thin films in diverse environments such as vacuum [41, 167-169], air [170, 171], hydrogen sulphide (H_2S) [28, 102, 172], chlorine [150, 173] and inert atmosphere such as argon (Ar) [167] and nitrogen (N_2) [174, 175]. Thermal annealing treatment in SnS solar absorbing thin films are found to be effective in reducing recombination and promoting grain growth and carrier mobility [101]. Contradicting reports exist for vacuum annealing, while Devika *et al.* [168] noticed reduced grain size and higher transmittance due to decrease in thickness following anneal, Ogah *et al.* [176] reported the opposite (increased grain size and reduced transmittance which is linked to improved crystallinity). This contradiction is bound to occur since their as-deposited SnS were different; in the former initial thickness was 0.5 µm re-evaporation during anneal will leave ultra-thin layer of SnS on the

glass substrate which is bound to allow high transmittance. While in the later thickness is >1.0 μm, cluster of grains will tend to coalesce to yield bigger grains. Thermally annealing SnS in air was found to change the conductivity from *p* to *n*-type with formation of SnO_2 without influencing the film structure [171]. To stop SnS oxidation and change in conductivity type, SnS annealing could be done in Ar or N_2. SnS treatment in inert atmosphere (Ar or N_2) can assist the grain growth with noticeable loss in stoichiometry of tin and sulphur [52, 167, 174]. However, thermal annealing in chlorine ambient has been found to react aggressively with the SnS, which result in the formation cracks and isolated domains [150, 173]. The SnS post anneal treatment in the presence of H_2S environment has been studied in several works [28, 102, 172]. This thermal treatment in H_2S is effective in suppressing the creation of sulphur vacancies V_S due to high sulphur loss following anneal and significantly enhancing grain growth. SnS heat treatment in H_2S ambient is one of the crucial factors that lead to the record SnS device efficiency to date [28]. Another way that has not been explored is the thermal annealing in selenium ambient that can allow S-Se substitution similar to CZTS [27], this study will investigate this possible new route in thermal annealing of SnS solar absorbing thin films.

2.4.3.3 Numerical simulation studies

Numerical simulation can provide easy route in examining the expected performance of a thin film solar cell. The use of simulation tools can also reduce the amount of material usage in the search to optimise fabrication conditions. One of the simulation tools which has been used for SnS device is the one-dimensional solar cell capacitance simulator structures (SCAPS-1D) [177]. The software was developed for the CdTe, CIGS and $CuInSe_2$ materials but can be modified to allow the use of other materials such as SnS. Ullah and Mari [178] reported successful use of SCAPS to analyse the effect of absorber layer thickness, operational temperature and illumination on performance of SnS-based thin films solar cells. They noticed that increase in layer thickness leads to increase in efficiency and devices perform optimally at room temperature. The simulated device showed maximum efficiency of 10.6%, V_{oc} of 0.92 V, J_{sc} of 13.4 $mAcm^{-2}$ and *FF* of 86.3%. The report did not speculate the limit of layer thickness,

which is crucial in the laboratory experiments. SCAPS software has equally been used to get insight on the optimal buffer layer for SnS heterojunctions [179]. Xu and Yang [58] have studied the properties of SnS heterojunctions with diverse buffer layers via numerical analysis. They explored buffer layers such as CdS, ZnS, ZnO and a-Si, and noticed that ZnS/SnS has best conversion efficiency of 16.26% due to its optimal band alignment with SnS. Therefore, the need to explore alternative buffer layer to replace conventional CdS is vital to enhance the performance of SnS devices.

2.4.4 The buffer layer

The buffer layer is used to form interface with the absorber layer to provide transition between the absorber and the TCO. The energy bandgap of buffer layer must be sufficiently large in order to maximise the transmission of incident light to the SnS absorber layer. It should exhibit *n*-type conductive in order to form anisotype heterojunction with the *p*-type absorber layer. In addition, the buffer layer should exhibit relatively high electrical conductivity to ensure that field region is largely located in the absorber layer to maximise carrier collection, as well minimise resistance losses in the transport of carriers to the external circuit [180].

Cadmium sulphide (CdS) is commonly used to form SnS/CdS heterojunction but there are evidences of non-optimal CBO with CdS [42, 58, 59, 181]. SnS/CdS heterojunction has a large negative CBO of -0.5eV, which gives rise to an increase of interface recombination [42, 181] and reduce the open circuit voltage (V_{oc}) of the solar cell. A small positive CBO of the range ($0 \text{ eV} < \Delta E_c < 0.1 \text{ eV}$) [181] is suitable to reduce the interface recombination and enhance open circuit voltage. The use of CdS buffer layer for SnS-based solar cells stagnated efficiency at 2.53% [98]. The search for suitable buffer layer to replace CdS is probably one of the challenges for SnS-based solar cells. To overcome this challenge, band alignment studies have been reported for wide bandgap alternative buffer layers of SnO_2 [59], ZnMgO [99, 105], Zn(O,S) [42] and InS_xO_y [181]. Sugiyama *et al.* [182] also investigated the band offsets of diverse alternative buffers layers such as SnS/SnS_2, SnS/In_2S_3, $SnS/ZnIn_2Se_4$, SnS/ZnO and

$SnS/Mg_{0.3}Zn_{0.7}O$ using photoelectron yield spectroscopy. They claimed that $SnS/Mg_{0.3}Zn_{0.7}O$ that exhibited type-I heterostructure is the most appropriate *n*-type layer for *p*-SnS in order to improve device performance. These investigations have led to the achievement of best efficiency of 3.88% to date using thermal evaporation and Zn(O,S) buffer layer.

2.4.5 The transparent conducting oxide layer

The transparent conducting oxide (TCO) is generally used as the front contact for thin film solar cells. It is normally *n*-type with good electrical conductivity and high transmittance in the visible and near infrared range. It is required that the sheet resistance of the TCO is no more than 10 Ωsq^{-1} to produce high efficiency solar cells. The most widely used TCOs are indium tin oxide (ITO), aluminium zinc oxide (AZO) and fluorine-doped tin oxide (FTO) [180]. In substrate configuration of devices TCO deposition is the final step before top metal grid, while in superstrate devices it is the initial step. The choice between the TCO sometimes greatly depend on the deposition temperature of the *p*-SnS and *n*-buffer layer, which are governed by the type of configuration. Therefore, for higher temperature deposition such as superstrate devices where TCO comes first, FTO is the material preferred, since it is more stable compared to ITO at elevated temperatures. However, for low temperature deposition, such as in substrate devices where SnS absorber and the *n*-buffer layer are deposited first with any post heat treatment, ITO is the material of choice since it has a high optical transmission for a given sheet resistance [180], the deposition process is explained in section 3.4.

2.4.6 Top contact grid

The top grid usually consist of either a metal layer or a stack of two layers. For a single metal layers, gold, indium or silver are often used. In two layers, the first layer of the front grid must establish an ohmic contact with the TCO and must have a high melting point to prevent diffusion to the device area during the period of operation and nickel is often used for this purpose. The second layer should exhibit good electrical property and aluminium is commonly used.

2.5 Conclusions

The review has shown that SnS can be deposited with a large variety of deposition methods however, thermal evaporation technique is the most scalable and easy to use route towards large-scale industrial manufacturing. In addition, SnS solar devices can be fabricated in substrate or superstrate configuration, but the best efficiencies to date were obtained in the substrate configuration where it is possible to separate absorber deposition and junction formation. This gives the advantage of treating the SnS surface before coating with buffer layer and optimise the CBO. Sulphur content is vital at the junction and the back contact for device performance but its volatility has proven to be a challenge for producing S-rich SnS absorber. To move forward with possible use of SnS absorber in solar cells, microscopic and crystallographic characteristics should be considered, as much of the variability in the optoelectronic properties correlates with the variation in the material quality, especially sulphur content.

Chapter 3

Experimental and Characterisation Methods

3.1 Introduction

This chapter describes the substrate and source preparations, the thin film deposition processes and the characterisation methods used throughout this work. The pre-deposition processes, which include the substrate and source material preparations, are presented in sections 3.2 and 3.3, respectively. Four main deposition methods were applied during the research activity. These methods, which included thermal evaporation, magnetron sputtering, electron beam evaporation and chemical bath deposition, are described in section 3.4. Section 3.5 follows by outlining the post deposition treatments required to optimize the properties of the SnS layers. Finally, the device fabrication processes and description of characterisation method used for both layers and photovoltaic devices described in section 3.6.

3.2. Substrate preparation

The substrates serve as a mechanical support for the thin films and selection of a suitable substrate is vital for SnS based solar absorbers. The substrate used in this work include the following: soda lime glass (Thermo scientific, $76 \times 26 \times 1$ mm^3) composed of soda (Na_2O) 16%, lime (CaO) 10 % and silica (SiO_2) 74%, quartz composed of SiO_2 with 99.999 % purity, fluorine-doped indium tin oxide (FTO) and indium tin oxide (ITO) coated glass composed of In 74%, O_2 18% and Sn 8%. Soda lime glass is the first choice in this study because of its cost effectiveness and it can withstand relatively high temperature up to 580 ^oC [109]. However, some impurities in SLG such as sodium (Na) can diffuse during thermal processes into the absorber layers and this can be detrimental for SnS photovoltaic applications [110]. To overcome this, quartz substrates were also used for comparison. For the superstrate configuration, ITO or FTO coated glass was used due to its relatively low resistivity of <15 Ω/sq. The cleanliness of the substrates is critical in getting a good quality and pinhole free thin film

as dust or lint on the substrate surface shadows the surface during evaporation. All the substrates were cleaned chemically (dilute decon-90 solution with deionised water) followed by ultrasonication via deionised water (DI) water for 15 min. The substrates were again rinsed with deionised water and blown dry under a nitrogen stream before being placed immediately in the evaporator. Care was take during cleaning process to avoid scratching of the surface of the glass coated with FTO and ITO.

3.3 Sample deposition methods

3.3.1 Thermal evaporation

The source materials used in this work (SnS, ZnS and In_2S_3) were all solids in pellets and powdered form, while $CdSO_4$, $NH_3.H_2O$ and thiourea were the source material for CdS growth . The SuperVac SnS pellets (T7-5014-M) with 99.999 % purity was sourced from Testbourne Limited, UK. The source material is carefully loaded inside the crucible and placed in upright position in the CH-8 shielded heat crucible connected to either of the source heaters (see figure 3.2) inside the chamber. The vacuum chamber is then evacuated to a pressure $\leq 8.0 \times 10^{-7}$ mbar.

The review of the thermal evaporation method is included in chapter 2. It is one of the most cost effective and easy to use type of physical vapour deposition (PVD) method. Here, the source materials were heated at sufficiently high temperature to increase their vapour pressures. The vapour stream emitted from the heated source material then traverses the chamber, hits the substrate and condenses as a thin film. As illustrated in figure 3.1, the film formation process has multiple steps occurring at microscopic level. These include arrival of atoms onto the substrate surface; sticking together of vapour atoms (adsorption); surface diffusing; bonding together and formation of crystals by the atoms (nucleation process) to the final formation of the new films [183-185]. All these steps are controlled by deposition rate, temperature, amount of evaporant and input power.

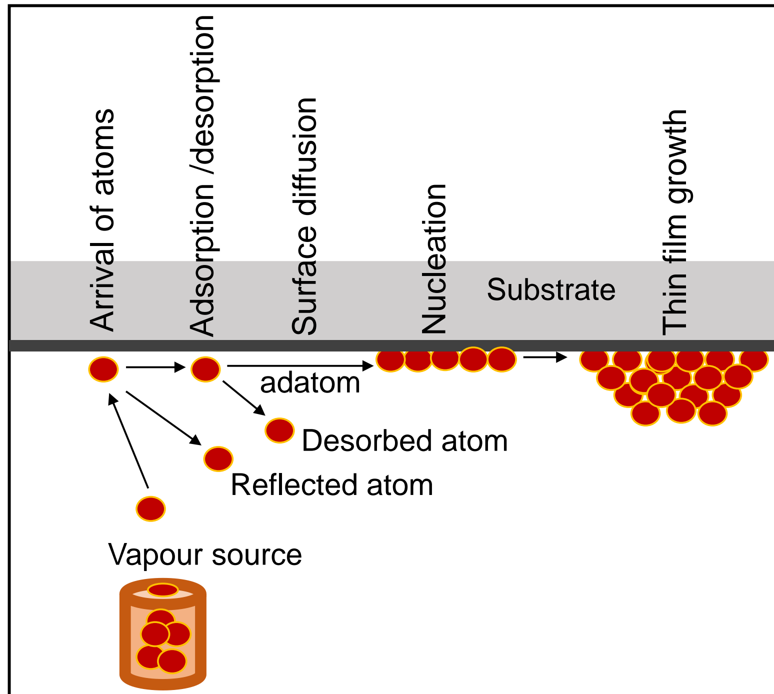

Figure 3.1 Theory of the formation of thin films on a flat substrate for thermal evaporation [186].

For all the deposition, high vacuum (Pa $\leq 8.0 \times 10^{-7}$ mbar) were used to avoid reaction between the vapour material and chamber environment. High vacuum is also necessary to ensure straight-line path for most of the emitted vapour atoms from the source to the substrate (300 mm distance). This creates a conducive environment during the film formation process ensuring little or no interaction between residual gases and vapour atoms. The conditions used are in agreement with the report that for a substrate to source distance in the range of 10 to 50 cm in a vacuum evaporator, pressure lower than 1.33×10^{-5} mbar are necessary to maintain a straight-line path for the vapour atoms [157]. A schematic diagram of the evaporation setup used in this work, Oerlikon Univex 250 is shown in figure 3.2.

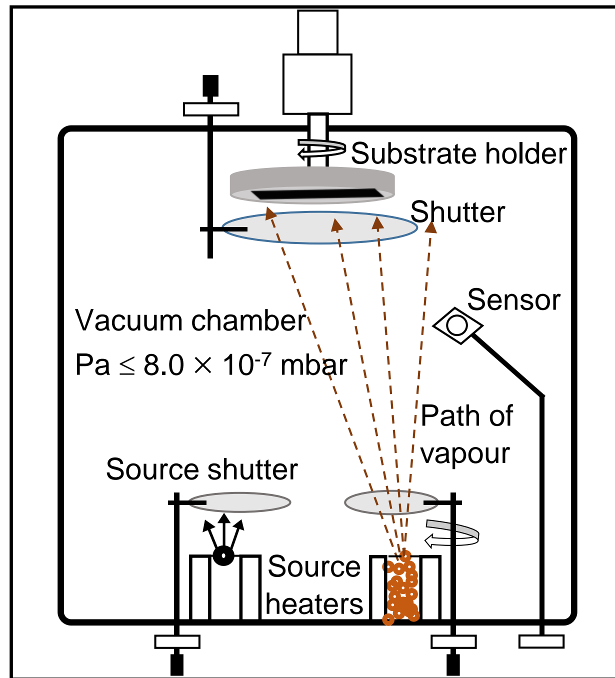

Figure 3.2 Schematic illustration of the thermal evaporation setup.

Irreversible temperature stripes and crayons were used to calibrate the substrate heater and data is shown in figure 3.3. These differences in the setup and measured temperatures is because of the separation between the heating element and substrate holder causing heat losses.

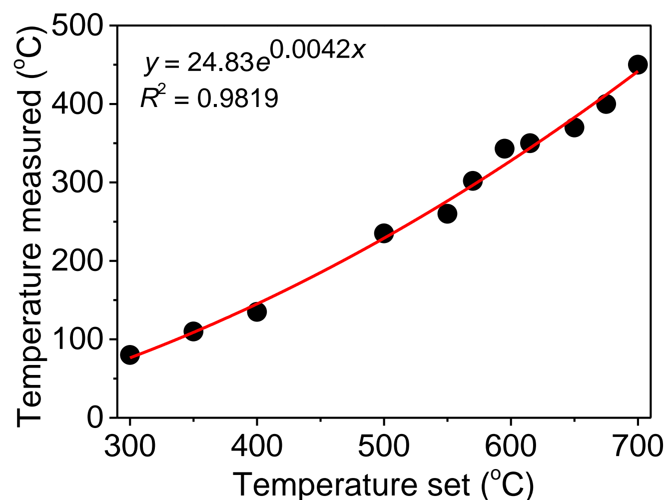

Figure 3.3. Oerlikon Univex substrate heater calibration

For the SnS solar absorber, the growth parameters used in this work are the substrate temperature T_s (from room temperature to 400 °C) and film thickness t (from 100 nm to

3500 nm). Other constant parameters were a substrate rotation of 10 rpm to enhance homogeneity, deposition rate of 3 nms^{-1} and source-substrate distance of 300 mm. The films were evaporated through resistance heating using a low voltage range of 0.8-1.0 V and high current ranging from 90 to 105 A to melt 3-8 mm SnS pieces. For the 8-12 mm ZnS pieces, the voltage were varied between 1.0-2.2 V and current measured to range from 110 to 180 A during the deposition. Similarly, a voltage range of 1.0-1.5 V and current ranging from 100-121 A were used to evaporate In_2S_3 powder source material. A quartz crystal sensor mounted inside the chamber was used to monitor the deposition in real time; and triggers the substrate shutter to close once the pre-set final film thickness was achieved. In order to calibrate the thermal evaporator, the tooling factor and Z-ratio of the source material was adjusted to achieve good agreement between the recorded and measured thickness.

3.3.2 Magnetron sputtering

Magnetron sputtering is a widely used PVD method that requires good vacuum conditions similar to thermal evaporation. It is mostly preferred for temperature and surface sensitive material deposition. During magnetron sputtering, energetic gas ions generated from a glow discharge plasma are accelerated towards a target containing the material to be deposited. To enable the ignition of plasma, a negative charge is applied to the target source material in a vacuum chamber containing an inert gas - such as argon. This causes free electrons (secondary electrons) to flow from the negatively charged target material and interact with the outer electronic shell of the argon gas atoms. The arrangement of the magnets create parallel magnetic field to the target surface and constrain free electron (e^-) motion to the vicinity of the target as illustrated in figure 3.4. Hence, the positively charged argon ions (Ar^+) attracted to the negatively charged target material at a very high velocity ejects atomic size particles from the source material to the surface of the substrate and are deposited as thin films [187-189].

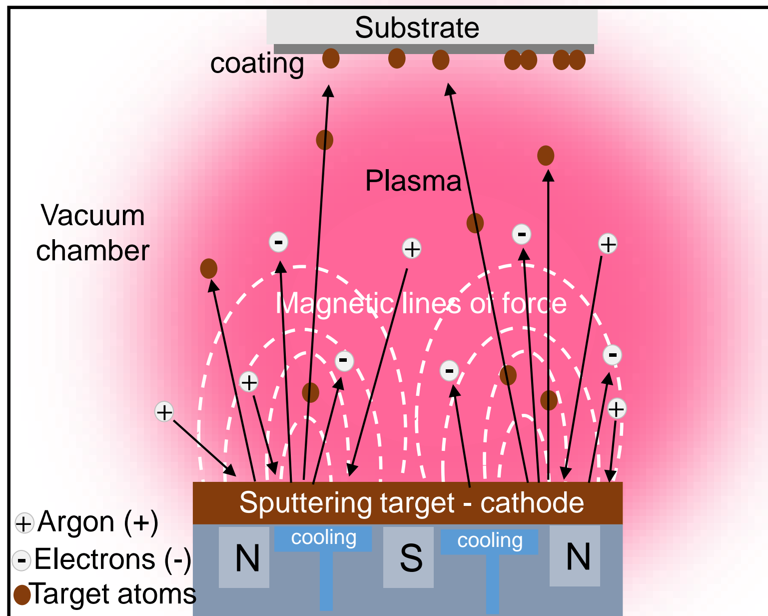

Figure 3.4. Schematic diagram of magnetron sputtering process.

In this work, magnetron-sputtering system (Teer Coatings UDP 350) was used to deposit Mo back contact, ZnO and ITO window layers. As illustrated in figure 3.5, the setup consists of three targets that run in direct current (DC) magnetron modes and one target operating in radio frequency (RF) magnetron mode.

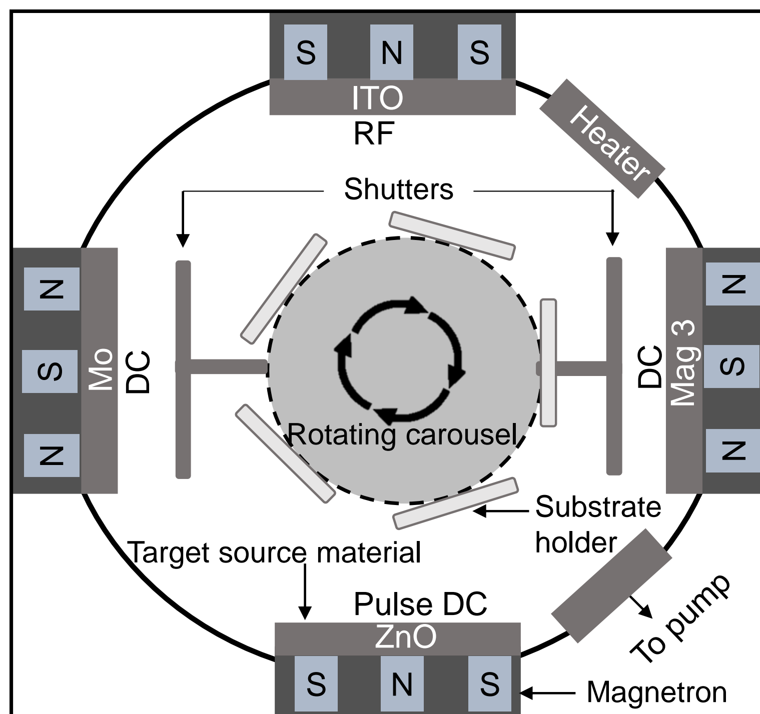

Figure 3.5. Schematic illustration of the teer coatings UDP 350 magnetron sputtering setup.

In DC mode, the target is directly conducting electricity and has limitations when it comes to dielectric target as the build-up of a positive charge on the surface of the target over time creates quality control issues on the films and can even terminate the discharge of sputtering atoms. RF modes enables the sputtering of dielectric materials by alternating the electric potential of the current to avoid a charge build-up of sputtering target materials [189]. Since DC power supply are easy to control, simple and relatively low cost in power consumption but cannot be used for insulators, pulsed DC and RF as well as DC for Mo deposition were considered in this work. In pulsed DC mode, the target is bombarded with powerful voltage spikes to clean its surface and prevent the build-up of a dielectric charge.

In this work, substrates were placed in the chamber parallel to the source target surface at a substrate-target distance of 70 mm before evacuating the chamber to $< 8.0 \times 10^{-6}$ mbar. DC magnetron sputtering (Mag 1) was used to deposit ~1 μm thickness of Mo thin film on SLG and quartz substrate to provide electrical back contact for the solar cells in substrate configuration. The source material target used for the deposition was supplied by PI-KEM Ltd, with dimension $248 \times 133 \times 10$ mm^3 and 99.95% purity. A pre-sputtering treatment was first done for 20 minutes to clean the source target surface and remove impurities. The Mo films were then deposited at room temperature for 43 minutes with a fixed current of ~3.0 A and voltage of 323 ± 30 V. The argon-mass flow rate was measured at 70.0 sccm with working pressure of 6.3×10^{-3} mbar and substrate carousel set to rotate at constant speed of 5 rpm.

The intrinsic zinc oxide (ZnO) window layer was deposited using pulsed DC magnetron sputtering (Mag 4) at room temperature with carousel rotation of 5 rpm. A source target of 100 mm diameter and 3 mm thickness with 99.99 % purity, bonded to a 3 mm thick copper back plate was used. After the standard 20 min pre-sputtering stage, a nominal 60 nm ZnO layer were deposited for 35 min in Ar/O_2 flow ratio of 25.0 with voltage and current of 506 V and 0.2 A, respectively. Immediately after ZnO deposition, the system was switched to RF magnetron sputtering (Mag 2) mode for in-situ ITO deposition at substrate temperature of ~150 °C. A source target with 99.99 % purity (In_2O_3/SnO_2; 90/10 wt%) of same dimension and

bonding ZnO was used for the sputtering. The substrates were heated for 30 min before a pre-sputtering stage of 20 min and the deposition of ~200 nm thick ITO with RF forward power of 200 W for 90 min at substrate rotation of 5 rpm, working pressure of ~ 3.1×10^{-3} mbar and argon-mass flow of 25.0 sccm.

3.3.3 Electron beam evaporation

Electron beam evaporation (E-beam) is a form of physical vapour deposition that allows for deposition of thin films of high-melting-point materials that would have been difficult to deposit using thermal evaporation. As illustrated in figure 3.6, in high vacuum (pressure $\leq 10^{-5}$ mbar) electrical current is passed through a tungsten filament that emits electrons. The electron beam using magnets bends and focus into the crucible to melt the source material. The vapour atoms travels outwards in all direction and condenses on the substrate as thin films [157, 190]. In this work, E-beam evaporation (Tecvac ECU 700) was used to deposit nickel (Ni) and aluminium (Al) front contact of the solar cell. The samples were covered with a shadow mask that creates cell area of 0.16 cm^2 before being placed in the chamber parallel to the source crucible at a distance of 400 mm and evacuated to a pressure $\leq 10^{-5}$ mbar. The electron beam is focused on the Ni and Al pellets in copper and graphite crucibles respectively, to melt pellets and create vapour atoms. The current was varied from 0.01 to 0.40 A with voltage of ~7kV and a substrate rotation of 10 rpm to enhance homogeneity of the film layers. The thickness were measured using a quartz crystal senor, the deposition rate of 0.2 nm/s and 2.0 nm/s were used to achieved the desired thickness of 50 and 1000 nm for Ni and Al, respectively.

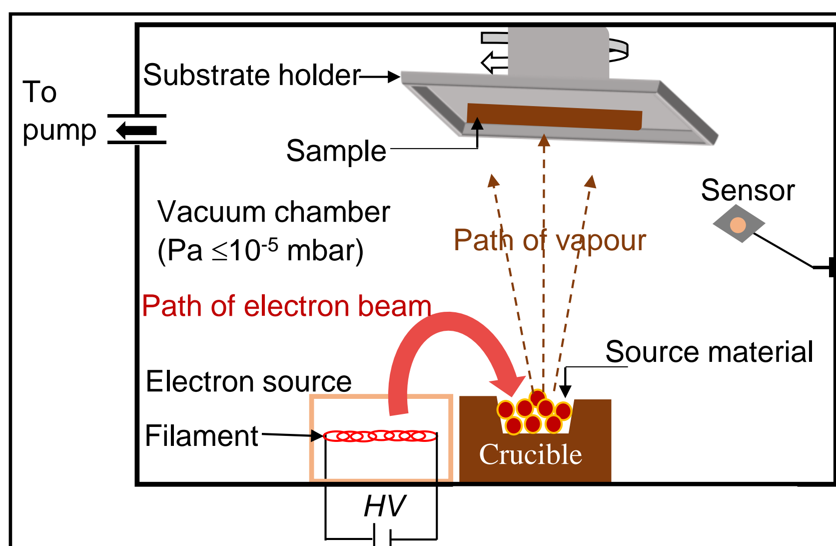

Figure 3.6 Schematic illustration of the electron beam evaporation process.

3.3.4 Chemical bath deposition

Chemical bath deposition (CBD) method provides an easy and low cost method of producing cadmium sulphide (CdS) thin films at relatively low temperatures through reactions between Cd and S ions in an alkaline solution [191]. In this process, high quality film layers are produced by intimate contact between the bath solution and substrate material allowing homogenous formation of thin films on the substrates [192]. The CBD process involves the dissolution of a soluble salt (cadmium salt) in an aqueous solution to release cations whereas the anions are provided from a suitable compound of non-metallic element (thiourea) that can decompose in the presence of hydroxide ions. The film grows through ion-by-ion condensation of Cd^{2+} and S^{2-} ions on the substrate when Cd^{2+} and S^{2-} ions exist over the solubility limit [191]. The film formation can occur by a process of homogenous nucleation in the volume of the solution or through the process of heterogeneous nucleation on the substrate. The typical process reaction steps for the homogeneous mechanism involving cadmium acetate are given by [193].

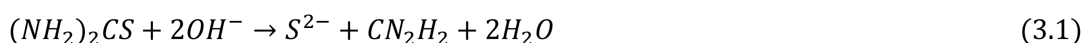

$$(NH_2)_2CS + 2OH^- \rightarrow S^{2-} + CN_2H_2 + 2H_2O \tag{3.1}$$

$$[Cd(NH_3)_4]^{2+} \rightarrow Cd^{2+} + 4NH_3 \tag{3.2}$$

$$Cd^{2+} + S^{2-} \rightarrow CdS \tag{3.3}$$

Sulphide ions (S^{2-}) are released by the hydrolysis of thiourea while, Cd^{2+} ions form from cadmium sulphate ($CdSO_4$) by coming with NH_3 in the range of pH 10-11[194]. In heterogeneous mechanism, $Cd(NH_3)_4^{2+}$ complexes adsorb on the substrate and film growth takes place by ionic exchange reaction with S^{2-} ions that reduces the overall speed of reaction and prevents $Cd(OH)_2$ formation [195, 196].

The CdS buffer layer used in making device in this work was deposited by CBD as illustrated in figure 3.6. The 318 mL of deionised water was poured into a double-walled beaker and brought to a stable temperature of 70 °C. Then 2 and 1.5 mM of $CdSO_4$ and $NH_3.H_2O$ respectively, were added to the solution successively while the solution was being stirred to ensure uniform thermal and chemical homogeneity for the formation of the film. The samples with configuration of substrate/Mo/SnS, substrate/Mo/SnSSe and ITO coated glass were then inserted into the solution (see figure 3.7) for 2 minutes before 12mM of thiourea was added to solution and left for 20 minutes with continuous stirring of the bath. Thereafter, the samples were removed from the bath, rinsed with DI water and dried using nitrogen gas. Finally, the samples were subjected to heat treatment at atmospheric pressure for 10 min at temperature of 200 °C to promote intermixing at the SnS/CdS junction before being transfer for ZnO and ITO deposition.

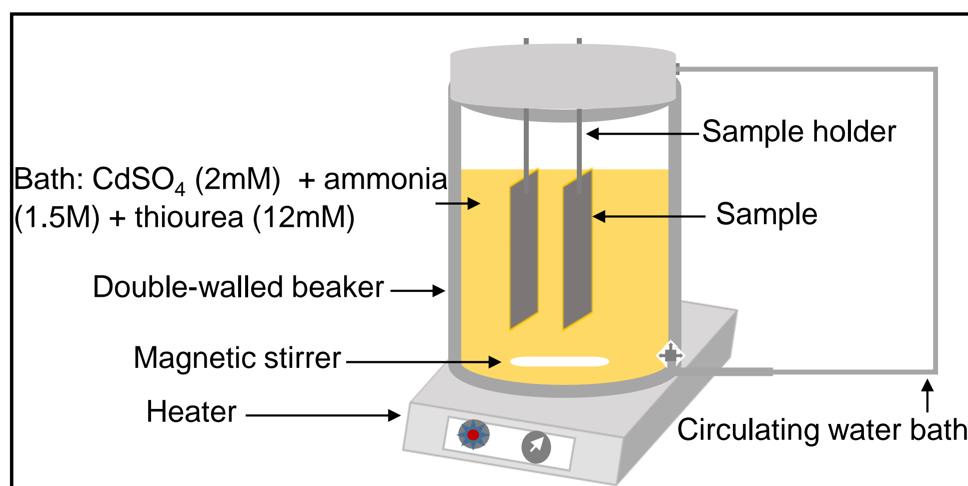

Figure 3.7 Schematic diagram of chemical bath deposition set up for CdS growth.

3.4 Post deposition heat treatment of the samples

Post deposition heat treatment of the light-absorbing thin film can improve the quality of the layers and enhances the device performance. A very high quality SnS layer comprised of large grains is required to facilitate the transport of photo-generated carriers, reduce grain boundary recombination and thus potentially enhance the power conversion efficiency of the solar cells. The post deposition heat treatment process usually leads to the formation of larger grains and the decreasing of the surface roughness [28, 157]. In this study, post deposition heat treatment was performed in vacuum, argon and nitrogen environments. In order to activate the absorber layer, enhance grain growth and power conversion efficiency, the possibility of Se/S substitution was investigated in both vacuum and argon environments.

The vacuum annealing treatment followed film deposition. The as-deposited sample was taken from the evaporator, carefully cut into three parts with one used as reference while, the other two parts were loaded back in the evaporator. The evaporator was then evacuated to a pressure of ~10^{-7} mbar before setting the substrate temperature at 400 and 450 ^{o}C for 60 min, for the second and third part of the sample, respectively.

In nitrogen (N_2) ambient heat treatment, the samples were investigated using two sets of experiments. For the first set, three samples of the as-deposited SnS films were annealed at temperature range of 400, 450 and 500 ^{o}C for 60 min at 1000 mbar N_2 flow in a tube furnace. In the second set, samples were treated with $SnCl_2$ and $MgCl_2$ solution prior to the annealing. This was performed by dipping the samples in a saturated solution of $SnCl_2$ and $MgCl_2$ for about 10 seconds, rinsed with deionised water before gently blown dry under a nitrogen stream. Then, the samples were moved into the tube furnace where the annealing took place at similar condition with the first set. A Carbolite annealing system (TZF-12/65/550) fitted with twin Eurotherm 2132 temperature controllers was used during the thermal annealing in N_2 flow.

In order to investigate the effect of Se/S substitution on the SnS absorber, the treatment was performed in both low vacuum and high vacuum environment using elemental selenium

vapour. Three set of experiments were conducted. In the first experiment, the Se and SnS pellets were co-evaporated in vacuum at substrate temperature of 350 °C using the similar process described in section 3.2. For the second experiment, SnS films were first deposited at similar substrate temperature with first experiment before evaporating Se pellets at temperature of 400 and 450 °C.

For the third experiment, the selenisation process involves placing the sample face down inside a cylindrical graphite box with 300 mg of selenium pellets placed on both ends of the box as illustrated in figure 3.8. The furnace was evacuated to a pressure of 5.5×10^{-3} mbar and backfilled with ~10 mbar of argon before increasing the temperature to the desired set point (range of 400-500 °C). The set point was controlled using timer and once it stabilises, the temperature was held constant for 20 min before the tube furnace is cooled to ≤ 40 °C to end the process and get the samples out (see figure 3.9, a typical example for a 450 °C set point).

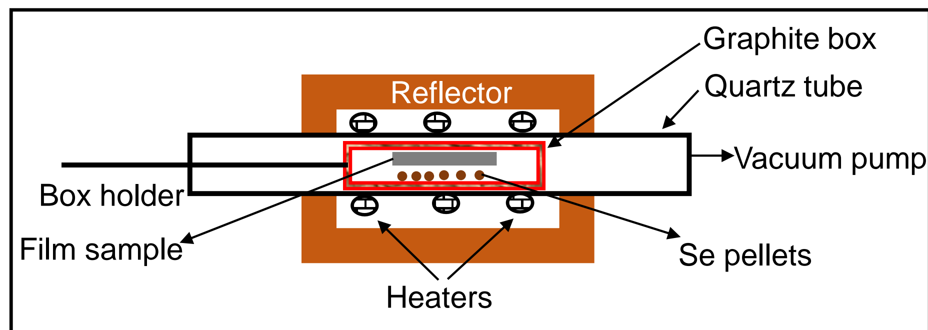

Figure 3.8 Schematic illustration of the tube furnace for Se anneal.

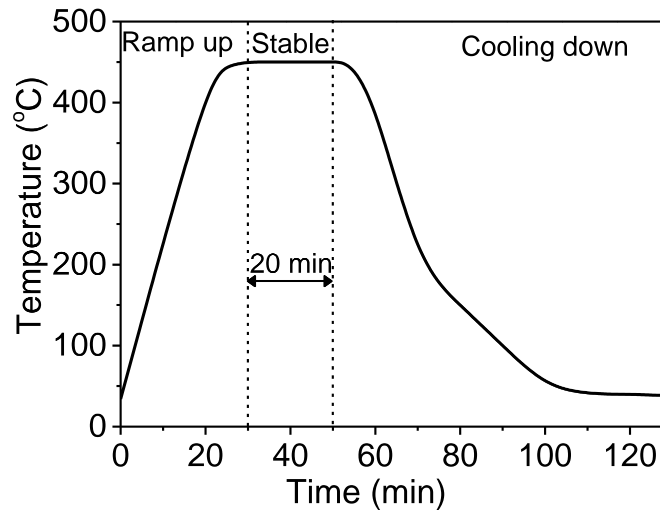

Figure 3.9 Typical measured temperature profile of the tube furnace for a 450 ± 10 °C set point.

3.5 Device fabrication processes

The devices were fabricated in both substrate and superstrate configurations. The substrate configuration followed the stacking sequence glass/Mo/SnS/ZnS/ZnO/ITO/Ni-Al (detail and diagram in chapter 2 section 2.3, figure 2.5). In this process, Mo (~1.0 µm thickness) was sputtered onto substrate (SLG or quartz) as the back contact of the device before depositing the SnS absorber layer onto it. Thereafter, some of the samples were either annealed in N_2 or Se environment (detailed in section 3.5) before coating with either ZnO, ZnS, In_2S_3 or CdS buffer layers. This was immediately followed by sputtering ZnO (~60 nm) and ITO (~200nm) before depositing Ni (50 nm) and Al (1000 nm) metallic front contact to complete the device.

For superstrate configuration (detailed in section 2.5), the substrates used were the commercial indium tin oxide (ITO) and fluorine-doped tin oxide (FTO) coated glass slides with surface resistivity of 15 Ω/sq. The n-buffer layer of either ZnO, ZnS, In_2S_3 or CdS with nominal thickness of 50-60 nm was first deposited on the ITO surface before coating with SnS absorber layers. Some of the films were thereafter subjected to heated treatment in either N_2 or Se environment to promote intermixing before finally depositing a gold (Au) back contact of 100 nm thickness at room temperature.

3.6 Characterisation techniques

3.6.1 Thickness measurement

Thickness is one of the most important thin film parameters for consideration as it determines to a great extend the properties of the film. In this work film thickness were measured by both in-situ monitoring of the quartz crystal and after the thin film deposition using a profilometer. Physical measurement was made using a Bruker DektakXT profilometer to compare to the crystal monitor reading. For the low thickness In_2S_3 and ZnS (80 ± 10 nm) grown at room and ~250 ^oC substrate temperatures, high temperature tape was used to mask a region on the samples during film deposition. The tape creates a step height when removed from the sample surface that enables easy measurement of the thickness by the vertical motion of the stylus tip over the step.

3.6.2 Scanning electron microscopy and energy dispersive X-ray spectroscopy

Scanning electron microscopy (SEM) provides insight into the material properties such as grain distribution, grain size, surface topographies, thickness and composition. A Tescan Mira3 high performance scanning electron microscope (operated at 5-20 kV and working distance of 5-15 mm) used in this study was equipped with energy dispersive X-ray Oxford instrument (X-Max 150) detector for analysing the elemental composition in the samples. The SEM scans the surface of the samples with a focused beam of electrons. When these high-energy electron beam strikes the sample surface, they interact with the sample atoms at various depths and produce a variety of radiations that contain details about the sample's surface topography, composition and view/map grain orientations. The theory of emission of electrons and X-rays are shown in figure 3.10. The penetration depth (R_e) is defined by electron energy of the penetrating beam voltage (E_b) into the sample and can be expressed as [197]:

$$R_e = E_b \frac{4.28 \times 10^{-6}}{\rho} \tag{3.4}$$

where ρ is the density of the sample material.

The modes of radiation used in this study include the secondary electrons (SE) that give information on the topography of the sample, backscattered electrons (BSE) that provide information on the topography/atomic contrast and the X-ray photons that provide important insight on the atomic and elemental composition of the sample.

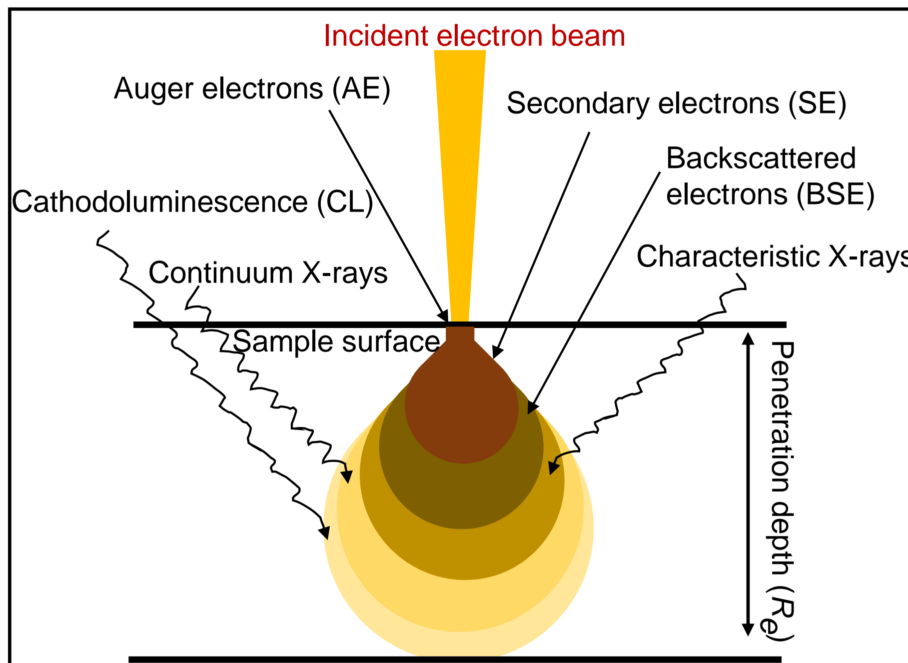

Figure 3.10 Schematic of the emission of the secondary electrons, backscattered electrons and characteristic X-rays.

3.6.3 X-Ray diffraction

The crystal structure of the samples in this study were examined using a Siemens D5000 X-ray diffractometer in Bragg-Brentano configuration using a CuK_α (λ = 1.5406 Å) radiation source, a step size of 0.02 and an acquisition time of 2 seconds/step. X-ray diffraction (XRD) provides vital insight on the structure of the crystal or the identity of a crystalline substance. XRD is a non-destructive technique that works on the principle of Bragg's law of diffraction as follows [197].

$$2d_{hkl} sin\theta = n\lambda \quad (3.5)$$

where d_{hkl} is the inter-planar spacing, θ is the angle between the incident and the diffracted X-rays, n is an integer (taken as 1 in this experiment) and λ is the wavelength of the radiation. This is illustrated in figure 3.11a while figure 3.11b represents a typical Bragg-Brentano configuration adopted in this study.

The data extracted from the analysis were thereafter compared with the reference powder diffraction files to identify the appropriate crystal structure and orientation of the films. The SnS film has orthorhombic crystal structure and its lattice parameters of SnS can be calculated as follows [198]:

$$\frac{1}{d_{hkl}} = \sqrt{\frac{h^2}{a^2} + \frac{k^2}{b^2} + \frac{l^2}{c^2}} \tag{3.6}$$

where $a \neq b \neq c$, are the lattice parameters. The crystallite size of the samples and micro strain were calculated using Williamson-Hall analysis [199]:

$$\beta cos\theta = \frac{0.94\lambda}{D} + 4\varepsilon sin\theta \tag{3.7}$$

where D is the crystallite size, λ is the wavelength of the X-ray radiation (1.5406 Å), β is the full width half maximum (FWHM) of the diffraction peak and θ is the Bragg angle. The linear fit to the data from the plot of $\beta cos\theta$ versus $4\sin\theta$ were used to estimate the average crystallite size (D) and the micro strain (ε) from the y-intercept and the slope of the fit, respectively. Crystallite size can also be estimated using Scherrer's relation [164]:

$$D = \frac{0.94\lambda}{\beta cos\theta} \tag{3.8}$$

where D, β, θ and λ retain their meaning as defined in equation (3.7).

While Williamson-Hall analysis deals with broadening due to grain size and micro strain, Scherrer's relation [164] is only due to grain size. The Scherrer's relation cannot measure the accurate values of crystallite size hence, W-H analysis was used in this study.

The lattice parameters ‘a’, ‘b’ and ‘c’ of a single crystal SnS thin film are given as 4.148, 11.48 and 4.117 Å, respectively [200]. In this study, lattice parameters were calculated using Eva software. The software was integrated into the XRD and it calculates data such as miller indices (hkl), Bragg’s angle and lattice parameters.

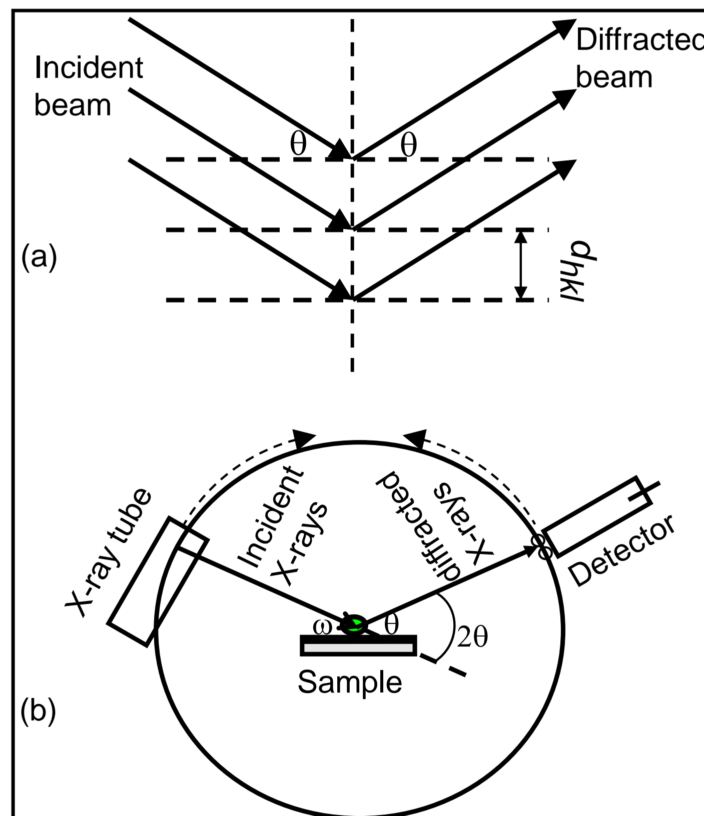

Figure 3.11 (a) X-ray diffraction from atomic planes and (b) typical Bragg-Brentano geometry.

3.6.4 Secondary ion mass spectrometry

Secondary ion mass spectrometry (SIMS) is a surface analysis technique used to study the composition of solid surface to the bulk of the material. The analysis enables the elemental, isotopic and molecular composition of the surface to be determined up to a depth of few nanometres. Figure 3.12 shows the working principle of SIMS, where a primary ion beam is used to bombard the surface of the sample under vacuum to generate secondary ions that are collected and analysed using a mass spectrometer. Only the positively or negatively charged particles which make up the secondary ions are detected by the mass spectrometer

and were used to provide the basis for the compositional analysis while, the neutral atoms which are the most abundant of the ejected atoms are not used.

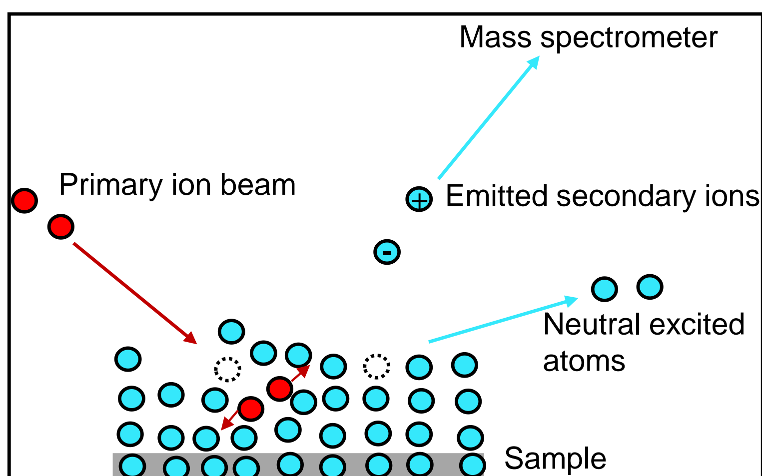

Figure 3.12 Schematic illustration of SIMS principle.

The elemental depth profiling was investigated by measuring the secondary ion count rate of the selected elements as a function of sputtering. In this study, SIMS was performed using a primary beam of oxygen ions (5 kV, 300 nA) rastered over a 0.5 x 0.5 mm^2 area (gating 10%) and quadrupole detector from Hiden Analytical.

3.6.5 Raman spectrometry

Raman spectroscopy is a non-destructive structural analytical tool based on the inelastic scattering of photons (usually from a laser) with elemental vibrational excitations in materials commonly used in the identification of crystalline as well as to observe vibrational, rotational and other low-frequency modes in a system. The laser light interacts with the molecular vibrations, phonons or other excitation in the system, resulting in the upward or downward shift of the laser photons energy. This shift in energy provides insight on the vibrational modes in the system. The theoretical basis of the Raman scattering effect is illustrated in figure 3.13. Since XRD technique is based on Bragg's law (details in section 3.6.3), the indexing of the crystalline phases can present some difficulties when there are overlapping of some SnS Bragg peaks with SnS_2 and Sn_2S_3 reflections. Crystalline materials are indistinquished if they

have similar atomic planar space, these feature are common in SnS materials due to the proximity of the d-spacing of the (hkl) diffraction peaks [39, 45, 201]. Raman analysis is thus used to complement the XRD analysis in detecting secondary phases in SnS thin films since it is based on the vibrational modes of the system [202, 203].

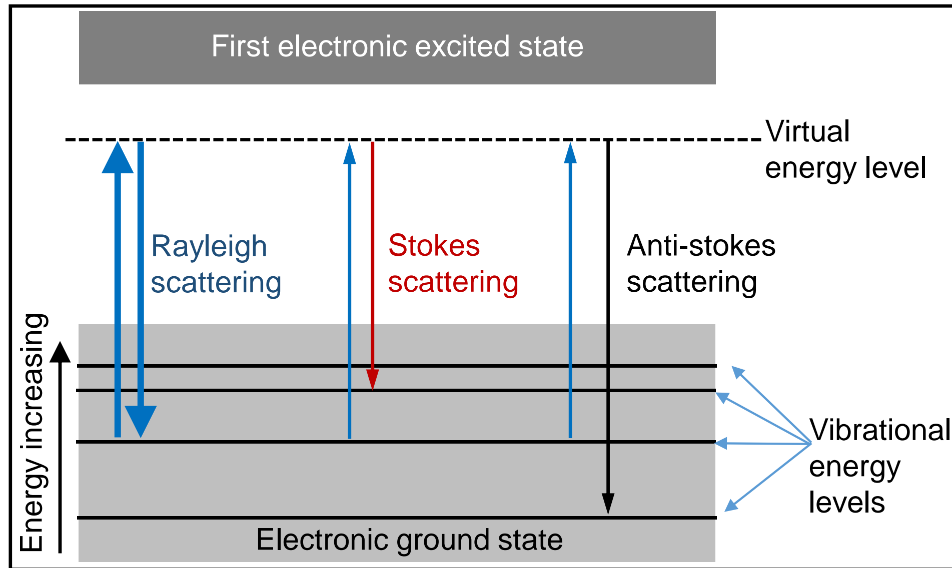

Figure 3.13 Schematic illustration of energy-level diagram in Raman scattering (the line thickness represents the signal strength from different transitions).

In this study, the phases of the SnS films were further verified using a Horiba Labram 300 Raman spectrometer of 632.8 nm wavelength using a HeNe laser.

3.6.6 Spectrophotometry

Optical properties of thin film absorbers characterise their ability to absorb incident light within the visible spectrum (~300-700 nm) and near infrared (up to 1400 nm) for absorbers. Ultraviolet-visible and near infrared spectroscopy (UV-Vis + NIR) is normally used to probe the absorption of light of thin film absorbers. The effectiveness of thin films at absorbing light generally depends on their absorption coefficient (α), which determines how far light of a certain wavelength can penetrate into the material before it is absorbed. For good thin film absorbers, the absorption coefficient are usually high such that only a shallow region of the

material allows the penetration of light. For a given material, the absorption coefficient (*α*) can be calculated from transmittance, *T*, and reflectance, *R*, measurements as follows [204]:

$$\alpha = -\left(\frac{1}{t}\right) \ln \left(\frac{[(1-R)^4 + 4T^2R^2]^{\frac{1}{2}} - (1-R)^2}{2TR^2} \right) \quad (3.8)$$

where *(t)* stands for the thickness of the film, the optical energy bandgap (E_g) can then be related to α as:

$$\alpha h\nu = c\left(h\nu - E_g\right)^n \quad (3.9)$$

where *h* is Planck's constant, *c* is a constant called the band tailing parameter, *n* is the frequency that depends on the nature of transition (*n* equals ½ or 2 in direct and indirect allowed transitions, respectively). In order to determine the absorption characteristics of the SnS thin films in this study, *T* and *R* were measured using a UV-Vis-2600 spectrophotometer over a wavelength range of 300 - 1400 nm for SnS, In_2S_3 and ZnS samples.

3.6.7 Hot point probe

Hot point probe was used to determine the conductivity type of the SnS samples. It provides a very simple way to distinguish between n-type and p-type type materials using two probes (hot and cold) connected to a sensitive galvanometer with the hot probe connected to the positive terminal and the cold probe connected to the negative terminal of the meter as illustrated in figure 3.14. When the two probes make contact with the sample surface, carriers diffuse from the contact point such that the charge of the dominant carrier determines the direction of the net current flow [205]. Positive deflection is obtained in the meter when applying the set up to n-type semiconductor while, a negative deflection is observed when applying it to a p-type semiconductor. For the SnS samples measured, a negative deflection was observed indicating a p-type conductivity for the SnS layers studied.

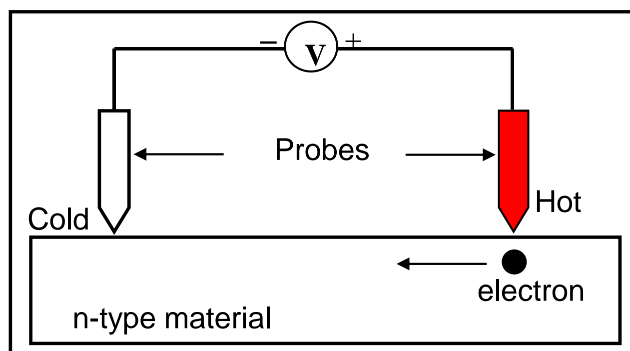

Figure 3.14 Schematic illustration of hot point probe set up.

3.6.8 Photoluminescence spectroscopy

Photoluminescence spectroscopy is a non-contact and non-destructive technique of probing the electronic structure of material. During this process, a light is directed to a sample where it can be absorbed to cause photo-excitation. In this study, photoluminescence (PL) measurement was performed using a Horiba Jobin Yvon iHR320 fully automated spectrometer fitted with an InGaAs PMT detector cooled to -30 °C to reduce noise. The measurement setup is shown in figure 3.15. A 532 nm continuous wave diode-pumped solid state (CW-DPSS) laser (MGL III-532 200 mW) was used as an excitation source. Power-dependent PL measurements were performed by adjusting the intensity of the laser beam using the MGL PSU-III-LED controller. PL measurements at varying temperatures were performed by placing the sample in a Janis SHI-4-2 closed cycle refrigeration cryostat using compressed He gas coupled with a Lakeshore Model 335 temperature controller. The laser light was chopped and focused onto the sample inside the cryostat and luminescence from the sample was focused into the entrance slit of the 320 mm focal length monochromator. The luminescence was filtered with a long-pass filter using a cut-off wavelength of 760 nm to prevent artefacts arising from laser radiation.

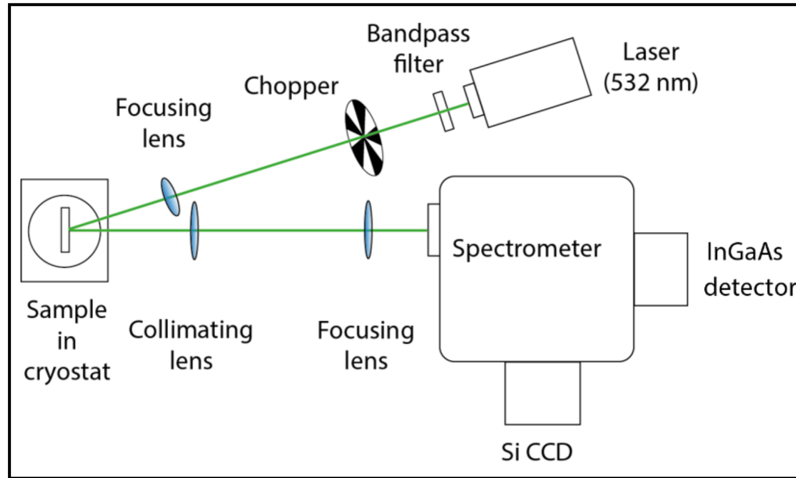

Figure 3.15 Photoluminescence spectroscopy set-up.

3.6.9 Simulated device characteristics

SCAPS modelling tool was used to simulate the current density-voltage (*J*-*V*) and access the properties of thin film layers. The need for numerical simulation is necessary, as the heterojunction interface (such as *p*-SnS/*n*-buffer) is more complex in practice to access optimal alignment. SCAPS modelling tool is designed for simulation of the properties of semiconductor structures based on solving one-dimensional Poisson and the electron-hole continuity equations given as [179]:

$$\frac{d^2}{dx^2}\Psi(x) = \frac{e}{\varepsilon_o \varepsilon_r}\left[p(x) - n(x) + N_D - N_A + \rho_p - \rho_n\right] \quad (3.10)$$

$$\frac{d}{dx}J_n(x) - e\frac{\partial n(x)}{\partial t} - e\frac{\partial \rho_n}{\partial t} = G(x) - R(x) \quad (3.11)$$

$$\frac{d}{dx}J_p(x) + e\frac{\partial p(x)}{\partial t} + e\frac{\partial \rho_n}{\partial t} = G(x) - R(x) \quad (3.12)$$

where Ψ is electrostatic potential, e is an electron charge, $\varepsilon_o\, \varepsilon_r$ the vacuum and relative dielectric permittivity, *p* and *n* the hole and electron concentrations, N_D and N_A the charged impurities of donor and acceptor types, ρ_p and ρ_n the holes and electrons distributions, J_n and

J_p the electron and hole current densities, $G(x)$ and $R(x)$ the charge generation and recombination rates, respectively. From the output provided by SCAPS simulation, thickness and buffer layer dependent properties of *J-V* characteristics and band alignment were estimated. The schematic structure of the solar cell adopted in SCAPS is shown in chapter 2, while the input layers parameters are presented in table 3.1.

Table 3.1 Key input modelling parameters used in SnS simulations [24, 57-59, 104, 206-211].

Parameters set in the simulation	SnS	ZnS	In_2S_3	CdS	ZnO
Thickness (nm)	800±20	60±10	60±10	50±10	50±10
Ionisation potential, I_p (eV)	5.37	7.25	7.20	6.90	7.65
Work function, φ_s (eV)	4.78	4.60	4.65	4.90	4.65
Electron affinity, χ (eV)	4.00	3.90	4.25	4.50	4.35
Energy bandgap, E_g (eV)	1.37	3.35	2.95	2.40	3.30
Relative dielectric permittivity ε_r	13	8.30	13.5	10	9
CB effective density (cm^{-3})	1.18×10^{18}	6.34×10^{18}	1.8×10^{19}	2.2×10^{18}	2.2×10^{18}
VB effective density (cm^{-3})	4.76×10^{18}	1.46×10^{19}	4.0×10^{13}	1.7×10^{19}	1.8×10^{19}
Electron mobility μ_n (cm^2Vs^{-1})	15	250	40	340	100
Hole mobility μ_p (cm^2Vs^{-1})	100	20	20	50	25
Acceptor density N_A (cm^{-3})	10^{15}	-	-	-	-
Donor density N_D (cm^{-3})	-	5.7×10^{17}	10^{18}	10^{17}	10^{18}

3.6.10 Experimental device characteristics

The *J-V* measurements were performed to probe the performance of the solar cells. To measure the *J-V* of the solar cells, the solar spectrum was recreated via Sun 2000 solar simulator model with AM1.5 spectrum (explained in chapter 1), adjusted to 1000 Wm^{-2} using the set-up shown in figure 3.16. The measurement was then performed in the dark and under

illumination at room temperature using a Keithley 2400 series source meter. The current was recorded with the help of a labtracer software as the voltage was swept from -0.2 - 0.5 V.

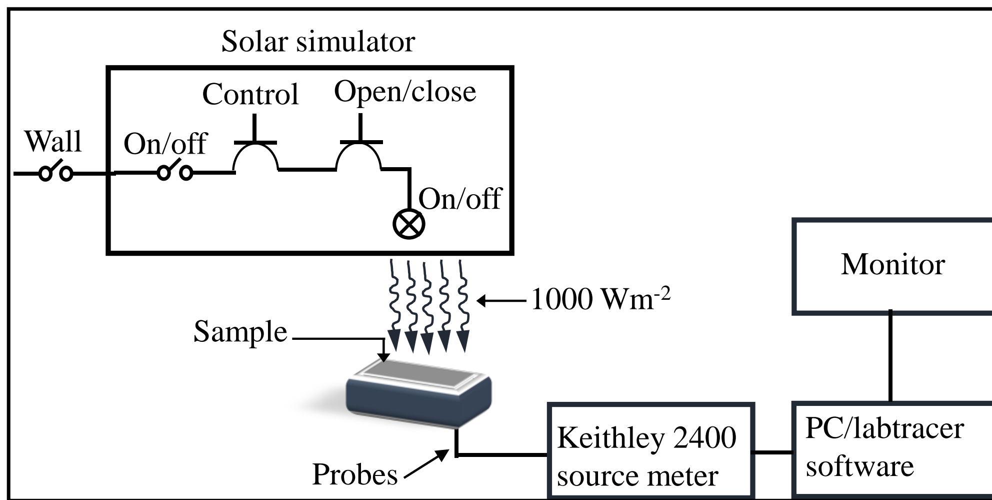

Figure 3.16 Schematic diagram of current - voltage measurement set-up.

Chapter 4

Growth and Characterisation of SnS Solar Absorbers

This chapter focuses on the growth and optimisation of SnS thin film photovoltaic absorbers deposited by thermal evaporation for application in p-n junctions thin film solar cells. A brief introduction presented in section 4.1 and sample description in section 4.2, are followed by a systematic study of the influence of film thickness, substrate temperature and type of substrate material on the properties of the SnS thin films presented in section 4.3. Finally, the conclusion to the chapter in 4.4.

4.1 Introduction

The study of SnS thin films microstructure, optical and crystallographic properties with the deposition variables such as thickness, temperature and substrate material are crucial for getting films that are suitable for photovoltaic device applications. The main challenges with the growth of SnS absorber layers are the formation of secondary phases such as SnS_2 and Sn_2S_3 due to dual valence of Sn (Sn^{2+} and Sn^{4+}), small grain sizes and non-adherence of the layers on the substrate surface.

The literature on the growth of SnS thin films by thermal evaporation technique shows that there is a strong interdependence between the deposition parameters and SnS thin film properties [39, 85, 95, 98, 212]. For instance, SnS film layer thickness range of 2.4-3.4 μm thermally evaporated at 300 °C substrate temperature was reported to exhibit a direct bandgap of 1.30-1.32 eV [95], while 65 and 800 nm thick films deposited at 200 and 350 °C substrate temperatures by same technique has a bandgap of 2.28 and 1.65 eV, respectively [39, 85].

In this study, the influence of film thickness, substrate temperate and substrate material type on the properties of SnS solar absorbing thin film were decoupled and systematically

investigated. Single phase SnS is vital as secondary phases have negative impact on the device performance, for example, SnS_2 acts as recombination centre for holes and electrons and Sn_2S_3 can promote hole trapping [61, 66]. Also stoichiometric p-type SnS phase is critical to enhance performance as studies have shown that a deviation from ideal stoichiometry of only 15% is enough to change SnS conduction from *p*- to *n*-type [66] and this has been one of the major reason for poor device performance to date. Substrate adherence is also crucial as film delamination can lead to device failure. Sodium (Na), a major constituent of SLG is known to diffuse during thermal processes (temperatures > 300 °C) and contaminates the film or enhance grain growth in other solar absorbers such as CdTe [213-215] and CZTS [216]. Quartz was used due to its purity compared to SLG to investigate if Na has any effect on SnS grain growth.

4.2 SnS sample properties

To obtain SnS thin films, 99.999% purity SnS pellets (T7-5014-M) with stoichiometric composition of tin and sulphur (Sn/S = 1.00) were deposited onto pre-cleaned soda lime glass (SLG, 76 × 26 × 1 mm^3) and quartz at high vacuum (<8.0 × 10^{-7} mbar) by thermal evaporation. The substrate holder was rotating at a constant speed of 10 rpm to ensure a homogenous layer of SnS films. In order to optimise the SnS layer properties, the following deposition parameters were used; substrate temperature T_s (from room temperature to 400 °C), film thickness t (from 100 to 3500 nm) and substrate material type (SLG, quartz, ITO and FTO coated glasses, Mo coated SLG and quartz).

4.3 Results and discussions

The thickness of the layers was measured using a stylus profilometer to confirm the values obtained from the crystal monitor. The morphology, composition, structure and optical properties were studied using SEM, EDS, SIMS, XRD, Raman and UV-VIS-NIR spectroscopy as explained in chapter 3 section 3.6.

4.3.1 Optimisation of SnS solar absorber thickness

The thickness of the solar absorbing layer is a vital parameter of photovoltaic device due to its ability to influence charge carrier absorbance and generation, as well as the power conversion efficiency of the solar cell. SnS simulations can provide improved insight of the thickness dependent operation of thin film solar cells and can remove any constraints in the sourcing of physical material. SnS layer thickness was varied from 100 nm to 3000 nm using solar cell design based on SnS/ZnS/ZnO/ITO structure, which provided the background for the experiments. The key input parameters were presented in chapter 3. Note that ZnS was used over CdS due to its higher energy bandgap.

4.3.1.1 Numerical simulation: Influence of thickness on device

The simulated current density-voltage (*J-V*) curves of SnS/ZnS/ZnO/ITO solar cells are shown in figure 4.1. The PV process was initiated in the simulation by illuminating the cell with 1 Sun (AM1.5), thereafter the SnS solar absorber thickness was varied to find out optimal thickness for SnS solar cell, while keeping that of ZnS, ZnO and ITO constant. Figure 4.2 shows the influence of SnS solar absorber thickness on the main parameters of the PV device.

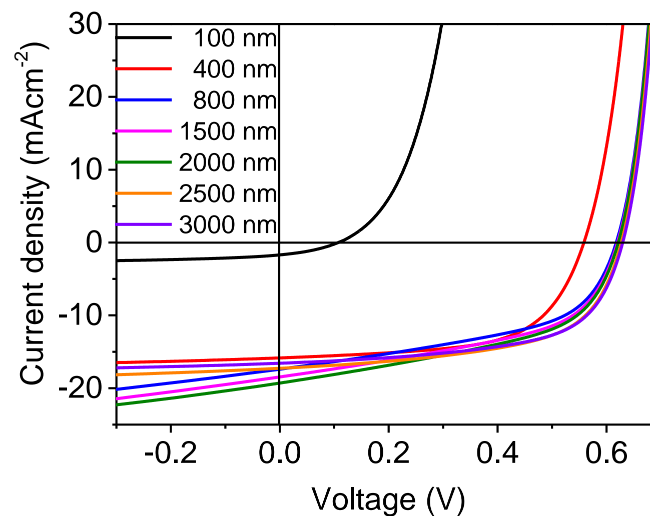

Figure 4.1. Illuminated *J-V* curves of simulated SnS/ZnS/ZnO/ITO device.

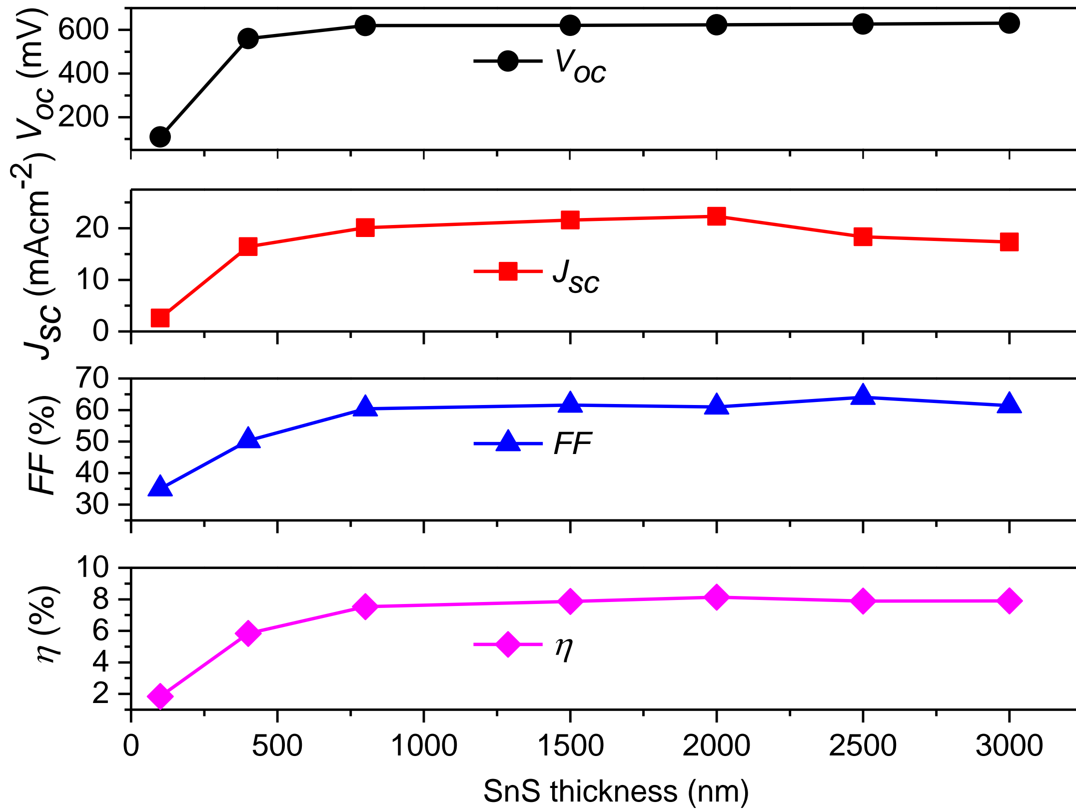

Figure 4.2. Influence of SnS absorber thickness.

Notice that the SCAPS data showed the saturation point for device efficiency to be 2000 nm with minimum threshold of 800 nm, same as short circuit current (J_{sc}). At the thickness of 800 and 3000 nm, the estimated efficiency is 7.53% and 7.81%, respectively. Similar behaviour was observed in the fill factor, short circuit current and open circuit voltage output of the device, where the variations with SnS layer thickness become negligible over a thickness of 800 nm except for J_{sc}, which appears to decrease at 2500 – 3000 nm. The proposed structure shows that lowering the absorber layer thickness to ~800 nm can give similar device performance with 3000 nm, which means reduction in material usage and cost. This is a vital step in the fabrication of solar cells therefore, the next sub-section will look at the physical properties of the SnS layers in the thickness range of 100 nm to ≥ 3000 nm.

4.3.1.2 Thickness dependent properties

The composition of the as-deposited films at a constant substrate temperature of 100 °C varied with the increase in film thickness (*t*) as shown in table 4.1. The Sn/S ratio varied between

0.84 - 1.86, whereas the starting material (pure SnS pellets) had a stoichiometric composition of tin and sulphur (Sn/S = 1.00 ± 0.01). The atomic composition reveals a marginal difference for film thickness ≤ 800 nm, thereafter it varied with considerable difference. This is due to differences in the vapour pressures of Sn and S as noticed in other reports [15, 217]. A typical EDX spectrum for the 800 nm thick film is shown in figure 4.3 (a) while figure 4.3 (b) indicates the points of measurements.

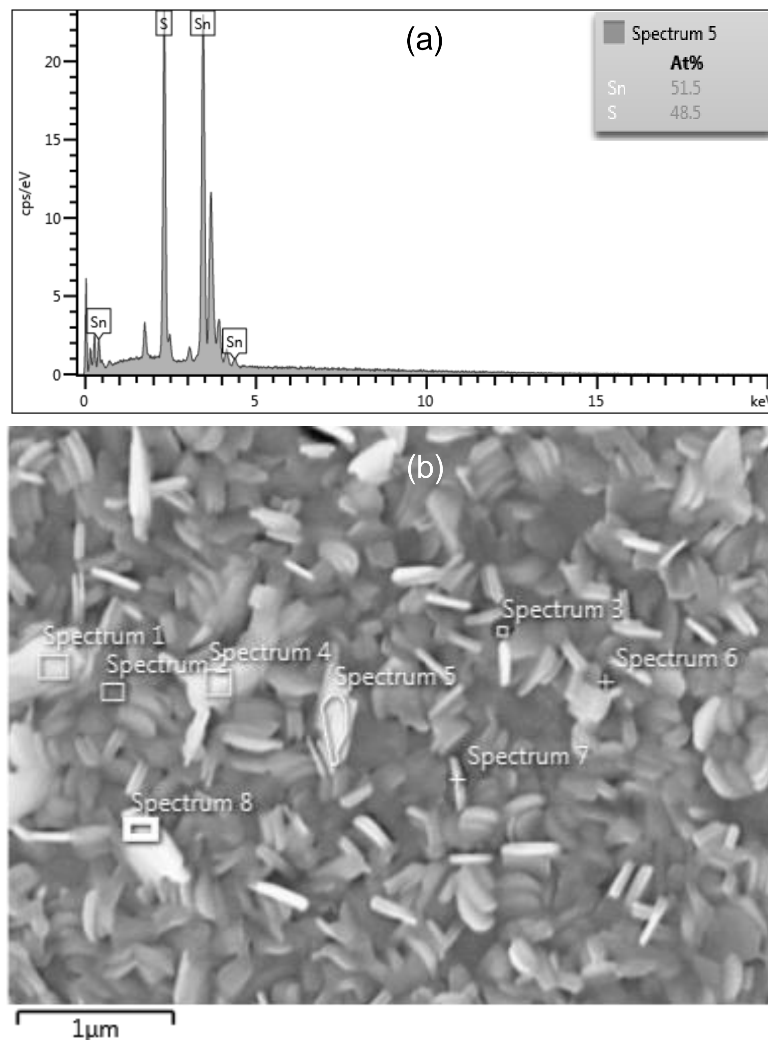

Figure 4.3 (a) EDX spectrum and (a) SEM point of EDX measurement.

The atomic compositions taken from multipoint, that is spectrum 1 to spectrum 8 (see figure 4.3b) were similar, the average value was estimated and included in table 4.1, which gave error value of ± 0.01.

This reveals that a thickness of 800 nm can be optimised for photovoltaic application due to its near stoichiometry of 0.94. The *p*-type conductivity in 100, 400 and 800 nm are mainly due to tin vacancy (V_{Sn}) otherwise called cation defect which acts as a shallow acceptor. Also 1500 and 2100 nm thick films are *p*-type because in Sn-rich limit, the sulphur vacancy (V_S) which has lower formation energy (see chapter 2 figure 2.2b) than V_{Sn}, does not significantly compensate the *p*-type conductivity [52]. This is because the ultra-deep level (2+) of V_S lies very close to the valence band maximum and therefore, with <15% sulphur loss, does not compensate the holes produced by V_{Sn}. However, for the 3500 nm thick layer the sulphur vacancy (V_S), which is significant (>30% sulphur loss) led to anion defect, which resulted in the conductivity type change from *p* to *n*-type.

Table 4.1. SnS thin film composition across the film thickness (*t*) range along with the energy bandgap (E_g) and Urbach energy (*Eu*) determined from optical measurements and conductivity type. The starting SnS evaporant material was measured at Sn/S = 1.00 using EDS.

$t \pm 20$ (nm)	Sn (at %)	S (at %)	Sn/S $\pm$ 0.01	E_g (eV) $\pm$ 0.05	E_u (eV) $\pm$ 0.005	Type
100	47.4	52.6	0.90	2.03	0.164	p
400	48.1	51.9	0.93	1.68	0.167	p
800	48.5	51.5	0.94	1.48	0.168	p
1500	54.4	45.6	1.19	1.46	0.183	p
2100	57.7	42.3	1.36	1.44	0.213	p
3500	65.0	35.0	1.86	1.26	0.219	n

The surface morphology of the SnS film of thickness range 100 nm to 3500 nm deposited at 100 °C on SLG was studied using SEM. The surface morphology (top view) of the films show randomly oriented needle and rice-like grains (see figure 4.4). The micrographs reveal a gradual change of the grains from island nature to a closely packed structure with the increase

of film thickness. The micrographs depicts a progressive increase in the grain size with increasing film thickness from 100 to 1500 nm, above the 1500 nm thickness no further visible increase in the grains can be seen. This indicates that further increasing the thickness at constant substrate temperature has no effect on grain growth, as the thermal energy at the substrate for the mobility of adatoms will be constant.

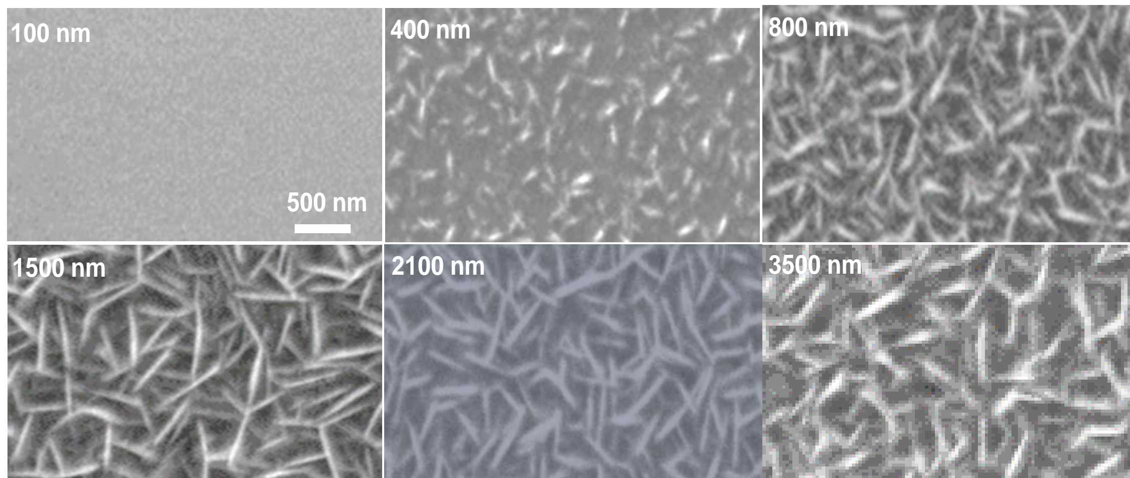

Figure 4.4 SEM micrographs of as-deposited SnS films (top view) at thickness range of 100-3500 nm and constant substrate temperature of 100 °C.

The wavelength dependence of optical transmittance was studied in the wavelength range 300-1400 nm for the as-deposited films. Figure 4.5 (a) shows the plots of the transmittance, $T(\lambda)$, and reflectance, $R(\lambda)$, spectra. A shift in absorption edge towards longer wavelength and decrease in transmittance as the film thickness increases are observed indicating increase in photon absorption with the deposition conditions. The absorption coefficient (α) was determined from T and R data, and the film thickness (t) (see chapter 3) and Tauc plots were used to determine the energy bandgap of the films. Both direct and indirect (E_g) have been reported for SnS thin films depending on preparation and growth conditions [125]. In this study, the plot of $(\alpha h\nu)^n$ vs $(h\nu)$ gave better fit for n = 1/2, indicating the films to have a direct allowed transitions with optical energy bandgap range of 1.26 - 2.03 eV for the varying film thicknesses (see figure 4.5b). As shown in figure 4.6, a trend of decrease in the bandgap energy with the increase in Sn/S atomic ratio was observed due to loss in Sulphur. The wider energy bandgap

of 2.03 eV observed at the lowest thickness film of 100 nm is due to its amorphous structure as depicted in the XRD spectra of figure 4.9 (a) and possible quantum confinement effect [218-221]. These results are also comparable to report from the literature, which showed increased population of SnS_2 and Sn_2S_3 secondary phases [99, 202, 222].

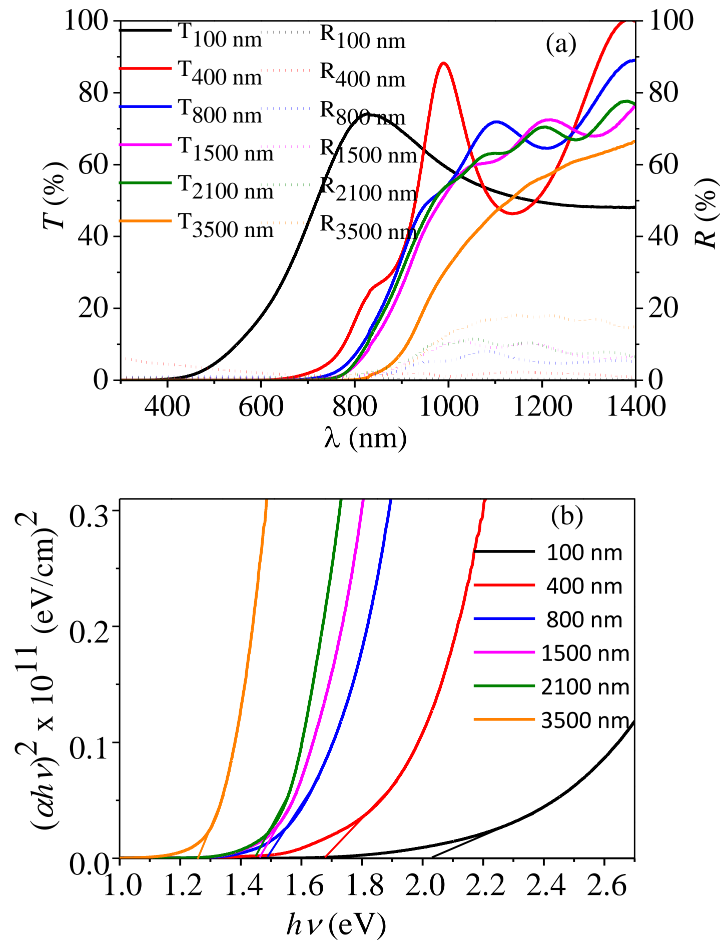

Figure 4.5 (a) Transmittance (solid lines) and reflectance (dotted lines) and (b) $(\alpha h\nu)^2$ versus $h\nu$ of the films as a function of layer thickness.

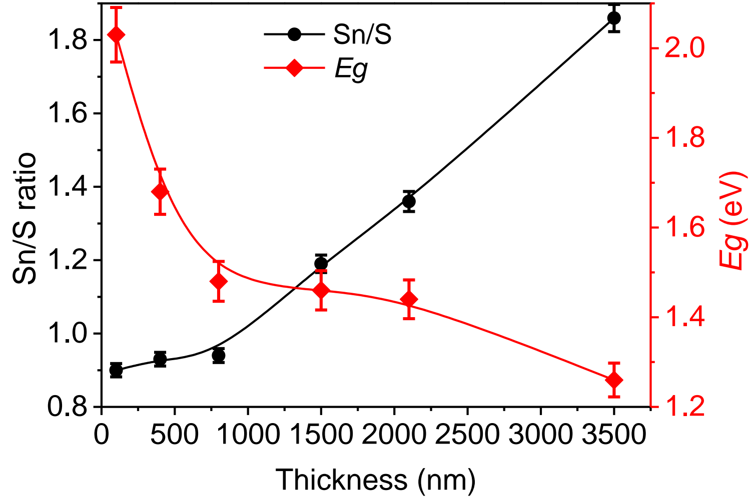

Figure 4.6 Sn/S atomic ratio and energy bandgap as a function of film thickness (the lines are guides for the eye).

Below the optical band edge, the relationship between (α) and photon energy ($h\nu$) is following the Urbach empirical rule [223, 224]. For single crystal, the fluctuations of atomic position during thermal vibration at high temperatures determines the nature of the band tail state. The Urbach rule is given as [223]:

$$\alpha = \alpha_o \exp\left(\frac{h\nu}{E_u}\right) \tag{4.1}$$

$$In\ \alpha = In\ \alpha_o + \left(\frac{h\nu}{E_u}\right) \tag{4.2}$$

where α_o denotes a pre-exponential term which is constant and E_u is Urbach energy which indicates the width of the exponential absorption edge. The logarithm of equation 4.1 results in equation 4.2. From the plot of *In* (α) against ($h\nu$) (see figure 4.7) near the absorption edge for the as-deposited SnS films at different film thickness, the Urbach energies were estimated as the inverse of the slope. Figure 4.8 shows the energy bandgap (*Eg*) and Urbach Energy (*Eu*) as a function of the film thickness. The E_u value is ranging from 0.164 to 0.219 eV across the thickness range as shown in table 4.1, indicating a slow increase up to 800 nm then large increase with thickness. This suggest the presence of intrinsic disorders in the films that increases with the film thickness indicating the increase in the width of the localised states

within the bandgap [225]. Notice that sulphur vacancy defects and crystalline structure disorder are present in the films with thickness above 800 nm. The crystalline disorders were evidenced in the XRD data where the film orientation changed from (111) to (020) with increased thickness (see figure 4.9a)

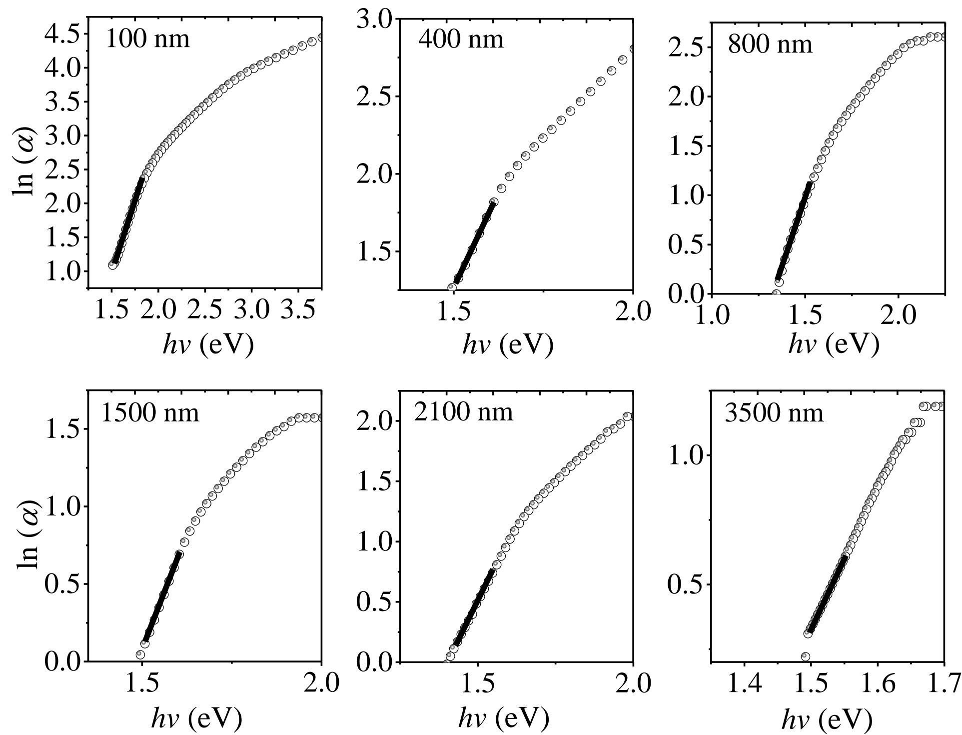

Figure 4.7 ln(α) versus $h\nu$ of the as-deposited SnS films as a function of thickness.

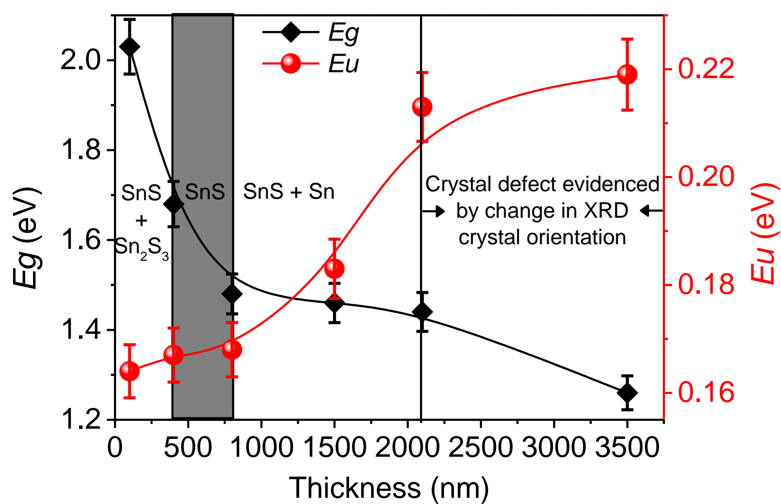

Figure 4.8 Energy bandgap (*Eg*) and Urbach Energy (*Eu*) as a function of film thickness (the lines are guides for the eye).

Figure 4.9 (a) shows the X-ray diffraction (XRD) spectra of the as-deposited SnS thin films. All reflections are indexed using references from the database on the joint committee on powder and diffraction standard powder diffraction file (JCPDS PDF), matching the orthorhombic SnS (PDF 039-0354), SnS_2 (PDF 023-0677) and Sn_2S_3 (PDF 014-0619).

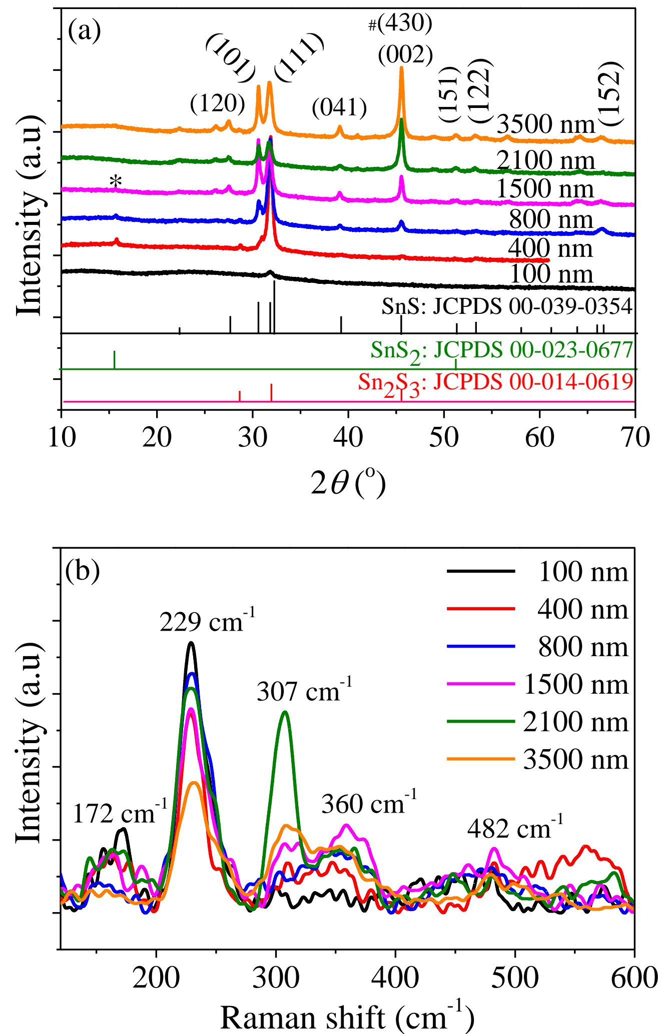

Figure 4.9 (a) XRD (* and # stands for SnS_2 and Sn_2S_3, respectively) and (b) Raman spectra of SnS films deposited at a constant temperature of 100 ºC as a function of layer thickness.

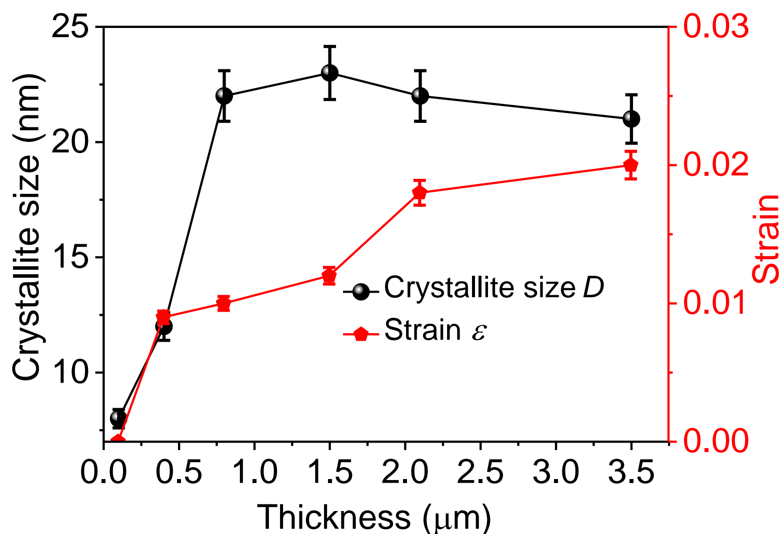

Figure 4.10 Crystallite size and strain as a function SnS film thickness (bars indicate ±10% error in determination of crystallite size and strain, while lines are guide for the eye).

The crystallographic analysis reveals the presence of secondary phases (SnS_2 and Sn_2S_3) across the thickness range with the (111) prominent peak changing to (002) as the film grow thicker (≥ 2100 nm). The crystallite size and strain (see figure 4.10) are found to increase with film thickness. The crystallite size revealed a saturation point of 1500 nm, above which it began to decrease due to re-evaporation of sulphur. The strain increased with film thickness because of compositional disorder earlier shown in figure 4.6. Raman analysis were also conducted to complement the XRD data and further investigate the phase impurity. In the instances where there is overlapping of SnS, SnS_2 and Sn_2S_3 phases in XRD spectra, Raman spectroscopy which is more sensitive to structural and compositional change of the material is accurately used to distinguish these phases [99]. Raman modes were observed at 172, 229, 307, 315, 360 and 482 cm^{-1} as shown in figure 4.9 (b). The observed peaks at 172 cm^{-1} and 229 cm^{-1} can be attributed to SnS [202, 226], while the peaks at 307 cm^{-1} and 315 cm^{-1} denotes the presences of Sn_2S_3 and SnS_2 respectively [203]. The existence of these secondary phases in the films are in agreement with XRD results. The small peak at 172 cm^{-1} can be attributed to B_{2g} mode, while the most intense peak for the samples at 229 cm^{-1} for all the thickness corresponds to A_g mode of SnS [153]. The A_g modes relates to the symmetric Sn – S bonding stretching mode in the a-c plane, while the B_{2g} mode represent the interaction along the inter-

layer ‘b’ axis [227]. Figure 4.11 shows the variation in the A_g and B_{2g} Raman mode positions as a function of film thickness. The A_g and B_{2g} modes revealed a systematic shift to a higher wavenumber with increasing layer thickness. This showed that thinner films have vibrations taking place at lower wavenumber than thicker films.

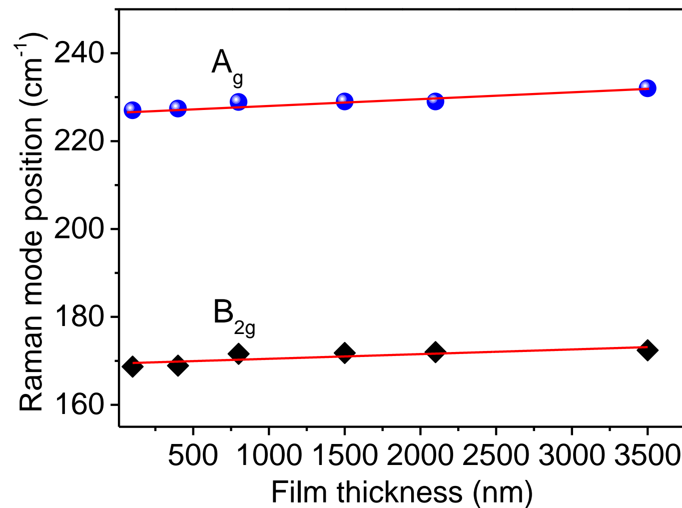

Figure 4.11 Variation in A_g and B_{2g} Raman mode positions as a function of film thickness.

The thickness dependent results discussed in this subsection show that the properties of SnS solar absorber can be tuned by altering the layer thickness. Films grown to a thickness of ~800 nm is found to be near stoichiometry with optimum energy bandgap compared to the films with lower or higher thickness. Therefore, with ~800 nm thickness, SnS solar absorber gave good performance in SnS-based thin film solar cells. Other parameters such as substrate temperate and type can also influence the properties of SnS solar absorber and results are presented in the next section.

4.3.2 Substrate temperature dependent properties

The films were deposited at substrate temperature range from room temperature to 400 °C on SLG with constant thickness of 800 ± 20 nm. The samples described here were deposited after the last phase of optimising thickness (detailed in section 4.3.1) where 800 nm thickness were found to provide adequate properties. The source preparation and deposition processes

(detailed in section 3.2) as well as the source material composition (stated in section 3.3.1) were the same unless otherwise stated.

Physical observation of the film showed that most of the films were pinhole free and its adherence to substrate increased with temperature: films grown > 300 ^{o}C adhered strongly to substrate surface unlike the samples deposited at lower temperature. The layers were darkish-grey at 200-300 ^{o}C and changed to grey at $\geq$ 350 ^{o}C. The surface morphology of the as-deposited films were studied using SEM. Figure 4.12 shows the surface micrographs of the films, which have randomly oriented rice and flake-like grains. The increase in temperature led to the growth of bigger grains. The recorded small grain sizes at lower substrate temperatures ($\leq$ 250 ^{o}C) is because the kinetic energy of the adatoms are low compared to higher temperatures and the coalescence of the nucleating atoms are restricted. This gave rise to high bandgap due to quantum confinement effect [200, 228]. Further increase in substrate temperature beyond 350 ^{o}C yield no visual change on the surface morphology. The small grain sizes observed at room temperature to 100 ^{o}C correlates with the broadening of Raman peaks (see figure 4.30a). Average grain sizes were quantified and the values increased from 20 $\pm$ 1.0 nm to 150 $\pm$ 7.5 nm with increase in substrate temperature from room to 400 ^{o}C (see figure 4.13). The growth of bigger grains are likely due to increase in adatoms mobility with temperature, promoting coalescences of smaller grains to form bigger grains. Other authors have reported similar behaviour of SnS grains prepared by thermal evaporation [164, 229].

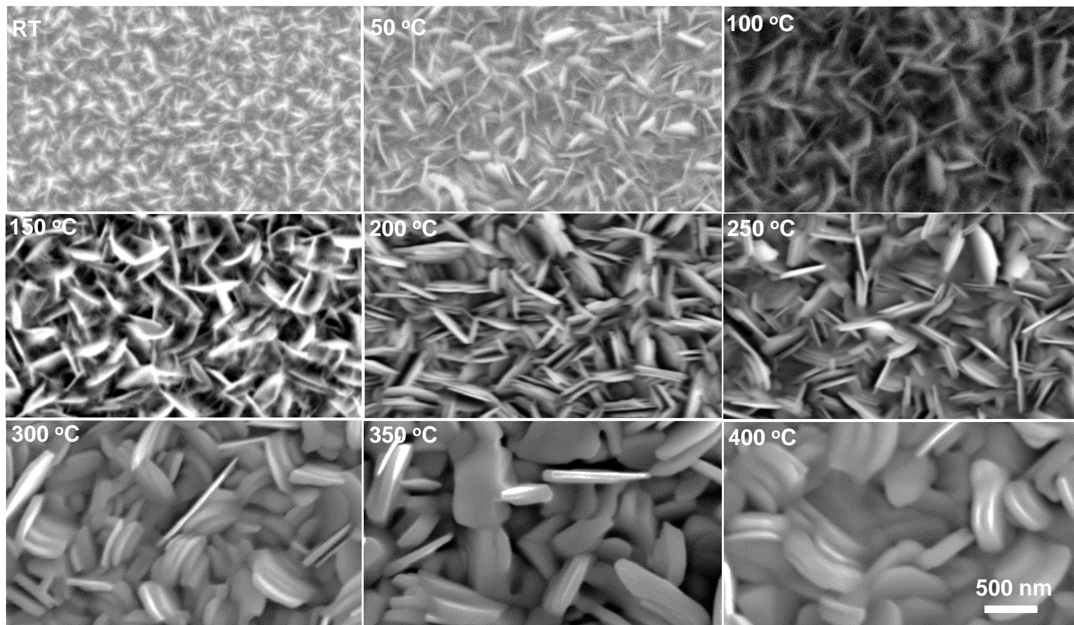

Figure 4.12 SEM micrographs of SnS films (top view) as a function of substrate temperature (scale bar is same for all images).

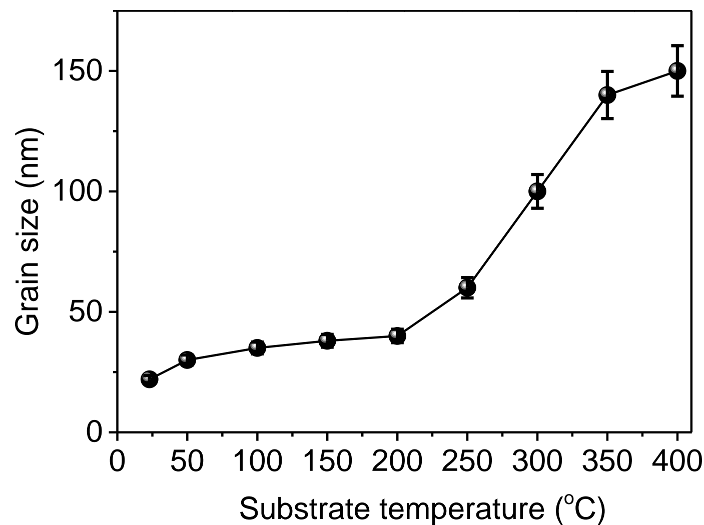

Figure 4.13 Average grain size (±5.0% error) as a function of substrate temperature.

The elemental composition of the deposited samples were determined by energy dispersive X-ray spectroscopy (EDS). This analysis was done to understand the stoichiometry of the constituent elements and it plays a vital role in determining the quality of thin films irrespective of the deposition method. EDX data was measured at multi points and a typical spectrum for the film deposited at 350 °C is shown in figure 4.14. The data taken from other points on the

sample are the same with stoichiometric Sn and S atomic composition. Table 4.2 shows the variation of Sn/S atomic ratio across the substrate temperature range. The films showed a gradual increase of the Sn/S ratio with substrate temperature, whereas the starting material (pure SnS pellets) had a stoichiometric composition of tin and sulphur (Sn/S = 1.00). The Sn/S range of 0.89 - 1.10 show a trend of decreasing S content (see figure 4.15) in the films as substrate temperature increases in agreement with reports in the literature [15, 230].

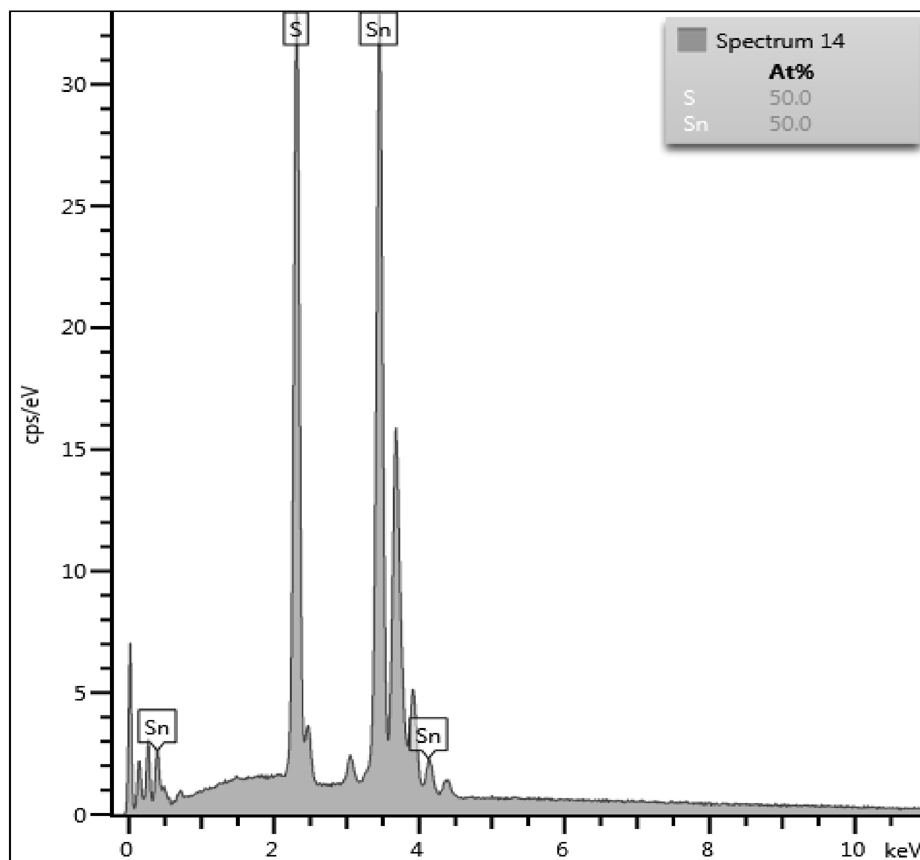

Figure 4.14 EDX spectrum of SnS films deposited at 350 ºC.

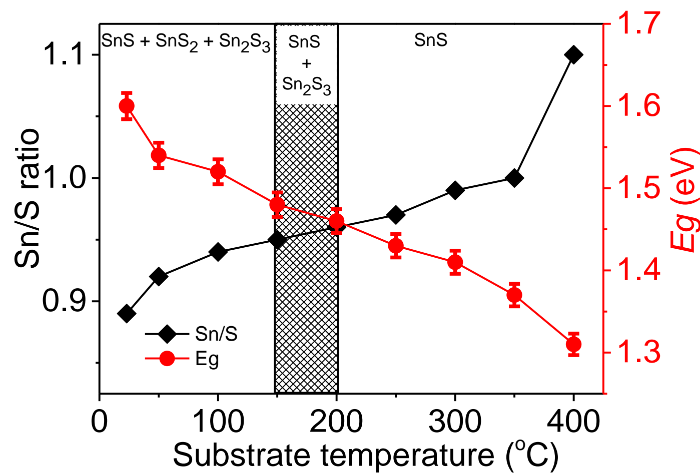

Figure 4.15 Sn/S ratio and energy bandgap of SnS films as a function of substrate temperature. Phases confirmed with XRD and Raman data (see figures 4.23 and 4.30).

Notice that the changing atomic ratio of Sn and S can also give insight into the phases present with respect to substrate temperature. Secondary phases of SnS_2 and Sn_2S_3 can be seen due to higher sulphur content at lower substrate temperature in good agreement with the XRD and Raman data therefore, fabrication of SnS solar absorbing layer should be made at temperatures well above 200 °C. The change in composition with growth conditions are due to re-evaporation at the surface of the growing films where the vapour pressure of S increases with temperature faster than that of Sn. For instance, the vapour pressure of sulphur P_S and tin P_{Sn} is 1.0×10^{-2} mbar at 102 °C and 1224 °C, respectively, giving a very large 1122 °C temperature difference [231].This behaviour can also be interpreted with reference to the kinetic energy of the evaporated atoms of tin and sulphur on the substrate. The kinetic energy of the sulphur atoms is higher compared to the heavy Sn atoms due to the high vapour pressure of S, as a result the S atoms will get to the substrate surface first [164, 229]. At low substrate temperature, the re-evaporation of S atoms will be negligible thereby resulting in sulphur rich films and as the temperature increases the sulphur will gradually become deficient.

Table 4.2. SnS thin film composition at different substrate temperatures range of room temperature (RT) to 400 °C along with key optical properties. The starting SnS evaporant material was measured at Sn/S = 1.00 using EDS. The energy bandgap E_g and Urbach energy E_u were determined from optical measurements, while absorption coefficient (α) was extracted at λ = 550 nm.

Sub. temp ±10 (°C)	Sn (at %)	S (at %)	Sn/S ± 0.01	α (×10^5 cm^{-1})	E_g (eV) ± 0.05	E_u (eV) ± 0.005
RT	47.2	52.8	0.89	0.05	1.60	0.156
50	48.0	52.0	0.92	0.08	1.54	0.163
100	48.5	51.5	0.94	0.27	1.52	0.168
150	48.8	51.2	0.95	0.34	1.48	0.171
200	48.9	51.1	0.96	0.34	1.46	0.167
250	49.2	50.8	0.97	0.85	1.43	0.169
300	49.3	50.7	0.97	0.87	1.41	0.171
325	49.5	50.5	0.98	0.92	1.40	0.172
350	50.0	50.0	1.00	1.11	1.37	0.170
400	52.4	47.6	1.10	1.20	1.31	0.186

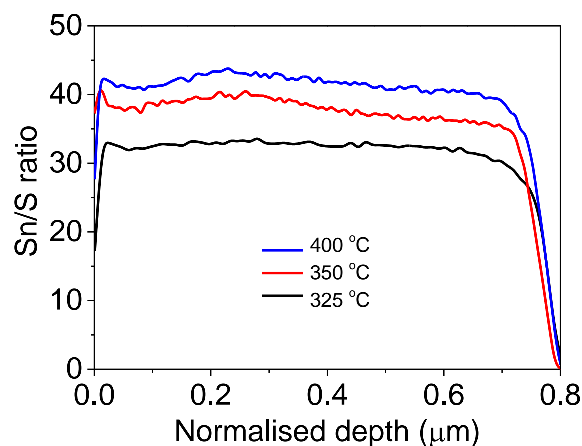

Figure 4.16 Sn/S ratio with film depth as determined from SIMS for substrate temperature of 325, 350 and 400 °C.

The composition uniformity with respect to the film thickness was probed by SIMS and is shown in figure 4.16 where the intensity ratio of Sn and S ions are plotted for three films. All films showed uniform profiles with depth of both Sn and S but the ratios showed the films becoming increasing Sn rich as substrate temperature increases in good agreement with the EDS data shown in table 4.2.

The transmittance, *T*, and reflectance, *R,* spectra of the as-deposited SnS thin films studied over the wavelength range of 300-1400 nm are plotted in figure 4.17 (a and b). The transmittance spectra demonstrated interference fringes which is an indication of good surface homogeneity and uniformity of the layers [232]. A sharp fall of the transmittance was observed for all films at the wavelength regarded as the fundamental absorption edge. The absorption edge shifts towards longer wavelength (red shift) with increase in substrate temperature, and this is associated with the change in composition described earlier. The optical absorption coefficient that indicates how strongly a material absorbs light was determined across the temperatures. The films show high absorption coefficient of 3.4×10^4 to 1.2×10^5 cm^{-1} (at λ = 550 nm) with increasing temperature. The energy bandgap of the film was determined by plotting the values of $(\alpha h\nu)^2$ vs $(h\nu)$ and extrapolating the linear region to the $h\nu$ axis as shown in 4.17 (c and d). The direct bandgap energy range of 1.31-1.60 eV recorded were found to decrease with increase in the substrate temperature. The high bandgap energy (1.48-1.60 eV) recorded at lower substrate temperatures range of room to 150 °C are due to presence of secondary phase, Sn_2S_3 that has a wide bandgap of ~1.64 eV [233] as confirmed with XRD and Raman data. The near stoichiometric SnS film (Sn/S = 1.00) grown at 350 °C substrate temperature has a direct bandgap of 1.37 eV. This bandgap is near optimum for photovoltaic cell applications and it is close to the reported bandgap of stoichiometric polycrystalline SnS, 1.35 eV [15]. The noticeable change in the bandgap with the substrate temperature is linked to the changing composition of the films (see table 4.2).

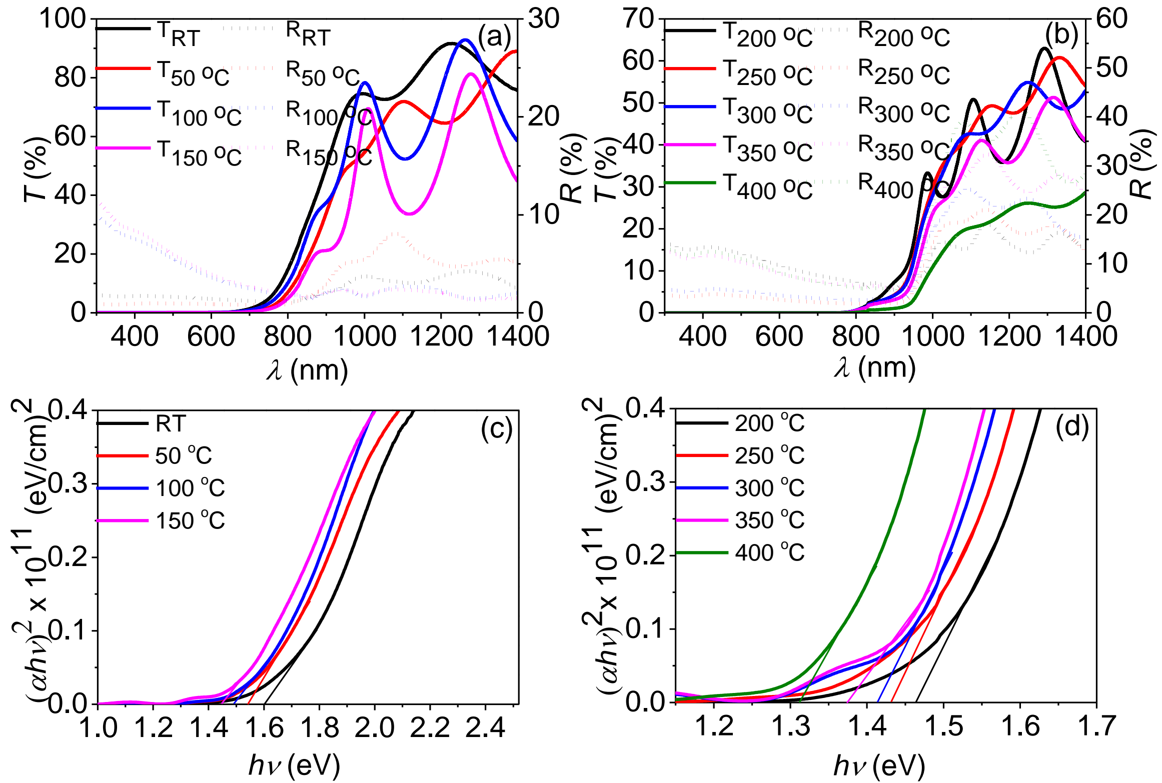

Figure 4.17 (a and b) Transmittance (solid lines) and reflectance (dotted lines) and (c and d) Tauc plot of the SnS thin films deposited on SLG as a function of substrate temperature.

To estimate the Urbach energy across the substrate temperature, ln(α) against ($h\nu$) was plotted across the temperature (see figure 4.18) and the inverse of their slope near the absorption edge were estimated as the Urbach energies. The E_u value is ranging from 0.156 to 0.186 eV as a function of substrate temperature (see figure 4.19 and table 4.2), similar behaviour exist with increasing film thickness discussed earlier, indicating that increase in both thickness and temperature lead to increase in the disordered atoms. For temperature of 250-350 °C, E_u is invariant (within the experimental error) while a large increase is observed for the highest temperature. This correlates well with the increase in Sn/S ratio (10% at 400 °C) resulting in an increase in the disordered atoms and defects in the structural bonding that can cause the absorption edge to spread at the lower region [224] and is the main reason for the observed variations.

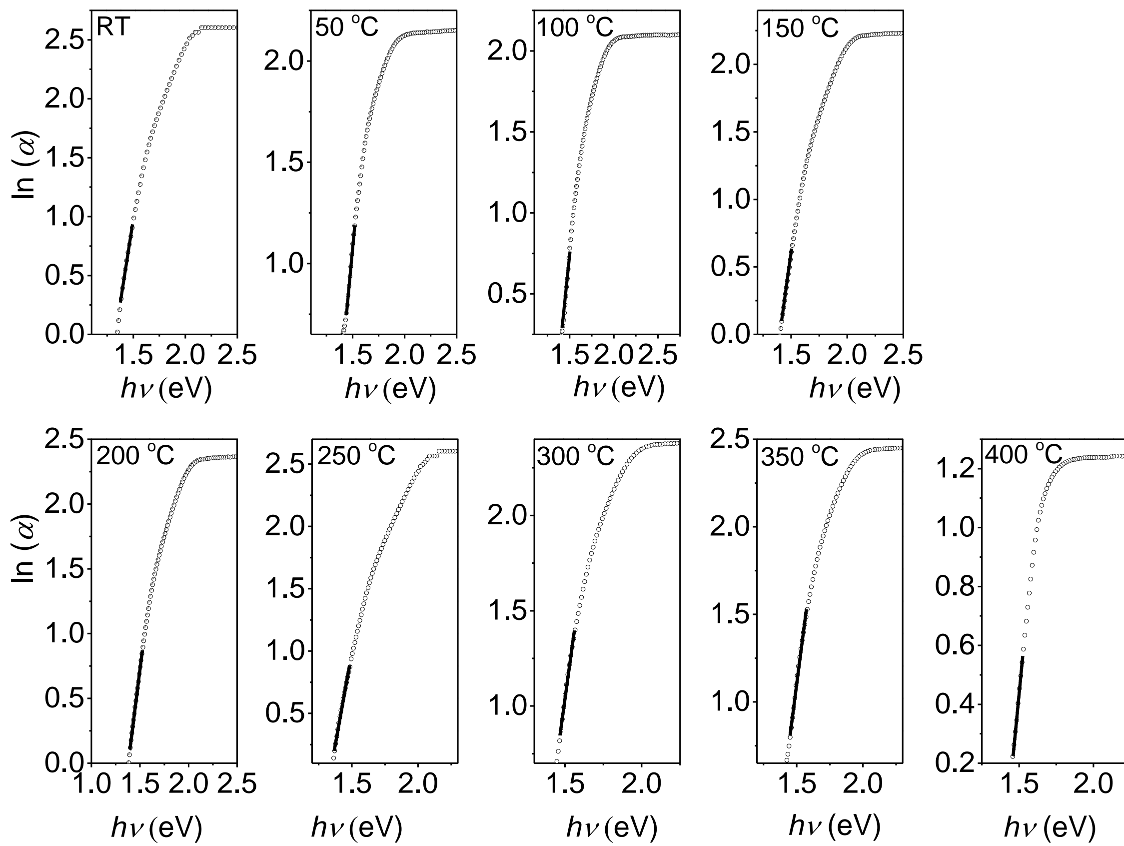

Figure 4.18 ln(α) versus $h\nu$ of the SnS films as a function of substrate temperature.

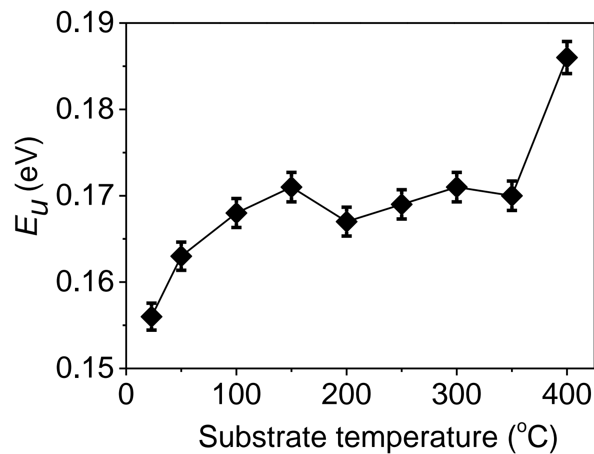

Figure 4.19 Urbach energy (E_u) as a function of substrate temperature (the line is a guide for the eye).

The refractive indexes were investigated for the films that exhibited only SnS phase, which is observed at substrate temperature of 200 to 400 °C. The calculations were performed as a

complex function of the photon energy with real part *n*, and imaginary part taken as the extinction coefficient, *k*. Both *k* and *n* were estimated from the following relations [223, 234]:

$$k = \frac{\alpha\lambda}{4\pi} \tag{4.3}$$

$$n = \frac{1+R}{1-R} + \sqrt{\left[\frac{4R}{(1-R)^2} - K^2\right]} \tag{4.4}$$

where *n* is the refractive index, *k* is the extinction coefficient, while λ, and *R* retain their meaning in this work. Figure 4.20 (a and b) show the behaviour of the refractive index and extinction coefficients of the films with wavelength as a function of substrate temperature. The refractive index of the SnS films decrease rapidly with increase in wavelength up to 860 nm and then stay monotonous. The extinction coefficient has high values at the lower wavelength region with peaks at ~600 nm, which correlates with the high absorption region of the films. Shaaban *et al.* [235] reported similar behaviour for nanocrystalline SnS films prepared by thermal evaporation. The *n* and *k* value range from 1.22-1.41 and 0.35-0.51, respectively (at λ = 550 nm) with increasing temperature (see figure 4.20c). This is a good value for reducing reflectance at the interface of the films.

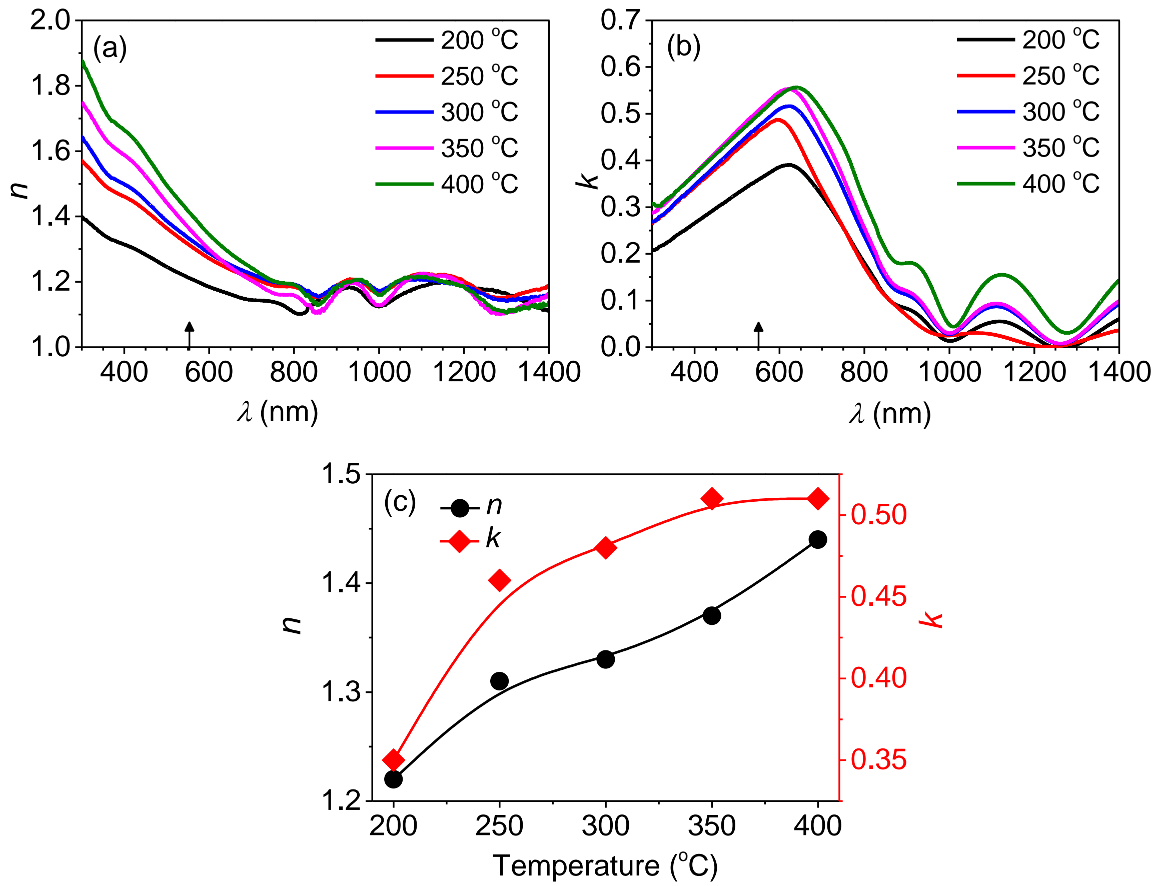

Figure 4.20 (a) refractive index (*n*), (b) extinction coefficient (*k*) with wavelength and (c) *n* and *k* values extracted at 550 nm wavelength.

Thin film materials are characteristed by a complex dielectric constant ($\varepsilon = \varepsilon_1 + i\varepsilon_2$) which is part of their fundamental intrinsic property. The real part of the dielectric constant (ε_1) governs how much it will slow down the speed of light in the material, whereas the imaginary part (ε_2) is responsible for the energy absorption from the electric field due to dipole motion [236]. ε_1 and ε_2 are related to *n* and *k* values and can be calculated using the following equations [157, 237].

$$\varepsilon_1 = n^2 - k^2 \tag{4.5}$$

$$\varepsilon_2 = 2nk \tag{4.6}$$

The ε_1 vary between 1.28 to 1.81 and ε_2 from 0.93 to 1.41 for a wavelength of 550 nm across the substrate temperature range (see figure 4.21). Reddy *et al* [48] reported similar behaviour

of ε_1 and ε_2 against photon energy for SnS films grown by spray pyrolysis. This increase in the real and imaginary parts of dielectric constants with the substrate temperature indicate the improvement in the optical response of the layers and reduction in the energy dissipative rate of the incident light. This shows that with increase in substrate temperature, the photon absoprtion of films are increased probably due to the growth of bigger grains.

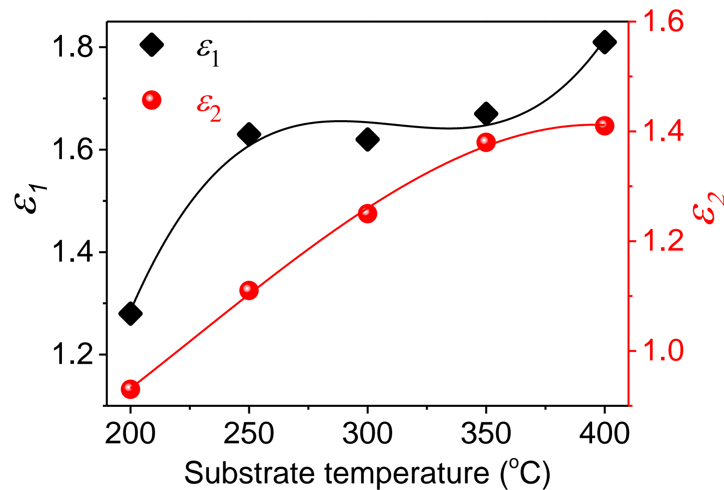

Figure 4.21 Real (ε_1) and imaginary (ε_2) part of dielectric constant (at λ = 550 nm) across the substrate temperature range (the lines are guides for the eye).

X-ray photoelectron spectroscopy (XPS) analysis was used to investigate the valence states and the binding energies of the mixed phase Sn-S system at lower substrate temperature (room to 150 °C). Notice that at this temperature range, films had all the three phases (SnS, SnS_2 and Sn_2S_3) present as earlier indicated (see figure 4.15). The wide scan and Sn3d narrow scan XPS spectra of the films at the lower substrate temperature are presented in figure 4.22.

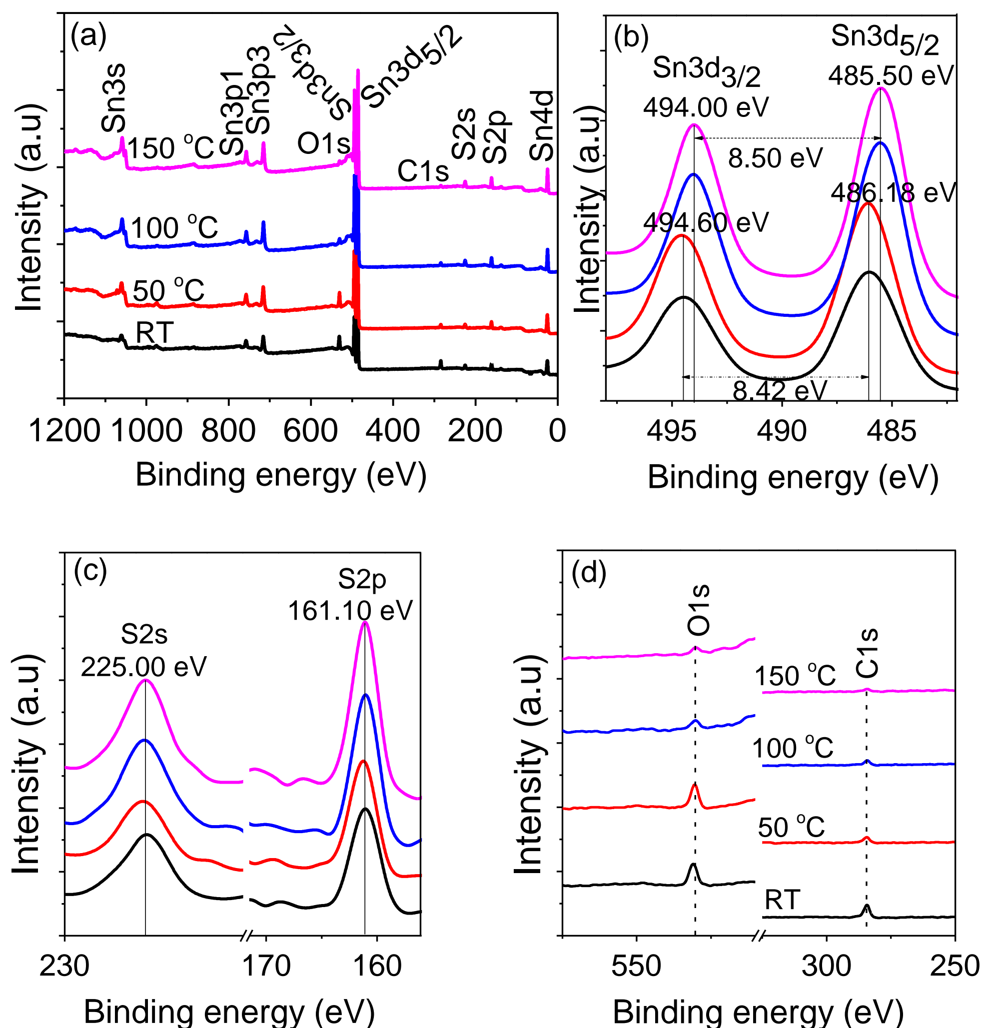

Figure 4.22 (a) XPS spectra of SnS films deposited on SLG at lower temperature (b) zoom of the Sn3d narrow scan and (c) S2s and S2p energy levels. The spectra are off-set for better visibility.

The Sn3d narrow spectra with two major peaks at $Sn3d_{5/2}$ and $Sn3d_{3/2}$ (see figure 4.22b) corresponds to binding energies of 486.18 eV and 494.60 eV for films grown at room and 50 °C temperature, respectively. Films grown at 100 °C and 150 °C reveal binding energies at 485.50 eV and 494.00 eV for the $Sn3d_{5/2}$ and $Sn3d_{3/2}$, respectively. These two spin orbital components of the films exhibit a split of 8.42eV to 8.50 eV with increasing temperature. A shift to lower binding energies of the $Sn3d_{5/2}$ peak from 486.18 eV to 485.50 eV is associated with increase in substrate temperature indicating a move to a lower oxidation state of Sn (see figure 4.22b) [238]. The binding energies of S2s and S2p remain constant across the

temperatures (see figure 4.22c), showing no change in the oxidation state of S, hence the possible change of Sn^{4+} to Sn^{2+} with increasing temperature. These changes in oxidation state of Sn accounts for the secondary phases associated with SnS as reported in literature [29, 61]. Presence of oxygen (O1s) and carbon (C1s) contamination were observed on the XPS survey of films as shown in narrow scan in figure 4.22(d). These contaminations were minimised due to increase in substrate temperature, which resulted in a shift to lower oxidation state of tin (Sn^{4+} to Sn^{+2}). The room temperature and 50 °C substrate temperature with binding energies 486.18 eV corresponds to Sn_2S_3, 100 °C and 150 °C with binding energies 485.50 corresponds to SnS [239], though these partly correlates with the XRD analysis discussed in the next paragraph but cannot be used to adequately distinguish the SnS phases.

XRD spectra of the SnS films as a function of temperature is shown in figure 4.23 (a). The diffractions peaks of all the samples matched well with orthorhombic structure of SnS (Herzenbergite) consistent with the powder diffraction file stated in the figures. The crystallography reveals the presence of secondary phases (SnS_2 and Sn_2S_3) at lower temperatures, consistent with the high sulphur atomic percentage. However, at high temperature range of 200 - 400 °C, the layers exhibited single phase only (also confirmed from the Raman analysis as detailed later) with the (111) and (040) planes giving rise to the most prominent peak. The XRD spectra show that the (111) plane is more likely associated with the substrate temperatures ≤ 300 °C while, the (040) diffraction plane is related to higher substrate temperatures (≥350 °C). The zoomed spectra (see figure 4.23b) shows a 0.04° shift in the 2θ values towards the lower Bragg's angle of the (111) plane as the temperature approaches ≥350 °C, which may be as a result of the increase in the crystallite size and decreased micro-strain. This is consistent with other reports [15, 45, 98, 165, 203, 240]. Other noticeable diffraction peaks include the (110), (120), (021), (101), (041), (141), (211), (122), (042), (080) and (232) Bragg reflections consistent with the reference powder diffraction pattern.

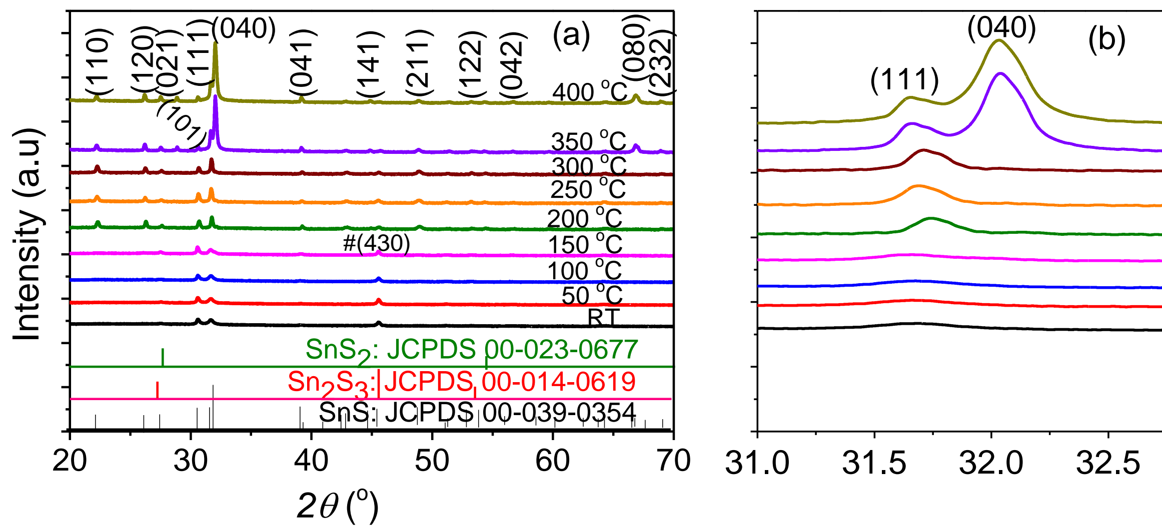

Figure 4.23 (a) XRD spectra as a function of substrate temperature and (b) zoom of (111) and (040) peaks.

The unit cell parameters are determined using Eva software integrated in the XRD machine. As shown in figure 4.24, the unit cell parameters revealed a marginal increase with temperature similar to other report [200] and these contributed to the decrease in energy bandgap with temperature listed in table 4.2 [241].

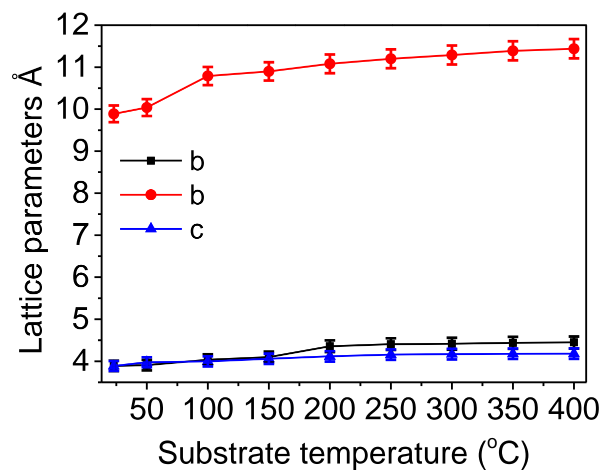

Figure 4.24 Unit cell parameters (2% error) as a function of substrate temperature.

Whilst XRD analysis can indicate the presence of secondary phases, the indexing of the phases can present some difficulties due to the overlapping of some SnS Bragg peaks with SnS_2 and Sn_2S_3 peaks. This simulatneous occurence of peaks of multiple SnS phases has been reported [45]. Figure 4.25 depicts XRD spectra that shows a typical overlapping of the

diffraction peaks. To complement XRD in identifying SnS phases Raman analysis, which will be discussed later was also conducted.

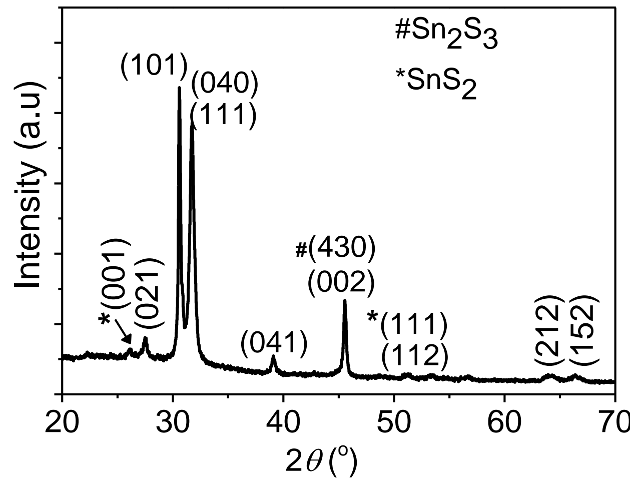

Figure 4.25 XRD spectra of as-deposited SnS films at 100 °C and thickness of 1.5 μm.

The texture coefficient (C_{hkl}) and the degree of preferred orientation (σ) of the films [242] were studied in order to quantify the effect of the substrate temperature on the crystal properties. The texture coefficients are defined as:

$$C_{hkl}=\frac{\frac{I_{hkl}}{I_{o,\,hkl}}}{\frac{1}{m}\sum_{m}\frac{I_{hkl}}{I_{o,\,hkl}}} \tag{4.7}$$

where m ($m = 8$) is the number of reflections, I_{hkl} is the intensity of the hkl reflection and $I_{o,\,hkl}$ is the intensity of the standard powder diffraction file. C_{hkl} gives the measure of the orientation of each hkl plane in comparison to a completely randomly oriented sample. The degree of preferred orientation (σ) of each sample was then determined from the standard deviation of all the C_{hkl} values as,

$$\sigma=\sqrt{\sum\frac{1}{m}(C_{hkl}-1)^{2}} \tag{4.8}$$

For a film to have a preferred orientation (non-random distribution of the crystallites), the texture coefficient at any of the (hkl) reflection must be greater than one [243-245]. Figure 4.26 shows the C_{hkl} values for the noticeable Bragg peaks as a function of substrate temperature ,

while figure 4.27 shows the variation of the $C_{(111)}$, $C_{(040)}$ and σ for the films deposited at higher substrate temperature range of 200-400 °C. At temperatures ≤ 300 °C the crystal structure is randomised indicated by absence of (040) plane and increase in the $C_{(hkl)}$ of (111), (110), (120) (101) and (430) diffraction planes (see figure 4.26). However, for temperatures ≥ 350 °C the results show a substantial increase of (040) in relation to other *hkl* reflections and being the only peak > 1 indicates that the crystallites are preferentially orientated in the (040) plane. This suggests that film deposited at temperature ≥ 350 °C show the set properties useful for the fabrication of SnS heterojunction devices.

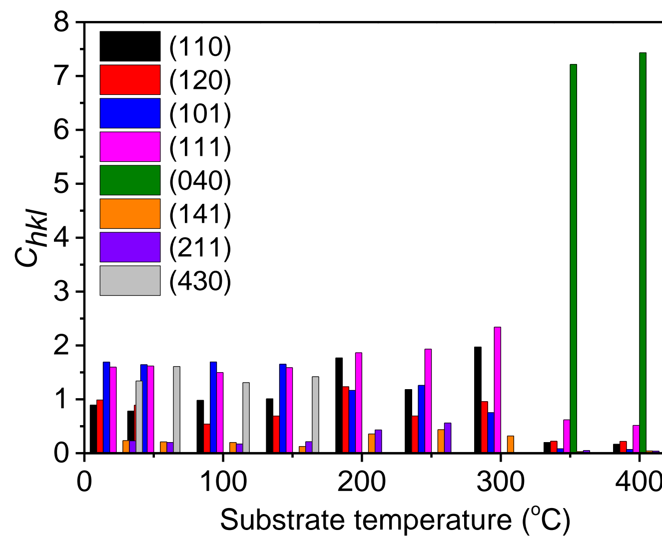

Figure 4.26 Texture coefficient (C_{hkl}) for the range of samples tested.

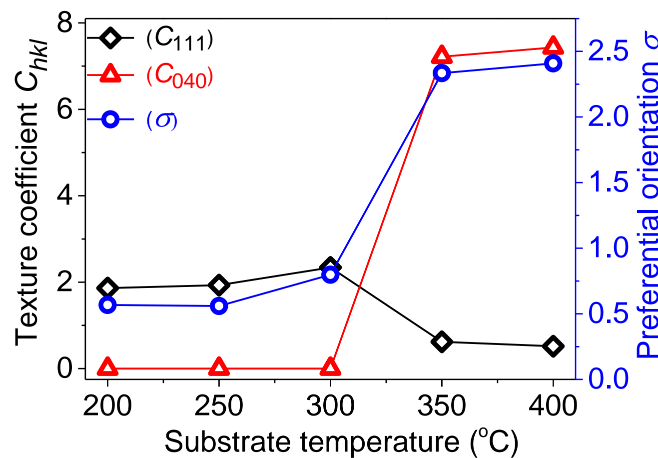

Figure 4.27 Texture coefficients $C_{(111)}$, $C_{(040)}$ and σ as a function of temperature.

The crystallite size (D) and strain (ε) are estimated from the XRD data by Williamson-Hall (W-H) method explained in chapter 3. The calculations were performed for the films that exhibited single SnS phase (temperature range of 200-400 °C) and all the eight (hkl) diffraction peaks observed. Figure 4.28 shows the W-H linear plots of $\beta\cos\theta$ versus $4\sin\theta$.

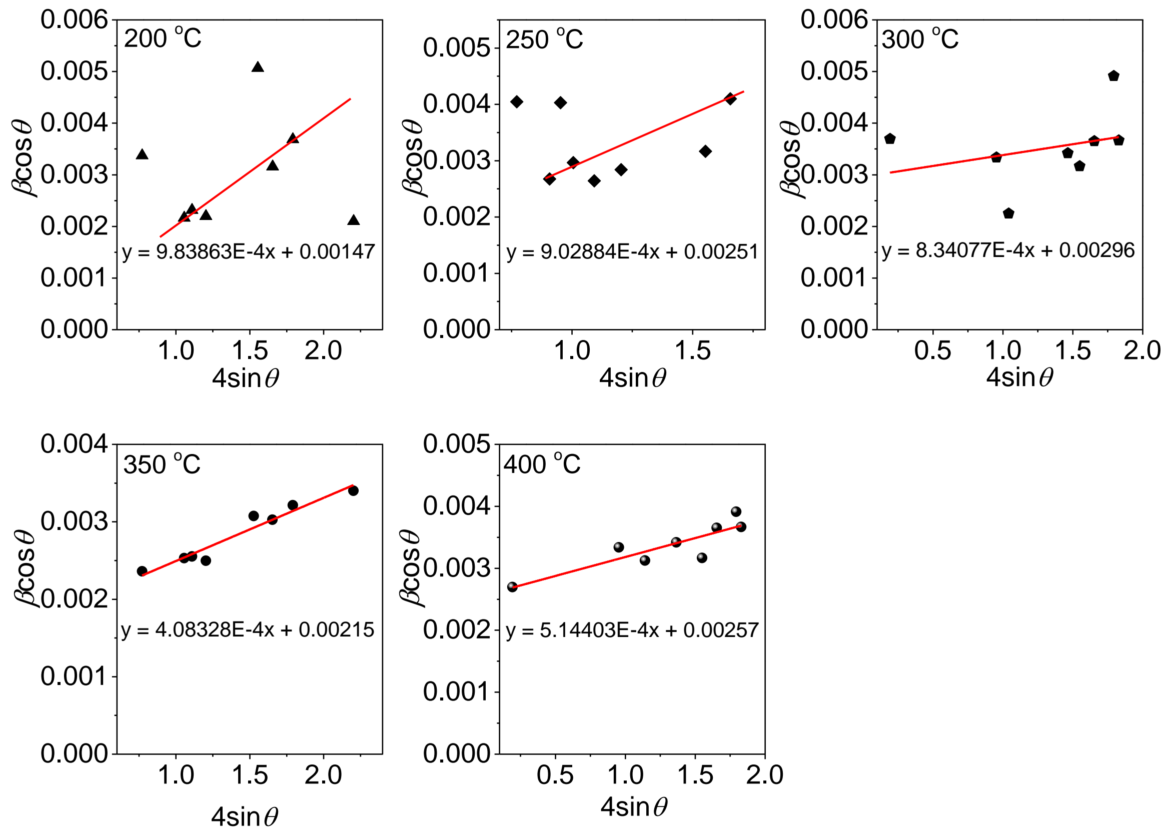

Figure 4.28 Williamson-Hall linear plots of $\beta\cos\theta$ versus $4\sin\theta$ for the films deposited at 200-400 °C substrate temperature.

A trend of increase in crystallite size and decrease in strain with substrate temperature was observed as shown in figure 4.29. The decrease in strain may indicate the formation of higher quality films at higher substrate temperatures [246]. The instrumental broadening in the analysis was removed using Eva software during the analysis. In addition, the diffractogram of a standard material (Silicon) with high crystallinity and sharp Bragg peaks was also measured. This diffractogram was used for the determination of the peak broadening which comes from the instruments slits.

This could be that at higher temperatures, residual stress of the films relaxes and thus strain is reduced. As with grain size, the increase in substrate temperature increases the mobility of adatoms that also results in the increase of the crystallite size and crystallinity of the films [247]. This observation is consistent with the increase in grain size observed in figure 4.13.

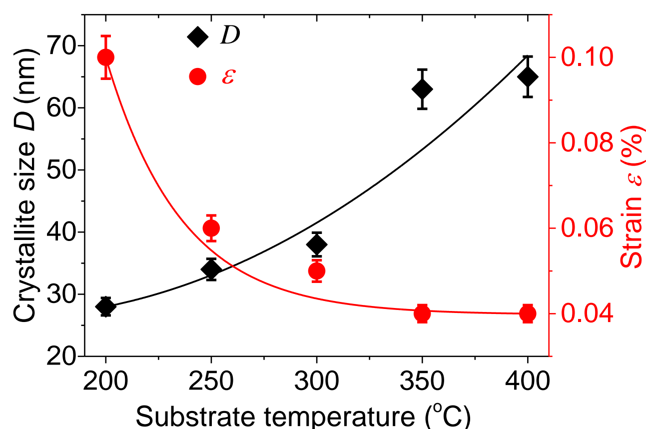

Figure 4.29 Crystallite size and strain for the range of samples tested (bars indicate ± 5% in determination of crystalite size and strain, while the lines are guide for the eye).

To reliably confirm the existence of only SnS phase at high substrate tempertaures following XRD data, Raman studies were conducted and the data are shown in figure 4.30 (a-c). At lower substrate temperatures, Raman modes at 172, 229, 307 and 360 cm^{-1} (see figure 4.30a) revealed the presence of secondary phases. The most intense peak for the samples is at 229 cm^{-1} for all the temperatures, which corresponds to A_g mode of SnS while the other SnS peak at 172 cm^{-1} are from B_{2g} modes [153]. These suggests that at low deposition temperatures, synthesising pure SnS crystal phase is not possible. However, at higher substrate temperatures, three main bands were observed, which are located at 140, 167 and 196 cm^{-1} (see figure 4.30b and zoomed data in figure 4.30c) for clarity and a minor band found at 98 cm^{-1}, these matched well with SnS crystal [202, 226]. No Raman bands belonging to Sn_2S_3 (307 cm^{-1}) and SnS_2 (312 cm^{-1}) [203] are detected across the high substrate temperature range therefore, the crystal structure of the films were that of SnS only. The most intense band for all the samples is at 167 cm^{-1} and corresponds to the B_{2g} mode of SnS while weaker bands at 98 and 196 cm^{-1} are from the A_g modes [226] while 140 cm^{-1} weak band is

assigned to the B_{3g} mode [221]. Figure 4.31 shows the influence of substrate temperature on the B_{2g} and A_g mode positions. A slight shift to lower wavenumbers with increase in temperature were observed, which indicate the presence of bigger grain size similar to other report [248]. Notice the B_{2g} modes were at higher wavenumbers for temperature <200 °C due to presence of secondary phases (SnS_2 and Sn_2S_3).

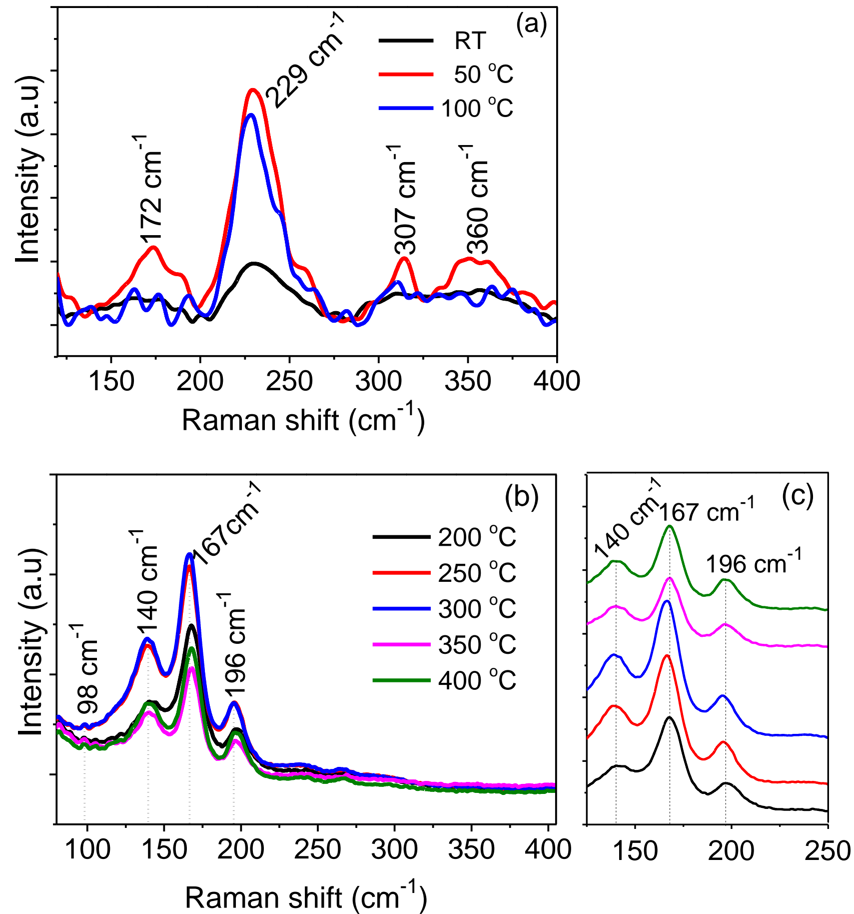

Figure 4.30 (a and b) Raman spectra of the SnS films grown as a function of substrate temperature (c) zoom of the main bands at higher temperature.

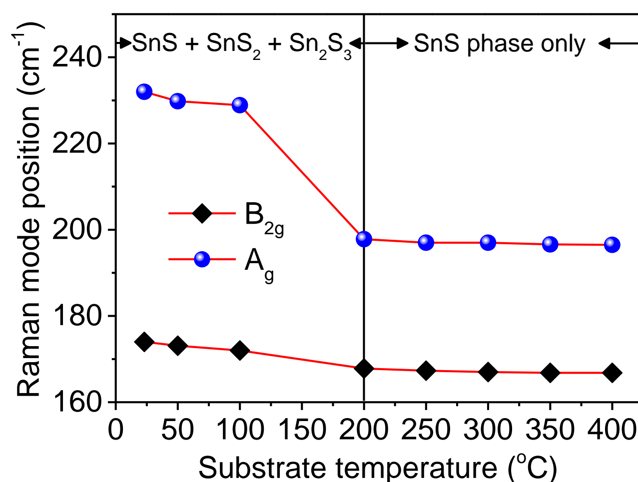

Figure 4.31 Variation in A_g and B_{2g} Raman mode positions as a function of substrate temperature.

Photoluminescence (PL) measurement were carried out for some SnS films to reveal further information on the optical quality of the films and their potential in carrier generation for devices. Figure 4.32 shows the PL emission spectra of the SnS films with photon excitation at 532 nm. SnS film grown at 350 °C has a broad emission peak centred on 1.3 eV, whereas films grown at 300 °C and 400 °C showed no emission peaks. In SnS based thin film material, PL spectra are related to the defects between band and defect level emissions [248]. No emission was observed for the SnS films deposited at temperatures lower or higher than 350 °C because of the insufficient energy of the adatoms to compensate defects and the re-evaporation of sulphur atoms, respectively. Similar behaviour of SnS/CdS sample has been reported [248].

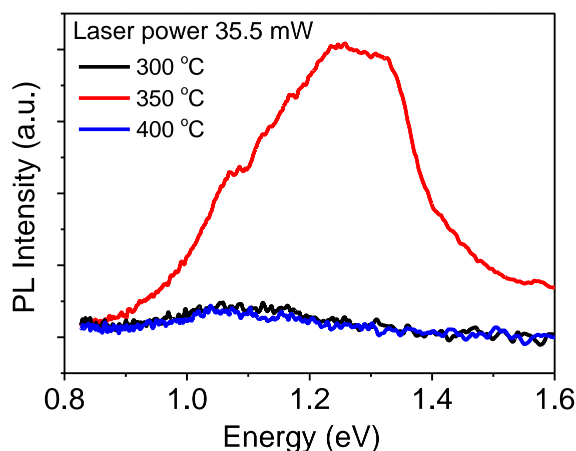

Figure 4.32 PL spectra of as-deposited SnS films recorded at 6K.

The related band of this peak is slightly lower than the bandgap calculated from UV-Vis spectrophotometry, this can be linked to emissions from vacancies or defects that are intrinsic to the growth processes of the films [89, 126]. This demonstrates that controlling the film composition and optical bandgap to some extent is critical to produce a film that will luminesce, a requisite for any implementation in solar devices.

4.3.3 Substrate type dependent properties

Different substrates have diverse influence on the microcrystalline structure, grain growth, optoelectronic properties and device performance of SnS-based solar absorber and solar cells [40, 107, 113]. These effects can result from the chemical nature, surface quality and thermal stability of the substrate material. Therefore, selection of suitable substrate is crucial to obtain good quality SnS absorber that can enhance device performance. In addition, substrate should be stable at the production temperature of the solar cell and there must be chemical compatibility between the substrate and SnS absorber, *i.e.* no chemical reaction should exist between the two as interdiffusion can cause inclusion of undesired atoms in both SnS absorber and substrate. This sub-section explores the use of diverse substrate for SnS deposition and investigated their properties with respect to their suitability for photovoltaic application. The substrates include soda lime glass (SLG), quartz (Q), indium tin oxide (ITO) and fluorine-doped tin oxide (FTO) coated glass, molybdenum (Mo) coated SLG and quartz. The key properties of the substrates used are presented in table 4.3.

Table 4.3. Thickness (t), thermal expansion coefficient (α), roughness (R_s), thermal (k) and electrical (σ) conductivities of the substrates [249-257]. *whether on SLG or quartz.

Sub	t (mm)	$\alpha 10^{-7}$ (/°C)	R_s (nm)	k (W/mK)	σ (S/m)
SLG	1.00	90.0	1.0	1.06	10^{-15}
Q	1.00	5.5	<2.0	1.30	10^{-18}
ITO	1.10	76.0	1.8	3.95	10^{4}
FTO	1.60	60.0	12.5	9.70	~10^{4}
Mo*	10^{-3}	52.0	12.0	142	>10^{7}

The films all showed stoichiometric composition (Sn/S = 1.00 ± 0.01), adherence to substrate surface and free from pinholes irrespective of the substrate type. The constant Sn/S ratio across the films shows that the chemical nature of the substrate has no influence on the composition of the films which is solely controlled by the growth parameters (temperature, thickness and rate). SEM analysis reveals randomly oriented rice and flake-like small grains in SnS grown on SLG and Mo coated SLG, while the grain shape changed to flakes and platelet-like structure when grown on ITO and FTO with noticeable grain growth (see figure 4.33). The films on quartz and Mo coated quartz substrates showed unifromly distributed bigger grains with less void over the substrate surface. Unlike kesterite or chalcopyrite materials, the absence of Na in the substrate induces a significant grain growth in SnS thin films (figure 4.33) with the average grain size increasing from 0.14 µm on SLG to 0.32 µm on quartz, ITO and FTO. This increase in grain size can also be explained by the fact that rough surfaces have more nucleation site [258], such that more grain growth will occur. Due to high roughness, grains can collide and coalesce to form a continous grains.

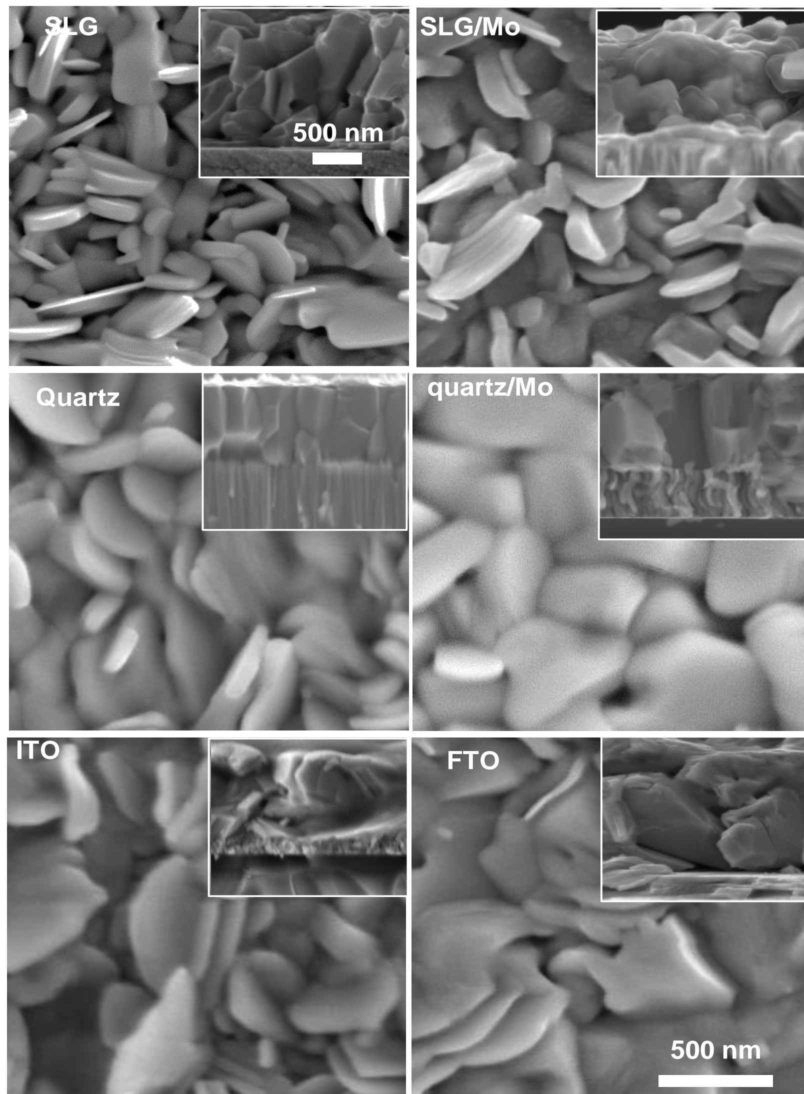

Figure 4.33 SEM micrographs (5kV) across the different substrates, inset: cross-section. Scale bars apply to the range of images.

Figure 4.34 (a) shows the transmittance, *T*, and reflectance, *R*, versus wavelength across the substrate. The optical properties of the layers deposited on Mo coated SLG and quartz are not given, as the visible light absorbing Mo layer restricted the measurement of the SnS absorption edge in transmission, only the reflectance was measured in this case. Similar to the films on reference SLG substrate, the transmittance of other substrates showed interference fringes indicating a good surface homogeneity and uniformity of the layers. The low transmittance in the visible region characterised the broad absorption nature of SnS thin films irrespective of the substrate nature.

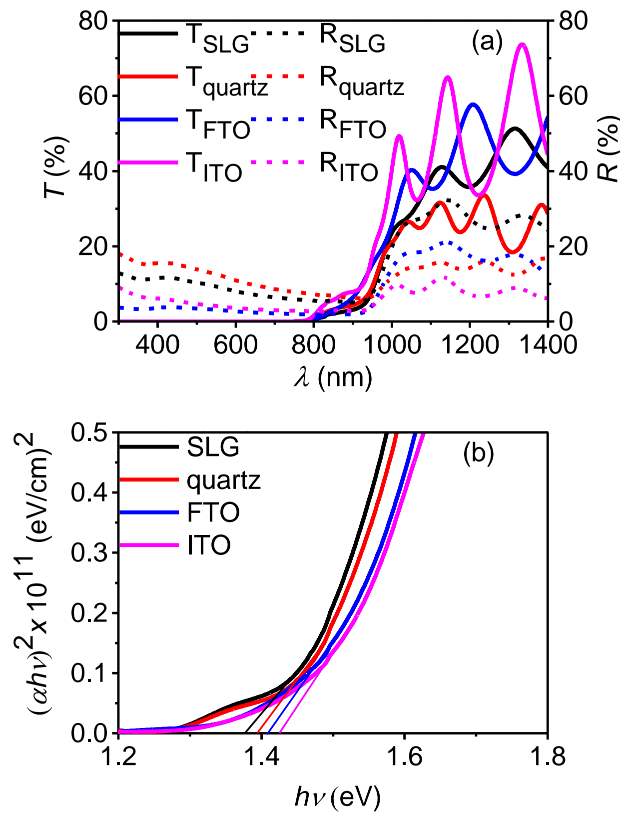

Figure 4.34 (a) Percentage transmittance (solid lines) and reflectance (dotted lines) with wavelength and (b) $(\alpha h\nu)^2$ with $h\nu$ of the SnS layers across the substrate.

The plot of $(\alpha h\nu)^n$ vs $(h\nu)$ fits better for $n = ½$, indicating the SnS films to have a direct allowed interband transitions with energy bandgap value of 1.39, 1.41 and 1.42 eV for the layers on quartz, FTO and ITO, respectively (see figure 4.34b) compared to the reference 1.37 eV for the film on SLG. The slight increase in energy bandgap of the Na-free samples of ITO and FTO can be linked to possible high diffusion of oxygen from ITO and FTO compared to SLG to the SnS films [146], as well as the decrease in the unit cell volume (see table 4.4).

The XRD spectra of the SnS films as a function of substrate material are shown in figure 4.35.

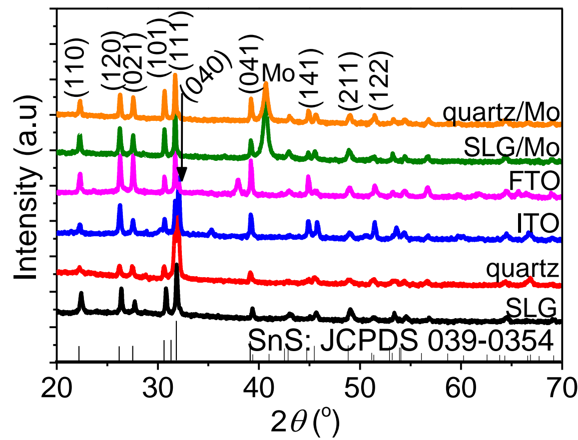

Figure 4.35 XRD spectra of SnS thin films as a function of substrate material.

The layers were highly crystallised irrespective of substrate type with similar features to SnS orthorhombic structure (powder diffraction file 039-0354). No secondary phase was detected across the substrates and the crystal structure depicted several diffraction peaks (see figure 4.35) with (101), (111) and (040) noticed as the most prominent peak. Following the calulation of the texture coefficient (C_{hkl}), the preferred orientation (σ) were established using equation 4.7 and 4.8 stated in the last sub-section, the result is presented in figure 4.36.

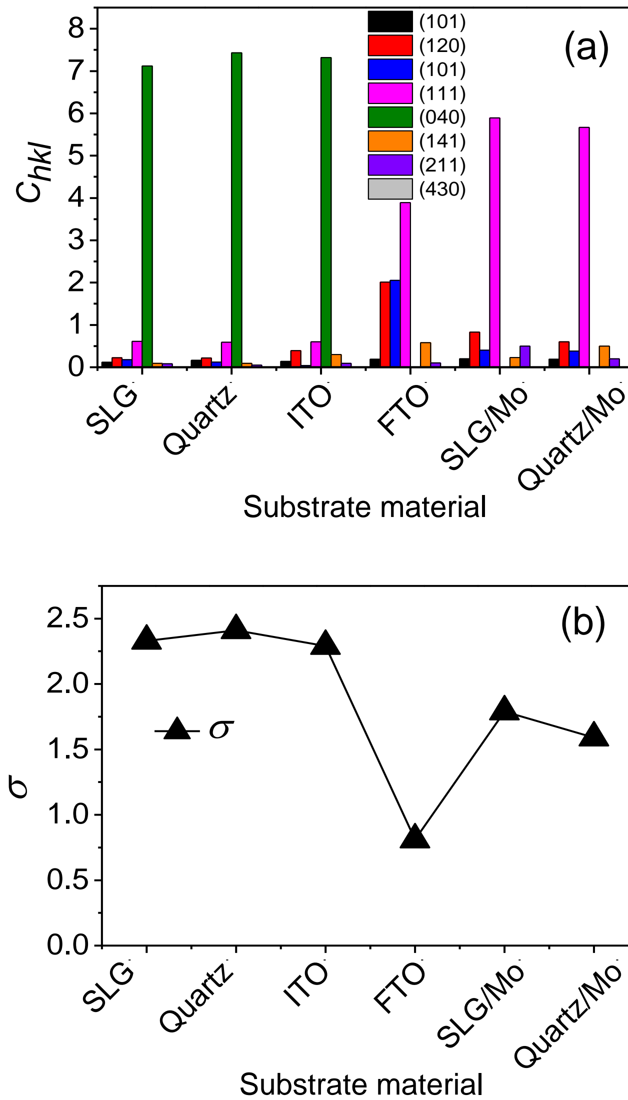

Figure 4.36 (a) Texture coefficient (C_{hkl}) and (b) degree of preferred orientation (σ) as a function of substrate material (the line is a guide for the eye).

Films on SLG, quartz and ITO exhibited strong (040) preferred orientation, while those on Mo coated SLG and quartz showed (111) preferred orientation in addition to the Mo peak. However, for the films deposited on FTO, the crystal structure became randomised such that C_{hkl} in (120) and (111) planes are greater than one. These variations in preferred orientation are linked to the differences in surface roughness and intrinsic properties of the substrates while film composition remains constant throughout. Rougher surfaces with several nucleation site, will have many grains with diverse orientation of crystallographic axes evidenced on films

deposited on FTO and Mo coated substrates. Films on SLG, Q and ITO with similar roughness exhibited similar crystal orientation.

Similar (040) preferred orientation has been observed for SnS thin films deposited on SLG [45] and ITO [40, 108] no report exist elsewhere for quartz substrate. Sall *et al.* [146] Bashkirov *et al.* [259] and Reddy *et al.* [40] synthesized SnS on Mo coated glass substrates via chemical spray pyrolysis, hot wall vacuum and sulfurisation methods, respectively and observed preferred orientation along (111) plane alongside the Mo peak in agreement with this work. Therefore, the orientation of SnS thin films on different substrates depend on the nature of the substrate, which in turn influences the crystallinity of the films. The variation of crystallite size (*D*) and lattice strain (ε) were also evaluated using XRD data via Williamson-Hall method. Strain arises due to differences in thermal coefficient of the substrates and the nucleating film, which can cause peak broadening and a shift in peak position [86]. Figure 4.37 shows the crystallite size and lattice strain across the substrates.

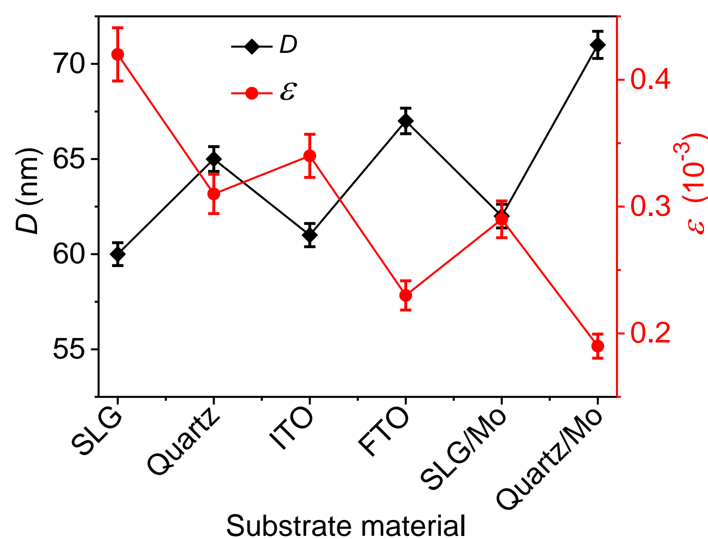

Figure 4.37 Crystallite size (*D*) and lattice strain (ε) versus substrate materials (lines are guide to the eye).

Slight variations in the *D* and ε are attributed to the difference in the surface roughness (see tables 4.3 and 4.4) as crystallites may tend to grow during coalesence of grains and lattice strain exhibited by the substrates. Increase in crystallite size with substrate type is in good

agreement with the grain sizes shown in the SEM images (see figure 4.33 and table 4.4). The smaller crystallite size noticed in the films on SLG compare to other substrates could be due to presence of higher concentration of strain, smoother surface and probably sodium (Na) contamination.

Table 4.4. Summary of observed parameters for SnS as a function of substrate type.

Substrate material	Lattice parameters ± 0.01 *a, b, c* (Å)	Unit cell volume ± 0.05 (Å^3)	Preferred orientation	Crystallite size ± 2.0 (nm)	Grain size ± 5 (nm)	Eg ± 0.05 (eV)
SLG	4.32, 11.26, 4.00	194.6	040	60	140	1.37
Quartz	4.23, 11.38, 4.02	193.5	040	65	280	1.39
ITO	4.21, 11.45, 3.98	191.9	040	61	230	1.42
FTO	4.41, 10.97, 3.98	192.5	111	67	320	1.41
SLG/Mo	4.42, 10.76, 4.07	193.6	111	62	210	-
Quartz/Mo	4.13, 11.39, 4.05	190.5	111	71	320	-

Note that bandgaps for the SLG/Mo and quartz/Mo substrates are not recorded because the visible light absorbing Mo layer restricted the measurement of the SnS absorption edge in transmission.

4.4 Conclusion

SnS thin films have been successfully deposited using thermal evaporation. The deposition at 350 ^{o}C with evaporation rate of 30 Å/s can produce pure phase polycrystalline and stoichiometric SnS film with near optimum energy bandgap of 1.37 eV. The effect of substrate temperature, layer thickness and substrate material on crystallographic, optical and microscopic properties of SnS solar absorbing thin films has been investigated. The morphological properties were considerably influenced by the nature of substrate and mildly independent of the layer thickness and growth temperatures. SnS_2 and Sn_2S_3 present at lower substrate temperatures were found to disappear at higher substrate temperatures ≥ 200 ^{o}C. High-temperature dependent analysis showed that the energy bandgap of the as-deposited SnS was red-shifted as the composition of the samples became deficient in sulphur and richer

in Sn. The high temperature-dependent experiments also showed that photoluminescence can only be generated for films grown at 350°C, which are stoichiometric, and of energy bandgap of 1.37 eV. Analysis of the experimental data demonstrated that it is imperative to control the deposition parameters to fabricate good quality SnS absorbers suitable for solar cells.

Chapter 5

Post Annealing Treatments and Se-S Substitution

5.1 Introduction

Optimisations of the deposition parameters detailed in chapter 4 (section 4.3), showed that the best SnS films were formed at a thickness of 800 nm and substrate temperature of 350 °C. The layers were stoichiometric with energy bandgap of 1.37 eV but still have voids and mix of small grains, which may limit their photovoltaic performance. This chapter focuses on the further optimisation of this as-deposited film with interest on the grain growth and reduction in grain boundaries via annealing treatment and the impact of selenium (Se) - sulphur (S) substitution.

In SnS-based thin film solar cells, a high quality and stoichiometric SnS films comprised of large grains are required to facilitate the transport of photo-generated carriers and reduce grain boundary recombination and thus enhance the power conversion efficiency of the devices. Post-annealing treatments are normally used to enhance the efficiency of thin film devices by improving the quality of the solar absorber layer. Post annealing treatment in SnS based thin films has been found to be very effective in reducing recombination and promoting grain growth and carrier mobility [101]. The SnS post deposition anneal treatment in the presence of the H_2S gas is one of the crucial factors that led to the record efficiency device to date [28, 102, 172]. The thermal treatment in H_2S is effective in suppressing the creation of sulphur vacancies V_S due to high sulphur loss following anneal and can significantly enhance grain growth.

However, the use of H_2S can cause possible life-threatening situations due to its toxicity. H_2S gas burns and produces other toxic vapours such as sulphur dioxide and being heavier than air, can accumulate in the laboratory. Therefore, this investigation is focused on finding an annealing environment, which can improve the SnS solar cell performance via enhancement

of grain growth and passivation of grain boundaries. The processes and diverse environments used in this study were stated in experimental section (see chapter 4). SnS films annealed at high temperatures may lead to sulphur deficiency and loss in stoichiometry of Sn and S, which may reduce the photoconductivity of the films [52]. The possible route to overcome this challenge is to anneal and substitute the sulphur with selenium via selenisation in either low or high vacuum environments. The link between the Se - S substitution in the SnS solar absorber with its grain growth is thus presented in section 5.3.

5.2 Post-deposition heat treatment of SnS thin films

The post deposition heat treatment was done in high vacuum (pressure $< 8.0 \times 10^{-7}$ mbar) or under atmospheric pressure. For the high vacuum, the as-deposited ~800 nm thick SnS sample was taken from the evaporator carefully cut into three parts with one used as reference while, the other two parts were moved back to the evaporator. These two samples were subsequently annealed for 60 min at a temperature of 400 and 450 °C in vacuum. In atmospheric annealing, a first set of samples was annealed in a quartz tube furnace, where an inert atmosphere of nitrogen (N_2) has been allowed to flow at operating pressure of 1000 mbar. The stable heat treatment duration was 60 min at a temperature of 400, 450 and 500 °C. In addition, a second set of samples was first dipped in saturated solution of $SnCl_2$ or $MgCl_2$ for 10 seconds before annealing in N_2 with same condition as first set.

The films after annealing were pinhole free and adhered strongly to the substrate with a colour change from grey to stormy grey for all the annealing environments. As shown in the SEM images of figure 5.1, the morphology of the as-deposited and annealed samples look approximately similar for samples annealed in vacuum, but the annealed sample has more packed grains with less void. Quantification of the grain sizes is not possible due to the non-uniform shapes of the grains. Post annealing in high vacuum seems to be ineffective in inducing grain growth in SnS thin films irrespective of deposition condition [260]. Figure 5.2 shows the SEM images of the SnS thin films that were annealed in N_2 ambient for 60 min. It can be seen that annealing under nitrogen slightly improved the grain growth, the films

revealed a compact and dense structure with no voids or cracks as the temperature is increase to 450 and 500 °C. This suggests a better connection between the grains, which decreases the possibility of pinhole formation and grain boundary recombination. Similar observation of nitrogen ambient pressure assisted growth of the grains in the films was reported by Naidu R *et al.* [174] for SnS photo absorber. Figure 5.3 shows the morphology of the samples after chlorine treatment. A modification of the grains is evident but the shapes of these grains made it difficult to say if chlorine treatment was of any benefit to the grain growth. $SnCl_2$ treated samples (see figure 5.3a) showed similar morphology to untreated samples annealed in nitrogen. On the other hand, the morphology of the sample after $MgCl_2$ treatment (see figure 5.3b) was characterised by several domains, separated by deep cracks. This suggests that $MgCl_2$ was too aggressive for the SnS thin film recrystallization. Similar behaviour of SnS thin films after chlorine treated has been reported [261, 262]. It can be understood that unlike CdTe layer where post chlorine treatment induces grain growth and enhance performance [213, 263], it has detrimental consequences in SnS thin films due to the formation of small grains, voids and deep fractures.

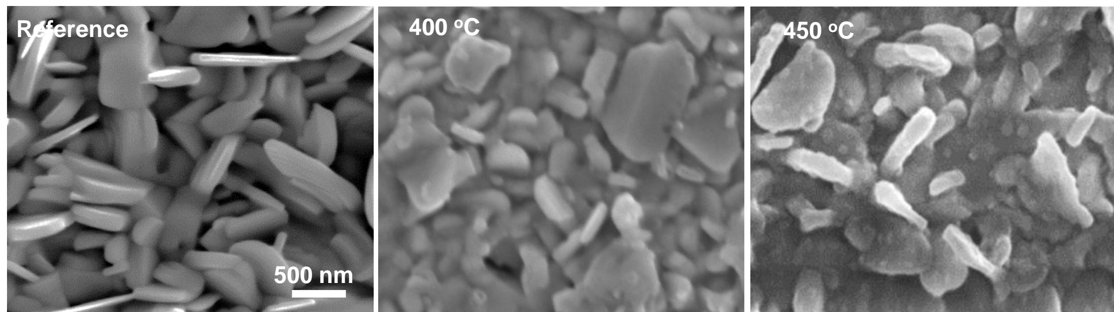

Figure 5.1. SnS film morphology of the reference and annealed samples in high vacuum for 60 min.

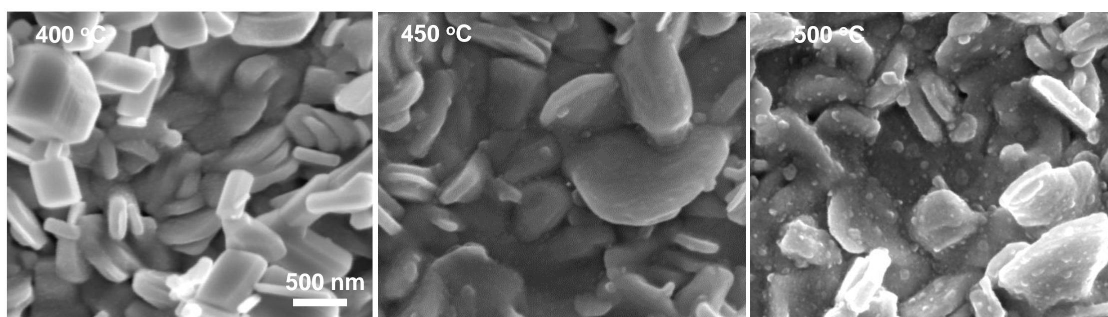

Figure 5.2. SnS morphology after annealing in N_2 atmosphere (1000 mbar) for 60 min.

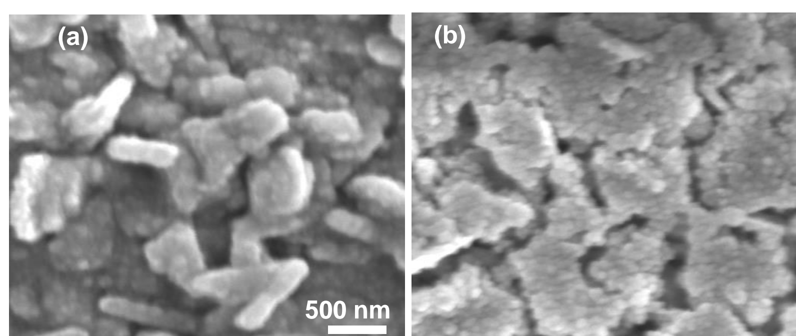

Figure 5.3. SnS morphology after (a) $SnCl_2$ and (b) $MgCl_2$ treatment and annealing at atmospheric pressure (1000 mbar) under N_2 for 60 min.

Figure 5.4 shows the relationship between the grain size and annealing temperature. Independent of environment, films annealed at 450 °C showed larger grains compared to films annealed at lower or higher temperatures. This can be attributed to the fact that annealing at lower temperatures (<450 °C) lack adequate thermal energy for coalescence of small grains, while higher temperatures (>450 °C) cause significant re-evaporation of S atoms.

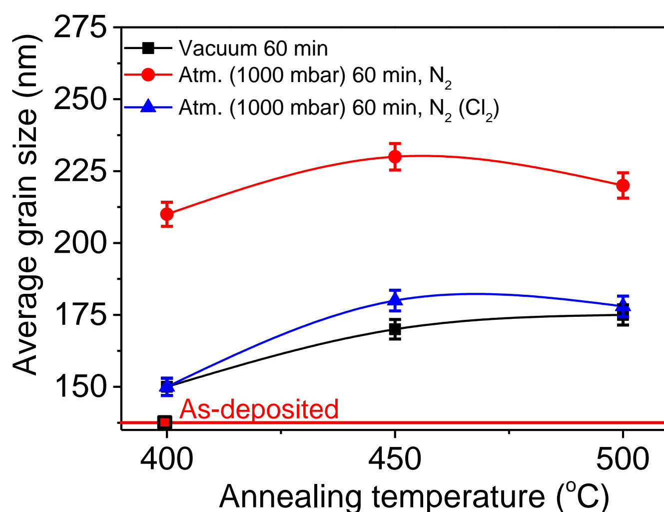

Figure 5.4. Grain size as a function of annealing temperature in different environment (bars indicate ± 5% in determination of average grain size).

Tables 5.1-5.3 show the atomic composition of Sn and S as well as the energy bandgap estimated from the optical measurement after post heat treatment. The vacuum annealed films lost stoichiometry because of re-evaporation at high temperature with high loss of sulphur atom due to high vapour pressure of sulphur compared to tin. The high deficiency of sulphur atom in the annealed SnS thin films in vacuum have been reported in literature [168, 264]. It is also evident from EDX results that the strong recrystallization of the films in both N_2 annealed and chlorine treated samples (see figure 5.2 and 5.3) were accompanied by high sulphur deficiency (see table 5.2 and 5.3) similar to the films annealed in vacuum. A typical EDX spectrum taken from the sample annealed at 450 °C in Nitrogen ambient under atmosphere pressure (1000 mbar) for 60 min is shown in figure 5.5.

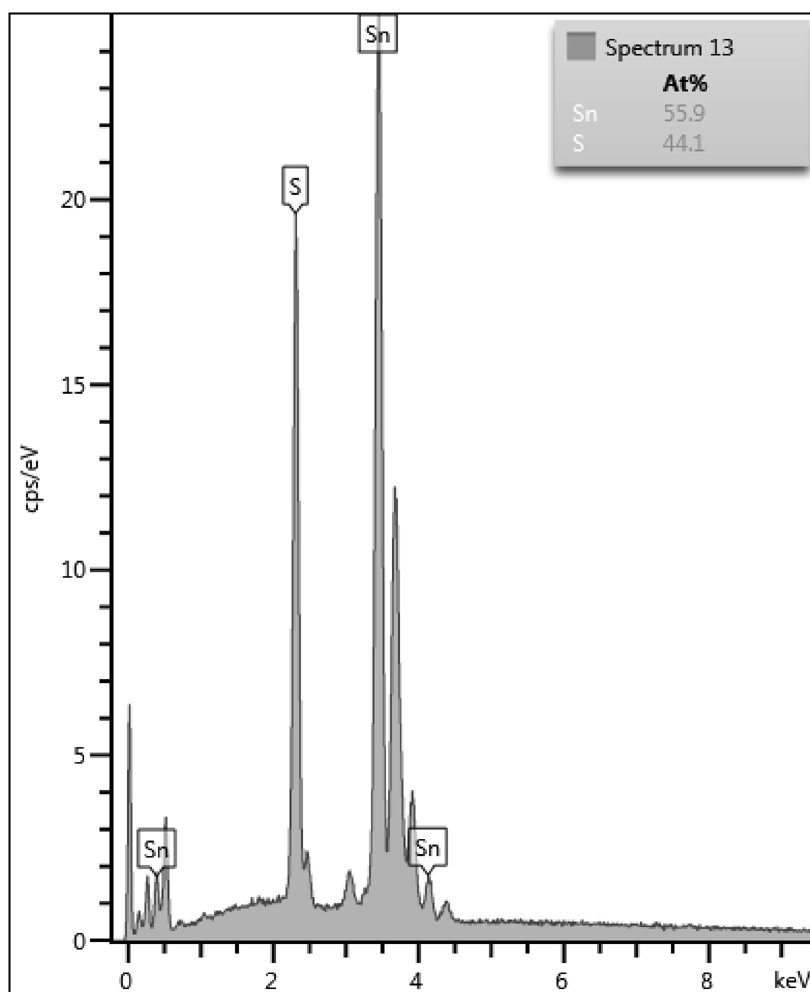

Figure 5.5 EDX spectrum of SnS sample annealed at 450 °C in Nitrogen ambient under atmosphere pressure (1000 mbar) for 60 min.

Table 5.1 Composition of the reference and annealed film in vacuum with energy bandgap.

Temperature (°C)	Sn (at %)	S (at %)	Sn/S ± 0.01	E_g ± 0.05 (eV)
As-deposited 350	50.0	50.0	1.00	1.37
400	52.7	47.3	1.11	1.24
450	53.6	46.4	1.16	1.22

Table 5.2. Anneal in N_2 under atmosphere pressure (1000 mbar) for 60 min.

Temperature (°C)	Sn (at %)	S (at %)	Sn/S ± 0.01	E_g ± 0.05 (eV)
400	53.5	46.5	1.15	1.28
450	55.9	44.1	1.27	1.27
500	56.8	43.2	1.31	1.25

Table 5.3. Anneal in N_2 atmosphere (1000 mbar) for 60 min after chlorine treatment.

Sample	Sn (at %)	S (at %)	Sn/S ± 0.01	E_g ± 0.05 (eV)
$MgCl_2$ 450 °C	53.2	46.8	1.14	1.26
$SnCl_2$ 450 °C	56.0	44.0	1.27	1.25

Figures 5.6(a-c) show the optical transmittance and reflectance spectra of the SnS films after post deposition heat treatment. For all the annealing conditions, the transmittance spectra shifted toward the infrared region, which become more evident on increasing the annealing temperature to ≥ 450 °C. The reflectance spectra equally shifted in the same direction. This indicates that for the visible region, almost all the radiation are absorbed in the annealed samples and can also absorb some incident photon in the near infrared region.

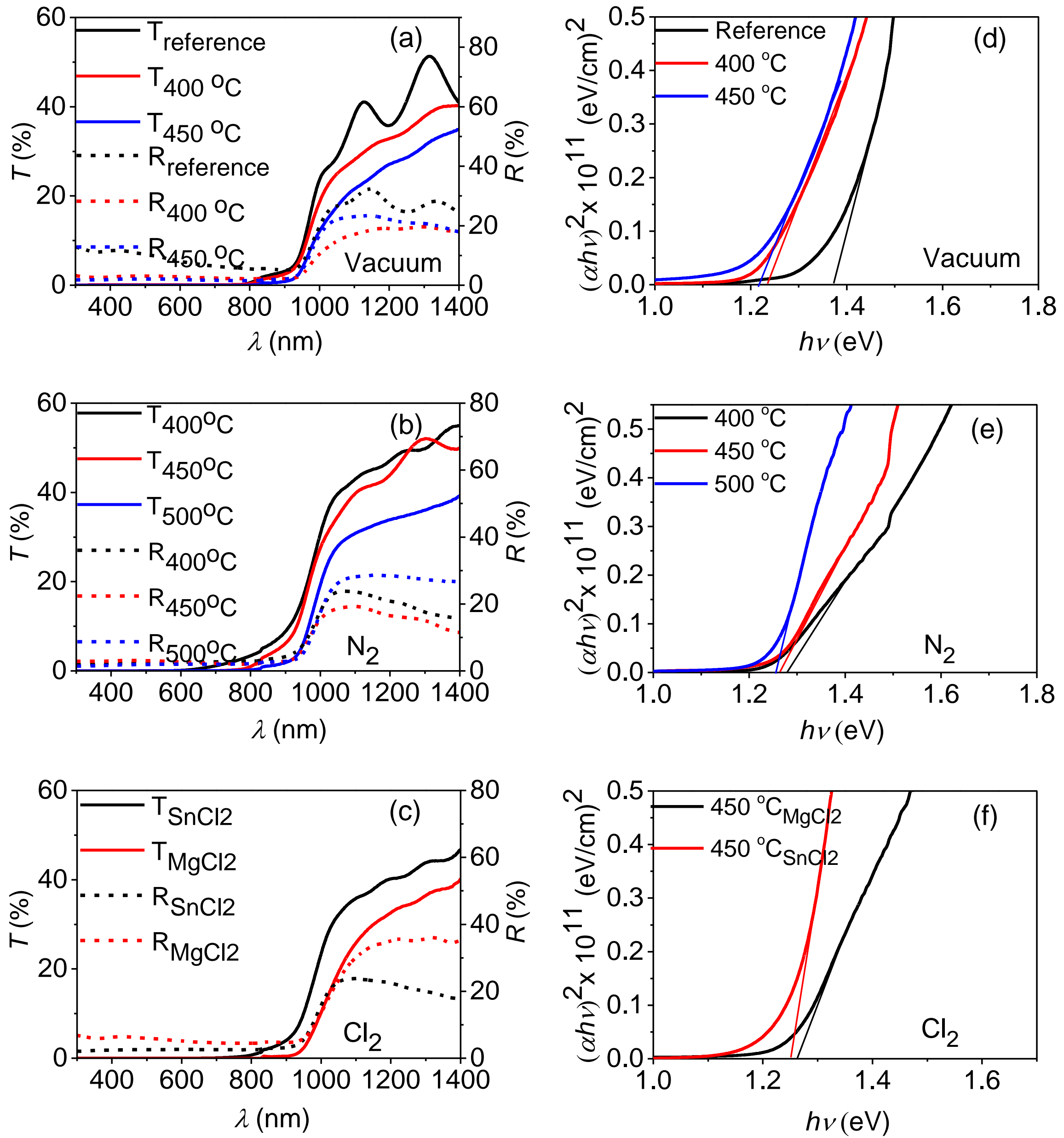

Figure 5.6 (a-c) transmittance (solid lines), reflectance (dotted lines) and (d-f) plots of $(\alpha h\nu)^2$ versus $h\nu$ of the SnS films annealed in (a) vacuum, (b) nitrogen and (c) chlorine treated.

The plots of $(\alpha h\nu)^2$ versus $h\nu$ shown in figure 5.6 (d-f) were used to estimate the energy bandgap of the annealed films by extrapolating the intercepts on the $h\nu$ axis. For the SnS films annealed in vacuum, energy bandgap value of 1.22 and 1.24 eV were estimated for the samples annealed at temperature of 400 and 450 °C, respectively, while the as-deposited layer showed a higher energy bandgap of 1.37 eV. This can be linked to the deviation of Sn/S ratio from stiochiomtric value following anneal due to the difference in vapour pressure of Sn

and S. A decrease in the energy bandgap of SnS films after anneal in vacuum has been reported in the literature [41, 169]. Similar behaviour was observed for the samples annealed in N_2 ambient where a direct energy bandgap range of 1.25 to 1.28 eV were estimated, this bandgap decreases with increaing annealing temperature in good agreement with Sn/S ratio variation. However, similar to both samples annealed in vacuum and N_2, a direct energy bandgap value of 1.26 and 1.25 eV were estimated for the films after $MgCl_2$ and $SnCl_2$ treatment, respectively. The reduction in the energy bandgap following annealing in these environment can be linked to the slight increase in grain size and changing Sn/S atomic composition.

Figures 5.7 (a-c) show the XRD spectra of the reference and the annealed SnS thin films. For the high vacuum annealing, the diffraction patterns were very similar to the as-deposited sample (see figure 5.7a) suggesting that this treatment did not modify the microcrystalline structure of the samples. All reflections of the vacuum annealed samples fit well with the reference orthorhombic pattern SnS (PDF 039-0354). Similar to the as-deposited samples, the layers after vacuum anneal are all single phase with same plane of (111) and (040) giving rise to the most prominent peak with no change in orientation. This indicates that the films retain their crystal structure and phase after vacuum annealing.

The XRD diffraction patterns after N_2 annealing are shown in figure 5.7 (b). It can be seen that annealing the samples in N_2 ambient brought about a significant reduction in the intensity of the prominent (040) due to substantial increase in other peaks. Increase in the peak intensity of (101) diffraction plane is evident across the annealing temperatures, which has been reported to be more beneficial for fabricating efficient SnS-based solar devices due to its higher ionisation potential compared to either (111) or (040) planes [40]. Higher ionisation potential can minimise the band discontinuities and enhance device performance. Similar diffraction patterns with decreased peak intensities have been reported for sprayed SnS thin films after post heat treatment in nitrogen ambient [175]. For the case of both $MgCl_2$ and $SnCl_2$ treatment (see figure 5.7c), the samples exhibit the main diffraction peaks of orthorhombic

SnS but with a strong modification of the relative peak intensities, the preferential orientation is drastically reduced probably due to been annealed under atmospheric pressure in N_2 or both N_2 and chlorine environment (see figure 5.9 b and c). As the samples shown in figure 5.7 (b and c) were annealed in atmospheric pressure under nitrogen, possible partial oxidation of some of the SnS films into tin dioxide (SnO_2) cannot be ruled out. Thus, SnO_2 was detected in these layers, the peak of which has been labelled with JCPDS 041-1445.

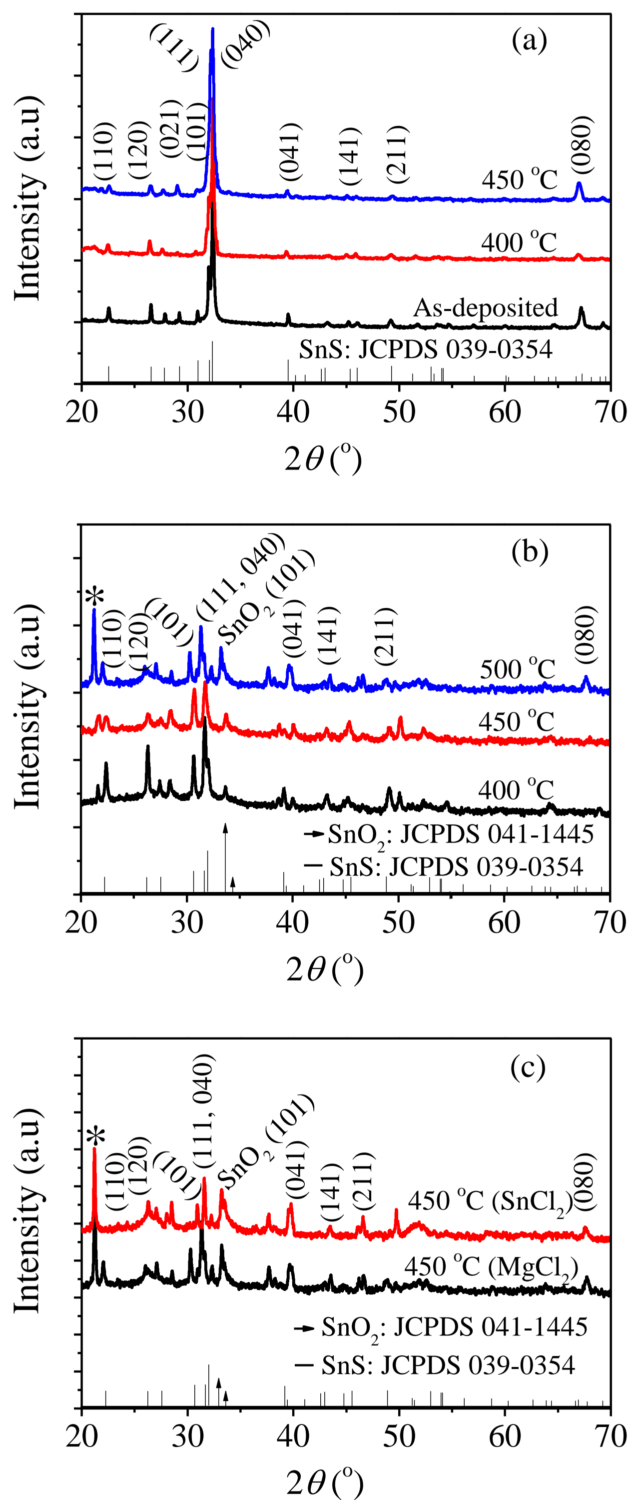

Figure 5.7 XRD spectra of SnS films annealed in (a) vacuum, (b) N_2 under atmosphere pressure (1000 mbar) for 60 min and (c) same condition as (b) after chlorine treatment (* stands for the reflection from the sample holder due to small size of the measured sample).

The unit cell volume was determined from the XRD data using the Eva software for the post annealed samples, this is shown in figure 5.8. The unit cell volume increased with the temperature irrespective of annealing environment. This revealed that the larger volume of the unit cell at high annealing temperature correlates well with the decrease in energy bandgap (see figure 5.6 d-f) as explained by Albanesi [241].

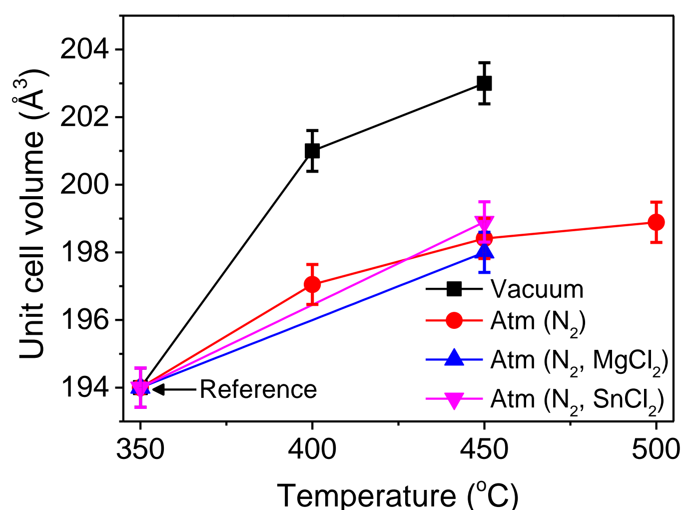

Figure 5.8 Variation in unit cell volume (Å^3) with annealing temperature (bars indicate $\pm$ 1.5 Å^3 instrumental error in determination of unit cell volume).

The texture coefficient (C_{hkl}) and the preferred orientation (σ) of the films is presented in figure 5.9. Films annealed in vacuum retained their crystallographic orientations evidenced by the strong (040) diffraction peak with other peaks being less than 1.0 when compared with the reference sample (see figure 5.9a). Under atmospheric pressure anneal (1000 mbar), samples annealed in nitrogen ambient showed a deviation of the preferred orientation from (040) to (111) diffraction plane as the anneal temperature goes higher than 450 °C. Notice that for the anneal temperatures $\geq$ 400 °C, samples displayed moderate texture as up to two samples had $\sigma > 1$. Similar behaviour was observed following chlorine treatment except for the layer treated with $SnCl_2$, which showed (111) orientation alongside the SnO_2 peak.

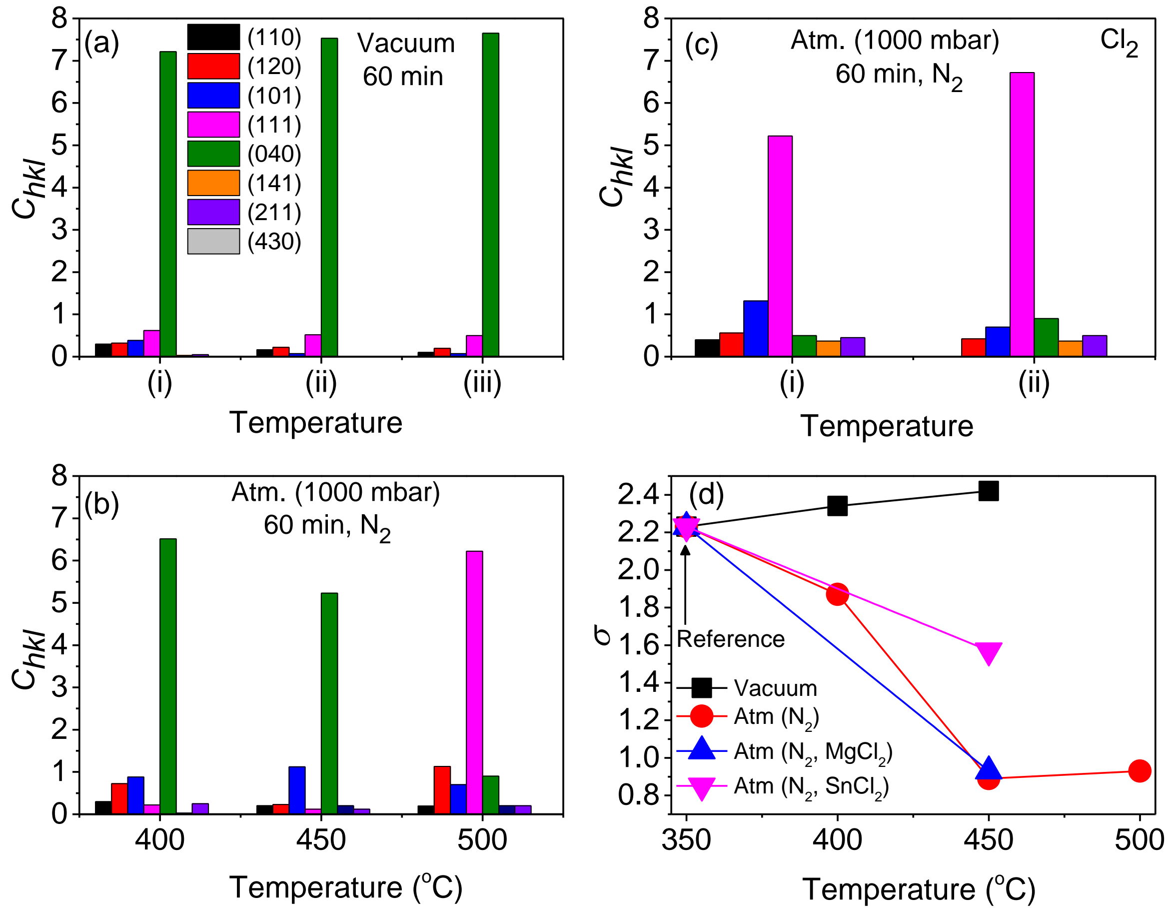

Figure 5.9 Texture coefficient (C_{hkl}) of SnS films annealed in (a) i, ii, iii stands for reference, 400 °C, 450 °C, respectively (c) i, ii represent $MgCl_2$, $SnCl_2$, while (d) degree of preferred orientation (σ) as a function of both annealing environment and temperature.

Although considerable recrystallization was achieved after post-deposition heat treatment of SnS films in N_2 and chlorine environments, the treatments were inadequate to induce significant grain growth. In addition, the persistence loss in sulphur after annealing may limit the performance of the SnS-based solar cells. The possible solution is annealing in an environment that can compensate for the sulphur loss. Therefore, the next section will focus on the possible substitution of sulphur with selenium atom.

5.3 Influence of Se/S substitution on the Sn(S,Se) solar absorber

The application of the post annealing treatment discussed in section 5.2 resulted to be ineffective to induce SnS grain growth, reach significant recrystallization and minimise grain

boundaries. Moreover, the high loss of sulphur in the annealed samples resulted to shift in stoichiometric that can affect the device performance. To overcome this limitation and enhance grain growth, Se - S substitution was therefore explored via selenisation technique. The choice of Se instead of S is because of its ability to activate solar absorber layers and significantly enhance power conversion efficiency of thin film solar cells based on kesterite and chalcopyrite. Selenisation has been a key route for inducing grain growth and improving the quality of chalcogenide absorbers such as Cu_2ZnSnS_4 (CZTS) [27, 265, 266]. Since few reports exists for selenisation of SnS films yet in the literature, the treatment was implemented on the SnS absorber in both low and high vacuum environment using elemental selenium pellets. Three sets of experiments were conducted. In the first experiment, the Se and SnS pellets were co-evaporated in high vacuum at substrate temperature of 350 ^{o}C using the similar process described in section 5.2. For the second experiment, SnS films were first deposited at similar substrate temperature with first experiment before evaporating Se pellets in high vacuum at temperature of 400 and 450 ^{o}C.

For the third experiment, the as-deposited SnS sample was taken from the evaporator, carefully cut into four parts with one used as reference while, the other three parts were moved to the tube furnace for selenisation. After loading each sample, the tube furnace was evacuated to a pressure of 5.5×10^{-3} mbar and backfilled with ~10 mbar of argon before increasing the selenisation temperature to desired set point. The temperature was varied between 400 to 500 ^{o}C using the process described in chapter 3. Figure 5.10 shows the morphology of the reference, co-evaporated (SnS and Se) and samples coated with Se in high vacuum, while figure 5.11 presents the variation in grain size with the selenisation conditions.

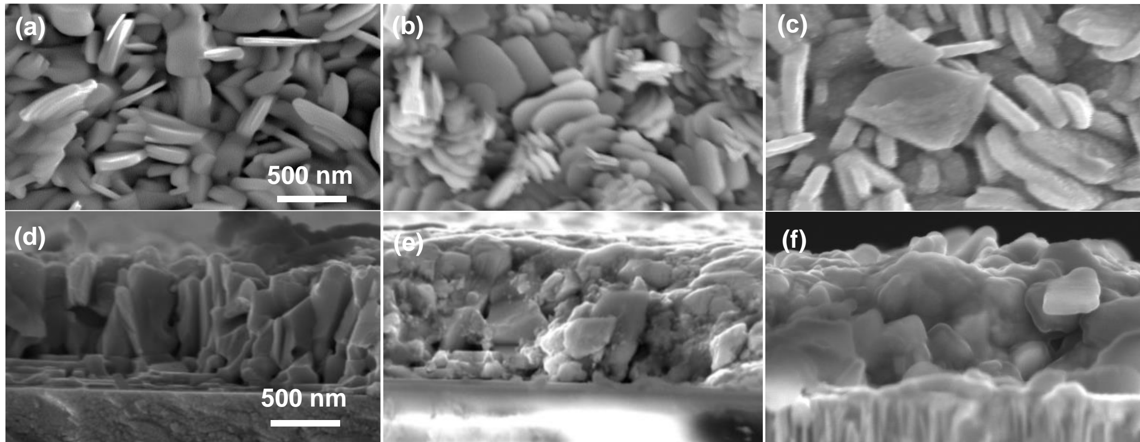

Figure 5.10 SEM images of SnS thin films (a) as-deposited (b) simultaneous deposition with Se and (c) successive Se coating in high vacuum. (c-f) respective cross-sectional image of samples.

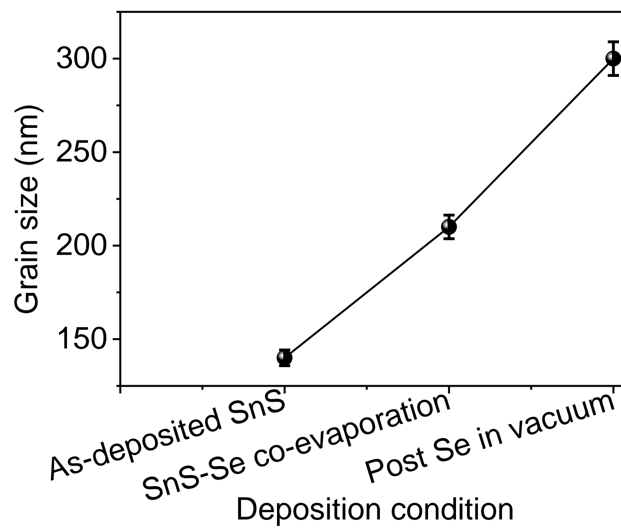

Figure 5.11 Variation in grain size with selenisation condition (bars indicate ± 5% error in determination of grain size).

A weak change in the film morphology and slight recrystallization was seen in the co-evaporated and high vacuum selenised samples in comparison with the reference sample (see figure 5.10). Average grain size slightly increased from 140 nm of the reference sample to 200 and 300 nm for the co-evaporated (SnS and Se) and samples coated with Se in high vacuum, respectively.

Figure 5.12 shows the morphology of the selenised samples in 10 mbar Ar using tube furnace, while figure 5.13 presents the variation in grain size with selenisation temperature.

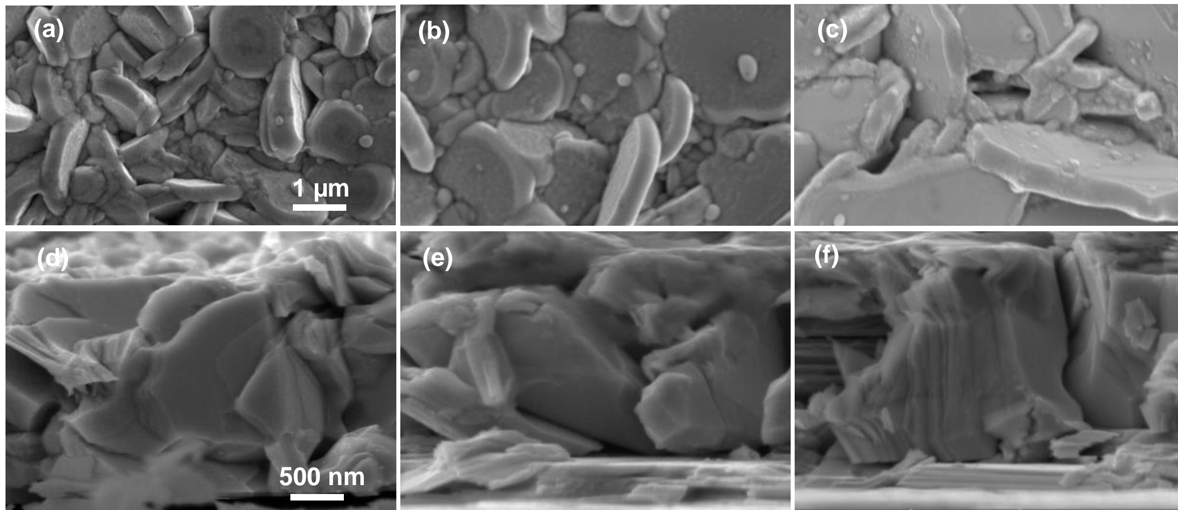

Figure 5.12 SEM images of Sn(S,Se) after selenisation at (a) 400 °C (b) 450 °C and (c) 500 °C temperature 10 mbar Argon for 20 min. (e-f) respective cross-sectional images of the samples.

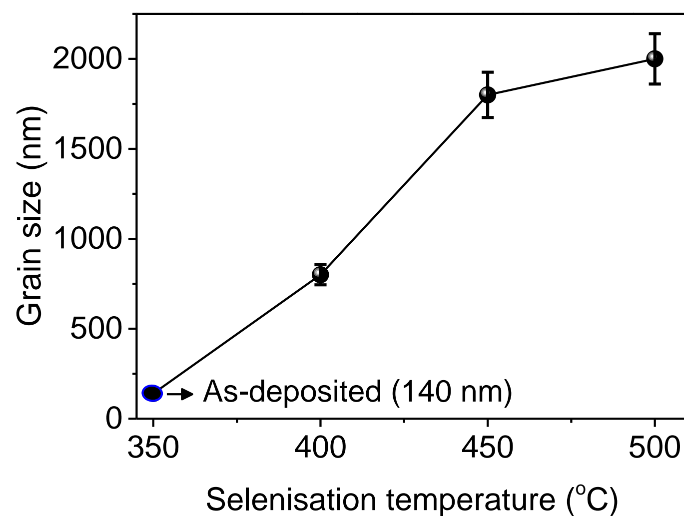

Figure 5.13 Variation in grain size with selenisation temperature (bars indicate ± 5% error in determination of grain size).

Samples selenised in low vacuum argon ambient showed significant growth of new large grains. It can been seen that increase in the selenisation temperature slightly influenced the morphology, the grains get bigger with temperature. The micrograph as well as the cross-

sectional image (see figure 5.12 a-f) indicate growth of compact, columnar and platelet like grain with a size which increased from 500 nm to ~2000 nm with the increase in temperature (see figure 5.13). The EDX spectrum of the sample selenised at 400 °C in 10 mbar Ar ambient is shown in figure 5.14. Notice that no oxygen was detected because the sample was allowed to naturally cool down in the low vacuum to prevent oxidation.

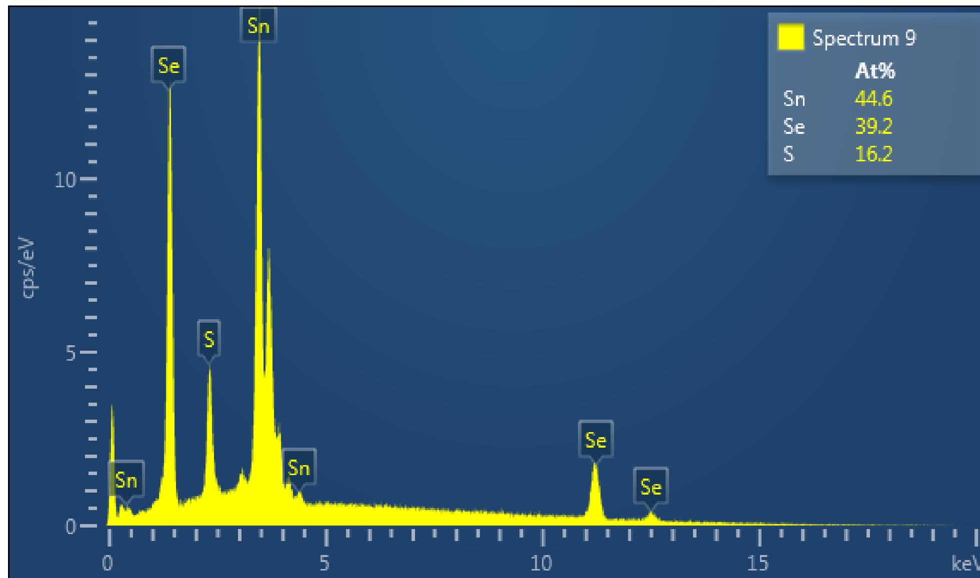

Figure 5.14 EDX spectrum of Sn(S,Se) sample selenised at 400 °C in 10 mbar Ar.

Tables 5.4 and 5.5 show the atomic composition of Sn, S and Se of the Se treated samples in high and low vacuum, respectively along with the energy bandgap estimated from optical measurement.

Table 5.4. SnS atomic composition (a) as-deposited, (b) simultaneous deposition with Se and (c) successive Se coating at high vacuum.

Sample (°C)	Sn (at %)	S (at %)	Se (at %)	Sn/(S+Se) ± 0.02	Se/(S+Se) ± 0.02	E_g (eV) ± 0.05
(a)	50.9	49.1	-	1.04	-	1.37
(b)	48.8	44.8	6.3	0.95	0.12	1.27
(c)	47.5	45.2	7.3	0.90	0.14	1.25

Table 5.5 Parameters of the selenised samples in Ar (10 mbar) for 20 min at different temperatures.

Temp. ±20 (°C)	Sn (at %)	S (at %)	Se (at %)	Sn/(S+Se) ± 0.02	Se/(S+Se) ± 0.02	E_g (eV) ± 0.05
400	44.6	16.2	39.2	0.81	0.71	1.26
450	48.3	4.2	47.5	0.93	0.92	1.25
500	46.6	3.8	49.6	0.87	0.93	1.17

For the selenised samples in high vacuum, the Se - S substitution was not effective as can be seen from table 5.4 that only about 10 - 15 % of sulphur was replaced by selenium in both co-evaporated and Se treated sample. However, significant Se - S substitution was achieved for samples annealed in low vacuum using tube furnace that was back filled with 10 mbar argon gas. As presented in table 5.5, about 70% of sulphur is replaced by selenium in the 400 °C selenisation temperature, which increase to over 90% with increase in annealing temperature. It is evident from table 5.5 that Sn(S,Se) film can be obtained with near stoichiometry for Sn and Se for the film selenised at 450 °C. This serves as one of the possible route to overcome the limitation of high sulphur deficiency in heat-treated SnS thin films. Elemental depth profiling was also performed to support EDS in assessing the Se - S substitution. The result is shown in figure 5.15 where the intensity of S and Se ions are plotted for selenisation temperature of 450 and 500 °C. In comparison with the reference sample. From the figure 5.15, it is evident that sulphur was effectively replaced by selenium in good agreement with the EDS data.

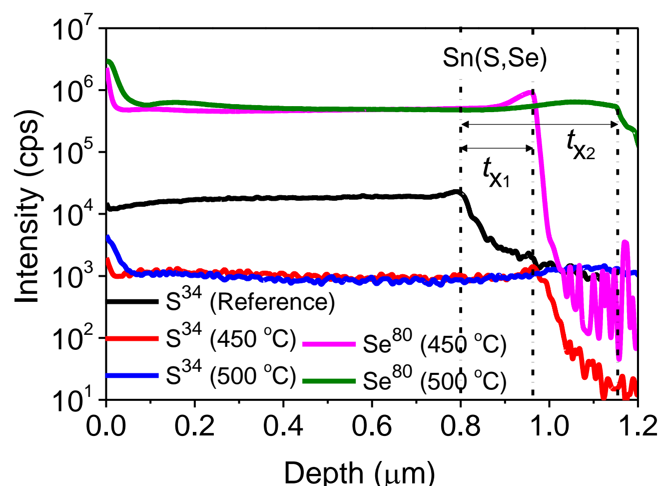

Figure 5.15 Se - S substitution in SIMS elemental depth profiles of Sn(S,Se) films (t_{x1} and t_{x2} shows change in layer thickness following selenisation at 450 and 500 °C, respectively).

The UV-Vis-NIR spectra were recorded for the Sn(S,Se) samples in the wavelength range of 300-1400 nm. The transmittance and reflectance spectra of the Se treated samples in low and high vacuum are very similar except for the layer selenised at 500 °C in the tube furnace, which exhibited a red shift in the absorption edge (see figure 5.16). From the Tauc plot shown in figure 5.16 (c and d), the plot of $(\alpha h\nu)^n$ vs $(h\nu)$ gave better fit for $n = 1/2$, indicating the films to have a direct allowed transitions. The samples exhibit lower values of energy bandgap range of 1.17 - 1.27 eV compared to the 1.37 eV of the as-deposited untreated SnS films due to the formation of Sn(S,Se), change in composition and increase in the unit cell volume. These values are similar to the reported optical bandgap range of 1.08-1.25 eV for electrodeposited and electro-synthesized Sn(S,Se) thin films [267, 268]. The reduction in the energy bandgap can be linked to S - Se exchange associated with the selenisation process, similar to its effect in chalcopyrite and kesterite materials where selenium is found to reduce energy bandgap in CZTS and CIGS.

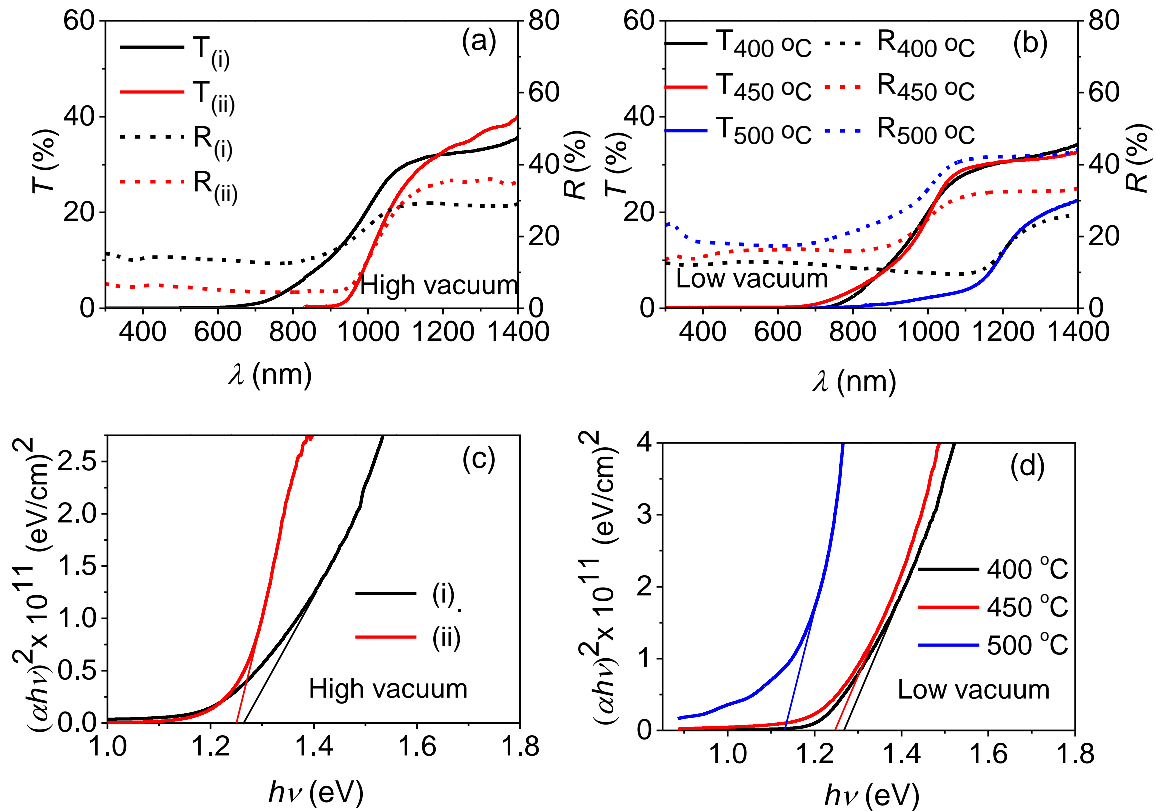

Figure 5.16 (a and b) transmittance (solid lines) and reflectance (dotted lines), (c) and (d) $(\alpha h\nu)^2$ versus $h\nu$ of Sn(S,Se), (I, ii stands for Se coating of SnS during and after deposition, respectively in high vacuum).

Figure 5.17 shows the XRD spectra of the Sn(S,Se) films. For the films selenised at high vacuum (see figure 5.17a), the diffraction peaks were found to match well with the orthorhombic SnS polycrystalline structure at 2θ values of 22.01, 26.20, 30.40, 31.54, 31.97, 39.33, 42.59, 48.91 and 66.82° corresponding to the reflection planes of (110), (120), (101), (111), (040), (041), (141), (211) and (080), respectively. In contrast to this observation, the co-evaporated SnSSe sample exhibited a modified structure with the (101) lattice plane appearing as the prominent peak and the (111), (040) planes appear to overlap. For the selenised samples in tube furnace (see figure 5.17b), the observed diffraction peaks matched well with the orthorhombic Sn(S,Se) diffraction pattern JCPDS 048-1225 [267]. The crystal structure was seen changing from randomised structure to (111) orientation with increasing selenisation temperature. The existence of SnS phase specifically the (040) plane after

selenisation cannot be ruled out, this will likely be overlapping with the (400) lattice plane of Sn(S,Se).

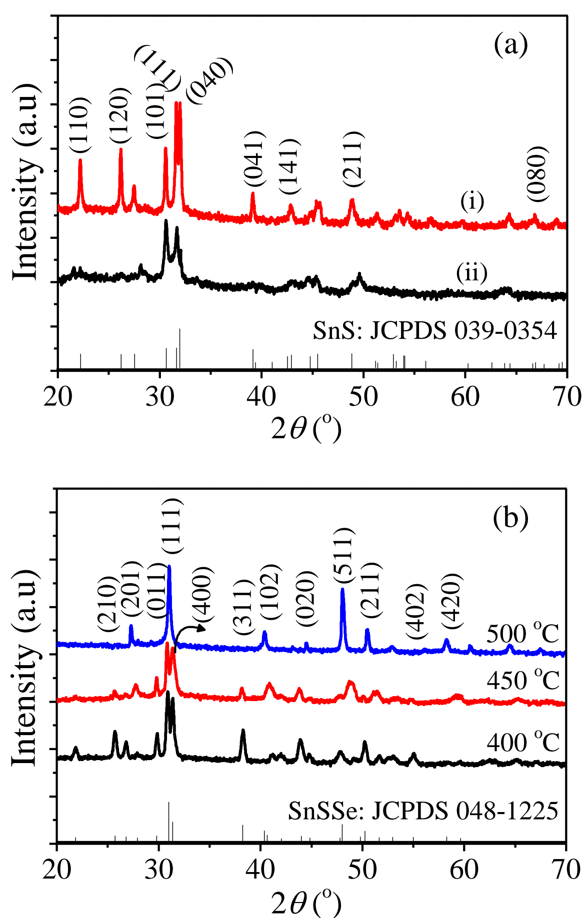

Figure 5.17 XRD spectra of selenised SnS films in (a) high vacuum and (b) tube furnace with argon ambient.

Tables 5.6 and 5.7 show the lattice parameters of Se treated samples in high and low vacuum, respectively along with the calculated unit cell volume. The lattice constants a and b are noticeably different for the SnS and Sn(S,Se) samples due to S - Se exchange. The lattice parameters for the selenised samples revealed an increase in the unit cell volume with increase in the selenisation temperature, which can be attributed to the recrystallisation effect. The increase in unit cell volume also correlate well with the decrease in bandgap listed in tables 5.4 and 5.5, which are in good agreement with the work of Makinistian and Albanesi [241].

Table 5.6 Lattice parameters of (a) as-deposited, (b) simultaneous deposition with Se and (c) successive Se coating at high vacuum.

Sample	Lattice parameters (Å)			Cell volume ± 0.03 (Å^3)
	a	b	c	
(a)	4.32	11.26	4.00	194.573
(b)	11.07	4.21	4.23	197.138
(c)	11.18	4.14	4.29	198.564

Table 5.7 Lattice parameters of the selenised samples in Ar (10 mbar) for 20 min at different temperatures.

Temperature (°C)	Lattice parameters (Å)			Cell volume ± 0.03 (Å^3)
	a	b	c	
400	11.21	4.08	4.33	198.040
450	11.23	4.07	4.35	198.822
500	11.45	4.03	4.41	203.493

The Raman spectra of the selenised sample Sn(S,Se) at 450 °C, which exhibited 90% S - Se substitution is shown in figure 5.18. The selenised sample revealed a shift in A_g and B_{2g} modes by 4.0 and 9.0 cm^{-1}, respectively towards the lower wavenumber due to the anion substitution with Se. The spectra also depicted a split of A_g mode for Sn(S,Se) at 181 and 192 cm^{-1}, which has been reported in Se based absorber materials [269].

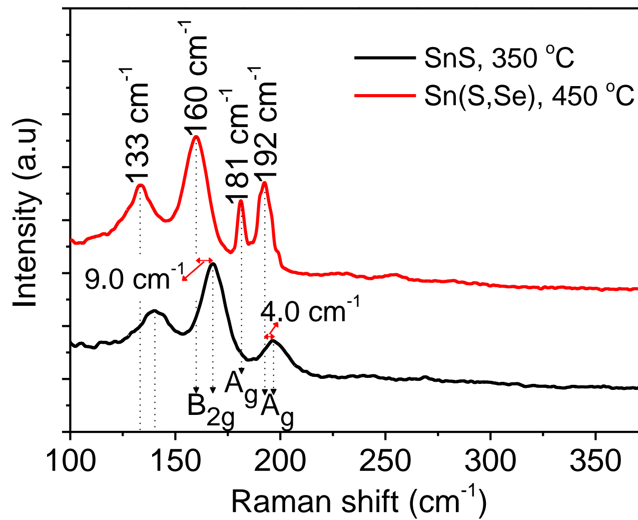

Figure 5.18 Raman spectra of as-deposited SnS and selenised Sn(S,Se) films.

Figure 5.19 shows the photoluminescence (PL) emission spectra of the selenised sample compared with the as-deposited film with photon excitation at 532 nm.

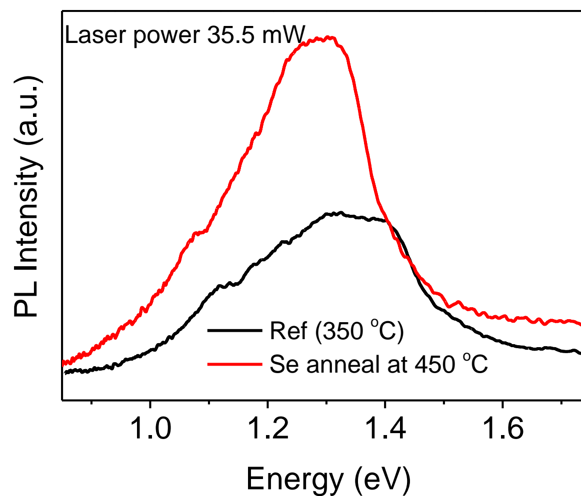

Figure 5.19 PL spectra of as-deposited and post Se annealed SnS film.

Selenium treated SnS sample shows higher potential in carrier generation and transport, it equally indicates better quality of the film due to narrowing of the peak. The shift of the peak position of the annealed sample correlates well with the observed decrease in the energy bandgap.

5.4 Conclusions

A simple and effective technique to considerably improve the grain growth of thermally evaporated SnS thin films by post-deposition heat treatment has been successfully studied. The films properties are found to be dependent on the annealing temperature and environment. Vacuum annealing were ineffective in both inducing grain growth and achieving recrystallisation. Nitrogen ambient revealed a recrystallised structure with slight increase in grain sizes and ~6% decrease in the bandgap compared to the reference 1.37 eV for the as-grown layer due to loss of sulphur (Sn/S ratio increased from 1.00 to 1.27 following anneal). The incorporation of Se under argon ambient led to substantial increase in grains with an average grain size of ~2.0 μm compared to 0.14 μm for as-grown films, with a nearly complete sulphur substitution by selenium. In addition, Se incorporation minimised voids while reducing the bandgap to 1.28 eV and improving photoluminescence yield.

Chapter 6

Role of Buffer Layer in SnS Heterojunction device

This chapter focuses on the search for best buffer layers for the fabrication of SnS solar cells. After a brief introduction in section 6.1, the properties of In_2S_3, ZnS and ZnO buffer layers that can serve as a possible replacement for toxic CdS are presented in section 6.2. The band alignment in the SnS thin film heterostructure is given in section 6.3, which was followed by devices results in 6.4 and the conclusion in 6.5.

6.1 Introduction

The alignment of the energy bands at the semiconductor heterojunctions play a significant role in the performance of thin film solar cells. Investigations on the conduction band offsets of SnS based thin films are crucial for device fabrications as band alignments determine the electrical transport properties at the interface. Cadmium sulphide (CdS) is commonly used to form SnS/CdS heterojunction but there are evidences of non-optimal conduction band offset (CBO) with CdS [42, 58, 59, 181]. SnS/CdS heterojunction has a large negative CBO of -0.5 eV, which gives rise to an increase of interface recombination [42, 181] and reduces the open circuit voltage (Voc) of the solar cell. Since a small positive CBO of the range (0 eV$<\Delta E_c<$0.1 eV) [181] is suitable to reduce the interface recombination, there is the need to optimize the use of alternative wide bandgap buffer layers such as In_2S_3, ZnO and ZnS. These alternative buffer layers have wider bandgaps than CdS, therefore devices incorporating any of these buffer layers are expected to show improved quantum efficiencies in the short-wavelength region. This can lead to a higher short-circuit current density and power conversion efficiency, as well as open circuit voltage if the band alignment is good.

In order to study the SnS band alignments, thin films of In_2S_3 and ZnS were prepared by thermal evaporation, while CdS was prepared using chemical bath deposition as described in chapter 3 subsection 3.3.1 and 3.3.4, respectively. Key optoelectronic properties of this buffer

layers were extracted from experimental data except ZnO, in addition to literature values to obtain the band alignment structures.

6.2 Properties of CdS, In_2S_3 and ZnS buffer layers

The microscopic, optical and crystallographic properties of 60 ± 10 nm thick In_2S_3 and ZnS buffer layers deposited at 200 °C have been investigated in an attempt to replace the conventional CdS and ensure a cadmium-free device as well reduce the effect of lattice mismatch at the junction formation. The substrate of 200 °C was chosen in order to promote intermixing at the SnS/n-buffer layer junction, in addition to being comparable with the post-growth heat treatment of CdS layer. Note that CdS layer was grown to a thickness of 50 ± 10 nm via CBD at bath temperature of 70 °C before being subjected to heat treatment at atmospheric pressure for 10 min at temperature of 200 °C.

The typical EDX spectra for the CdS and In_2S_3 samples are shown in figure 6.1. The atomic composition obtained from EDX analysis showed the Cd/S, In/S and Zn/S ratio to be 1.09, 0.64 and 1.03, respectively (see table 6.1). This indicates that the constituent elements is non-stoichiometric for In_2S_3 and stoichiometric for the CdS and ZnS. This further showed that ZnS and In_2S_3 can be successfully fabricated via thermal evaporation.

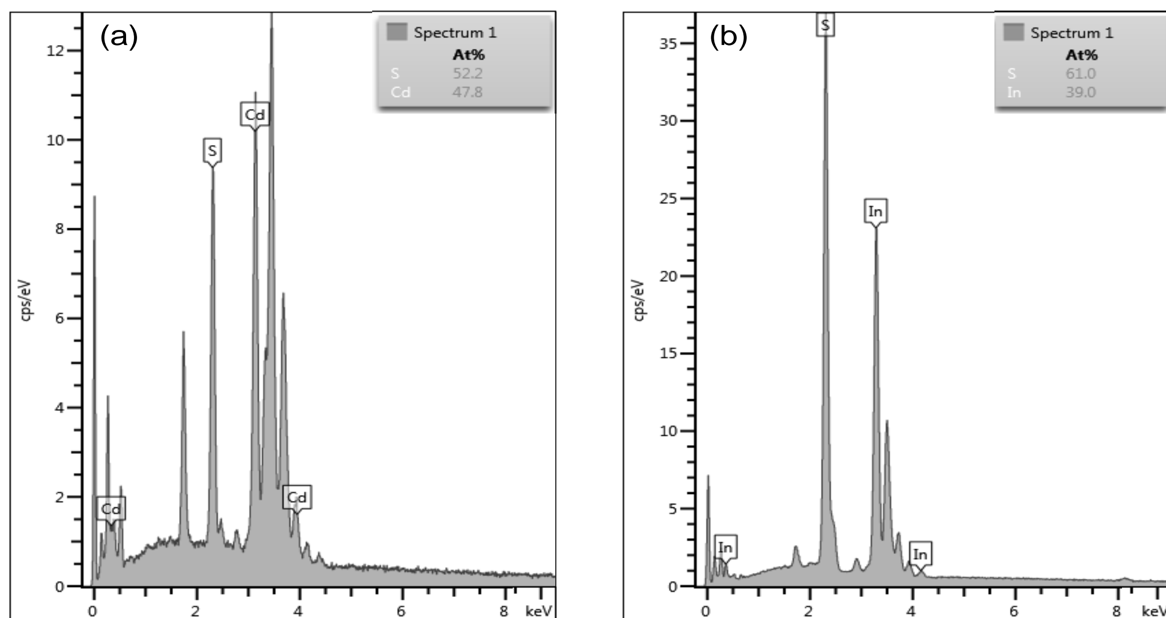

Figure 6.1 EDX spectra for the (a) CdS and (b) In_2S_3 samples.

Table 6.1. Atomic composition of the *n*-buffer layers. Notes: Cd, In and Zn in column 2 heading respectively represent the atomic percentage of the elements in first, second and third rows for CdS, In_2S_3 and ZnS. This is same with last column.

n-buffer	Cd; In; Zn (at %)	S (at %)	Cd/S; In/S; Zn/S (± 0.01)
CdS	52.2	47.8	1.09
In_2S_3	39.1	60.9	0.64
ZnS	50.8	49.2	1.03

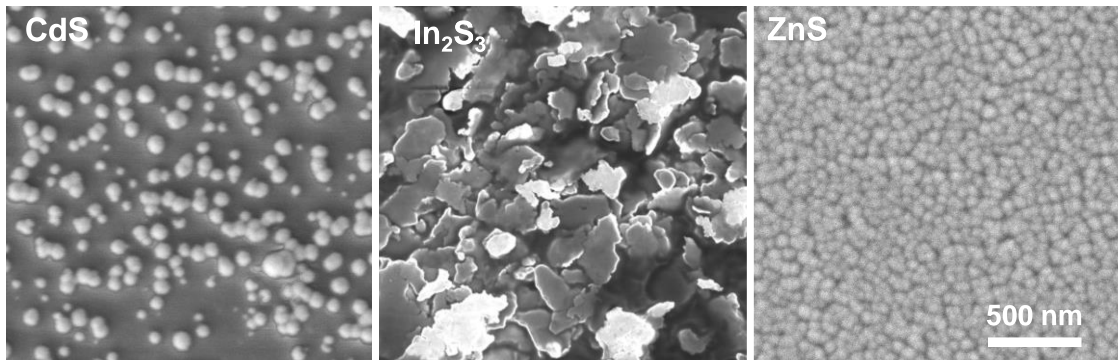

Figure 6.2 SEM micrographs (top view) of *n*-buffer layers.

The surface morphology of the CdS, In_2S_3 and ZnS thin films are shown in figure 6.2. SEM images indicate that the thin films consist of CdS and ZnS nanoparticle of circular shapes, while that of In_2S_3 exhibited nano-flakes and platelet-like shape. The average grain size from the SEM were found to be 92, 174 and 80 nm for the CdS, In_2S_3 and ZnS films, respectively. These values are greater than the excitonic Bohr radius (r_B) of 5.8 nm for CdS [270], 2.5 - 4.1 nm for In_2S_3 [271] and 2.5 nm for ZnS [272] due to agglomeration and possible coalescence of grains.

Figure 6.3 (a-c) shows the transmittance (solid line) and reflectance (dotted line) for the CdS, In_2S_3 and ZnS buffer layers. The layers were transparent in the visible and near infrared range, which are suitable for enhancing short-circuit current and device performance. In addition, it

suggests that the films can transmit higher energy photons, which corresponds to the higher energy bandgaps.

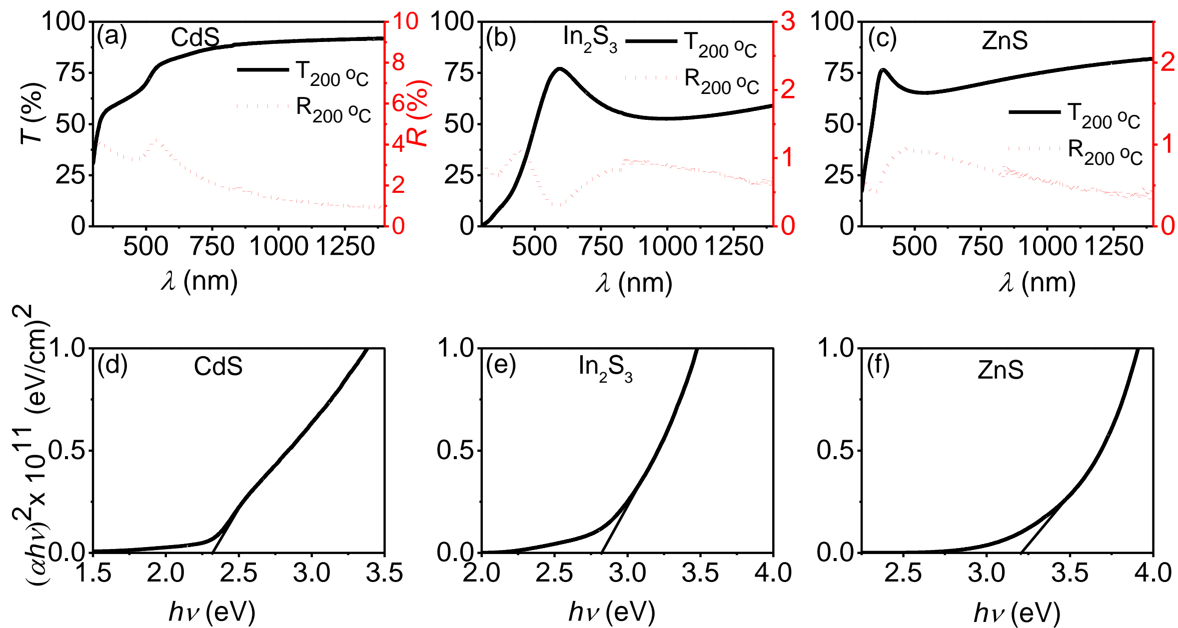

Figure 6.3 (a-c) transmittance (solid lines) and reflectance (dotted lines) and (c-d) Tauc plot of the buffer layers. Note that vertical legends in (a) and (d) remain same for (b, c) and (e, f), respectively.

Figure 6.3 (d-f) shows the extrapolation of the curve $(\alpha h\nu)^2$ versus $h\nu$ of CdS, In_2S_3 and ZnS, respectively that give the direct energy bandgap of the films. From the Tauc plot, energy bandgap of CdS, In_2S_3 and ZnS were found to be 2.34 ± 0.05, 2.82 ± 0.05 and 3.20 ± 0.05 eV, respectively. Recorded 2.34 eV energy band for CdS in this study is smaller than reported 2.38 - 2.4 eV [273, 274] due to post growth heat treatment as this can cause increase in grain size. Increase in grain size of thin films or nanoparticle is associated with lowering of energy bandgap. In_2S_3 has a direct energy bandgap value of 2.82 eV, which is similar with the maximum energy bandgap value of 2.83 eV reported in literature by Rodriguez-Hernandez *et al.* [275]. The high bandgap values can be attributed to the very thin layer of films. Similarly, ZnS exhibited energy bandgap of 3.20 eV that is comparable to other reports [276, 277] for very thin layer of ZnS. These values have advantage over the commonly used CdS that has a narrower bandgap of 2.34 eV if they can minimise the high conduction band offsets when

applied to the SnS heterojunctions. The extinction coefficient (*k*) and refractive index (*n*) of the samples were obtained using equations (4.3) and (4.4), respectively stated in chapter 4. Figure 6.4 shows the behaviour of the *k* and *n* for CdS, In_2S_3 and ZnS thin films as a function of wavelength.

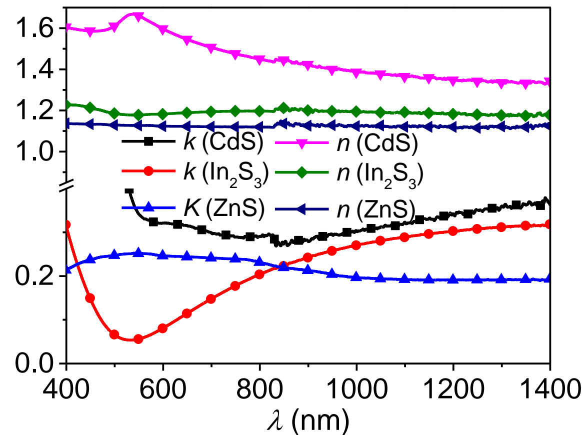

Figure 6.4 Extinction coefficient and refractive index of CdS, In_2S_3 and ZnS buffer layers.

As shown in figure 6.4, all samples exhibited low extinction coefficient (< 0.4) while, the refractive index values of 1.13, 1.22 and 1.6 are obtained for the ZnS, In_2S_3 and CdS respectively. The refractive index value for ZnS is low compared to that of In_2S_3 and CdS making this sample better buffer layer choice for making SnS-based solar cells. Refractive index of buffer should be as low as possible in order to minimise reflection of light entering the absorber layer and prevent losses in the solar cell efficiency. This is because the working efficiency of solar cells are restrained by high refractive index. For instance in silicon (Si) solar cells with high refractive index of 3.4, more than 40% of the incident light is reflected and generates losses, which significantly lessens the efficiency of the device [278, 279].

Figure 6.5 shows the XRD diffraction patterns of the CdS, In_2S_3 and ZnS thin films. CdS layer was subsequently annealed at 200 °C following deposition.

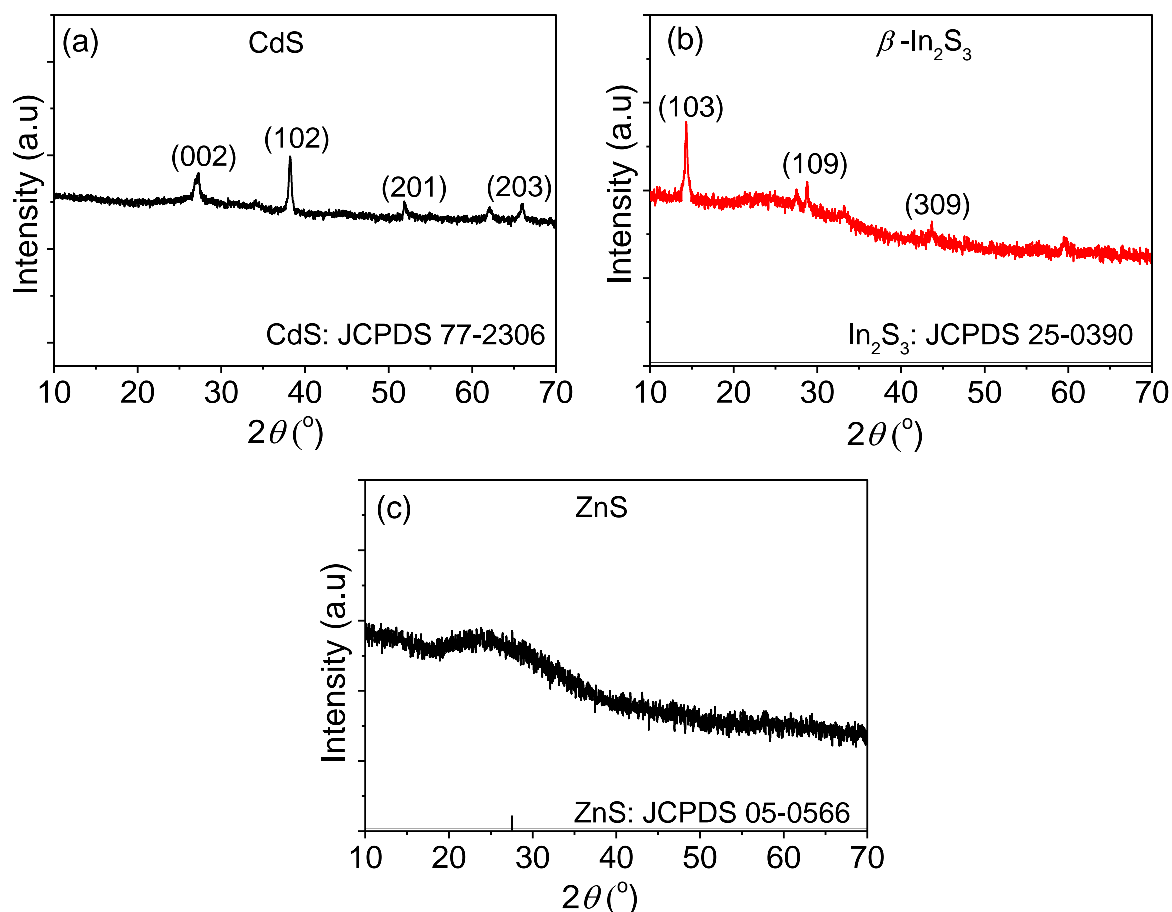

Figure 6.5 (a-c). XRD spectra of the buffer layers.

Figure 6.5 (a) shows that the CdS film has a polycrystalline structure with main characteristics reflections matching well with the JCPDS card no. 77-2306. Noticeable peaks are assigned to the (002), (102), (201) and (203) planes of the cadmium sulphide possessing hexagonal crystal structure. The relatively stronger peak along the (102) plane indicates that the CdS film is oriented along the 'c' axis. Such orientation will likely lead to significant mismatch at the interface with the SnS. Similarly, the reflections in 6.5 (b) were identified to be the tetragonal β-In_2S_3 phase matching well with JCPDS 25-0390. Notice that the layers are also polycrystalline with noticeable peaks assigned to the (103), (109) and (309) planes. Similar behaviour of In_2S_3 films has been reported in literature [280, 281]. Similar to CdS the layer is highly oriented along 'c' axis. On the other hand, ZnS thin film (see figure 7.3c) exhibited a noticeable amorphous broadening in the spectra, verifying the poor crystallinity of the film due to its being very thin and visibly high transparent.

6.3 SnS band alignment studies

Band alignment properties are critical in understanding the current-voltage mechanism of heterojunction solar cells. Few reports on the SnS band-alignments exist in the literature probably due to the novelty of this material. In heterojunction solar cells, band alignments mostly affect the electronic transport properties by acting as barriers to the charge carriers at the interface thereby limiting the power conversion efficiency. The energy band structure of the thin film heterojunction in principle depends on electron affinities, energy bandgaps and work functions of the two semiconductor layers forming the junction. In this study, the potential use of In_2S_3, ZnS and ZnO to replace the toxic CdS as buffer layer for SnS solar cell fabrication was explored. The energy band diagram was used to estimate the band offsets of both valence band (ΔE_v) and the conduction band (ΔE_c) through Anderson rule [282]. Optoelectronic parameters of SnS, ZnS , In_2S_3, CdS and ZnO were listed in chapter 3.

Since all the electron affinities are known (see table 3.1 in chapter 3), the CBO can be calculated using the Anderson model of which the shape of the band bending once the two semiconductors are at intimate contact has been predicted [24, 282]. The conduction band offset values are estimated to be -0.50, -0.35, -0.25 and 0.10 eV for the SnS/CdS, SnS/ZnO , SnS/In_2S_3 and SnS/ZnS heterostructures, respectively. The knowledge of these conduction band offset values give a good insight about the potential performance of ZnS, In_2S_3 and ZnO thin films as alternative buffer layers in SnS-based solar cells. From the calculated CBO values, a positive ΔE_C indicates that a conduction band of buffer layer is above that of SnS while, negative ΔE_C shows that a conduction band of the buffer layer is below that of SnS. The ΔE_C should be zero or small positive (≤ 0.1) for optimum performance of solar cells. Positive ΔE_C will make the photo-generated carrier to be blocked thereby reducing the *FF*, while negative ΔE_C will lead to lowering of *FF* and V_{oc} because of carrier recombination at the interface [283, 284]

The band alignment at the interface of the SnS/n-buffer heterostructures are obtained at thermodynamic equilibrium. The plots of which before and after intimate contact are shown in figure 6.6 and 6.7, respectively, where E_o, E_c, E_v and E_f are the vacuum energy level, conduction band minima, valence band maxima and Fermi level, respectively.

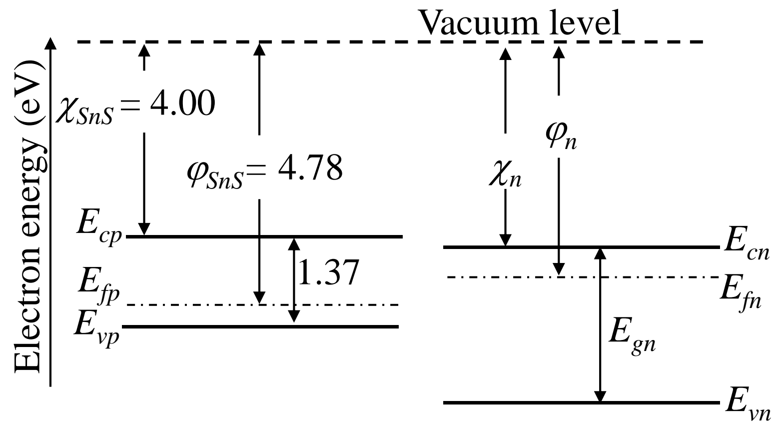

Figure 6.6 Energy band diagram of SnS and *n*-buffer films before the formation of the *p*-*n* heterojunction (all numbers in eV).

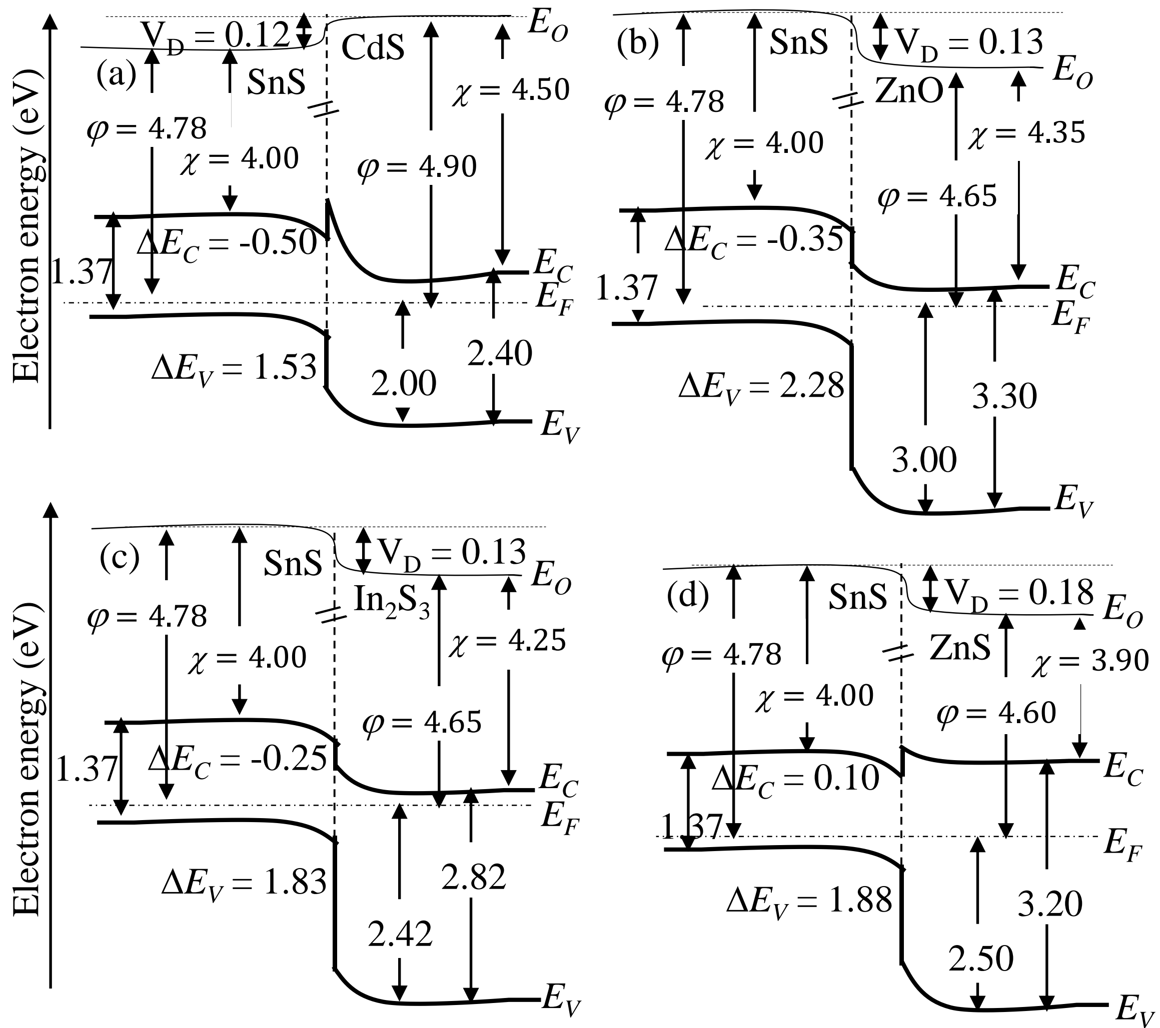

Figure 6.7 Energy band diagrams for SnS thin film heterojunction in equilibrium condition with (a) SnS/CdS, (b) SnS/ZnO, (c) SnS/ $In_2S_3$and (d) SnS/ZnS interface. All numbers in eV.

As shown in figure 6.7, there exists electron barrier in all the interfaces that can potentially limit the photovoltaic performance of the devices. The SnS/CdS interface (see figure 6.7a) has a staggered type II heterostructure and a high conduction band offset of -0.50 eV with a spike-like barrier that in theory will block the drift of photo-generated electron across the interface and lead to the degraded collection efficiency. Similar value and type II structure at SnS/CdS has been reported in the literature for SnS/CdS heterojunction [59, 132, 181].

Similarly, SnS/ZnO and SnS/In_2S_3 junctions (see figure 6.7b and 6.7c) exhibited staggered type II structure with a cliff-like barrier at their interface, which are equally detrimental to device

performance. In this kind of structure, most of the carrier may tend to recombine around the interface. Therefore, it can be suggested that the SnS/CdS, SnS/In_2S_3 and SnS/ZnO hetero-structures cannot get desirable photovoltaic performances. On the other hand, the SnS/ZnS interface (see figure 6.7d) tends to form a straddled type I structure with a small ΔE_C of 0.1 eV suggesting the effectiveness of this junction to reduce the interface recombination in the SnS-based solar cell.

Further analysis of the SnS band alignment with n-buffer layer was performed using solar cell capacitance simulator (SCAPS), which is a dedicated software for photovoltaic device analysis [177]. Key input simulation parameters were listed in chapter 3. Figure 6.8 show the simulated energy band diagrams of the SnS/CdS, SnS/ZnO , SnS/In_2S_3 and SnS/ZnS heterostructures.

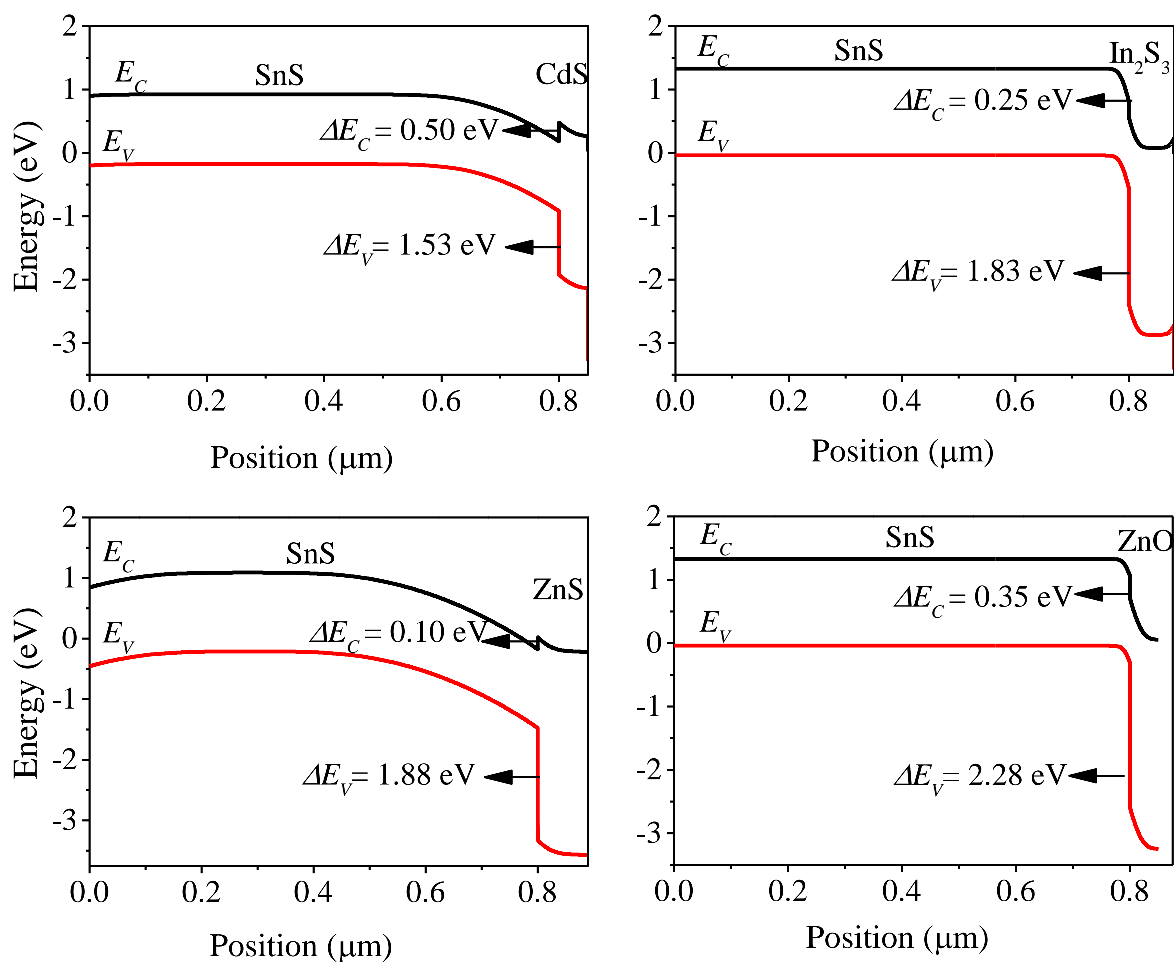

Figure 6.8 Simulated energy band diagrams of SnS heterojunctions.

As shown in figure 6.8, the simulated energy band diagrams show similar features to the theoretical structures shown in figure 6.7. For the cliff like band alignment in the CBO of SnS/In_2S_3 and SnS/ZnO where the band edge of In_2S_3 and ZnO are below that of SnS, the potential difference that can be generated between the quasi-Fermi levels at the interface under illumination will be limited. This barrier can lead to increase of recombination between majority carriers that can result in reduction of the open circuit voltage and fill factor [285]. The spike like alignment structure in the CBO of SnS/CdS and SnS/ZnS can be less detrimental to open circuit voltage. However, the high ΔE_C of the SnS/CdS (-0.5 eV) interface will block the photo-generated electrons from crossing over the spike barrier while that of SnS/ZnS (0.1 eV) can easily allow drift of photo-generated electrons [285, 286]. Therefore, selection of suitable n-buffer layer is crucial in realising good efficiencies, using SnS absorber layer and ZnS could be one of the potential buffer layers for fabricating SnS-based photovoltaic solar devices. ZnS is therefore the preferable buffer layer for fabrication of SnS solar cells due to its optimal ΔE_C of 0.1 eV.

6.4 SnS device properties

The solar cell device in substrate configuration were characterised using an illuminated current density-voltage (J-V) characteristics under a simulated (Air Mass 1.5) spectrum. For the simulated device, the governing principle of SCAPS software and characterisation processes are stated in chapter 3, experimental section. The simulation is done to access the optimal performance of SnS based solar cell with alternative buffer layers of ZnS, In_2S_3 and ZnO to replace the conventional CdS. The main input simulation parameters are stated in the experimental section, chapter 3 in table 3.1 and by introducing these into SCAPS for the buffer layers, changes in the values of efficiency (η), open circuit voltage (V_{OC}), short circuit current (J_{SC}) and fill factor (FF) were observed. Figure 6.9 shows the current-voltage characteristics of the SnS/n-buffer heterojunction under illumination, while the corresponding V_{OC}, J_{SC}, FF and η are listed in table 6.2.

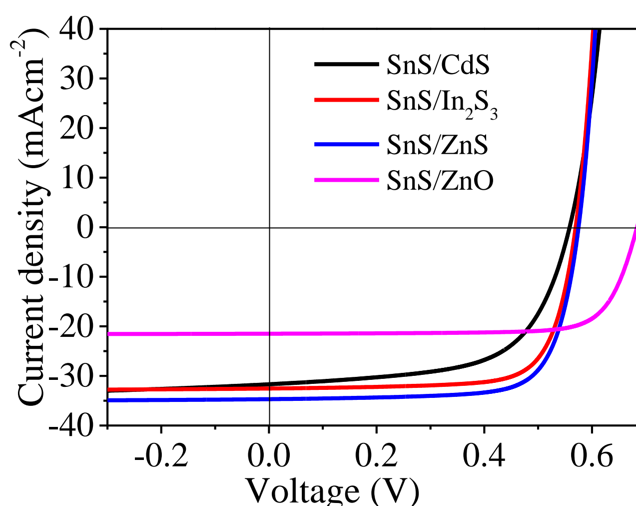

Figure 6.9 Current density - voltage curves of simulated SnS/n-buffer layer heterojunctions under standard AM 1.5 illumination.

Table 6.2. The photovoltaic properties of different simulated SnS heterojunction solar cells

Heterojunction	$V_{OC} \pm 10$ (mV)	$J_{SC} \pm 2$ (mAcm^{-2})	$FF \pm 5.0$(%)	$\eta \pm 0.2$ (%)
SnS/CdS	537	32.6	60.93	6.92
SnS/In_2S_3	562	32.8	54.92	7.35
SnS/ZnS	578	35.0	58.77	7.81
SnS/ZnO	682	21.0	48.91	5.62

Note that interface defects are introduced in the simulation in order to bring the simulation results closer to the physical experiments. These defect states normally degrade the photovoltaic properties of the cells by acting as a carrier recombination centre thereby limiting the photo-generated carrier.

For the fabricated devices, the optimised SnS thin films (described in section 4.3) were incorporated into solar cell using the four different buffer layers in substrate configuration: SLG/Mo/SnS/CdS/i-ZnO/ITO/Ni-Al with CdS subsequently replaced with ZnS, In_2S_3 and ZnO. The CdS buffer layer was prepared using chemical bath deposited described in section 3.3.4, ZnO deposited with pulse DC magnetron sputtering stated in section 3.3.2 while, ZnS and

In_2S_3 deposited using similar method stated in section 4.2. The detailed device fabrication processes are given in chapter three (section 3.5). Figure 6.10 (a) and (b) shows a typical cross-sectional SEM image and a photo of the completed device in substrate configuration.

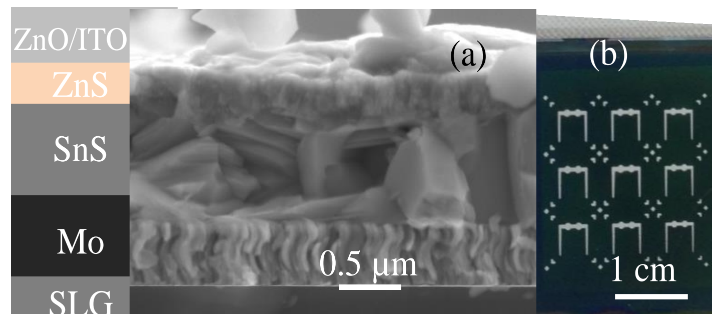

Figure 6.10 (a) cross sectional SEM image of a fabricated device and (b) top-view photo of a typical fabricated solar cell in substrate configuration with nine 0.16 cm^2 devices.

The data from the *J-V* measurements were used to extract the photovoltaic properties such as the open circuit voltage, short circuit current, fill factor and efficiency. The *J-V* curves of the different heterojunction devices are shown in figure 6.11 with the device parameters extracted from the data summarised in table 6.3.

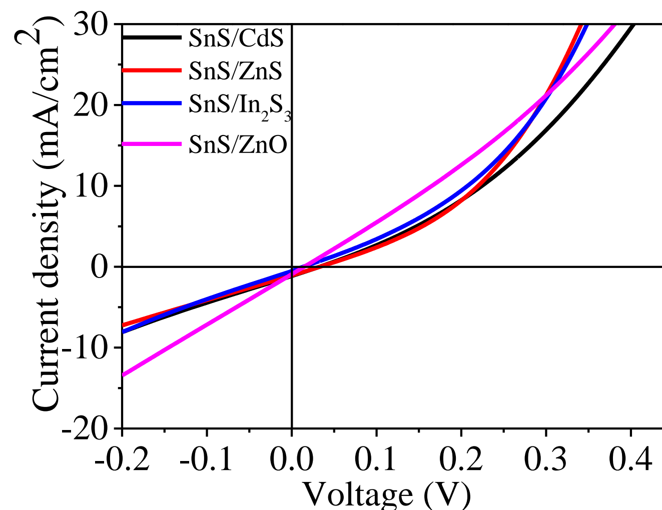

Figure 6.11 *J-V* curves of fabricated SnS/n-buffer layer heterojunctions under standard AM 1.5 illumination.

Table 6.3 Photovoltaic properties of different fabricated SnS heterojunction solar cells

Heterojunction	$V_{OC} \pm 2$ (mV)	$J_{SC} \pm 0.5$ (mAcm^{-2})	$FF \pm 2.0$(%)	$\eta \pm 0.01$ (%)
SnS/CdS	31	8.1	25.7	0.17
SnS/ZnS	32	8.0	32.7	0.20
SnS/ In_2S_3	10	8.5	21.2	0.02
SnS/ZnO	10	13.0	32.2	0.04

Notice from table 6.3 that the devices were inefficient with the SnS/CdS and SnS/ZnS devices showing similar photovoltaic characteristics of open circuit voltage, short circuit current, fill factor, efficiency of 31 mV, 8.1 mAcm^{-2}, 25.7%, 0.17% and 32 mV, 8.0 mAcm^{-2}, 32.7%, 0.20%, respectively. However, the device incorporating ZnS exhibited improved conversion efficiency and fill factor compared to devices using CdS, ZnO and In_2S_3 buffer layer. These values are within the range reported in the literature with similar technique [287]. This shows that SnS based thin films solar cell devices free of cadmium is feasible with ZnS. Quantum efficiencies were not measured as the devices are inefficient. The low open circuit voltage recorded across the device structures are due to high carrier recombination through defects at the p-SnS/n-buffer interface resulting in very low efficiency.

However, attempt was also made to improve device performance by incorporating selenium in the post-deposition annealing treatment. Note that at selenisation temperature of 450 ^{o}C for 20 min under 10 mbar argon pressure led to near complete S-Se substitution and stoichiometric Sn/Se atomic composition. From the Schockley-Queisser efficiency limits shown in literature (chapter 2, figure 2.4), S-Se cation exchange has been found to increase the efficiency of devices such as CZTS and CIGS. For examples 11.0% efficiency of CZTS was increased to 12.6% by S-Se substation [14]. *J-V* curves of one of the SnS devices fabricated following S-Se substitution and incorporation ZnS buffer layer is shown in figure 6.12.

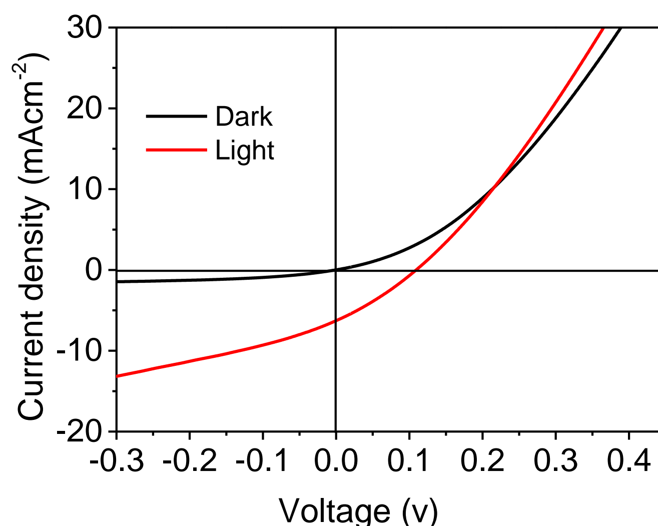

Figure 6.12 *J-V* curves of devices incorporating selenium.

The photovoltaic parameters can be derived from the figure 6.12 which include V_{oc} = 110 ± 2 mV, J_{sc} = 13.1 ± 0.5 mAcm^{-2}, FF = 33.5 ± 2% and η = 0.43 ± 0.01%. All devices fabricated following selenisation at temperature of 450 °C showed similar photovoltaic characteristics. The device is still inefficient but the improvement in the open circuit voltage shows that selenising SnS absorber layer can lead to good intermixing at the junction and reduce interface recombination. Further improvement in this direction can guarantee enhancement of photovoltaic performance of SnS solar cells.

6.5 Conclusions

The energy band discontinuities for the SnS/CdS, SnS/In_2S_3, SnS/ZnO and SnS/ZnS heterojunctions and their influence on the photovoltaic properties was investigated. The estimated conduction band offsets were -0.50, -0.35, -0.25 and 0.10 eV, while the valence band offsets were 1.53, 2.28, 1.83 and 1.88 eV for the SnS/CdS, SnS/ZnO , SnS/In_2S_3 and SnS/ZnS heterostructures, respectively. The high negative values of the conduction band offsets will block the collection of photo-generated carrier, which has negative effect on the photovoltaic properties. From the input parameters and device fabrication, SnS/ZnS heterojunction exhibits the highest conversion efficiency of 7.81 and 0.20% for the simulated and fabricated device, respectively. Therefore, ZnS has potential to replace CdS in the SnS-

based solar cell devices and further optimising the quality of the ZnS layer to minimise the interface defects can lead to improved photovoltaic performance.

Chapter 7

Conclusions

This chapter summarises the work done during this study with suggestions for further work to develop SnS solar absorbing thin films into a more efficient technology.

7.1 Thesis summary

This thesis details the deposition and optimisation of SnS solar absorbing thin films. This study specifically investigated the effect of three aspects of deposition parameters on thermally evaporated SnS solar absorbers. These were (a) the role of the SnS layer thickness, (b) the control of stoichiometry via change in substrate temperature and (c) the type of substrate material, which may alter the quality of the SnS films. In addition, emphasis was placed on promoting further recrystallisation in the SnS thin film via post-annealing treatments and sulphur-selenium substitution. A brief description of the range of deposition and characterisation methods used were explained in chapter 3.

In chapter 4, following numerical simulation to provide improved insight on the absorber layer thickness, SnS thin films were successfully deposited to thickness range of 100 - 3500 nm at constant substrate temperature of 100 ^{o}C. The SnS films had randomly oriented needle and rice-like grains, which showed a progressive increase in grain size with increasing film thickness from 100 to 1500 nm. Above the 1500 nm thickness no further visible increase in the grains can be seen. The layer atomic composition showed a marginal difference for film thickness $\leq$ 800 nm, thereafter it varied with a considerable difference. All the layers had *p*-type conductivity except the ultrathin 100 nm layer, which showed *n*-type conductivity. For all the thicknesses, the SnS films depicted a high absorption coefficient (> 10^4 cm^{-1}) in the visible light region. Films grown to a thickness of 800 nm was found to be near stoichiometry with optimum energy bandgap compared to the thinner or thicker films.

In addition, the effect of substrate temperature on the microscopic, optical and crystallographic properties of SnS films were systematically investigated. The temperature dependent study revealed that higher substrate temperatures led to an increase in adatoms mobility, which promoted coalescences of smaller grains to form bigger grains. The increase in grain size with substrate temperature however stagnated after 350 °C such that further increase in temperature added no impact. As the substrate temperature increases, the Sn/S atomic composition range of 0.89 - 1.10 showed that the SnS absorber layer became poorer in sulphur. Secondary phases such as SnS_2 and Sn_2S_3 are formed at lower substrate temperatures (< 200 °C), while temperatures greater than 200 °C had only polycrystalline SnS phase. The energy bandgap of films were significantly influenced by the changing atomic composition. Only the SnS film deposited at 350 °C substrate temperature was stoichiometric (Sn/S = 1.00) and had energy bandgap of 1.37 eV. The crystallography of the films revealed that (111) diffraction plane is more likely associated with the substrate temperatures ≤ 300 °C while, the (040) diffraction plane is related to higher substrate temperatures (≥350 °C). Photoluminescence measurement demonstrated that controlling the film composition and optical bandgap to some extent is critical to produce a film that will luminesce, a requisite for any implementation in solar devices.

The substrate dependent experiments included in chapter 4 demonstrated that films properties are strongly influenced by the type of substrate material used. Films on SLG, quartz and ITO exhibited strong (040) preferred orientation, while those on Mo coated SLG and quartz showed (111) preferred orientation. On the other hand, for the films deposited on FTO, the crystal structure became randomised. No secondary phase was detected across the substrates. A slight increase of about 3% was measured for the energy bandgap of films deposited on Na-free substrate of quartz, ITO and FTO compared to the reference 1.37 eV for the film deposited on SLG. SEM analysis reveals randomly oriented rice and flake-like small grains in the films deposited on SLG and Mo coated SLG, while the grain shape changed to flakes and platelet-like structure when grown on ITO and FTO with noticeable grain growth. The films on both

quartz and Mo coated quartz substrates showed uniformly distributed bigger grains with less void over the substrate surface. Unlike kesterite or chalcopyrite materials, the absence of Na in the substrate induces a significant grain growth in SnS thin films with the average grain size increasing from 0.14 μm on SLG to ~0.32 μm on quartz, ITO and FTO.

Chapter 5 focused on optimisation of the films via post-annealing treatments in diverse environment. The as-deposited 800 nm thick film at 350 °C were subjected to heat treatment in diverse environments such as vacuum, N_2 and Se for temperatures greater than the growth temperature. The crystallographic, optical and microscopic properties of the films were found to be dependent on the annealing temperature and environment. Vacuum annealing were ineffective in both inducing grain growth and achieving recrystallisation. N_2 ambient revealed a recrystallised structure with slight increase in grain sizes and a 6% decrease in the energy bandgap compared to the reference 1.37 eV for the as-grown layer due to loss of sulphur (Sn/S ratio increased from 1.00 to 1.27 following anneal). The incorporation of Se led to substantial increase in grains with an average grain size of 2.0 μm compared to 0.14 μm for as-grown films, with a nearly complete sulphur substitution by selenium {(Se/(S+Se) = 0.92)}. In addition, Se incorporation minimised voids while reducing the bandgap to 1.28 eV and improving photoluminescence yield.

Finally, the search for best buffer layers to replace the traditional CdS for the fabrication of SnS solar cells is presented in chapter 6. This was followed by band alignment studies and numerical simulation of *J-V* characteristics using SCAPS. To achieve this, properties of thermally evaporated In_2S_3 and ZnS are investigated. Atomic composition ratio of 1.07 and 0.64 for Zn/S and In/S showed that a good quality ZnS and In_2S_3 thin film buffer layers, respectively can be obtained via thermal evaporation. The higher energy bandgap values of 3.35 and 2.85 eV gave ZnS and In_2S_3, respectively advantage over the commonly used CdS that has a narrower energy bandgap of 2.4 eV. CBO calculations showed that only the SnS/ZnS interface had small postive value (ΔE_C = 0.1 eV), since high negative CBO can block the collection of photo-generated carrier, which has negative effect on the photovoltaic

properties, it can be said that ZnS is the best choice. SnS/ZnS heterojunction also exhibited the highest conversion efficiency of 7.81% for the simulated device and a device with this strutcure was fabricated. Therefore, ZnS has potential to replace CdS in the SnS-based solar cell devices and further optimising the quality of the ZnS layer to minimise the interface defects can lead to improved photovoltaic performance.

7.2 Suggestions for future works

Following the work presented in this thesis, a number of research challenges remain and more investigation is required to further improve the quality and performance of SnS thin films and devices. The following experiments can be further explored:

- Develop suitable surface etching for SnS solar absorber layer to passivate the surface, reduce interface and surface recombination effects in SnS solar cells.
- The influence of the post-deposition annealing treatments on electrical and electronic properties, as well as the possible diffusion of impurities to the SnS solar absorber layer can be further investigated.
- Notice chlorine treatment led to recrystallised layers but too aggressive as it caused deep fractures, further investigations should be carried out using different concentrations of $SnCl_2$ or $MgCl_2$. This can also be extended to SnS/ZnS layer stack.
- Optimising the alternative buffer layers studied in this work via variation of their constituent elements (Zn_xS_y) and (In_xS_y). The buffer layer, if optimised, can lower the CBO, give good band alignment and enhance the transport of photo-generated carriers.
- Further post-deposition annealing studies in selenium environment is needed to fully optimise its influence of lowering interface recombination.

List of references

[1] F. Creutzig, P. Agoston, J. C. Goldschmidt, G. Luderer, G. Nemet, and R. C. Pietzcker, "The underestimated potential of solar energy to mitigate climate change," *Nature Energy,* vol. 2, p. 17140, 2017.

[2] S. S. Hegde, A. G. Kunjomana, M. Prashantha, C. Kumar, and K. Ramesh, "Photovoltaic structures using thermally evaporated SnS and CdS thin films," *Thin Solid Films,* vol. 545, no. 0, pp. 543-547.

[3] L. M. Peter, "Towards sustainable photovoltaics: the search for new materials," *Philosophical Transactions of the Royal Society A: Mathematical, Physical and Engineering Sciences,* vol. 369, no. 1942, pp. 1840-1856, 2011.

[4] M. Moalem, "We could power the entire world by harnessing solar energy from 1% of the sahara," Quora, Ed., ed: Forbes Media LLC, 2016.

[5] N. S. Lewis, "Powering the Planet," *MRS Bulletin,* vol. 32, no. 10, pp. 808-820, 2007.

[6] R. W. Miles, K. M. Hynes, and I. Forbes, "Photovoltaic solar cells: An overview of state-of-the-art cell development and environmental issues," *Progress in Crystal Growth and Characterization of Materials,* vol. 51, no. 1, pp. 1-42, 2005.

[7] A. G173-03. Standard Tables for Reference Solar Spectral Irradiances: Direct Normal and Hemispherical on 37° Tilted Surface.

[8] C. Honsberg and S. Bowden. (2019). *Photovoltaic education network* Available: https://www.pveducation.org/index.php

[9] N. M. Haegel *et al.*, "Terawatt-scale photovoltaics: Trajectories and challenges," *Science,* vol. 356, no. 6334, pp. 141-143, 2017.

[10] L. B. Lauryn, Z. Pawel, L. Stephan, S. T. Eric, and Z. Andriy, "A review of defects and disorder in multinary tetrahedrally bonded semiconductors," *Semiconductor Science and Technology,* vol. 31, no. 12, p. 123004, 2016.

[11] A. E. Becquerel, "Mémoires sur les effets électriques produits sous l'influence des rayons solaires," *Comptes Rendus de l'Academie des Sciences,* vol. 9, pp. 561-567, 1839.

[12] D. A. Jenny, J. J. Loferski, and P. Rappaport, "Photovoltaic effect in GaAs pn junctions and solar energy conversion," *Physical Review,* vol. 101, no. 3, pp. 1208-1209, 1956.

[13] R. W. Miles, G. Zoppi, and I. Forbes, "Inorganic photovoltaic cells," *Materials Today,* vol. 10, no. 11, pp. 20-27, 2007.

[14] M. A. Green *et al.*, "Solar cell efficiency tables (Version 53)," *Progress in Photovoltaics: Research and Applications,* vol. 27, no. 1, pp. 3-12, 2019.

[15] M. Devika *et al.*, "Microstructure dependent physical properties of evaporated tin sulfide films," *Journal of Applied Physics,* vol. 100, no. 2, p. 023518, 2006.

[16] C. Hu and R. M. White, Solar cells: from basic to advanced systems New York: Mc Graw-Hill, 1983, p. 294.

[17] A. Luque and S. Hegedus, *Handbook of photovoltaic science and engineering*, 2nd ed. Chichester, West Sussex, U.K.: Wiley, 2011, p. 1132.

[18] B. V. Zeghbroeck, Principles of semiconductor devices 2011. Available: http://ecee.colorado.edu/~bart/book/book/title.htm. Accessed on 23/01/2019.

[19] S. M. Sze and M. K. Lee, *Semiconductor devices: physics and technology*, 3rd ed. New York: John Wiley & Sons, Inc., 2012.

[20] R. F. Pierret and G. W. Neudeck, *Modular series on solid state devices: Advanced semiconductor fundamentals* 2nd Edition ed. Upper Saddle River, New Jersey Pearson Education, Inc., 2002.

[21] U. K. Mishra and J. Singh, *Semiconductor device physics and design* Dordrecht, Netherlands: Springer, 2008, p. 559.

[22] R. L. Anderson, "Experiments on Ge-GaAs heterojunctions," *Solid-State Electronics,* vol. 5, no. 5, pp. 341-351, 1962.

[23] W. G. Oldham and A. G. Milnes, "Interface states in abrupt semiconductor heterojunctions," *Solid-State Electronics,* vol. 7, no. 2, pp. 153-165, 1964.

[24] B. L. Sharma and R. K. Purohit, *Semiconductor heterojunctions* Pergamon Press, 1974.

[25] B. Qi and J. Wang, "Fill factor in organic solar cells," *Physical Chemistry Chemical Physics,* vol. 15, no. 23, pp. 8972-8982, 2013.

[26] N. M. Mangan *et al.*, "A path to 10% efficiency for tin sulfide devices," in *IEEE 40th Photovoltaic Specialist Conference (PVSC)*, Denver, USA, 2014, pp. 2373-2378.

[27] Y. Qu, G. Zoppi, and N. S. Beattie, "Selenization kinetics in Cu2ZnSn(S,Se)4 solar cells prepared from nanoparticle inks," *Solar Energy Materials and Solar Cells,* vol. 158, pp. 130-137, 2016.

[28] P. Sinsermsuksakul *et al.*, "Overcoming efficiency limitations of SnS-based solar cells," *Advanced Energy Materials,* p. 1400496, 2014.

[29] T. Jiang and G. A. Ozin, "New directions in tin sulfide materials chemistry," *Journal of Materials Chemistry,* 10.1039/A709054D vol. 8, no. 5, pp. 1099-1108, 1998.

[30] G. Barone *et al.*, "Deposition of tin sulfide thin films from tin(iv) thiolate precursors," *Journal of Materials Chemistry,* vol. 11, no. 2, pp. 464-468, 2001.

[31] R. Herzenberg, "Kolbeckin, Sn_2S_3, ein neues Zinnmineral," *CentralBlatt fuer Mineralogie, A,* pp. 345-355, 1932.

[32] P. Woulfe, "Experiments to show the nature of aurum mosaicum," *Philosophical Transactions, the Royal Society, London,* vol. 61, pp. 114-130, 1771.

[33] J. S. Anderson and M. J. Ridge, "Distribution equilibria in the system tin-stannous sulphide," *Transactions of the Faraday Society,* vol. 39, no. 0, pp. 93-98, 1943.

[34] W. Albers, C. Haas, H. J. Vink, and J. D. Wasscher, "Investigations on SnS," *Journal of Applied Physics,* vol. 32, pp. 2220-2225, 1961.

[35] H. Wiedemeier and F. Csillag, "The thermal expansion and high temperature transformation of SnS and SnSe," *Zeitschrift für Kristallographie - Crystalline Materials,* vol. 149, no. 1-2, pp. 17-29, 1979.

[36] H. Noguchi, A. Setiyadi, H. Tanamura, T. Nagatomo, and O. Omoto, "Characterization of vacuum-evaporated tin sulfide film for solar cell materials," *Solar Energy Materials and Solar Cells,* Article vol. 35, no. C, pp. 325-331, 1994.

[37] N. K. Reddy and K. T. R. Reddy, "Tin sulphide films for solar cell application," in *26th IEEE Photovoltaic Specialists Conference* Anaheim, CA, USA, 1997, pp. 515-518.

[38] C. Cifuentes, M. Botero, E. Romero, C. Calderón, and G. Gordillo, "Optical and structural studies on SnS films grown by co-evaporation," *Brazilian Journal of Physics,* vol. 36, pp. 1046-1049, 2006.

[39] R. W. Miles, O. E. Ogah, G. Zoppi, and I. Forbes, "Thermally evaporated thin films of SnS for application in solar cell devices," *Thin Solid Films,* vol. 517, no. 17, pp. 4702-4705, 2009.

[40] V. R. M. Reddy, S. Gedi, B. Pejjai, R. KotteTulasi Ramakrishna, G. Zoppi, and C. Park, "Influence of Different Substrates on the Properties of Sulfurized SnS Films," *Science of Advanced Materials,* vol. 8, no. 1, pp. 247-251, 2016.

[41] S. S. Hegde, A. G. Kunjomana, P. Murahari, B. K. Prasad, and K. Ramesh, "Vacuum annealed tin sulfide (SnS) thin films for solar cell applications," *Surfaces and Interfaces,* vol. 10, pp. 78-84, 2018.

[42] L. Sun, R. Haight, P. Sinsermsuksakul, S. Bok Kim, H. H. Park, and R. G. Gordon, "Band alignment of SnS/Zn(O,S) heterojunctions in SnS thin film solar cells," *Applied Physics Letters,* vol. 103, no. 18, 2013.

[43] M. Parenteau and C. Carlone, "Influence of temperature and pressure on the electronic transitions in SnS and SnSe semiconductors," *Physical Review B,* vol. 41, no. 8, pp. 5227-5234, 1990.

[44] N. Sato, M. Ichimura, E. Arai, and Y. Yamazaki, "Characterization of electrical properties of SnS thin films prepared by the electrochemical deposition method," in *3rd World Conference on Photovoltaic Energy Conversion*, Osaka, Japan, 2003, vol. 1, pp. 38-41.

[45] O. E. Ogah, G. Zoppi, I. Forbes, and R. W. Miles, "Thin films of tin sulphide for use in thin film solar cell devices," *Thin Solid Films,* vol. 517, no. 7, pp. 2485-2488, 2009.

[46] N. Sato, M. Ichimura, E. Arai, and Y. Yamazaki, "Characterization of electrical properties and photosensitivity of SnS thin films prepared by the electrochemical deposition method," *Solar Energy Materials and Solar Cells,* vol. 85, no. 2, pp. 153-165, 2005.

[47] K. T. Ramakrishna Reddy, N. Koteswara Reddy, and R. W. Miles, "Photovoltaic properties of SnS based solar cells," *Solar Energy Materials and Solar Cells,* vol. 90, no. 18, pp. 3041-3046, 2006.

[48] N. K. Reddy and K. T. R. Reddy, "Optical behaviour of sprayed tin sulphide thin films," *Materials Research Bulletin,* vol. 41, no. 2, pp. 414-422, 2006.

[49] M. Leach, K. T. R. Reddy, M. V. Reddy, J. K. Tan, D. Y. Jang, and R. W. Miles, "Tin Sulphide Thin Films Synthesised using a Two Step Process," *Energy Procedia,* vol. 15, pp. 371-378, 2012.

[50] M. Calixto-Rodriguez, H. Martinez, A. Sanchez-Juarez, J. Campos-Alvarez, A. Tiburcio-Silver, and M. E. Calixto, "Structural, optical, and electrical properties of tin sulfide thin films grown by spray pyrolysis," *Thin Solid Films,* vol. 517, no. 7, pp. 2497-2499, 2009.

[51] T. H. Sajeesh, A. R. Warrier, C. S. Kartha, and K. P. Vijayakumar, "Optimization of parameters of chemical spray pyrolysis technique to get n and p-type layers of SnS," *Thin Solid Films,* vol. 518, no. 15, pp. 4370-4374, 2010.

[52] J. Vidal *et al.*, "Band-structure, optical properties, and defect physics of the photovoltaic semiconductor SnS," *Applied Physics Letters,* vol. 100, no. 3, p. 032104, 2012.

[53] P. Nwofe, K. Reddy, and R. Miles, "Type conversion of p-SnS to n-SnS using a $SnCl_4/CH_3OH$ heat treatment," presented at the 39th IEEE Photovoltaic Specialists Conference, Tampa, Florida, 2013.

[54] F.-Y. Ran, Z. Xiao, Y. Toda, H. Hiramatsu, H. Hosono, and T. Kamiya, "n-type conversion of SnS by isovalent ion substitution: Geometrical doping as a new doping route," *Scientific Reports,* Article vol. 5, p. 10428, 2015.

[55] Z. Xiao, F.-Y. Ran, H. Hosono, and T. Kamiya, "Route to n-type doping in SnS," *Applied Physics Letters,* vol. 106, no. 15, p. 152103, 2015.

[56] P. Sinsermsuksakul, R. Chakraborty, S. B. Kim, S. M. Heald, T. Buonassisi, and R. G. Gordon, "Antimony-Doped Tin(II) Sulfide Thin Films," *Chemistry of Materials,* vol. 24, no. 23, pp. 4556-4562, 2012.

[57] F. Baig, Y. H. Khattak, B. Mari, S. Ullah, H. Ullah, and S. Ahmed, "Efficiency enhancement of SnS solar cell using back surface field," in *2018 1st International Conference on Power, Energy and Smart Grid (ICPESG)*, 2018, pp. 1-5.

[58] J. Xu and Y. Yang, "Study on the performances of SnS heterojunctions by numerical analysis," *Energy Conversion and Management,* vol. 78, pp. 260-265, 2014.

[59] M. Sugiyama, K. T. R. Reddy, N. Revathi, Y. Shimamoto, and Y. Murata, "Band offset of SnS solar cell structure measured by X-ray photoelectron spectroscopy," *Thin Solid Films,* vol. 519, no. 21, pp. 7429-7431, 2011.

[60] J. Kim, J. Kim, S. Yoon, J.-y. Kang, C.-W. Jeon, and W. Jo, "Single Phase Formation of SnS Competing with SnS2 and Sn2S3 for Photovoltaic Applications: Optoelectronic Characteristics of Thin-Film Surfaces and Interfaces," *The Journal of Physical Chemistry C,* vol. 122, no. 6, pp. 3523-3532, 2018.

[61] J. M. Skelton, L. A. Burton, A. J. Jackson, F. Oba, S. C. Parker, and A. Walsh, "Lattice dynamics of the tin sulphides SnS_2, SnS and Sn_2S_3: vibrational spectra and thermal transport," *Physical Chemistry Chemical Physics,* vol. 19, no. 19, pp. 12452-12465, 2017.

[62] L. A. Burton and A. Walsh, "Phase Stability of the Earth-Abundant Tin Sulfides SnS, SnS_2 and Sn_2S_3," *The Journal of Physical Chemistry C,* vol. 116, no. 45, pp. 24262-24267, 2012.

[63] L. Ehm, K. Knorr, P. Dera, A. Krimmel, P. Bouvier, and M. Mezouar, "Pressure-induced structural phase transition in the IV–VI semiconductor SnS," *Journal of Physics: Condensed Matter,* vol. 16, no. 21, p. 3545, 2004.

[64] J. A. Andrade-Arvizu, M. Courel-Piedrahita, and O. Vigil-Galán, "SnS-based thin film solar cells: perspectives over the last 25 years," *Journal of Materials Science: Materials in Electronics,* journal article vol. 26, no. 7, pp. 4541-4556, July 01 2015.

[65] B. Pałosz, W. Steurer, and H. Schulz, "Refinement of SnS2 polytypes 2H, 4H and 18R," *Acta Crystallographica Section B,* vol. 46, no. 4, pp. 449-455, 1990.

[66] L. A. Burton *et al.*, "Synthesis, Characterization, and Electronic Structure of Single-Crystal SnS, Sn_2S_3, and SnS_2," *Chemistry of Materials,* vol. 25, no. 24, pp. 4908-4916, 2013.

[67] S. Prasert, H. Jaeyeong, N. Wontae, H. A. S., and G. R. G., "Atomic Layer Deposition of Tin Monosulfide Thin Films," *Advanced Energy Materials,* vol. 1, no. 6, pp. 1116-1125, 2011.

[68] R. Schlaf, N. R. Armstrong, B. A. Parkinson, C. Pettenkofer, and W. Jaegermann, "Van der Waals epitaxy of the layered semiconductors SnSe2 and SnS2: morphology and growth modes," *Surface Science,* vol. 385, no. 1, pp. 1-14, 1997.

[69] A. Sánchez-Juárez, A. Tiburcio-Silver, and A. Ortiz, "Fabrication of SnS2/SnS heterojunction thin film diodes by plasma-enhanced chemical vapor deposition," *Thin Solid Films,* vol. 480-481, pp. 452-456, 2005.

[70] L. A. Burton *et al.*, "Electronic and optical properties of single crystal SnS2: an earth-abundant disulfide photocatalyst," *Journal of Materials Chemistry A,* 10.1039/C5TA08214E vol. 4, no. 4, pp. 1312-1318, 2016.

[71] G. Su *et al.*, "Chemical Vapor Deposition of Thin Crystals of Layered Semiconductor SnS2 for Fast Photodetection Application," *Nano Letters,* vol. 15, no. 1, pp. 506-513, 2015.

[72] A. Sanchez-Juarez and A. Ortíz, "Effects of precursor concentration on the optical and electrical properties of Sn X S Y thin films prepared by plasma-enhanced chemical

vapour deposition," *Semiconductor Science and Technology,* vol. 17, no. 9, p. 931, 2002.

[73] S. López, S. Granados, and A. Ortíz, "Spray pyrolysis deposition of Sn_2S_3 thin films," *Semiconductor Science and Technology,* vol. 11, no. 3, pp. 433-439, 1996.

[74] M. Khadraoui *et al.*, "Optical and electrical properties of Sn2S3 thin films grown by spray pyrolysis," *Solid State Communications,* vol. 150, no. 5, pp. 297-300, 2010.

[75] E. Güneri, F. Göde, B. Boyarbay, and C. Gümüş, "Structural and optical studies of chemically deposited Sn2S3 thin films," *Materials Research Bulletin,* vol. 47, no. 11, pp. 3738-3742, 2012.

[76] D. I. Bletskan, "Phase equilibrium in the binary systems A^{IV} B^{VI} Part. III Systems Sn-Chalcogenides," *Journal of Ovonic Research* vol. 1, no. 5, pp. 61-69, 2005.

[77] E. C. Greyson, J. E. Barton, and T. W. Odom, "Tetrahedral Zinc Blende Tin Sulfide Nano- and Microcrystals," *Small,* vol. 2, no. 3, pp. 368-371, 2006.

[78] A. Walsh and G. W. Watson, "Influence of the Anion on Lone Pair Formation in Sn(II) Monochalcogenides: A DFT Study," *The Journal of Physical Chemistry B,* vol. 109, no. 40, pp. 18868-18875, 2005.

[79] J. M. Skelton, L. A. Burton, F. Oba, and A. Walsh, "Chemical and Lattice Stability of the Tin Sulfides," *The Journal of Physical Chemistry C,* vol. 121, no. 12, pp. 6446-6454, 2017.

[80] A. Rabkin, S. Samuha, R. E. Abutbul, V. Ezersky, L. Meshi, and Y. Golan, "New Nanocrystalline Materials: A Previously Unknown Simple Cubic Phase in the SnS Binary System," *Nano Letters,* vol. 15, no. 3, pp. 2174-2179, 2015.

[81] A. R. H. F. Ettema, R. A. de Groot, C. Haas, and T. S. Turner, "Electronic structure of SnS deduced from photoelectron spectra and band-structure calculations," *Physical Review B,* vol. 46, no. 12, pp. 7363-7373, 1992.

[82] L. S. Price, I. P. Parkin, A. M. E. Hardy, R. J. H. Clark, T. G. Hibbert, and K. C. Molloy, "Atmospheric Pressure Chemical Vapor Deposition of Tin Sulfides (SnS, Sn2S3, and SnS2) on Glass," *Chemistry of Materials,* vol. 11, no. 7, pp. 1792-1799, 1999.

[83] V. Robles, J. F. Trigo, C. Guillén, and J. Herrero, "SnS absorber thin films by co-evaporation: Optimization of the growth rate and influence of the annealing," *Thin Solid Films,* vol. 582, pp. 249-252, 2015.

[84] T. J. Whittles, L. A. Burton, J. M. Skelton, A. Walsh, T. D. Veal, and V. R. Dhanak, "Band Alignments, Valence Bands, and Core Levels in the Tin Sulfides SnS, SnS_2, and Sn_2S_3: Experiment and Theory," *Chemistry of Materials,* vol. 28, no. 11, pp. 3718-3726, 2016.

[85] S. Cheng and G. Conibeer, "Physical properties of very thin SnS films deposited by thermal evaporation," *Thin Solid Films,* vol. 520, no. 2, pp. 837-841, 2011.

[86] S. N. Nwankwo, S. Campbell, K. T. R. Reddy, N. S. Beattie, V. Barrioz, and G. Zoppi, "Temperature controlled properties of sub-micron thin SnS films," *Semiconductor Science and Technology,* vol. 33, no. 6, p. 065002, 2018.

[87] B. D. Malone, A. Gali, and E. Kaxiras, "First principles study of point defects in SnS," *Physical Chemistry Chemical Physics,* 10.1039/C4CP03010A vol. 16, no. 47, pp. 26176-26183, 2014.

[88] Y. Kumagai, L. A. Burton, A. Walsh, and F. Oba, "Electronic Structure and Defect Physics of Tin Sulfides, *Physical Review Applied,* vol. 6, no. 1, p. 014009, 2016.

[89] T. H. Sajeesh, N. Poornima, C. S. Kartha, and K. P. Vijayakumar, "Unveiling the defect levels in SnS thin films for photovoltaic applications using photoluminescence technique," *Physica Status Solidi (A),* vol. 207, no. 8, pp. 1934-1939, 2010.

[90] T. H. Sajeesh, K. B. Jinesh, M. Rao, C. S. Kartha, and K. P. Vijayakumar, "Defect levels in SnS thin films prepared using chemical spray pyrolysis," *physica status solidi (a),* vol. 209, no. 7, pp. 1274-1278, 2012.

[91] L. A. Burton, Y. Kumagai, A. Walsh, and F. Oba, "DFT investigation into the underperformance of sulfide materials in photovoltaic applications," *Journal of Materials Chemistry A,* 10.1039/C7TA00673J vol. 5, no. 19, pp. 9132-9140, 2017.

[92] W. Shockley and H. J. Queisser, "Detailed Balance Limit of Efficiency of p-n Junction Solar Cells," *Journal of Applied Physics,* vol. 32, no. 3, pp. 510-519, 1961.

[93] J. J. Loferski, "Theoretical Considerations Governing the Choice of the Optimum Semiconductor for Photovoltaic Solar Energy Conversion," *Journal of Applied Physics,* vol. 27, no. 7, pp. 777-784, 1956.

[94] A. Rothwarf and K. W. Böer, "Direct conversion of solar energy through photovoltaic cells," *Progress in Solid State Chemistry,* vol. 10, pp. 71-102, 1975.

[95] P. A. Nwofe, K. T. R. Reddy, J. K. Tan, I. Forbes, and R. W. Miles, "Thickness Dependent Optical Properties of Thermally Evaporated SnS Thin Films," *Physics Procedia,* vol. 25, no. 0, pp. 150-157, 2012.

[96] M. Sharon and K. Basavaswaran, "Photoelectrochemical behaviour of tin monosulphide," *Solar Cells,* vol. 25, no. 2, pp. 97-107, 1988.

[97] B. Subramanian, C. Sanjeeviraja, and M. Jayachandran, "Cathodic electrodeposition and analysis of SnS films for photoelectrochemical cells," *Materials Chemistry and Physics,* vol. 71, no. 1, pp. 40-46, 2001.

[98] Y. Kawano, J. Chantana, and T. Minemoto, "Impact of growth temperature on the properties of SnS film prepared by thermal evaporation and its photovoltaic performance," *Current Applied Physics,* vol. 15, no. 8, pp. 897-901, 2015.

[99] V. R. Minnam Reddy, S. Gedi, C. Park, M. R.W, and R. R. K.T, "Development of sulphurized SnS thin film solar cells," *Current Applied Physics,* vol. 15, no. 5, pp. 588-598, 2015.

[100] P. Sinsermsuksakul *et al.*, "Enhancing the efficiency of SnS solar cells via band-offset engineering with a zinc oxysulfide buffer layer," *Applied Physics Letters,* vol. 102, no. 5, p. 053901, 2013.

[101] H. H. Park *et al.*, "Co-optimization of SnS absorber and Zn(O,S) buffer materials for improved solar cells," *Progress in Photovoltaics: Research and Applications,* vol. 23, no. 7, pp. 901-908, 2015.

[102] V. Steinmann *et al.*, "3.88% efficient tin sulfide solar cells using congruent thermal evaporation," *Advanced Materials,* vol. 26, no. 44, pp. 7488-7492, 2014.

[103] G. Biswajit, D. Madhumita, B. Pushan, and D. Subrata, "Fabrication of the SnS/ZnO heterojunction for PV applications using electrodeposited ZnO films," *Semiconductor Science and Technology,* vol. 24, no. 2, p. 025024, 2009.

[104] A. Schneikart, H. J. Schimper, A. Klein, and W. Jaegermann, "Efficiency limitations of thermally evaporated thin-film SnS solar cells," *Journal of Physics D: Applied Physics,* vol. 46, no. 30, pp. 1-7, 2013.

[105] T. Ikuno, R. Suzuki, K. Kitazumi, N. Takahashi, N. Kato, and K. Higuchi, "SnS thin film solar cells with $Zn_{1-x}Mg_xO$ buffer layers," *Applied Physics Letters,* vol. 102, no. 19, p. 193901, 2013.

[106] J. Nelson, *The Physics of Solar Cells* (The Physics of Solar Cells).

[107] J. M. Phillips, "Substrate Selection for Thin-Film Growth," *MRS Bulletin,* vol. 20, no. 4, pp. 35-39, 2013.

[108] N. Revathi, S. Bereznev, J. Iljina, M. Safonova, E. Mellikov, and O. Volobujeva, "PVD grown SnS thin films onto different substrate surfaces," *Journal of Materials Science: Materials in Electronics,* vol. 24, no. 12, pp. 4739-4744, 2013.

[109] M. A. Martinez and C. Guillén, "Comparison between large area dc-magnetron sputtered and e-beam evaporated molybdenum as thin film electrical contacts," *Journal of Materials Processing Technology,* vol. 143-144, pp. 326-331, 2003.

[110] V. Steinmann *et al.*, "The impact of sodium contamination in tin sulfide thin-film solar cells," *APL Materials,* vol. 4, no. 2, p. 026103, 2016.

[111] D. Schmid, M. Ruckh, and H. W. Schock, "A comprehensive characterization of the interfaces in Mo/CIS/CdS/ZnO solar cell structures," *Solar Energy Materials and Solar Cells,* vol. 41-42, pp. 281-294, 1996.

[112] M. Wang, M. A. Hossain, and K.-L. Choy, "Effect of sodium treatment on the performance of electrostatic spray assisted vapour deposited copper-poor $Cu(In,Ga)(S,Se)_2$ solar cells," *Scientific reports,* vol. 7, no. 1, pp. 6788-6788, 2017.

[113] A. Basak, A. Hati, A. Mondal, U. P. Singh, and S. K. Taheruddin, "Effect of substrate on the structural, optical and electrical properties of SnS thin films grown by thermal evaporation method," *Thin Solid Films,* vol. 645, pp. 97-101, 2018.

[114] M. Devika, N. K. Reddy, F. Patolsky, and K. R. Gunasekhar, "Ohmic contacts to SnS films: Selection and estimation of thermal stability," *Journal of Applied Physics,* vol. 104, no. 12, p. 124503, 2008.

[115] L. A. Burton and A. Walsh, "Band alignment in SnS thin-film solar cells: Possible origin of the low conversion efficiency," *Applied Physics Letters,* vol. 102, no. 13, pp. 132111-3, 2013.

[116] N. K. Reddy, M. Devika, and K. R. Gunasekhar, "Stable and low resistive zinc contacts for SnS based optoelectronic devices," *Thin Solid Films,* vol. 558, pp. 326-329, 2014.

[117] M. Patel and A. Ray, "Evaluation of Back Contact in Spray Deposited SnS Thin Film Solar Cells by Impedance Analysis," *ACS Applied Materials & Interfaces,* vol. 6, no. 13, pp. 10099-10106, 2014.

[118] R. E. Banai, M. W. Horn, and J. R. S. Brownson, "A review of tin (II) monosulfide and its potential as a photovoltaic absorber," *Solar Energy Materials and Solar Cells,* vol. 150, pp. 112-129, 2016.

[119] P. Pramanik, P. K. Basu, and S. Biswas, "Preparation and characterization of chemically deposited tin(II) sulphide thin films," *Thin Solid Films,* vol. 150, no. 2, pp. 269-276, 1987.

[120] M. T. S. Nair and P. K. Nair, "Simplified chemical deposition technique for good quality SnS thin films," *Semiconductor Science and Technology,* vol. 6, no. 2, p. 132, 1991.

[121] M. Ristov, G. Sinadinovski, M. Mitreski, and M. Ristova, "Photovoltaic cells based on chemically deposited p-type SnS," *Solar Energy Materials and Solar Cells,* vol. 69, no. 1, pp. 17-24, 2001.

[122] A. Tanusevski, "Optical and photoelectric properties of SnS thin films prepared by chemical bath deposition," *Semiconductor Science and Technology,* vol. 18, no. 6, p. 501, 2003.

[123] C. Gao and H. Shen, "Influence of the deposition parameters on the properties of orthorhombic SnS films by chemical bath deposition," *Thin Solid Films,* vol. 520, no. 9, pp. 3523-3527, 2012.

[124] D. Cabrera-German, J. A. García-Valenzuela, M. Cota-Leal, M. Martínez-Gil, R. Aceves, and M. Sotelo-Lerma, "Detailed characterization of good-quality SnS thin films obtained by chemical solution deposition at different reaction temperatures," *Materials Science in Semiconductor Processing,* vol. 89, pp. 131-142, 2019.

[125] E. Güneri, F. Gode, C. Ulutaş, F. Kirmizigul, G. Altindemir, and C. Gumus, "Properties of p-type sns thin films prepared by chemical bath deposition," *Chalcogenide Letters,* vol. 7, pp. 685-694, 2010.

[126] B. Ghosh, M. Das, P. Banerjee, and S. Das, "Fabrication and optical properties of SnS thin films by SILAR method," *Applied Surface Science,* vol. 254, no. 20, pp. 6436-6440, 2008.

[127] C. Gao, H. Shen, L. Sun, H. Huang, L. Lu, and H. Cai, "Preparation of SnS films with zinc blende structure by successive ionic layer adsorption and reaction method," *Materials Letters,* vol. 64, no. 20, pp. 2177-2179, 2010.

[128] M. Jayachandran, S. Mohan, B. Subramanian, C. Sanjeeviraja, and V. Ganesan, "Studies on the brush plated SnS thin films," *Journal of Materials Science Letters,* journal article vol. 20, no. 4, pp. 381-383, 2001.

[129] N. Sato, M. Ichimura, E. Arai, and Y. Yamazaki, "Characterization of electrical properties of SnS thin films prepared by the electrochemical deposition method," in *3rd World Conference onPhotovoltaic Energy Conversion, 2003. Proceedings of*, 2003, vol. 1, pp. 38-41.

[130] M. V. Junie Jhon and I. Masaya, "Fabrication of Electrodeposited SnS/SnO 2 Heterojunction Solar Cells," *Japanese Journal of Applied Physics,* vol. 51, no. 10S, p. 10NC38, 2012.

[131] K. T. Ramakrishna Reddy, P. Purandhara Reddy, P. K. Datta, and R. W. Miles, "Formation of polycrystalline SnS layers by a two-step process," *Thin Solid Films,* vol. 403-404, pp. 116-119, 2002.

[132] S. Mutsumi *et al.*, "Sulfurization growth of SnS thin films and experimental determination of valence band discontinuity for SnS-related solar cells," *Japanese Journal of Applied Physics,* vol. 50, no. 5S2, p. 05FH03, 2011.

[133] T. Hirano, T. Shimizu, K. Yoshida, and M. Sugiyama, "Sulfurization growth of SnS films and fabrication of ZnO/SnS heterojunction for solar cells," in *37th IEEE Photovoltaic Specialists Conference*, 2011, pp. 1280-1282.

[134] Q. Ji, H. L. Shen, F. Jiang, W. Wang, and Y. H. Zeng, "Research on the optoelectronic properties of SnS thin films prepared by two-stage process," presented at the Imaging Science and Photochemistry, 2013.

[135] G.-P. Wei *et al.*, "Investigation on SnS film by RF sputtering for photovoltaic application," in *Proceedings of 1994 IEEE 1st World Conference on Photovoltaic Energy Conversion - WCPEC (A Joint Conference of PVSC, PVSEC and PSEC)*, 1994, vol. 1, pp. 365-368 vol.1.

[136] L. Zhao *et al.*, "In situ growth of SnS absorbing layer by reactive sputtering for thin film solar cells," *RSC Advances,* vol. 6, no. 5, pp. 4108-4115, 2016.

[137] V. K. Arepalli, Y. Shin, and J. Kim, "Influence of working pressure on the structural, optical, and electrical properties of RF-sputtered SnS thin films," *Superlattices and Microstructures,* vol. 122, pp. 253-261, 2018.

[138] H. Nozaki, M. Onoda, M. Sekita, K. Kosuda, and T. Wada, "Variation of lattice dimensions in epitaxial SnS films on MgO(001)," *Journal of Solid State Chemistry,* vol. 178, no. 1, pp. 245-252, 2005.

[139] W. Wang *et al.*, "Molecular beam epitaxy growth of high quality p-doped SnS van der Waals epitaxy on a graphene buffer layer," *Journal of Applied Physics,* vol. 111, no. 9, p. 093520, 2012.

[140] S. F. Wang, W. Wang, W. K. Fong, Y. Yu, and C. Surya, "Tin Compensation for the SnS Based Optoelectronic Devices," *Scientific reports,* vol. 7, pp. 39704-39704, 2017.

[141] A. Tanuševski and D. Poelman, "Optical and photoconductive properties of SnS thin films prepared by electron beam evaporation," *Solar Energy Materials and Solar Cells,* vol. 80, no. 3, pp. 297-303, 2003.

[142] J. Henry, K. Mohanraj, S. Kannan, S. Barathan, and G. Sivakumar, "Structural and optical properties of SnS nanoparticles and electron-beam-evaporated SnS thin films," *Journal of Experimental Nanoscience,* vol. 10, no. 2, pp. 78-85, 2015.

[143] S. Gedi, V. R. M. Reddy, J.-y. Kang, and C.-W. Jeon, "Impact of high temperature and short period annealing on SnS films deposited by E-beam evaporation," *Applied Surface Science,* vol. 402, pp. 463-468, 2017.

[144] Yanuar, G. E.-H. Moussa, F. Guastavino, and C. Llinares, "Preparation and characterization of SnS thin films obtained by close-spaced vapor transport for solar cell application," in *IEEE proceedings: Mediterranean Conference for Environment and Solar.* , Beirut, Lebanon, 2000, pp. 66-68.

[145] Y. Hamzah, F. Guastavino, C. Llinares, K. Djessas, and G. Masse, "SnS thin films grown by close-spaced vapor transport," *Journal of Materials Science Letters,* vol. 19, pp. 2135-2137, 2000.

[146] T. Sall, M. Mollar, and B. Marí, "Substrate influences on the properties of SnS thin films deposited by chemical spray pyrolysis technique for photovoltaic applications," *Journal of Materials Science,* journal article vol. 51, no. 16, pp. 7607-7613, 2016.

[147] T. Sall, B. M. Soucase, M. Mollar, and J. A. Sans, "SnS Thin Films Prepared by Chemical Spray Pyrolysis at Different Substrate Temperatures for Photovoltaic Applications," *Journal of Electronic Materials,* journal article vol. 46, no. 3, pp. 1714-1719, 2017.

[148] G. H. Yue, Y. D. Lin, X. Wen, L. S. Wang, Y. Z. Chen, and D. L. Peng, "Synthesis and characterization of the SnS nanowires via chemical vapor deposition," *Applied Physics A,* journal article vol. 106, no. 1, pp. 87-91, 2012.

[149] P. Kevin, D. J. Lewis, J. Raftery, M. Azad Malik, and P. O'Brien, "Thin films of tin(II) sulphide (SnS) by aerosol-assisted chemical vapour deposition (AACVD) using tin(II) dithiocarbamates as single-source precursors," *Journal of Crystal Growth,* vol. 415, pp. 93-99, 2015.

[150] A. J. Clayton, S. J. C. Irvine, C. M. E. Charbonneau, P. Siderfin, and V. Barrioz, "A new approach to thin-film SnS PV using MOCVD," *Materials Research Innovations,* vol. 19, no. 7, pp. 477-481, 2015.

[151] J.-P. Park *et al.*, "Preparation of SnS Thin Films by MOCVD Method Using Single Source Precursor, Bis(3-mercapto-1-propanethiolato) Sn(II)," *Bulletin of the Korean Chemical Society,* vol. 33, no. 10, 2012.

[152] A. J. Clayton, C. M. E. Charbonneau, W. C. Tsoi, P. J. Siderfin, and S. J. C. Irvine, "One-step growth of thin film SnS with large grains using MOCVD," *Science and Technology of Advanced Materials,* vol. 19, no. 1, pp. 153-159, 2018.

[153] L. L. Cheng *et al.*, "Preparation of SnS films using solid sources deposited by the PECVD method with controllable film characters," *Journal of Alloys and Compounds,* vol. 545, pp. 122-129, 2012.

[154] J. Chen, P. Liu, M. Chen, S. Wang, G. Wang, and M. Liu, "Fabrication of SnS Using PECVD Method With Combined Solid Sources," *IEEE Transactions on Plasma Science,* vol. 42, no. 10, pp. 2792-2793, 2014.

[155] I.-H. Baek *et al.*, "Synthesis of SnS Thin Films by Atomic Layer Deposition at Low Temperatures," *Chemistry of Materials,* vol. 29, no. 19, pp. 8100-8110, 2017.

[156] K. Reddy, P. Prathap, and R. Miles, "Thin films of tin sulphide for application in photovoltaic solar cells," presented at the Photovoltaics: Developments, Applications and Impact. Energy Science, Engineering and Technology, New York, 2010.

[157] K. L. Chopra, *Thin Film Phenomena*. New York: McGraw-Hil, 1969.

[158] J. A. Venables, *Introduction to Surface and Thin Film Processes*. Cambridge: Cambridge University Press, 2000, p. 372.

[159] K. Deraman, S. Sakrani, B. B. Ismatl, W. Yussof, and R. D. Gould, "Electrical conductivity measurements in evaporated tin sulphide thin films," *International Journal of Electronics,* vol. 76, pp. 917-922, 1994.

[160] P. A. Nwofe, K. T. R. Reddy, J. K. Tan, I. Forbes, and R. W. Miles, "On the Structural and Optical Properties of SnS Films Grown by Thermal Evaporation Method," *Journal of Physics: Conference Series,* vol. 417, no. 1, p. 012039, 2013.

[161] N. K. Reddy, Y. B. Hahn, M. Devika, H. R. Sumana, and K. R. Gunasekhar, "Temperature-dependent structural and optical properties of SnS films," *Journal of Applied Physics,* vol. 101, no. 9, p. 093522, 2007.

[162] N. K. Reddy, M. Devika, Y.-B. Hahn, and K. R. Gunasekhar, "Impact of chemical treatment on the surface, structure, optical and electrical properties of SnS thin films," *Applied Surface Science,* vol. 268, pp. 317-322, 2013.

[163] N. K. Reddy, "Growth-Temperature Dependent Physical Properties of SnS Nanocrystalline Thin Films," *ECS Journal of Solid State Science and Technology,* vol. 2, pp. 259-263, 2013.

[164] S. Hegde, K. Ag, R. Karuppannan, K. Chandrasekharan, and P. Murahari, "Preparation and Characterization of SnS Thin Films for Solar Cell Application," *International Journal of Soft Computing and Engineering (IJSCE),* vol. 1, pp. 24-26, 2011.

[165] M. Devika *et al.*, "Thickness effect on the physical properties of evaporated SnS films," *Journal of the electrochemical society,* vol. 154, pp. 67-73, 2007.

[166] P. A. Priyal Jain, "Parameters influencing the optical properties of SnS thin films," *Journal of Semiconductors* vol. 34, no. 9, pp. 26-31, 2013.

[167] D. Avellaneda, B. Krishnan, A. C. Rodriguez, T. Roy, and S. Shaji, "Heat treatments in chemically deposited SnS thin films and their influence in CdS/SnS photovoltaic structuresLE," *Journal of Materials Science: Materials in Electronics,* vol. 26, pp. 5585-5592, 2015.

[168] M. Devika, N. K. Reddy, K. Ramesh, K. R. Gunasekhar, E. S. R. Gopal, and K. T. R. Reddy, "Influence of annealing on physical properties of evaporated SnS films," *Semiconductor Science and Technology,* vol. 21, no. 8, p. 1125, 2006.

[169] J. Xu, Y. Yang, and Z. Xie, "Effect of vacuum annealing on the properties of sputtered SnS thin films," *Chalcogenide Letters,* vol. 11, no. 10, pp. 485-491, 2014.

[170] P. A. Nwofe, R. W. Miles, and K. T. R. Reddy, "Effects of sulphur and air annealing on the properties of thermally evaporated SnS layers for application in thin film solar cell devices," *Journal of Renewable and Sustainable Energy,* vol. 5, no. 1, p. 011204, 2013.

[171] M. Ristov, G. Sinadinovski, I. Grozdanov, and M. Mitreski, "Chemical deposition of tin (II) sulphide thin films," *Thin Solid Films,* vol. 173, no. 1, pp. 53-58, 1989.

[172] K. Hartman *et al.*, "Impact of H_2S annealing on SnS device performance," in *2014 IEEE 40th Photovoltaic Specialist Conference (PVSC)*, 2014, pp. 0362-0364.

[173] S. D. Mare *et al.*, "A study of SnS recrystallization by post deposition treatment," in *2016 IEEE 43rd Photovoltaic Specialists Conference*, 2016, pp. 0431-0434.

[174] R. Naidu *et al.*, "Impact of vacuum and nitrogen annealing on HVE SnS photoabsorber films," *Materials Science in Semiconductor Processing,* vol. 71, pp. 252-257, 2017.

[175] S. Polivtseva *et al.*, "Post-deposition thermal treatment of sprayed SnS films," *Thin Solid Films,* vol. 633, pp. 179-184, 2017.

[176] O. E. Ogah, K. R. Reddy, G. Zoppi, I. Forbes, and R. W. Miles, "Annealing studies and electrical properties of SnS-based solar cells," *Thin Solid Films,* vol. 519, no. 21, pp. 7425-7428, 2011.

[177] M. Burgelman, P. Nollet, and S. Degrave, "Modelling polycrystalline semiconductor solar cells," *Thin Solid Films,* vol. 361-362, pp. 527-532, 2000.

[178] H. Ullah and B. Marí, "Numerical analysis of SnS based polycrystalline solar cells," *Superlattices and Microstructures,* vol. 72, pp. 148-155, 2014.

[179] M. M. Ivashchenko, A. S. Opanasyuk, I. P. Buryk, and D. V. Kuz'min, "Numerical Simulation of SnS-Based Solar Cells," *Journal of Nano- and Electronic Physics,* vol. 10, no. 3, p. 03004, 2018.

[180] S. Zhang, *Organic Nanostructured Thin Film Devices and Coatings for Clean Energy* Boca Raton: CRC Press, 2010, p. 254.

[181] A. M. A. Haleem and M. Ichimura, "Experimental determination of band offsets at the SnS/CdS and SnS/InSxOy heterojunctions," *Journal of Applied Physics,* vol. 107, no. 3, p. 034507, 2010.

[182] M. Sugiyama, T. Shimizu, D. Kawade, K. Ramya, and K. T. R. Reddy, "Experimental determination of vacuum-level band alignments of SnS-based solar cells by photoelectron yield spectroscopy," *Journal of Applied Physics,* vol. 115, no. 8, p. 083508, 2014.

[183] K. S. S. Harsha, *Principles of vapor deposition of thin films* New York: Elsevier Ltd, 2006, p. 1160.

[184] D. A. Jameel, "Thin film deposition processes " *International Journal of Modern Physics and Applications,* vol. 1, no. 4, pp. 193-199, 2015.

[185] L. Eckertova, *Physics of thin films*, Second revised ed. New York: Plenum press, 1986, p. 340.

[186] X. Tan *et al.*, "Study on the effect of film formation process and deposition rate on the orientation of the CsI:Tl thin film," *Journal of Crystal Growth,* vol. 476, pp. 64-68, 2017.

[187] P. J. Kelly and R. D. Arnell, "Magnetron sputtering: a review of recent developments and applications," *Vacuum,* vol. 56, no. 3, pp. 159-172, 2000.

[188] C. Dida Georgiana, A. Mihai, A. Roxana, M. Adnana, O. C. Andrei, and D. Munteanu, "Magnetic sputtering technique used for coatings deposition; technologies and applications," presented at the 7th International Conference on Materials Science and Engineering, Brasov, 2011.

[189] M. Hughes, "What is Sputtering? Magnetron Sputtering ",

[190] J. Singh, F. Quli, D. E. Wolfe, J. T. Schriempf, and J. Singh, "An overview: Electron beam-physical vapor deposition technology-present and future applications," P. S. U. Applied Research Laboratory, Ed., ed 1999.

[191] J. Y. Choi, K.-J. Kim, J.-B. Yoo, and D. Kim, "Properties of cadmium sulfide thin films deposited by chemical bath deposition with ultrasonication," *Solar Energy,* vol. 64, no. 1, pp. 41-47, 1998.

[192] R. A. Bourdreau and R. D. Rauh, "Chemical Bath Deposition of Thin Film Cadmium Selenide for Photoelectrochemical Cells," *Journal of the Electrochemical Society,* vol. 130, pp. 513-516, 1983.

[193] D. Lincot and R. Ortega, "Chemical bath deposition of cadmium sulfide thin films. In situ growth and structural studies by combined quartz crystal microbalance and electrochemical impedance techniques," *Journal of the Electrochemical Society,* vol. 1398, pp. 1880-1889, 1992.

[194] P. C. Rieke and S. B. Bentjen, "Deposition of cadmium sulfide films by decomposition of thiourea in basic solution," *Chemistry of Materials,* vol. 5, pp. 43-53, 1993.

[195] N. R. Pavaskar, C. A. Menezes, and A. P. B. Sinha, "Photoconductive CdS films by a chemical bath deposition process," *Journal of the Electrochemical Society,* vol. 124, pp. 743-748, 1977.

[196] H. Il'chuk, P. Shapoval, and V. Kusnezh, "Chemical surface deposition of CdS ultra thin films from aqueous solutions," *InTech* 2011.

[197] D. Abou-Ras, T. Kirchartz, and U. Rau, *Advanced characterization techniques for thin film solar cells*. Weinheim, Germany: Wiley-Vch Verlag GmbH & Co. KGaA., 2011.

[198] Ariswan, H. Sutrisno, and R. Prasetyawati, "Crystal Structure, Optical, and Electrical Properties of SnSe and SnS Semiconductor Thin Films Prepared by Vacuum Evaporation Techniques for Solar Cell Applications," *IOP Conference Series: Materials Science and Engineering,* vol. 202, no. 1, p. 012042, 2017.

[199] V. D. Mote, Y. Purushotham, and B. N. Dole, "Williamson-Hall analysis in estimation of lattice strain in nanometer-sized ZnO particles," *Journal of Theoretical and Applied Physics,* vol. 6, no. 1, p. 6, 2012.

[200] P. Jain and P. Arun, "Influence of grain size on the band-gap of annealed SnS thin films," *Thin Solid Films,* vol. 548, pp. 241-246, 2013.

[201] B. Ghosh, R. Bhattacharjee, P. Banerjee, and S. Das, "Structural and optoelectronic properties of vacuum evaporated SnS thin films annealed in argon ambient," *Applied Surface Science,* vol. 257, no. 8, pp. 3670-3676, 2011.

[202] F. Ballipinar and A. C. Rastogi, "Tin sulfide (SnS) semiconductor photo-absorber thin films for solar cells by vapor phase sulfurization of Sn metallic layers using organic sulfur source," *Journal of Alloys and Compounds,* vol. 728, pp. 179-188, 2017.

[203] S. Di Mare *et al.*, "SnS Thin Film Solar Cells: Perspectives and Limitations," *Coatings,* vol. 7, no. 2, p. 34, 2017.

[204] S. Martín, G. Zoppi, R. Aninat, I. Forbes, and C. Guillén, "Study of the Al-grading effect in the crystallisation of chalcopyrite CuIn1−xAlxSe2 thin films," *Materials Chemistry and Physics,* vol. 140, no. 1, pp. 236-242, 2013.

[205] A. Axelevitch and G. Golan, "Hot-probe method for evaluation of majority charged carriers concentration in semiconductor thin films," *Electronics and Energetics,* vol. 26, no. 3, pp. 187-195, 2013.

[206] F. Mesa *et al.*, "Junction formation of Cu(3)BiS(3) investigated by Kelvin probe force microscopy and surface photovoltage measurements," *Beilstein journal of nanotechnology,* vol. 3, pp. 277-284, 2012.

[207] J. C. Bernède, N. Barreau, S. Marsillac, and L. Assmann, "Band alignment at *β*-In_2S_3/TCO interface," *Applied Surface Science,* vol. 195, no. 1, pp. 222-228, 2002.

[208] Y. Kwon, J. Seo, Y. Kang, D. Kim, and J. Kim, "Bifacial CdS/CdTe thin-film solar cells using a transparent silver nanowire/indium tin oxide back contact," *Optics Express,* vol. 26, no. 2, pp. A30-A38, 2018.

[209] X. Yang, B. Chen, J. Chen, Y. Zhang, W. Liu, and Y. Sun, "ZnS thin film functionalized as back surface field in Si solar cells," *Materials Science in Semiconductor Processing,* vol. 74, pp. 309-312, 2018.

[210] S. Lee, S. Kim, S. Shin, Z. Jin, and Y.-S. Min, "Band structure of amorphous zinc tin oxide thin films deposited by atomic layer deposition," *Journal of Industrial and Engineering Chemistry,* vol. 58, pp. 328-333, 2018.

[211] V. Quemener *et al.*, "The work function of n-ZnO deduced from heterojunctions with Si prepared by ALD," *Journal of Physics D: Applied Physics,* vol. 45, no. 31, p. 315101, 2012.

[212] M. M. El-Nahass, H. M. Zeyada, M. S. Aziz, and N. A. El-Ghamaz, "Optical properties of thermally evaporated SnS thin films," *Optical Materials,* vol. 20, no. 3, pp. 159-170, 2002.

[213] K. Durose, M. A. Cousins, D. S. Boyle, J. Beier, and D. Bonnet, "Grain boundaries and impurities in CdTe/CdS solar cells," *Thin Solid Films,* vol. 403-404, pp. 396-404, 2002.

[214] M. Emziane, K. Durose, D. P. Halliday, N. Romeo, and A. Bosio, "The distribution of impurities in the interfaces and window layers of thin-film solar cells," *Journal of Applied Physics,* vol. 97, no. 11, p. 114910, 2005.

[215] R. Dhere *et al.*, "Effect of Na incorporation on the growth and properties of CdTe/CdS devices," *in 31st IEEE Photovoltaic Specialists Conference,* pp. 279-282, 2005.

[216] W. M. HLAINGOo, J. L. Johnson, A. Bhatia, E. A. Lund, M. M. Nowell, and M. A. Scarpulla, "Grain Size and Texture of Cu2ZnSnS4 Thin Films Synthesized by Cosputtering Binary Sulfides and Annealing: Effects of Processing Conditions and Sodium," *Journal of Electronic Materials,* journal article vol. 40, no. 11, p. 2214, 2011.

[217] P. A. Nwofe, K. T. R. Reddy, and R. W. Miles, "Influence of Deposition Time on the Properties of Highly-Oriented SnS Thin Films Prepared Using the Thermal Evaporation Method," *Advanced Materials Research,* vol. 602-604, pp. 1409-1412, 2013.

[218] S. Sohila *et al.*, "Synthesis and characterization of SnS nanosheets through simple chemical route," *Materials Letters,* vol. 65, no. 8, pp. 1148-1150, 2011.

[219] Y. Azizian-Kalandaragh, A. Khodayari, Z. Zeng, C. S. Garoufalis, S. Baskoutas, and L. C. Gontard, "Strong quantum confinement effects in SnS nanocrystals produced by ultrasound-assisted method," *Journal of Nanoparticle Research,* journal article vol. 15, no. 1, p. 1388, 2013.

[220] B. G. Jeyaprakash, R. A. kuma, K.Kesavan, and A. Amalarani, "structural and optical characterisation of spray deposited SnS thin film," *Journal of American Science,* vol. 6, pp. 22-26, 2010.

[221] S. Sohila, M. Rajalakshmi, C. Ghosh, A. K. Arora, and C. Muthamizhchelvan, "Optical and Raman scattering studies on SnS nanoparticles," *Journal of Alloys and Compounds,* vol. 509, no. 19, pp. 5843-5847, 2011.

[222] S. A. Bashkirov, V. F. Gremenok, V. A. Ivanov, V. V. Lazenka, and K. Bente, "Tin sulfide thin films and Mo/p-SnS/n-CdS/ZnO heterojunctions for photovoltaic applications," *Thin Solid Films,* vol. 520, no. 17, pp. 5807-5810, 2012.

[223] A. S. Hassanien and A. A. Akl, "Influence of composition on optical and dispersion parameters of thermally evaporated non-crystalline Cd50S50−xSex thin films," *Journal of Alloys and Compounds,* vol. 648, pp. 280-290, 2015.

[224] I. Studenyak, M. Kranjčec, and M. Kurik, "Urbach rule in solid state physics," *International Journal of Optics and Applications,* vol. 4, pp. 76-83, 2014.

[225] Y. Gupta and P. Arun, "Influence of Urbach tail on the refractive index of p-SnS thin films," *physica status solidi c,* vol. 14, no. 1-2, p. 1600207, 2017.

[226] T. Raadik, M. Grossberg, J. Raudoja, R. Traksmaa, and J. Krustok, "Temperature-dependent photoreflectance of SnS crystals," *Journal of Physics and Chemistry of Solids,* vol. 74, no. 12, pp. 1683-1685, 2013.

[227] H. R. Chandrasekhar, R. G. Humphreys, U. Zwick, and M. Cardona, "Infrared and Raman spectra of the IV-VI compounds SnS and SnSe," *Physical Review B,* vol. 15, no. 4, pp. 2177-2183, 1977.

[228] Y. Azizian-Kalandaragh, A. Khodayari, Z. Zeng, C. S. Garoufalis, S. Baskoutas, and L. C. Gontard, "Strong quantum confinement effects in SnS nanocrystals produced by ultrasound-assisted method," *Journal of Nanoparticle Research,* p. 1388, 2013.

[229] M. Devika, N. K. Reddy, K. Ramesh, V. Ganesan, E. S. R. Gopal, and K. T. R. Reddy, "Influence of substrate temperature on surface structure and electrical resistivity of the

evaporated tin sulphide films," *Applied Surface Science,* vol. 253, no. 3, pp. 1673-1676, 2006.

[230] N. R. Mathews, C. Colín García, and I. Z. Torres, "Effect of annealing on structural, optical and electrical properties of pulse electrodeposited tin sulfide films," *Materials Science in Semiconductor Processing,* vol. 16, no. 1, pp. 29-37, 2013.

[231] D R Lide ed, *CRC Handbook of Chemistry and Physics Internet Version*. Boca Raton, FL: CRC Press, 2005.

[232] H. Metin Gubur and R. Esen, "Annealing studies on CBD grown US thin films," *Journal of Crystal Growth,* vol. 258, pp. 141-148, 2003.

[233] M. C. S. Kumar and T. S. Reddy, "Effect of substrate temperature on the physical properties of co- evaporated Sn2S3 thin films," *Ceramics International* vol. 42, pp. 12262-12269, 2016.

[234] R. Mariappan, T. Mahalingam, and V. Ponnuswamy, "Preparation and characterization of electrodeposited SnS thin films," *Optik - International Journal for Light and Electron Optics,* vol. 122, no. 24, pp. 2216-2219, 2011.

[235] E. R. Shaaban, M. S. A. El-Sadek, M. El-Hagary, and I. S. Yahia, "Spectroscopic ellipsometry investigations of the optical constants of nanocrystalline SnS thin films," *Physica Scripta,* vol. 86, no. 1, p. 015702, 2012.

[236] S. Sarkar, N. S. Das, and K. K. Chattopadhyay, "Optical constants, dispersion energy parameters and dielectric properties of ultra-smooth nanocrystalline BiVO4 thin films prepared by rf-magnetron sputtering," *Solid State Sciences,* vol. 33, pp. 58-66, 2014.

[237] S. H. Wemple and M. DiDomenico, "Behavior of the Electronic Dielectric Constant in Covalent and Ionic Materials," *Physical Review B,* vol. 3, no. 4, pp. 1338-1351,1971.

[238] M. V. Reddy, P. Babu, K. T. R. Reddy, and R. W. Miles, "X-ray photoelectron spectroscopy and X-ray diffraction studies on tin sulfide films grown by sulfurization process," *Journal of Renewable and Sustainable Energy,* vol. 5, no. 3, p. 031613, 2013.

[239] M. Cruz, J. Morales, J. P. Espinos, and J. Sanz, "XRD, XPS and 119Sn NMR study of tin sulfides obtained by using chemical vapor transport methods," *Journal of Solid State Chemistry,* vol. 175, no. 2, pp. 359-365, 2003.

[240] K. T. Ramakrishna Reddy, P. A. Nwofe, and R. W. Miles, "Determination of the minority carrier diffusion length of SnS using electro-optical measurements," *Electronic Materials Letters,* journal article vol. 9, no. 3, pp. 363-366, 2013.

[241] L. Makinistian and E. A. Albanesi, "Study of the hydrostatic pressure on orthorhombic IV–VI compounds including many-body effects," *Computational Materials Science,* vol. 50, no. 10, pp. 2872-2879, 2011.

[242] G. Zoppi, K. Durose, S. J. C. Irvine, and V. Barrioz, "Grain and crystal texture properties of absorber layers in MOCVD-grown CdTe/CdS solar cells," (in English), *Semiconductor Science and Technology,* Article vol. 21, no. 6, pp. 763-770, 2006.

[243] J. S. Cruz, K. M. Leyva, N. R. Mathews, A. M. Galván, and X. Mathew, "Physical properties of vacuum evaporated tin sulfide thin films," *Chalcogenide Letters,* vol. 12, pp. 415-427, 2015.

[244] P. N. Jaya, R. Jayakrishnan, B. C. Nandu, and R. K. Pandey, "In situ Sb-doped CdTe films," *Semiconductor Science and Technology,* vol. 13, no. 3, p. 340, 1998.

[245] E. Guneri, C. Gumus, F. Mansur, and F. Kirmizigul, "Studies on the properties of sprayed SnO_2 thin films as a function of substrate-nozzle distance and substrate temperature," *Optoelectronics and Advanced Materials - Rapid Communications,* vol. 3, pp. 383-389, 2009.

[246] S. Lalitha, S. Ramakrishnan, S. Senthilarasu, A. Subbarayan, and K. Natarajan, "Characterization of CdTe thin film - Dependence of structural and optical properties on temperature and thickness," *Solar Energy Materials and Solar Cells,* vol. 82, pp. 187-199, 2004.

[247] R. Sathyamoorthy, S. K. Narayandass, and D. Mangalaraj, "Effect of substrate temperature on the structure and optical properties of CdTe thin film," *Solar Energy Materials and Solar Cells,* vol. 76, no. 3, pp. 339-346, 2003.

[248] T. Tosuke and M. Sugiyama, "PL properties and defects of SnS layers based on n-type buffer layers/p-type SnS structures," *Japanese Journal of Applied Physics,* vol. 58, no. 5, p. 051004, 2019.

[249] M. F. Ashby, Material profiles: materials and the environment 2nd edition Boston: Butterworth-Heinemann, 2013, pp. 459-595.

[250] E. Yu, S.-C. Kim, H. J. Lee, K. H. Oh, and M.-W. Moon, "Extreme wettability of nanostructured glass fabricated by non-lithographic, anisotropic etching," *Scientific reports,* vol. 5, pp. 9362-9362, 2015.

[251] Plansee. (2019). *Molybdenum - a good all-rounder, material properties of molybdenum*

[252] L. Optex, "Quartz slide & coverslips ", ed: Laser optex Inc., 2019.

[253] M. Nasr Saleh and G. Lubineau, "Understanding the mechanisms that change the conductivity of damaged ITO-coated polymeric films: A micro-mechanical investigation," *Solar Energy Materials and Solar Cells,* vol. 130, pp. 199-207, 2014.

[254] T. Ashida *et al.*, "Thermal transport properties of polycrystalline tin-doped indium oxide films," *Journal of Applied Physics,* vol. 105, no. 7, p. 073709, 2009.

[255] Ossila, "Ossila enabling materials science: FTO coated glass ", ed: Ossila Ltd, 2019.

[256] C. Agashe, J. Hüpkes, G. Schöpe, and M. Berginski, "Physical properties of highly oriented spray-deposited fluorine-doped tin dioxide films as transparent conductor," *Solar Energy Materials and Solar Cells,* vol. 93, no. 8, pp. 1256-1262, 2009.

[257] J. D. Walker, H. Khatri, V. Ranjan, J. Li, R. W. Collins, and S. Marsillac, "Electronic and structural properties of molybdenum thin films as determined by real-time spectroscopic ellipsometry," *Applied Physics Letters,* vol. 94, no. 14, p. 141908, 2009.

[258] J. L. Holbrough, J. M. Campbell, F. C. Meldrum, and H. K. Christenson, "Topographical control of crystal nucleation," *Crystal Growth and Design,* vol. 12, no. 2, pp. 750-755, 2012.

[259] S. A. Bashkirov, V. F. Gremenok, V. A. Ivanov, V. V. Shevtsova, and P. P. Gladyshev, "Influence of substrate material on the microstructure and optical properties of hot wall deposited SnS thin films," *Thin Solid Films,* vol. 585, pp. 40-44, 2015.

[260] D. Avellaneda, B. Krishnan, A. C. Rodriguez, T. K. Das Roy, and S. Shaji, "Heat treatments in chemically deposited SnS thin films and their influence in CdS/SnS photovoltaic structuresLE," *Journal of Materials Science: Materials in Electronics,* vol. 26, pp. 5585-5592, 2015.

[261] A. Clayton, S. Irvine, C. M. E. Charbonneau, P. Siderfin, and V. Barrioz, *A new approach to thin-film SnS PV using MOCVD*. 2015, pp. 477-481.

[262] S. Di Mare *et al.*, "A study of SnS recrystallization by post deposition treatment," presented at the IEEE 43rd photovoltaic specialists conference (PVSC), 2016.

[263] J. D. Major, R. E. Treharne, L. J. Phillips, and K. Durose, "A low-cost non-toxic post-growth activation step for CdTe solar cells," *Nature,* vol. 511, p. 334, 2014.

[264] D. Mudusu, K. R. Nandanapalli, S. Reddy, R. Karuppannan, and K. Gunasekhar, "Influence of rapid thermal annealing (RTA) on the structural and electrical properties of SnS films," *Journal of Materials Science: Materials in Electronics,* vol. 20, no. 11, pp. 1129-1134, 2009.

[265] G. Bree, C. Coughlan, H. Geaney, and K. M. Ryan, "Investigation into the Selenization Mechanisms of Wurtzite CZTS Nanorods," *ACS Applied Materials & Interfaces,* vol. 10, no. 8, pp. 7117-7125, 2018.

[266] G. Chen, W. Wang, B. Zhang, S. Chen, Z. Huang, and B. Zhuang, "Influence of selenization atmosphere on the Cu2ZnSn(S,Se)4 thin films and its correlation to the performance of solar cells," *Materials Research Bulletin,* vol. 94, pp. 164-169, 2017.

[267] T. Mahalingam, D. Vikraman, G. Ravi, R. Chandramohan, K. Adaikalam, and J.-K. Rhee, "Role of Deposition Potential on the Optical Properties of SnSSe Thin Films," *Electrochemical society transactions,* vol. 35, no. 37, pp. 1-10, 2011.

[268] V. Dhanasekaran, K. Sundaram, J. Jung, and T. Mahalingam, "Microstructural properties evaluation of SnSSe alloy films," *Journal of Materials Science: Materials in Electronics,* journal article vol. 26, no. 3, pp. 1641-1648, 2015.

[269] S. Luo, X. Qi, H. Yao, X. Ren, Q. Chen, and J. Zhong, "Temperature-Dependent Raman Responses of the Vapor-Deposited Tin Selenide Ultrathin Flakes," *The Journal of Physical Chemistry C,* vol. 121, no. 8, pp. 4674-4679, 2017.

[270] R. S. Yadav, P. Mishra, R. Mishra, M. Kumar, and A. C. Pandey, "Growth mechanism and optical property of CdS nanoparticles synthesized using amino-acid histidine as chelating agent under sonochemical process," *Ultrasonics Sonochemistry,* vol. 17, no. 1, pp. 116-122, 2010.

[271] B. Pejova and I. Grozdanov, "Semiconducting In_2S_3 quantum dots in thin film form: sonochemical versus conventional chemical synthesis and investigation of their structural and optical properties," *Czechoslovak Journal of Physics,* vol. 56, no. 1, pp. 75-84, 2006.

[272] V. L. Gayou, B. Salazar Hernández, R. Delgado Macuil, G. Zavala, P. Santiago, and A. I. Oliva, "Structural Studies of ZnS Nanoparticles by High Resolution Transmission Electron Microscopy," *Journal of Nano Research,* vol. 9, pp. 125-132, 2010.

[273] M. A. Islam *et al.*, "Comparison of Structural and Optical Properties of CdS Thin Films Grown by CSVT, CBD and Sputtering Techniques," *Energy Procedia,* vol. 33, pp. 203-213, 2013.

[274] D. J. Kim, Y. M. Yu, J. W. Lee, and Y. D. Choi, "Investigation of energy band gap and optical properties of cubic CdS epilayers," *Applied Surface Science,* vol. 254, no. 22, pp. 7522-7526, 2008.

[275] P. E. Rodríguez-Hernández *et al.*, "Structural and optical properties of In_2S_3 thin films grown by chemical bath deposition on pet flexible substrates," *Chalcogenide Letters,* vol. 14, pp. 331-335, 2017.

[276] K. Benyahia, A. Benhaya, and M. S. Aida, "ZnS thin films deposition by thermal evaporation for photovoltaic applications," *Journal of Semiconductors,* vol. 36, no. 10, p. 103001, 2015.

[277] D. H. Hwang, J. H. Ahn, K. N. Hui, K. S. Hui, and Y. G. Son, "Structural and optical properties of ZnS thin films deposited by RF magnetron sputtering," *Nanoscale Research Letters,* journal article vol. 7, no. 1, p. 26, 2012.

[278] S. B. Khan, S. Irfan, Z. Zhuanghao, and S. L. Lee, "Influence of Refractive Index on Antireflectance Efficiency of Thin Films," (in eng), *Materials (Basel),* vol. 12, no. 9, p. 1483, 2019.

[279] D. Wan, H.-L. Chen, T.-C. Tseng, C.-Y. Fang, Y.-S. Lai, and F.-Y. Yeh, "Antireflective Nanoparticle Arrays Enhance the Efficiency of Silicon Solar Cells," *Advanced Functional Materials,* vol. 20, no. 18, pp. 3064-3075, 2010.

[280] S. Rasool, G. Phaneendra Reddy, K. T. Ramakrishna Reddy, M. Tivanov, and V. F. Gremenok, "Effect of Substrate Temperature on Structural and Optical Properties of In_2S_3 Thin Films Grown by Thermal Evaporation," *Materials Today: Proceedings,* vol. 4, no. 14, pp. 12491-12495, 2017.

[281] C. Sanz, C. Guillén, M. T. Gutiérrez, and J. Herrero, "Investigation of optical, structural, and chemical properties of indium sulfide thin films evaporated at low temperature by modulated flux deposition," *physica status solidi (a),* vol. 210, no. 2, pp. 320-326, 2013.

[282] R. L. Anderson, "Germanium-Gallium Arsenide Heterojunctions [Letter to the Editor]," *IBM Journal of Research and Development,* vol. 4, no. 3, pp. 283-287, 1960.

[283] G. B. Turner, R. J. Schwartz, and J. L. Gray, "Band discontinuity and bulk vs. interface recombination in $CdS/CuInSe_2$ solar cells," presented at the 20th IEEE PV Specialist Conference, Las Vegas, 1988.

[284] Y. Hashimoto, K. Takeuchi, and K. Ito, "Band alignment at $CdS/CuInS_2$ heterojunction," *Applied Physics Letters,* vol. 67, no. 7, pp. 980-982, 1995.

[285] G. Shoushuai *et al.*, "Interfaces of high-efficiency kesterite Cu 2 ZnSnS(e) 4 thin film solar cells," *Chinese Physics B,* vol. 27, no. 1, p. 018803, 2018.

[286] T. Minemoto *et al.*, "Theoretical analysis of the effect of conduction band offset of window/CIS layers on performance of CIS solar cells using device simulation," *Solar Energy Materials and Solar Cells,* vol. 67, no. 1, pp. 83-88, 2001.

[287] A. Yago *et al.*, "Comparison of buffer layers on SnS thin-film solar cells prepared by co-evaporation," *physica status solidi c,* vol. 14, no. 6, p. 1600194, 2017.